Antenna Miniaturization in Complex Electromagnetic Environments

Designs and Measurements of Electrically Small Antennas for Hearing-Aid Applications

Zhang, Jiaying

Publication date:
2011

Document Version
Publisher's PDF, also known as Version of record

Technical University
of Denmark

Antenna Miniaturization in Complex Electromagnetic Environments:

Designs and Measurements of Electrically Small Antennas for Hearing-Aid Applications

Jiaying Zhang

February 2011

DTU Electrical Engineering
Department of Electrical Engineering

Technical University of Denmark
Department of Electrical Engineering
Electromagnetic Systems
DK-2800 Kgs. Lyngby
Denmark

Submitted in partial fulfillment of the requirements for the degree of Doctor of Philosophy at the Technical University of Denmark.

Preface

This dissertation presents the research work during my study towards a Ph.D. degree in the Electromagnetic Systems Group (EMS), Electrical Engineering Department, Technical University of Denmark (DTU).

The Ph.D. project is part of a major project "Wireless Coupling in Small Autonomous Apparatus" carried out from 2007-2011 in a cooperation between the Technical University of Denmark (Danmarks Tekniske Universitet), Danish Technological Institute (Teknologisk Institut), and Widex with financial support from the Danish National Advanced Technology Foundation (Højteknologifonden). The Ph.D. project constitutes one of six work packages in the major project and deals with antenna miniaturization; primarily for hearing-aid applications. This is a relatively new field for wireless technology in general and antenna technology in particular, and there was no fixed specifications for the antenna performance and parameters from the outset of the Ph.D. project. The wireless communication link budget was developed through an iterative process during the course of the project; e.g. several operation frequencies were considered and investigated before the final frequency was chosen about 2 years into the project. Also, the choice of the specific hearing-aids for which the antenna prototype should be developed was not made before 2 years into the project. For this reason, the antenna designs and investigations presented in this thesis are for various frequencies and various antenna sizes, and most are of a general nature not readily suitable for a specific hearing-aid. Furthermore, the project was conducted under a confidentiality agreement between the 3 partners and in consequence this thesis does not provide specific information about the hearing-aids, the communication link, and precise antenna designs for specific hearing-aids. The thesis documents an investigation of miniaturized loop antennas, the development of new measurement techniques for miniaturized antennas, and an

investigation of the influence of the human head on the antenna performance. While all efforts have been exercised to respect the confidentiality agreement, it will be clear to the reader that the research work is aimed at hearing-aid applications.

Acknowledgements

First and foremost, I would like to express my sincere thanks to my supervisors Olav Breinbjerg and Sergey Pivnenko, for giving me your inspirations, supports, suggestions and comments in my project during the past three years. I would like to thank Anne Kok for helping me to translate part of my dissertation into Danish.

I spent six years in the EMS group, DTU, including my master study. The wonderful international working environment in the group let me have a joyful stay in Denmark. I thank all my colleagues and friends in Denmark who assisted during this dissertation. I would also like to thank all the dissertation committee members for their time spending in reviewing this work.

My special thanks go to Professor Richard W. Ziolkowski, for receiving me two weeks to visit his group. This is a very memorable experience for me. I am very grateful to have the opportunity to work with him and his Ph.D. students, Chin-Ching Lin and Ning Zhu.

Finally, this dissertation is dedicated to my parents, Xiujuan Bao and Jinxiang Zhang, for their support through all these years.

Lyngby, Feb 2011

Jiaying Zhang

Abstract

Hearing-aids today constitute devices with an advanced technology, and wireless communication integrated into hearing-aids will introduce a range of completely new functionalities. The antenna is an important component in any wireless system, and the demand for compact wireless systems with stringent specifications makes the antenna size reduction a significant challenge. Antenna miniaturization is thus one of the key technologies in designing a successful wireless unit for the hearing-aid application. This dissertation is focused on three areas that are related to the integration of a wireless communication system into the heading-aids, and these are the antenna miniaturization, the measurement techniques for electrically small antennas and the influence of complex environments on the characteristics of electrically small antennas, respectively.

Antenna Miniaturization
In this dissertation, we present several novel designs of electrically small loop antennas for the hearing-aid application. First antenna design is a two-dimensional (2-D) planar differential-fed electrically small loop. The working mechanism of this antenna is based on the capacitive loading and the inductive coupling between two small loops. An analytical model, simulations, fabrications and measurements are presented for this antenna. Second antenna design is a planar two-turn electrically small loop antenna. The working mechanism of this antenna is based on the capacitive loading, and both the capacitive and inductive coupling between two small loops that are of a comparable size are taken into account. An analytical model is provided to give a guidance in the impedance tuning. Third, several three-dimensional (3-D) folded electrically small loop antennas are proposed, the properties of which are significantly improved compared to the 2-D planar electrically small loop antennas.

Measurement Techniques for ESAs
In this dissertation we proposed two novel measurement techniques for electrically small antennas. A modified Wheeler cap method for the radiation efficiency measurement of balanced electrically small antennas is proposed. This method provides the following advantages. First, no balun is required during the measurement and thus the problems of narrow impedance bandwidth and extra scattering effect caused by the balun are avoided. As a result, the proposed method is valid in a broad frequency band. Second, the application of proposed method and the proper use of the circle fitting for the measured scattering parameters ensure that the cavity resonances do not have any significant effect on the measurement results. By using the Wheeler cap method in the proposed way, most of its limitations and disadvantages are avoided. The method is, therefore, suitable for input impedance and radiation efficiency measurement for most types of antennas in a broad frequency band. The antennas under test are not limited to be electrically small and these can be balanced or unbalanced, symmetric or asymmetric type. Moreover, the modified Wheeler cap method for measurements of small antennas in complex environments is further developed. A cable-free impedance and gain measurement technique for electrically small antennas is also proposed. The electromagnetic model of this technique is derived by using the spherical wave expansion, and it is valid for arbitrary electrically small AUT at arbitrary distances between the probe and AUT. The whole measurement setup is modeled by the cascade of three coupled multiple-port networks. The electromagnetic model, the simulation results, and the obtained measurement results are presented.

Influence of the Complex Environments on ESA Characteristics
The influence of complex environments on the characteristics of electrically small antennas is also investigated such as the human head phantom and the hearing-aids. First, the sensitivity analysis of the head phantom parameters on the antenna characteristics is presented, including the influence of the head permittivity and conductivity. Second, the sensitivity analysis of the positions of electrically small antennas is presented, including the orientations and locations of antennas and the distance between the small antenna and head. Third, the influence of the hearing-aid shell material on the antenna characteristics is investigated.

Jiaying Zhang

Resumé

Allerede i dag omfatter høreapparater avanceret teknologi, og integration af trådløs kommunikation i apparaterne vil muliggøre en række helt nye funktionaliteter. Antennen er en vigtig komponent i ethvert trådløst system, og efterspørgslen efter kompakte trådløse systemer med strenge specifikationer gør minimering af antennens størrelse til en betydelig udfordring. Minimering af antennen er derfor en af de centrale teknologier ved design af en vellykket trådløs enhed til høreapparatanvendelser.

I denne afhandling præsenterer vi en række nye designs af elektrisk små sløjfeantenner til høreapparatanvendelser. Først beskrives designet af en plan, differentiel input, elektrisk lille sløjfeantenne. Virkemåden er baseret på den kapacitive belastning og den induktive kobling mellem to små sløjfer. Den analytiske model, simuleringer, fremstilling og målinger præsenteres. Dernæst foreslås en to-vindings elektrisk lille sløjfeantenne. Virkemåden er baseret på den kapacitive belastning og både den kapacitive og den induktive kobling mellem to sløjfer, som er sammenlignelige i størrelse. Den analytiske model fremlægges for at give hjælp til impedanstuningen. For det tredje foreslås flere tre-dimensionelle (3-D) foldede elektriske små sløjfeantenner, hvis egenskaber er betydeligt forbedret i forhold til 2-D plane elektrisk små sløjfeantenner. Virkemåden er baseret på den kapacitive belastning og den induktive kobling mellem to sløjfer. Den store sløjfe er foldet på en bestemt måde for bedre at kunne udnytte enhedens volumen.

I denne afhandling har vi foreslået flere nye teknikker til måling af elektrisk små antenner (ESA'er) som kan sammenfattes, som følger. En modificeret Wheeler cap metode til måling af strålingseffektivitet af balancerede ESA'er er foreslået. Denne metode giver følgende fordele. For det første er en balun ikke nødvendig for målingen, og dermed undgås problemerne med

lille impedans båndbredde og ekstra spredning opstået pga. balunen. For det andet er den forslåede metode brugbar i et bredt frekvensbånd. For det tredje har hulrumsresonanser ingen væsentlige effekter på måleresultaterne med den rette brug af cirkel tilpasning af de målte s-parametre. Ved den rette brug af Wheeler cap metoden kan de fleste af dens begrænsninger og ulemper undgås. Metoden er derfor velegnet til måling af indgangsimpedans og strålingseffektivitet for de fleste typer antenner i et bredt frekvensområde. Antennerne er ikke begrænset til at være ESA'er, og kan være af den balancerede eller ubalancerede, og symmetriske eller asymmetriske typer. Desuden er anvendelsen af denne modificerede Wheeler cap metode i komplekse omgivelser videreudviklet. En måleteknik for kabelfri impedans og gain for ESA i komplekse omgivelser foreslås. Den elektromagnetiske model af denne teknik er udledt ved hjælp af den sfæriske bølgeekspansionsteknik, som er gyldig for vilkårlige antenner under test (AUT) på vilkårlige afstande mellem sonden og AUT. Hele målingsopsætningen er derefter modelleret som en kaskade af tre koblede multiportsnetværk. Den elektromagnetiske model, simuleringsresultater samt måleresultaterne præsenteres.

I denne afhandling præsenterer vi også den påvirkning som komplekse omgivelser har på ESA'er, såsom menneskehovedmodel og høreapparater. Først præsenteres følsomhedsanalysen af menneskehovedmodellens parametre, herunder afhængighed af hovedets permittivitet og ledningsevne. Dernæst præsenteres følsomhedsanalysen af placeringen af ESA'er, herunder orientering og placeringen af ESA'er samt afstanden mellem ESA og hoved. Endelig undersøges også indflydelsen af høreapparatets ydermateriale.

Contents

CHAPTER

ONE

Introduction

This Ph.D. project is part of a major project ”Wireless Coupling in Small Autonomous Apparatus” carried out from 2007-2011 in a cooperation between the Technical University of Denmark (Danmarks Tekniske Universitet), Danish Technological Institute (Teknologisk Institut), and Widex with financial support from the Danish National Advanced Technology Foundation (Højteknologifonden). The Ph.D. project constitutes one of six work packages in the major project and deals with antenna miniaturization; primarily for hearing-aid applications.

Hearing-aids today constitute devices with an advanced technology, and wireless communication integrated into hearing-aids will introduce a range of completely new functionalities. This Ph.D. project concerns the antenna systems for wireless communication with hearing-aids. It aims at designing highly miniaturized antennas for hearing-aids, where the antennas are not only geometrically small but also electrically small. It is noted that the antennas are to function in very complex environments that influence the performance of the antennas significantly. It is necessary to take into account this influence in the design of the small antennas. Moreover, the development of highly accurate measurement facility is necessary to investigate the characteristics of the small antennas. In this chapter, the background, justification, purpose and outline of this Ph.D. project are provided.

1.1 Background and State of the Art

In recent years, there has been a strong interest in antenna miniaturization techniques for numerous applications, such as hearing-aids, cell phones,

portable wireless equipments, sensors, RFIDs, implantable medical devices, as well as other ultra small devices [1–6]. This is because the antenna is a very crucial component in a wireless communication system, which plays the roles of transforming the RF signals into electromagnetic waves and vice versa. Nowadays for many small devices and wireless systems, their maximum dimensions are limited by the size of the antennas. The designing of highly miniaturized antennas with the acceptable bandwidth and radiation efficiency is extremely important to make the wireless devices compact.

However, it is challenging to design a small antenna with the acceptable performances for a particular application. This is due to the tradeoff fact between the performances and the dimensions of an antenna. The dimensions of an antenna are mainly determined by its working frequency, and the traditional minimum length of a resonant antenna is about one half of a wavelength at its frequency of operation. The antenna performances such as the impedance bandwidth and radiation efficiency are functions of the antenna geometry. When the antenna dimensions are reduced, its bandwidth and radiation efficiency also decrease, which are viewed as a result of the antenna miniaturization. Antenna miniaturization is a very promising technology that enables wireless communications among ultra small devices, and this is the driving force of this research. To investigate the performances of small antennas and understand their working mechanisms, several basic terms and parameters of antennas will be briefly discussed as follows.

1.1.1 Performance Parameters of Electrically Small Antennas

Electrically Small Antennas (ESAs)
An antenna is considered to be electrically small when its maximum physical dimension is much less than the free-space wavelength, λ, and thus it is noted that the frequency must be identified for the term "electrically small" to be valid. Several definitions have been given for ESAs, which are provided in [7–9]. A commonly used definition for ESAs, proposed by H. A. Wheeler [7], is that an antenna satisfies the condition

$$\frac{l}{\lambda} < \frac{1}{2\pi}, \tag{1.1}$$

where l is the maximum dimension of the antenna, λ is the working wavelength and $\lambda/2\pi$ is called radian-wavelength. Ronold W. P. King [8] defined an antenna as ESA when it satisfies the condition

$$\frac{l}{\lambda} < \frac{1}{10}. \tag{1.2}$$

In this dissertation, we adopt the definition proposed by R. C. Hansen [9] that an antenna is electrically small when

$$ka < 1, \tag{1.3}$$

where k is the wavenumber, $2\pi/\lambda$, and a is the radius of the minimum sphere enclosing the antenna. It is noted that higher order spherical modes become evanescent for $ka < 1$. By adopting this definition, a short dipole with a length less than λ/π, a small loop with a diameter less than λ/π, and a patch with a diagonal dimension less than λ/π are ESAs. In this project, we deal with small antennas that are geometrically small as well as electrically small. When the dimension of an ESA is much smaller than the free space wavelength, the ESA essentially is a capacitor or inductor with a certain amount of radiation. The difference between the ESAs and lumped components is that there is the radiation provided by ESAs, although the amount may be small. In general, there are three basic types of ESAs, which are the small electric dipole, the small magnetic dipole and the combination of them.

Several important parameters are being used to characterize the performances of ESAs. Here we concern about the most important ones, which are the directivity $D(\theta, \phi)$, radiation efficiency e_{rad}, gain $G(\theta, \phi)$, quality factor Q and impedance bandwidth BW. These parameters are presented and explained as follows before we start to discuss the ESAs.

Antenna Directivity $D(\theta, \phi)$
In the usual spherical (r, θ, ϕ) coordinate system, the electric far fields $\vec{E}(r, \theta, \phi)$ are expressed as [10]

$$\vec{E}(r, \theta, \phi) = \frac{\exp(-jkr)}{r}\vec{F}(\theta, \phi), \tag{1.4}$$

where k is the wave number and $\vec{F}(\theta, \phi)$ is the radiation vector. The magnetic far fields $\vec{H}(r, \theta, \phi)$ are then written as

$$\vec{H}(r, \theta, \phi) = \frac{\exp(-jkr)}{\eta_0 r}\hat{r} \times \vec{F}(\theta, \phi), \tag{1.5}$$

where η_0 is the intrinsic impedance of vacuum. The Poynting vector $\vec{S}(r, \theta, \phi)$ is defined as

$$\vec{S}(r, \theta, \phi) = \frac{1}{2}\vec{E}(r, \theta, \phi) \times \vec{H}^*(r, \theta, \phi) = \frac{F^2(\theta, \phi)}{2\eta_0 r^2}\hat{r}, \tag{1.6}$$

where $F(\theta, \phi) = |\vec{F}(\theta, \phi)|$. Then the radiated power P_{rad} is determined by integrating the power flow density, $S(r, \theta, \phi)$, over the far field radiation sphere

that is

$$P_{rad} = \int \int_{\text{Radiation Sphere}} S(r,\theta,\phi) r^2 \sin\theta d\theta d\phi. \tag{1.7}$$

where $S(r,\theta,\phi)$ is given by $S(r,\theta,\phi) = \frac{F^2(\theta,\phi)}{2\eta_0 r^2}$. The radiation intensity $U(\theta,\phi)$ is defined as the radiated power per unit solid angle which is

$$U(\theta,\phi) = \frac{dP_{rad}(\theta,\phi)}{d\Omega} = S(r,\theta,\phi) r^2, \tag{1.8}$$

where Ω is the solid angle. The directivity $D(\theta,\phi)$ is an important parameter which describes how the antenna radiates power in different directions. $D(\theta,\phi)$ is defined as the ratio of the radiation intensity in the direction (θ,ϕ) to the averaged radiation intensity in all directions [10].

$$D(\theta,\phi) = \frac{U(\theta,\phi)}{\frac{1}{4\pi}\int_0^{2\pi}\int_0^{\pi} U(\theta,\phi)\sin\theta d\theta d\phi}. \tag{1.9}$$

It is noted that the directivity is a function of the direction (θ,ϕ) to the far-field observation point. In many cases only the maximum directivity of an antenna is provided in the antenna specification datasheet. The maximum directivity D_{max} is a single constant that is

$$D_{max} = \max[D(\theta,\phi)]. \tag{1.10}$$

For the $\hat{z}$-directed ESAs that radiate the electric or magnetic Hertzian dipole mode, the electric field intensity is proportional to the factor $\sin\theta$, and the maximum directivity is D_{max}=1.5.

Antenna Radiation Efficiency e_{rad}

The radiation efficiency e_{rad} of an antenna is defined as the ratio of the radiated power P_{rad} to the accepted power P_{acc} that is [10]

$$e_{rad} = \frac{P_{rad}}{P_{acc}} = \frac{P_{rad}}{P_{rad} + P_{loss}}, \tag{1.11}$$

where $P_{acc} = P_{rad} + P_{loss}$ and P_{loss} represents the power due to the ohmic loss. The radiation efficiency e_{rad} can also be expressed in terms of the radiation resistance R_{rad} and ohmic loss resistance R_{loss}, which is

$$e_{rad} = \frac{R_{rad}}{R_{rad} + R_{loss}}, \tag{1.12}$$

where R_{rad} and R_{loss} are the equivalent resistances in which the power P_{rad} and P_{loss} are dissipated.

Moreover, another commonly used term is the overall efficiency of an antenna, which includes all possible losses for an antenna. It is defined as the ratio of the total radiated power P_{rad} to the input power P_{input}, that is

$$e_{overall} = \frac{P_{rad}}{P_{input}} = \frac{P_{rad}}{P_{acc}/(1-|\Gamma|^2)} = (1-|\Gamma|^2)e_{rad}, \tag{1.13}$$

where Γ is the reflection coefficient at the input terminal of an antenna.

Antenna Gain $G(\theta, \phi)$
The gain of an antenna in the direction (θ, ϕ) is determined from the directivity $D(\theta, \phi)$ and its radiation efficiency e_{rad}, that is

$$G(\theta, \phi) = e_{rad} D(\theta, \phi). \tag{1.14}$$

The maximum antenna gain, G_{max}, is often provided for an antenna, which is

$$G_{max} = \max[G(\theta, \phi)]. \tag{1.15}$$

Similarly, the realized gain of an antenna in the direction (θ, ϕ) can be determined from

$$G_{realized}(\theta, \phi) = (1-|\Gamma|^2)e_{rad} D(\theta, \phi). \tag{1.16}$$

Antenna Quality Factor Q
The quality factor, Q, of an antenna is defined to be 2π times the ratio of the maximum stored energy to the dissipated and radiated energy during one period of the time-harmonic field, that is

$$Q = 2\pi \frac{W_{stored}}{P_{acc}T} = 2\pi \frac{W_{stored}}{(P_{dissipated} + P_{rad})T} = \frac{2\omega \max(W_e, W_m)}{P_{dissipated} + P_{rad}}, \tag{1.17}$$

where W_{stored} is the stored energy, W_e and W_m are the time-average stored electric and magnetic energy, P_{rad} and $P_{dissipated}$ are the radiated and dissipated power, P_{acc} is the accepted power at the input terminal of the antenna and ω is the radian frequency. In the last expression of (1.17), the assumption of $e_{rad} = 1$ leads to the relation $P_{rad} = e_{rad}P_{acc} = P_{acc}$. Moreover, the antenna is assumed tuned to be resonant, which may be realized by the self-resonance or by adding a lossless and non-radiating lumped matching circuit.

The minimum quality factor Q of an ESA is well studied in [7, 9, 11–30]. Assuming that the antenna is enclosed by a minimum sphere with a radius a, it is well-known that the minimum quality factor Q of an ESA that radiates a single TE_{10} or TM_{10} mode is [11, 13]

$$Q_{\min,\, TE_{10}\,\text{or}\,TM_{10}} = e_{rad}\left[\frac{1}{ka} + \frac{1}{(ka)^3}\right], \tag{1.18}$$

where e_{rad} is the radiation efficiency of an ESA.

For an ESA that radiates equally excited TE_{10} and TM_{10} modes, the minimum quality factor Q becomes [13]

$$Q_{\min,\, TE_{10} \text{ and } TM_{10}} = e_{rad} \left[\frac{1}{2} \left(\frac{2}{ka} + \frac{1}{(ka)^3} \right) \right]. \tag{1.19}$$

Antenna Bandwidth BW

It is shown that several well known methods are being used to characterize Q. For ESAs, the quality factor Q is approximately inversely proportional to antenna bandwidth BW. Fante, Yaghjian and Best have studied the relations between the quality factor and fractional bandwidth of an antenna [17, 18]. These results will be summarized briefly here.

It seems that Fante [17] is the first to give the relation between the 3-dB fractional bandwidth and the quality factor of an antenna. He started the discussion by considering the input impedance of an antenna system,

$$Z = R_{rad} + jX = \frac{1}{|I|^2}[P_{rad} + j2\omega(W_m - W_e)]. \tag{1.20}$$

He showed that for a high-Q system that is resonant at $\omega = \omega_0$, there are the relations $[dR_{rad}/d\omega]|_{\omega=\omega_0} \simeq 0$ and $X(\omega_0) = 0$. The impedance Z can be further expressed by using the Taylor series expansion around ω_0 which is

$$Z = R_{rad} + jX \simeq R_{rad} + j(\omega - \omega_0)[\frac{dX(\omega)}{d\omega}]|_{\omega=\omega_0} + \cdots. \tag{1.21}$$

The half-power (3-dB) points occur when $|(\omega - \omega_0)[\frac{dX(\omega)}{d\omega}]|_{\omega=\omega_0}| = R_{rad}$, from which the fractional bandwidth can be determined from

$$BW \simeq \frac{2R_{rad}}{\omega_0[\frac{dX(\omega)}{d\omega}]|_{\omega=\omega_0}} = \frac{2P_{rad}}{\omega_0|I|^2[\frac{dX(\omega)}{d\omega}]|_{\omega=\omega_0}}. \tag{1.22}$$

Finally, the fractional bandwidth BW is found to be

$$\begin{aligned} BW &\simeq [\frac{\omega_0(W_e + W_m)}{P_{rad}} + F(\omega_0)]^{-1} = [\frac{2\omega_0 W_e}{P_{rad}} + F(\omega_0)]^{-1} \\ &= [\frac{2\omega_0 W_m}{P_{rad}} + F(\omega_0)]^{-1} = [Q + F(\omega_0)]^{-1}, \end{aligned} \tag{1.23}$$

where $F(\omega_0)$ is derived to be

$$F(\omega_0) \leq \frac{2}{BW}[\frac{\sum_{n,m} |\Delta C_{nm}|^2}{\sum_{n,m} |C_{nm}|^2}]^{1/2}. \tag{1.24}$$

The coefficients C_{nm} are proportional to the mode excitation coefficients of the TE and TM modes, and the term $\sum_{n,m} |C_{nm}|^2$ represents the total radiated power at $\omega = \omega_0$. The term $\sum_{n,m} |\Delta C_{nm}|^2$ represents the change in C_{nm} over one half of the antenna bandwidth.

It is noted that due to the presence of the term $F(\omega_0)$ the fractional bandwidth is not necessarily equal to the inverse of Q. However, for the cases where the term $F(\omega_0)$ is small, there is the following approximation

$$BW \simeq \frac{1}{Q}. \tag{1.25}$$

He also mentioned that for some special antennas such as linear radiators with a symmetric current distribution or for very small antennas, it can be shown that $F(\omega_0) = 0$. In summary, the equation (1.25) is valid under the following assumptions which are

- The antenna is a high-Q system and is lossless.
- The derivative of the radiated power tends to zero around $\omega = \omega_0$.
- The term $F(\omega_0)$ is small compared to Q, for instance, the antenna is electrically small.

Another relation between the antenna bandwidth BW and quality factor Q is given in Yaghjian and Best's work [18]. In these derivations, the antennas are assumed to be resonant antennas, which are self-resonant antennas or tuned antennas by adding a non-radiating and lossless series reactance. They derived the exact and approximated expressions of the quality factor Q for tuned antennas at resonance or antiresonance frequencies, which is expressed in terms of antenna frequency dependent impedance. It is found that Q is approximately proportional to the magnitude of the frequency derivative of the input impedance, $|Z_0^{'}(\omega_0)|$, and is valid for all frequencies. They also defined the fractional matched voltage standing wave ratio (VSWR) bandwidth, B_{VSWR}, as well as the approximated expression of B_{VSWR}. It is found that B_{VSWR} is inversely proportional to the magnitude of $|Z_0^{'}(\omega_0)|$ (approximately). Hence, the quality factor Q is inversely proportional to the fractional VSWR bandwidth, B_{VSWR}, approximately.

They started the analysis by considering the input impedance of an antenna system is

$$Z(\omega) = R(\omega) + jX(\omega). \tag{1.26}$$

When this antenna is tuned to the resonance, the input impedance of the tuned antenna becomes

$$Z_0(\omega) = R_0(\omega) + jX_0(\omega) = R_0(\omega) + j[X(\omega) + X_s(\omega)], \tag{1.27}$$

where $X_s(\omega)$ is the series reactance. At the frequency of ω_0, there is

$$X_0(\omega_0) = X(\omega_0) + X_s(\omega_0) = 0. \tag{1.28}$$

The quality factor Q of a tuned antenna is approximately determined from the antenna input impedance

$$Q(\omega_0) \simeq \frac{\omega_0}{2R(\omega_0)}|Z_0^{'}(\omega_0)| = \frac{\omega_0}{2R(\omega_0)}\sqrt{(R^{'}(\omega_0))^2 + (X^{'}(\omega_0) + \frac{X(\omega_0)}{\omega_0})^2}, \tag{1.29}$$

where $R^{'}(\omega_0)$ and $X^{'}(\omega_0)$ are the frequency derivatives of the un-tuned antenna resistance and reactance, respectively.

They also give the definition of the fractional matched VSWR bandwidth, B_{VSWR}, as well as the approximated expression of B_{VSWR}. For an antenna resonant at the frequency of ω_0, the matched VSWR bandwidth B_{VSWR} is defined as the difference between the two frequencies above and below ω_0 at which the VSWR equals a constant. Thus B_{VSWR} is given by

$$B_{VSWR}(\omega_0) = \frac{\omega^+ - \omega^-}{\omega_0} \simeq \frac{4\sqrt{\beta}R_0(\omega_0)}{\omega_0|Z_0^{'}(\omega_0)|}, \tag{1.30}$$

where ω^- and ω^+ are the two frequencies below and above ω_0. The above relation holds for the conditions that $B_{VSWR} << 1$ or $\beta \leq 1$.

Hence, a relation between the matched VSWR bandwidth B_{VSWR} and the quality factor Q is formulated as follows.

$$Q(\omega_0) \simeq \frac{2\sqrt{\beta}}{B_{VSWR}(\omega_0)}, \text{and } \sqrt{\beta} = \frac{VSWR - 1}{2\sqrt{VSWR}} \leq 1. \tag{1.31}$$

The equation (1.29) and (1.31) holds under the assumptions that the antenna exhibits a single resonance within the VSWR bandwidth and the match VSWR bandwidth is not too large.

1.1.2 Electrically Small Dipoles

In general there are three basic types of ESAs which are the small electric dipole, the small magnetic dipole and the combination of them. In this subsection, the basic physical insight and mechanisms of ESAs are explained,

by taking the small electric dipole and magnetic dipole (loop) as examples. The input impedance, bandwidth, radiation efficiency and the dependence of these performances on the electrical length of ESAs are discussed. Then a comparison between these two types of ESAs is presented.

The small electric dipole is one of the simplest types of ESAs. The radiation properties in far fields are introduced first. In a usual $r\theta\phi$-coordinate system, the electric far fields of a small dipole which is center-fed and with the center being placed at the origin are written as [31]

$$\vec{E}(r,\theta,\phi) = \frac{\exp(-jkr)}{r}\vec{F}(\theta,\phi), \tag{1.32}$$

where $\vec{F}(\theta,\phi)$ is the radiation vector and it is given by [31]

$$\vec{F}(\theta,\phi) = \frac{jk\eta}{4\pi}\hat{r}\times\hat{r}\times\vec{P}(\theta,\phi), \tag{1.33}$$

and

$$\begin{aligned}\vec{P}(\theta,\phi) &= \int_v \vec{J}(\vec{r'})\exp(jk\hat{r}\times\vec{r'})dv' \\ &= \int_v \vec{J}(\vec{r'})\exp(jk[x'\sin\theta\cos\phi + y'\sin\theta\sin\phi + z'\cos\theta])dv'\end{aligned} \tag{1.34}$$

For a $\hat{z}$-directed small dipole with its center at the origin, the radiation vector $\vec{F}(\theta,\phi)$ becomes

$$\begin{aligned}\vec{F}_{z-directed}(\theta,\phi) &= \frac{jk\eta}{4\pi}\hat{\theta}\sin\theta\int_{-l/2}^{l/2} I(z')\exp(jkz'\cos\theta)dz' \\ &\simeq \frac{jk\eta}{4\pi}\hat{\theta}\sin\theta\int_{-l/2}^{l/2} I(z')dz' \\ &\simeq \frac{jk\eta}{4\pi}\hat{\theta}\sin\theta A,\end{aligned} \tag{1.35}$$

where $A = \int_{-l/2}^{l/2} I(z')dz'$. In equation (1.35), the term $\sin\theta$ represents the element factor, and the integration term, $\int_{-l/2}^{l/2} I(z')\exp(jkz'\cos\theta)dz'$, represents the space factor. In the far field region of ESAs, we have the relation that $kz' << 1$, and thus the space factor is approximately simplified to $\int_{-l/2}^{l/2} I(z')dz'$=A, which represents the area under the curve of the electric current on the dipole. Hence, it is seen that the radiation vector $\bar{F}(\theta,\phi)$ depends on two terms, which are the element term $\sin\theta$ and the current distribution on the dipole. Since the current distribution on the wire antenna is sinusoidal

and should go to zero at the wire end, and considering the length of a small dipole is only a fraction of one wavelength, the current distribution on a small dipole can be approximated by a linear triangle, as shown in Figure 1.1. For this current distribution, the area under the curve is found to be $A = \frac{1}{2}|I_A|l$. While Figure 1.2 illustrates the current distribution of an ideal dipole with the same length, which is compared to the current distribution of the small dipole in Figure 1.1. The current distribution of the ideal dipole is uniform, and thus the curve under the current distribution is a rectangle, the area under which is $A = |I_A|l$. Hence, it is found that the radiated electric field of an ideal dipole is two times of that of the small dipole. This fact also shows that the electric field can be increased by enlarging the area under the curve of the current distribution, or in other words, by making the current distribution more uniform. Moreover, in many cases the changes in the current distribution can be realized by adding some top-loaded capacitive elements at the end of the wire antenna.

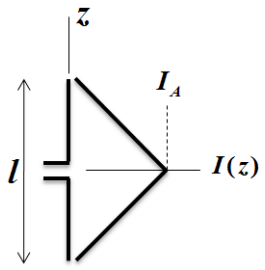

Figure 1.1: Small Dipole.

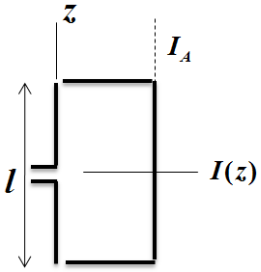

Figure 1.2: Ideal Dipole.

The input impedance of an antenna, Z_A, is composed of the real and imaginary parts, $Z_A = R_A + jX_A$, where R_A is the input resistance and X_A is the reactance, respectively. The input resistance R_A of an antenna includes the dissipations in two ways, which are the radiation and the ohmic loss on the antenna structure. Thus, R_A is expressed as $R_A = R_{rad} + R_{loss}$.

The Radiation Resistance R_{rad}

The radiation resistance, R_{rad}, is defined as the equivalent resistance in which the radiated power P_{rad} is dissipated when the current flowing through it is I_A, where I_A is the current at the input terminal of the antenna. Hence, to this end, the radiated power is related to the radiation resistance and the input electric current as

$$P_{rad} = \frac{1}{2}|I_A|^2 R_{rad}. \tag{1.36}$$

While on the other hand, the radiated power can also be determined from the

radiation vector $\bar{F}(\theta, \phi)$ that is

$$P_{rad} = \frac{1}{2\eta} \int_{4\pi} |\bar{F}(\theta, \phi)^2| \sin\theta d\theta d\phi. \tag{1.37}$$

By comparing the above two equations, together with (1.35), the expression of the radiation resistance is found to be

$$\begin{aligned} R_{rad} &= \frac{2}{|I_A|^2} \frac{1}{2\eta} \int_{4\pi} [\frac{jk\eta}{4\pi} \sin\theta A]^2 \sin\theta d\theta d\phi \\ &= \frac{80\pi^2}{\lambda^2} (\frac{A^2}{|I_A|^2}), \end{aligned} \tag{1.38}$$

where A is the area under the electric current curve and I_A is the input current at the antenna terminal. It shows that R_{rad} depends on the current distribution on the dipole, which is proportional to the square of the area under the current curve, A^2, and again R_{rad} can be increased by making the current distribution more uniform. This is the basic fact to increase the radiated field, radiation resistance and radiation efficiency of small dipoles.

For an ideal dipole, the area A is determined from $A = \int_{-l/2}^{l/2} I(z')dz' = |I_A|l$, and thus the radiation resistance equals

$$R_{rad,ideal} = \frac{80\pi^2}{\lambda^2} (\frac{A^2}{|I_A|^2}) = \frac{80\pi^2}{\lambda^2} (\frac{|I_A|^2 l^2}{|I_A|^2}) = 80\pi^2 (\frac{l}{\lambda})^2. \tag{1.39}$$

While for a small dipole, the area A is determined from $A = \int_{-l/2}^{l/2} I(z')dz' = \frac{1}{2}|I_A|l$, and thus the radiation resistance becomes

$$R_{rad,small} = \frac{80\pi^2}{\lambda^2} (\frac{A^2}{|I_A|^2}) = \frac{80\pi^2}{\lambda^2} (\frac{\frac{1}{4}|I_A|^2 l^2}{|I_A|^2}) = 20\pi^2 (\frac{l}{\lambda})^2. \tag{1.40}$$

Hence it shows that for the ideal dipole and small dipole the radiation resistance only depends on the square of the electrical length, that is $(\frac{l}{\lambda})^2$. It also shows a relation that is $R_{rad,ideal} = 4R_{rad,small}$. Figure 1.3 presents the analytical value of R_{rad} versus different electrical lengths. Moreover, several typical R_{rad} values for the small dipoles are found to be:

- $R_{rad}(\text{dipole length} = \frac{\lambda}{100}) = 0.0197\,\Omega$,
- $R_{rad}(\text{dipole length} = \frac{\lambda}{20}) = 0.4935\,\Omega$,
- $R_{rad}(\text{dipole length} = \frac{\lambda}{10}) = 1.9739\,\Omega$.

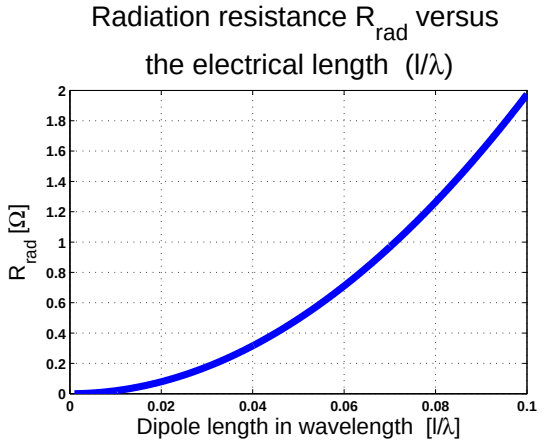

Figure 1.3: R_{rad} versus the electrical lengths.

The Ohmic Loss Resistance R_{Loss}
The ohmic loss resistance is related to the skin depth δ_s which is defined as

$$\delta_s = \frac{1}{\sqrt{\pi \mu_0 \sigma f}}, \tag{1.41}$$

where σ is the metal conductivity and $\mu_0 = 4 \times 10^{-7}\pi$ H/m is the vacuum permeability.

For an ideal dipole with a uniform current distribution, R_{loss} equals

$$R_{loss,\,ideal} \simeq \frac{l}{\sigma(2\pi a \delta_s)} = \frac{l}{2\pi a} R_s, \ (\Omega) \tag{1.42}$$

where l is the length of the wire antenna, a is the wire radius and R_s is the surface resistance which is written as

$$R_s = \frac{1}{\sigma \delta_s} = \sqrt{\frac{\pi f \mu_0}{\sigma}} = \sqrt{\frac{\omega \mu_0}{2\sigma}}, \ (\Omega) \tag{1.43}$$

The ohmic resistance of the small dipole is also less than that of the ideal dipole. R_{loss} is determined by comparing the two expressions of the dissipated power P_{loss} as follows

$$\begin{cases} P_{loss} = \frac{1}{2}\int_{-l/2}^{l/2} \frac{1}{\sigma(2\pi a \delta_s)} |I(z')|^2 dz' = \frac{1}{2}\frac{R_s}{2\pi a}\int_{-l/2}^{l/2} |I(z')|^2 dz' \\ P_{loss} = \frac{1}{2}|I_A|^2 R_{loss} \end{cases}. \tag{1.44}$$

Then the expression of $R_{loss,\,short}$ is found to be

$$R_{loss,\,short} \simeq \frac{1}{2\pi a} R_s \frac{\int_{-l/2}^{l/2} |I(z')|^2 dz'}{|I_A|^2}, \tag{1.45}$$

where

$$I(z') = I_A(1 - \frac{2|z'|}{l}),\ |z'| \leq \frac{l}{2}. \tag{1.46}$$

By using the expression of I_z in (1.46), it gives a relation that is $\frac{\int_{-l/2}^{l/2} |I(z')|^2 dz'}{|I_A|^2} = \frac{l}{3}$; thus the ohmic resistance in (1.45) becomes

$$R_{loss,\,short} \simeq \frac{R_s}{2\pi a}\frac{l}{3}, \tag{1.47}$$

which shows the ohmic resistance of a small dipole is one-third of that of an ideal dipole.

The Radiation Efficiency e_{rad}

For a small dipole with the electric current distribution on the wire being triangular, the radiation efficiency is determined by inserting (1.40) and (1.47) to (**??**) , that is

$$e_{rad} = \frac{R_{rad}}{R_{rad} + R_{loss}} = \frac{20\pi^2(\frac{l}{\lambda})^2}{20\pi^2(\frac{l}{\lambda})^2 + \frac{l}{2\pi a}\frac{R_s}{3}}. \tag{1.48}$$

Several methods are used to improve the radiation efficiency of a small dipole. For instance, the current distribution on the wire antenna can be enlarged by using the capacitive top-loaded technique, and then the radiation efficiency is found to be

$$e_{rad} = \frac{R_{rad}}{R_{rad} + R_{loss}} = \frac{\frac{80\pi^2}{\lambda^2}}{\frac{80\pi^2}{\lambda^2} + \frac{l}{2\pi a}R_s\left[\frac{\int_{l+l'} I^2(z')dz'}{(\int_{-l/2}^{l/2} I(z')dz')^2}\right]}. \tag{1.49}$$

It is noted that the integration path for the ohmic resistance is $(l + l')$, where l' accounts for the path that is added due to the loading elements. When such technique is employed, the term R_{rad} increases due to the changed current distribution and the term R_{loss} also increases due to the losses caused by the loading elements. Hence, the radiation efficiency is improved only in the case that the increase in R_{rad} is larger than that in R_{loss}.

It is found that radiation resistance and ohmic loss resistance of a small dipole are less than that of an ideal dipole of the same length. For the small dipole, its radiation resistance equals one-fourth of that of the ideal dipole, while its ohmic resistance is one-third of that of the ideal dipole. Hence, the radiation efficiency of the small dipole is lower than that of the ideal dipole.

The Reactance X_A
The ESA behaves a large input reactance. The small dipole is capacitive while the small loop is inductive. The reactance of a small dipole approximately equals [32]

$$X_A = -\frac{120}{\pi \frac{l}{\lambda}} \left[ln(\frac{l}{2a}) - 1 \right] \text{ (ohm)}. \tag{1.50}$$

Then the total input impedance of a small dipole is determined from

$$Z_A = R_{rad} + R_{ohmic} + jX_A = \left[20\pi^2 (\frac{l}{\lambda})^2 + \frac{R_s}{2\pi a} \frac{l}{3} \right] - j \frac{120}{\pi \frac{l}{\lambda}} \left[ln(\frac{l}{2a}) - 1 \right]. \tag{1.51}$$

Observations for the Small Dipole: R_{rad}, R_{loss} and e_{rad} versus the Electrical Length $\frac{l}{\lambda}$
First, the radiation resistance only depends on the square of the dipole electrical length, that is $(\frac{l}{\lambda})^2$. Second, R_{Loss} is proportional to the dipole electrical length and it also depends on the frequency of operation, which is

$$R_{loss} = \frac{l}{3} \frac{R_s}{2\pi a} = \frac{l}{6\pi a} \sqrt{\frac{\pi f \mu}{\sigma}} = (\frac{l}{\lambda}) \frac{1}{6\pi a} \sqrt{\frac{c^2 \pi \mu}{f \sigma}}. \tag{1.52}$$

The following observations are obtained for the small dipole:

- Dependence on the **electrical length** (l/λ):
  R_{rad} is proportional to the square of the electrical length, that is $(\frac{l}{\lambda})^2$, while R_{loss} is linearly proportional to the electrical length that is $(\frac{l}{\lambda})$. Hence, it is seen that the radiation efficiency increases with the increase of the electrical length, because the increase in R_{rad} is faster than that in R_{loss}.

- Dependence on the **frequency of operation**:
  As shown in (1.52), R_{loss} is proportional to $\sqrt{(1/f)}$. Hence, for the same electrical length, a higher frequency results in a lower ohmic resistance and better radiation efficiency. Figure 1.4 and Figure 1.5 illustrate R_{loss} and e_{rad} versus the electrical lengths at different frequencies.

- Dependence on the **wire radius** a:
  The thicker wire provides a larger equivalent cross section area, which is $2\pi a \delta_s$, with δ_s being the skin depth; thus R_{loss} is inversely proportional to the wire radius a. Hence, using a thick wire results in a reduction in the ohmic resistance and an increase in the radiation efficiency accordingly.

- Dependence on the **conductivity** σ:
  R_{loss} is proportional to $\sqrt{(1/\sigma)}$. Using a material of high conductivity results in a decrease in the ohmic resistance and an increase in the radiation efficiency. Typically the copper is a common choice. The comparison in R_{loss} and e_{rad} by using materials of different conductivity are given in Figure 1.4 and Figure 1.5, respectively.

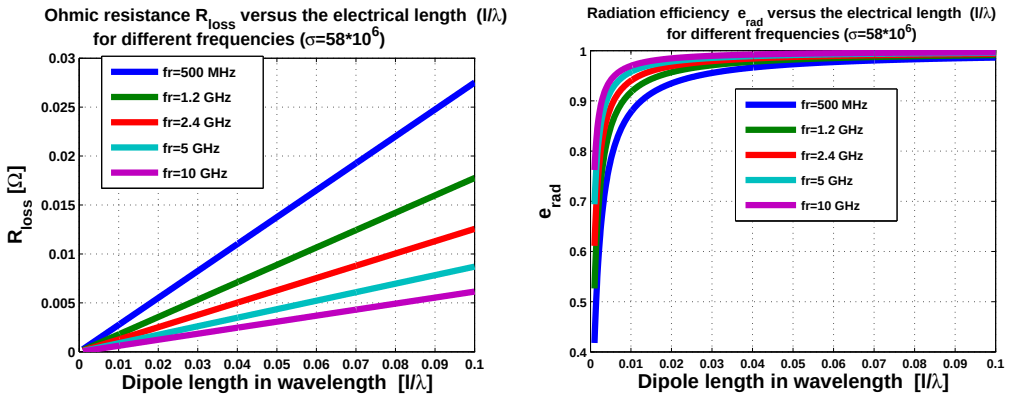

Figure 1.4: R_{loss} and e_{rad} versus the electrical lengths at different frequencies, with the conductivity being $\sigma = 58 \times 10^6 \mathrm{S/m}$.

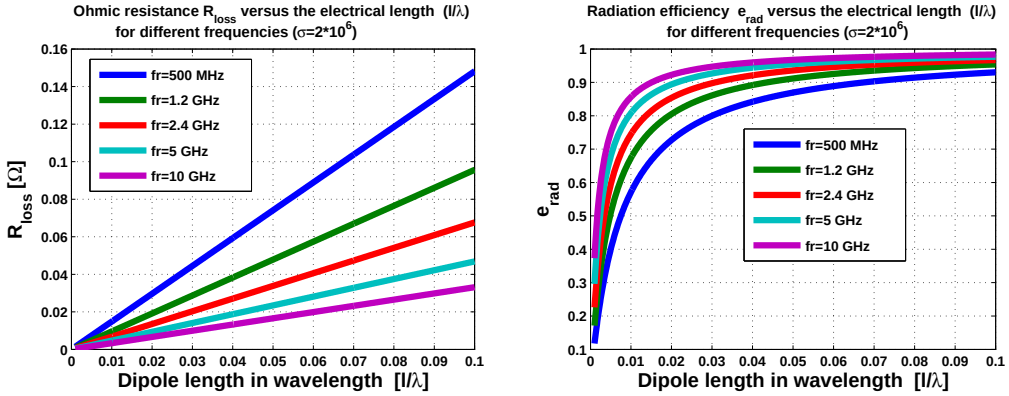

Figure 1.5: R_{loss} and e_{rad} versus the electrical lengths at different frequencies, with the conductivity being $\sigma = 2 \times 10^6 \mathrm{S/m}$.

Observations for the Small Dipole: R_{rad}, R_{loss} and e_{rad} versus the Physical Length l

For a small dipole of the same physical length l, how R_{rad}, R_{loss} and e_{rad} change with the other antenna parameters are also presented. This analysis gives the straightforward dependence of antenna performances on the

physical length, frequency, wire radius and conductivity, respectively. The expressions for R_{rad}, R_{loss}, and e_{rad} are rewritten and summarized in (1.53),

$$\begin{cases} R_{rad,smalldipole} = 20\pi^2(\frac{l}{\lambda})^2 = 20\pi^2 l^2 \frac{f^2}{c^2}, \\ R_{loss,smalldipole} = \frac{1}{3}\frac{l}{2\pi a}\sqrt{\frac{\pi f \mu}{\sigma}}, \\ e_{rad,smalldipole} = \frac{R_{rad}}{R_{rad}+R_{loss}} = \frac{20\pi^2 l^2 \frac{f^2}{c^2}}{20\pi^2 l^2 \frac{f^2}{c^2}+\frac{1}{3}\frac{l}{2\pi a}\sqrt{\frac{\pi f\mu}{\sigma}}} = \frac{20\pi^2 \frac{1}{c^2}}{20\pi^2 \frac{1}{c^2}+\frac{1}{6\pi a l}\sqrt{\frac{\pi\mu}{\sigma f^3}}}, \end{cases} \tag{1.53}$$

and the observations are summarized as follows:

- Dependence on the**physical length** l:
  It is seen from (1.53) that R_{loss} is linearly proportional to the dipole length l, while R_{rad} is proportional to the square of the physical length that is l^2. Although both R_{rad} and R_{loss} are frequency dependent, the increase in R_{rad} versus l is faster than that in R_{loss}, and thus the radiation efficiency increases as the physical length increases.

- Dependence on the **frequency of operation**:
  As shown in (1.53), R_{loss} is proportional to $\sqrt{f}$, and meanwhile R_{rad} is proportional to f^2. Hence, as the frequency increases the increase in R_{rad} is larger than that in R_{loss} and thus the radiation efficiency increases. Figure 1.6 shows the R_{loss}, R_{loss} and e_{rad} versus the dipole physical length at different frequencies.

- Dependence on the **wire radius** a:
  The thicker wire provides a larger equivalent cross area $2\pi a\delta_s$ and thus R_{loss} is inversely proportional to a. Hence, using a thick wire results in a reduction in the ohmic resistance and an increase in the radiation efficiency.

- Dependence on the **conductivity** σ:
  R_{loss} is proportional to $\sqrt{(1/\sigma)}$. Hence, using a material of high conductivity results in a reduction in the ohmic resistance and an increase in the radiation efficiency. Again, the copper is a common choice.

1.1.3 Electrically Small Loop Antennas

For an electrically small loop that is placed on the xy-plane in a usual $r\theta\phi$-coordinate with the loop center being at the origin, the radiation vector

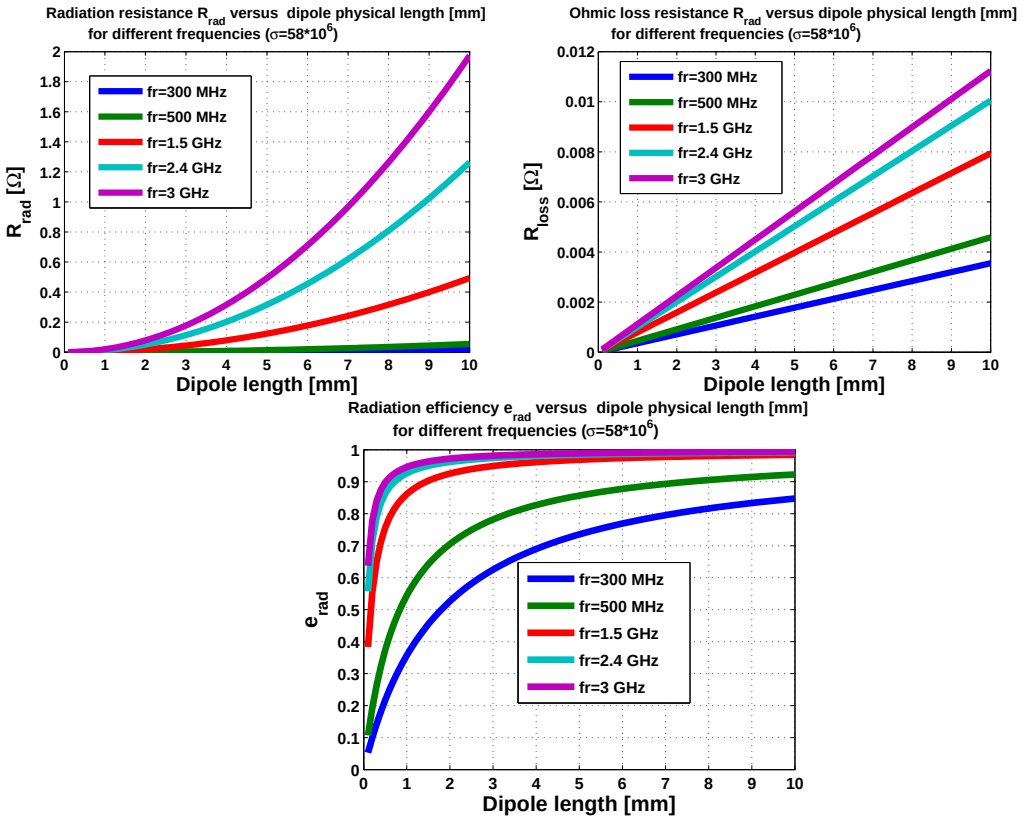

Figure 1.6: R_{rad}, R_{loss} and e_{rad} versus the dipole physical lengths at different frequencies, with the conductivity being $\sigma = 58 \times 10^6$S/m and wire radius a being 0.675 mm.

$\bar{F}(\theta, \phi)$ of this small loop is found to be

$$\begin{aligned} \bar{F}(\theta,\phi) &= \frac{jk\eta}{4\pi}\hat{r} \times \hat{r} \times \int_v \vec{J}(\vec{r'}) \exp(jk\hat{r} \times \vec{r'}) dv' \\ &\simeq \frac{k^2\eta}{4\pi}(I_A A) \sin\theta \hat{\phi}, \end{aligned} \tag{1.54}$$

where a is the wire radius, r is the loop radius, A is area cover by the loop and I_A is the input current at the loop terminal. $\vec{J}$ represents an uniform current distribution which is

$$\vec{J} = I_A \hat{\phi} \delta(\rho - r)\delta(z). \tag{1.55}$$

Similar to previous procedures for the small electric dipole, the radiation resistance is determined by comparing the expressions of P_{rad} as follows

$$\begin{cases} P_{rad} = \frac{1}{2\eta} \int_{4\pi} |\bar{F}(\theta,\phi)|^2 \sin\theta d\theta d\phi \\ P_{rad} = \frac{1}{2}|I_A|^2 R_{rad} \end{cases}. \tag{1.56}$$

Then the expression of R_{rad} is found to be

$$R_{rad} = \frac{320\pi^4}{\lambda^4}\frac{|(I_A|A)^2}{|I_A|^2} = 320\pi^4(\frac{A}{\lambda^2})^2 = 20\pi^2(\frac{l_{loop}}{\lambda})^4. \tag{1.57}$$

where l_{loop} is the loop circumference.

The ohmic resistance is determined by comparing the expressions of P_{loss} as follows

$$\begin{cases} P_{loss} = \frac{1}{2}\int_{l_{loop}} \frac{1}{\sigma(2\pi a\delta_s)} I^2(l')dl' = \frac{1}{2}\frac{R_s}{2\pi a}(|I_A|^2 l_{loop}) \\ P_{loss} = \frac{1}{2}|I_A|^2 R_{loss} \end{cases}, \tag{1.58}$$

Then the expression of R_{loss} is found to be

$$R_{loss} = \frac{l_{loop}}{2\pi a}R_s = \frac{l_{loop}}{2\pi a}\sqrt{\frac{\pi f\mu}{\sigma}} = (\frac{l_{loop}}{\lambda})\frac{1}{2\pi a}\sqrt{\frac{c^2\pi\mu}{f\sigma}}. \tag{1.59}$$

The electrically small loop is inductive and the inductance L for a small circular loop is determined from [32]

$$L = \mu a\left[ln(\frac{8a}{r}) - 1.75\right]. \tag{1.60}$$

For the small loop, the radiation resistance R_{rad} is proportional to $(l_{loop}/\lambda)^4$, while R_{loss} is proportional to (l_{loop}/λ), as shown in (1.57) and (1.59). It is found that e_{rad} increases as the electrical length increases. Besides the electrical length, R_{loss} also depends on the frequency of operation, wire radius and conductivity. A high frequency, large wire radius and high conductivity result in a low ohmic resistance and thus a better radiation efficiency. Moreover, for the circular loop, the radiation efficiency is found to be

$$\begin{aligned} e_{rad} &= \frac{R_{rad}}{R_{rad}+R_{loss}} = \frac{20\pi^2(\frac{l_{loop}}{\lambda})^4}{20\pi^2(\frac{l_{loop}}{\lambda})^4 + (\frac{l_{loop}}{\lambda})\frac{1}{2\pi a}\sqrt{\frac{c^2\pi\mu}{f\sigma}}} \\ &= \frac{20\pi^2}{20\pi^2 + \frac{1}{2\pi a}\sqrt{\frac{c^2\pi\mu}{f\sigma}}(\frac{l_{loop}}{\lambda})^{-3}} \end{aligned} \tag{1.61}$$

Moreover, it is noted that the radiation resistance R_{rad} increases significantly by using the multiple-turn loop (N turns). This is because the electric current in the loop is proportional to the turn N and the electric field is also proportional to the turn N. Thus, the radiated power and radiation resistance

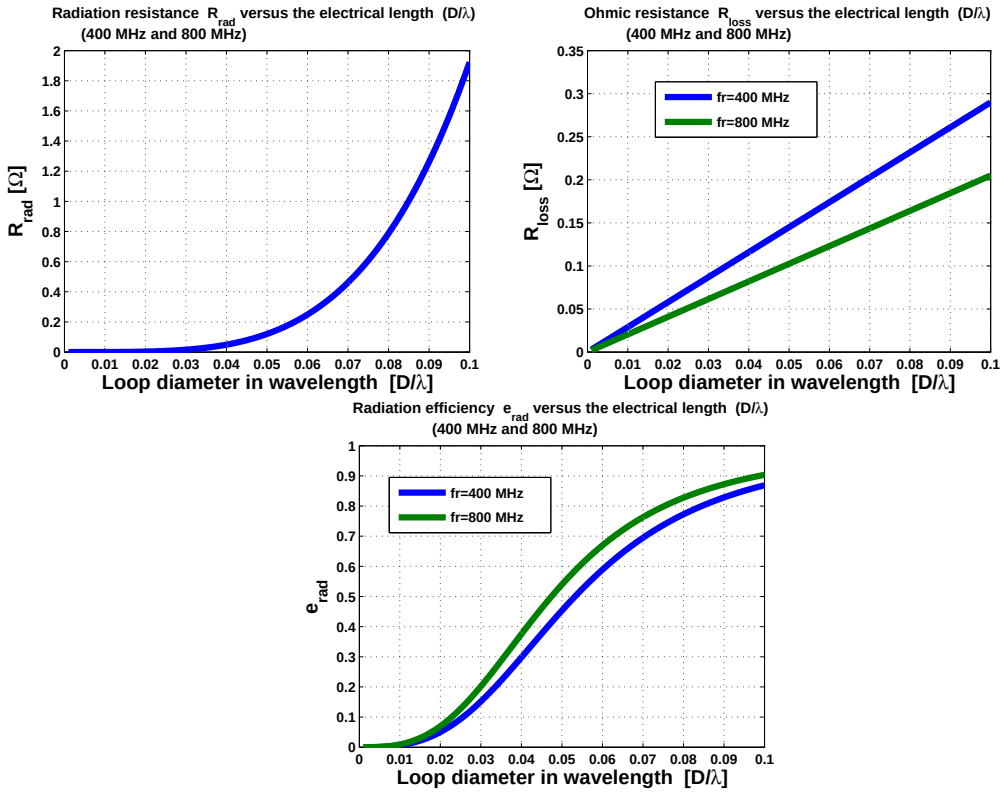

Figure 1.7: R_{rad}, R_{loss} and e_{rad} versus the loop diameter at 400 MHz and 800 MHZ, respectively, with conductivity being $\sigma = 58 \times 10^6 S/m$ and wire radius being $0.675mm$.

are proportional to N^2. On the other hand, the addition of the conductor in extra turns also results in an increase in the ohmic loss, but the ohmic loss resistance is only increased by N times. Hence, the radiation efficiency increases as the number of turn N increases, under an assumption that the coupling between each turn is ignored. However, when several turns are used the coupling between each turn needs to be considered which results in a decrease in the radiation efficiency. An alternative way to increase the radiation resistance is using the ferrite material as the winding core. The physical insight is understood by examining the phase constant β, which is $\beta = \omega\sqrt{\mu\varepsilon} = \omega\sqrt{\mu_0\varepsilon_0}\sqrt{\mu_{eff}} = \frac{2\pi}{\lambda}\sqrt{\mu_{eff}}$. μ_{eff} is the effective relative permeability and it depends on the shape and size of the ferrite core. For an N-turn loop with a ferrite core, the radiation resistance becomes

$$R_{rad} = 20\pi^2 N^2 (\frac{l_{loop}}{\lambda/\sqrt{\mu_{eff}}})^4 = 20\pi^2 N^2 \mu_{eff}^2 (\frac{l_{loop}}{\lambda})^4, \tag{1.62}$$

which shows R_{rad} is proportional to N^2 and μ_{eff}^2.

1.2 Overview in Antenna Miniaturization Techniques

Several miniaturization techniques are being used for ESAs which are briefly summarized as follows.

External Matching Circuit: Using Lumped Components
Although ESA behaves a small resistance and a large reactance, the input impedance of the ESA can be matched to the system characteristic impedance, for instance 50Ω, by designing an external matching circuit. In general, there are three types of commonly used matching networks which are designed in terms of lumped elements. These are L-section, Π-section and T-section matching networks, respectively [33, 34], which are named from their shape. Considering the limited space in small devices, the narrow-band L-section matching network may be preferable. The narrow-band matching means the matching is designed for one single frequency only, which is the center frequency. The matching is perfect at the center frequency and degrades away from it. At the center frequency, the roles of the matching network are eliminating the antenna reactance and shifting the antenna resistance level to the system characteristic impedance. The bandwidth of an ESA is mainly determined by the ratio of the antenna resistance to its reactance. Moreover, the cascade of two or three sections of matching networks are used to increase the bandwidth, but at the expense of extra losses introduced by the lumped components.

For a small dipole with a length of 1 cm and at the frequency of 800 MHz, the resistance and reactance are $R_A = 0.1482$ ohm and $X_A = -1865.8$ ohm, respectively. As shown in Figure 1.8, the matching circuit is designed using the L-section, the cascade of two L-sections and the cascade of three L-sections, respectively. The ideal components are assumed in the matching networks. Figure 1.9 presents the bandwidth of this antenna with each matching network, from which it is seen that the bandwidth is broadened by using the cascade matching sections. The -10 dB impedance bandwidth are 0.02%, 0.03% and 1% for the L-section, two L-sections and three L-sections, respectively. It shows that the impedance bandwidth is improved by using the cascade matching networks, but the improved bandwidth of the ESA is still narrow.

The Self-Resonant ESAs: Using the Capacitive or Inductive Coupling Mechanisms
The input impedance of an ESA can be matched to the system characteristic impedance without using any additional matching network and lumped components, by using a capacitive or inductive coupling mechanism. First, the imaginary part of the antenna impedance is tuned to zero by the com-

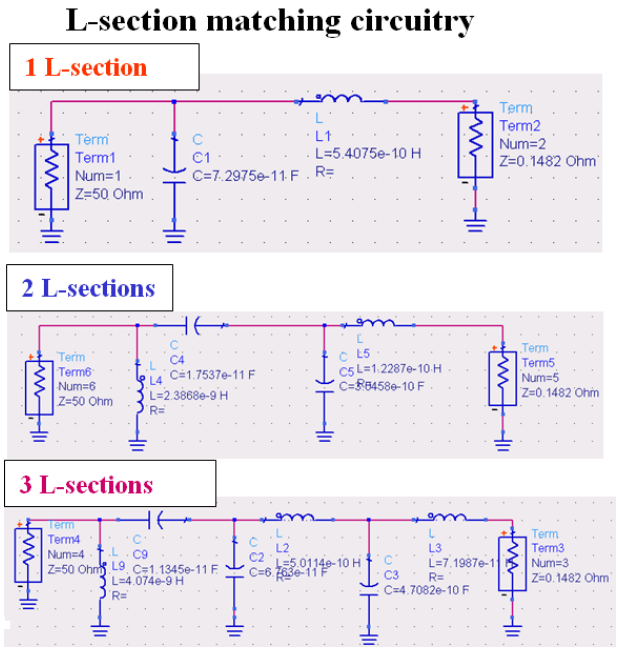

Figure 1.8: The matching network for an ESA by using a single L-section, cascade of two L-sections and cascade of three L-sections, respectively. The ideal lumped components are assumed in the matching networks.

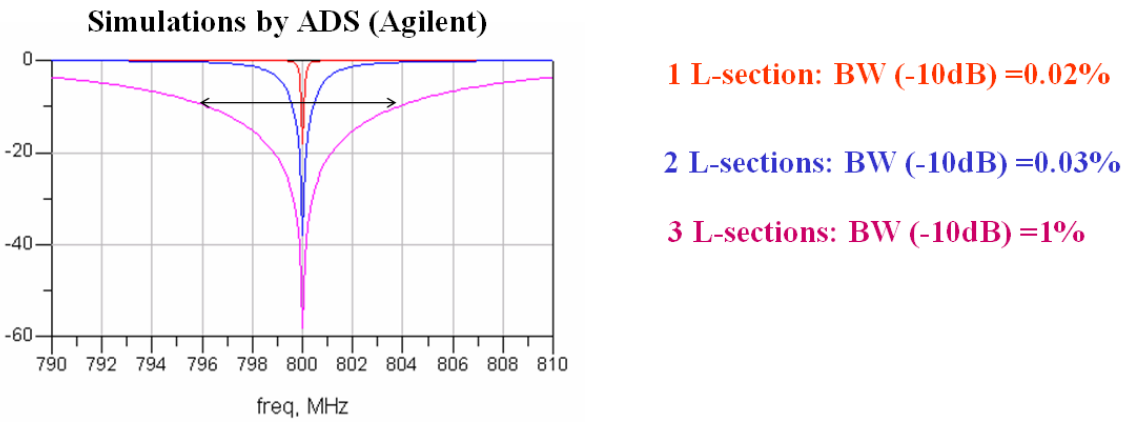

Figure 1.9: The bandwidth for the ESA with a matching network of single L-section, cascade of two L-sections and cascade of three L-sections, respectively

pensation of the loading element. Since the tolerance and aging problems of lumped components result in the changes in the antenna properties, a distributed printed loading element is preferred to replace the loading lumped components. Second, by feeding the ESA through a capacitive or inductive

coupling element, an appropriate resistance level that is matched to the system characteristic impedance can be obtained. The role of the coupling mechanism is viewed as an impedance transformer. There are four types of basic ESAs that can be designed using these coupling mechanisms, which are

- Electrically Small Loop Antenna Excited by an Inductive Element
- Electrically Small Loop Antenna Excited by a Capacitive Element
- Electrically Small Dipole Antenna Excited by an Inductive Element
- Electrically Small Dipole Antenna Excited by a Capacitive Element

For instance, an electrically small loop antenna can be excited either by a very small inductive loop element or a small capacitive dipole element. The working mechanisms for these two designs are based on the inductive and capacitive coupling between the excitation element and loop antenna, respectively. It is noted that the radiation efficiency of the self-resonant ESA is mainly determined by the radiating element itself, because the feeding element is much smaller than the radiating element. The excitation element will introduce a little shift in the antenna resonance frequency. It is necessary to take this shift into account in the antenna impedance tuning.

High Permittivity and Permeability Dielectric Loaded Antennas
Another commonly used antenna miniaturization technique is to load the antenna by using the high permittivity and permeability dielectrics, for instance a loaded microstrip patch. It gives a size reduction factor of antennas on the order of $\sqrt{\varepsilon_r \mu_r}$, where ε_r and μ_r are the relative permittivity and permeability of the antenna substrate. For a microstrip antenna with the dimensions being length L, width W and thickness h, the bandwidth is related to the design parameters in the form [35]

$$BW(VSWR \leq 2) = \frac{8}{3\sqrt{2\varepsilon_r}} \frac{h}{\lambda_0} \frac{W}{L} 100\%. \tag{1.63}$$

It is seen that the antenna bandwidth is inversely proportional to the relative permittivity ε_r, and is independent of the relative permeability μ_r. The major drawback of this method is that the EM energy within the near-field region is difficult to radiate out of the dielectric, which is due to the wave-impedance mismatch between the dielectric material and surrounding air region. Strong resonance behavior of this type of antenna structure only allows the impedance matching over a very narrow bandwidth.

Folded Geometry: Microstrip Antennas and Fractal Antennas
The conventional rectangular patch antenna resonates when its length equals one half of a wavelength. By introducing a shorting wall at the center of the patch, the size of the patch antenna is reduced to a quarter wavelength. Moreover, by folding the patch with a shorting wall, the overall size of the two-layer patch antenna is further reduced to one-eighth wavelength [36–38]. The multiple-layer folded patch antenna is further developed by folding the patch in an appropriate way, which results in a highly miniaturized antenna. The approximate resonant length L of the N-layer folded patch antenna is found to be [39]

$$L = \frac{\lambda_0}{4N\sqrt{\varepsilon_r}}, \tag{1.64}$$

where ε_r is the relative dielectric constant of the patch substrate.

Fractals are broken curves that are categorized into main geometric types of the deterministic fractals and random fractals. Random fractals are very familiar which can be used to describe the real-world objects in the nature, such as clouds, mountains and coastlines. Deterministic fractals take a generator and are generated in an iterative fashion. Usually fractals are described as being self-similar or self-symmetric. Fractals have advantages in the research areas of antenna miniaturization, wideband and multiband applications. Due to the space-filling properties of some fractal shapes, these geometries are used to miniaturize antennas where an electrically large feature is efficiently packed into a small area. Hence, the nature of fractal antennas are physically small and electrically large antennas. Since the electrical length plays an important role in the antenna design, the input impedance matching for these small antennas is improved. The self-similar nature in fractal geometries can also be utilized for the wideband and multiband antennas as well.

Metamaterial-Inspired ESAs:
Recently it is reported that the sub-wavelength resonant ESAs can be designed theoretically, in which an electrically small dipole is covered by the negative permittivity shell ($\epsilon_r < 0$). It holds the potential for far smaller antennas in the future. However, the realization and fabrication of the low loss metematerial shell is of great challenges.

Instead of using the real metamaterial, the metamaterial-inspired electrically small antennas were presented in [40], in which a metamaterial-inspired parasitic element is introduced in the near-field of ESAs. The parasitic element is used as a unit cell of the metamaterial. These ESAs are resonant and matched to the source without any external matching network, which are also efficient

and electrically small. Several such metamaterial-inspired electrically small antennas are presented in [41–49].

Optimizations using the Genetic Algorithm:

Genetic algorithm (GA) is a stochastic direct search method based on the principle and concepts of the natural selection and evolution [50, 51]. GAs have the advantages of solving complex problems and have also been used in many electromagnetic (EM) applications [52]. Figure 1.10 shows the typical structure of a genetic algorithm. At the beginning of the computation, a number of individuals are randomly initialized. The objective function is then evaluated for these individuals, from which the initial generation is produced. If the optimization criteria are not met, a new generation starts. In the new cycle, first, the individuals are selected according to their fitness for the production of the offspring. Second, the parents are recombined to produce the offspring. Third, all offspring will be mutated with a certain probability. The fitness of the offspring is then computed. Fourth, the offspring are inserted into the population replacing their parents, producing a new generation. The above cycle is performed until the optimization criteria is reached.

The optimization procedures are described briefly to illustrate the method for the antenna application. The optimization is performed by using GA in conjunction with an EM simulator such as the commercial package HFSS [53]. Figure 1.11 presents the main control process of the optimization. It shows that the GA optimization is evaluated in Matlab and the the antenna is investigated using the EM simulator HFSS, which is programmed using VB scripts. An interface script is required to create a link between HFSS scripts and GA optimization scripts. Then a main control script is created to combine the EM simulator and GA optimization scripts, and exchange the information in-between. The main task is described as follows. First, HFSS is controlled and called in Matlab, and all the drawings, solution setups and simulations in HFSS are controlled through the so-called HFSSAPI, which is written in Matlab scripts and is used to control HFSS. The initial antenna parameters provided by the GA optimization are used in the HFSS simulations. Second, GA optimization is performed in Matlab to evaluate the objective function, by using the simulation results exported from HFSS. The objective function is the antenna characteristic that needs to be optimized, such as the antenna input impedance, bandwidth and radiation efficiency. The cycle is performed until the optimization criteria are reached.

Commercial Available Small Antennas:
Several commercial available small antennas are evaluated and compared in

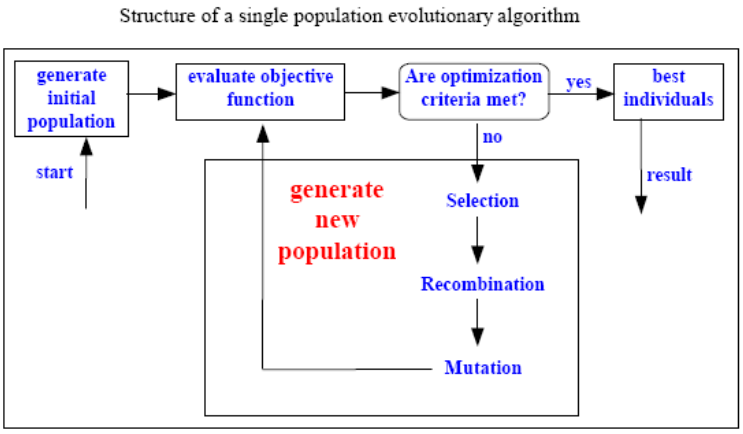

Figure 1.10: Structure of a single population evolutionary algorithm of GA.

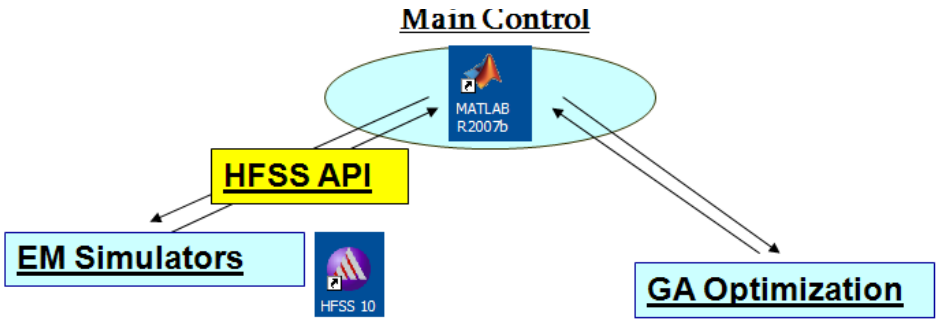

Figure 1.11: The main control process of the GA optimization.

this project. Most of these small antennas are chip antennas which are printed on high permittivity ceramics or uses LTCC techniques. Another commonly used type is the optimized fractal antennas. The advantages of these small antennas are their high performances which are presented by the manufacturer in datasheet, such as the impedance matching, bandwidth and radiation efficiency, etc. These high performance are the exact demands in commercial market.

The company `Sarantel` (www.sarantel.com) develops and manufactures very advanced miniature filtering antennas for mobile, wireless and handheld devices. These antennas are made by using high permittivity dielectric materials to shrink the antenna size, but maintaining high radiation efficiency. `Antenova` (www.antenova.com) is another leading developer and supplier of high performance antennas and RF antenna modules for mobile handsets, portable devices and laptop computers. Their balanced high

dielectric antennas (HDA) enable integrated antennas to be small and efficient, operate across multiple bands and offer more robust performances. Fractus (www.fractus.com) develops small antennas for wireless devices from mobile phones and TV to Bluetooth headsets. Yageo Corporation (www.yageo.com) announced the release of 2012 LTCC antenna, with the dimensions of 2.0 x 1.2 x 1.1 mm^3, which is the world's smallest ceramic antenna designed for the dynamic Bluetooth and WLAN applications.

However, these antennas may be not as efficient as their manufacturers announced for two reasons. First, the good performances of these small antennas can only be obtained by mounting the antenna on a PCB board of the required size in the datasheet, and an external matching network is even added for some of them. The resonance frequency is determined by the chip antenna together with the PCB ground plane and extra matching network. The measurement results may change significantly if a ground plane with a different size is employed. Second, it is well known that the measurements for ESAs represent a great challenge which is due to the leaking current on the outer conductor of the feed line. For instance, for ESAs with low radiation efficiency, the measured efficiency can be strongly overestimated due to this effect. Hence, their measurements may not be performed in an appropriate way when the announced performances exceed theoretical limitations.

1.3 Purposes of the Dissertation and Research Challenges

Hearing-aids today constitute devices with an advanced technology, and wireless communication integrated into hearing-aids will introduce a range of completely new functionalities. The antenna is an important component in any wireless system, and the demand for compact wireless systems with stringent specifications makes the antenna size reduction a significant challenge. Antenna miniaturization is thus one of the key technologies in designing a successful wireless unit for the hearing-aid application.

Recently, there is a strong demand for the hearing-aid with a wireless communication integration in the commercial market [54]. However, the design of ESAs for hearing-aid applications, which must be highly miniaturized and operated in a very complex environment, is not yet a well developed technology. Thus, this is one of the research areas that will be studied in this dissertation. Moreover, the measurement techniques and instruments for ESAs are also not well developed. Although several measurement techniques are being used for ESAs, some well known problems remain unsolved, such as the

disturbance of the leaking current and scattering effect of the feed line. Accurate measurement techniques for the input impedance and radiation properties need to be addressed for ESAs.

1.3.1 Purposes of the Dissertation

The purpose of this dissertation is to develop ESAs for the hearing-aid application and explore the appropriate measurement techniques for ESAs. In details, this Ph.D. project consists of three major areas of investigation for the antennas in wireless communication systems with hearing-aids. The specific tasks of this dissertation are outlined as follows.

- **Task 1** The design of the highly miniaturized ESAs which are used for the hearing-aid application is a main task. The desired ESAs are functioned to communicate between the hearing-aids and external devices which are placed at least 10-meter away from the hearing-aids, as well as the communication path between two hearing-aids on human ears. The drawback of the antenna miniaturization is a reduction in the bandwidth and radiation efficiency of ESAs; thus the properties of these ESAs are required to satisfy the specifications listed in the communication link budget.
- **Task 2** The development of the input impedance, radiation efficiency and gain measurement techniques and instruments for ESAs is another task. Accurate experimental characterization of small antennas in complex environments requires development of new measurement techniques. The measurements may be performed at the DTU Spherical Near-Field Antenna Test Facility operated by the Technical University of Denmark (DTU) as an external reference laboratory for the European Space Agency. This is a state-of-the-art facility that for several years has served Danish and European industry with high-accuracy measurements and calibrations of antennas. However, for the measurement of small antennas of the present project it will be necessary to design and implement new measurement set-ups and techniques for two reasons. First, since the ESA will eventually operate in a complex environment comprising the hearing-aids and a person's head, it is necessary that the measurements are also conducted in a model of this environment. Hence, a so-called human head phantom must be designed and implemented. Second, since the antennas are electrically small the measurements will be strongly influenced by the electrical and mechanical support equipments used during the measurement, a calibration for this is

required or this will necessitate the development of other measurement techniques than those used for traditional antennas to determine the efficiency (or gain) of the ESAs.

- **Task 3** The influences of the complex environments on the characteristics of the ESAs will also be investigated, i.e. human head phantom, as well as the device that the antenna is integrated into. The ESAs are to function in very complex environments that will significantly influence the performance of the antennas. An antenna radiating a primary RF field will induce currents in all nearby objects and these currents will then radiate a secondary RF field that interferes - in a potentially destructive manner - with the primary RF field. It is thus necessary in the design of the antennas to take into account the influence of the complex environment. For an antenna integrated into a hearing-aid, this means that the influence of the hearing-aid itself, the human ear and the human head must be included in the analysis. Mobile phone communication faces a similar challenge and much of the experience gained in this field over the past 10 years can be exploited in the present work. However, the mobile phone communication is always between the phone and a distant base station. The communication paths for the functionalities envisaged in this project is of course different from that of mobiles, and will be more complicated than that of mobiles. Thus, this is one of the research areas that will be studied in this dissertation.

1.3.2 Research Challenges in Antenna Miniaturizations

To achieve the above goals, the research challenges in antenna miniaturizations and small antenna measurement techniques are discussed in this subsection. The antenna miniaturization will raise new research questions. Three major characteristics of the small antennas are considered as follows.

The Impedance Matching
The highly miniaturized ESA essentially is a capacitor or inductor with a certain amount of radiation. The resistance of an ESA is small while the reactance of an ESA is very large. The perfect impedance matching of an antenna, at the resonance frequency, requires that the antenna resistance equals the characteristic impedance of the feed line and the antenna reactance equals zero. Hence, the impedance matching of an ESA is difficult and thus the bandwidth is narrow. The first challenge of the antenna miniaturization is that the ESA must be matched to the characteristic impedance of a transmission line to maximize the accepted power, while the bandwidth of the ESA

that needs to be maintained to an acceptable level for the specified application.

The Radiation Efficiency
The radiation efficiency e_{rad} is defined as the ratio of the radiated power to the accepted power. The dissipated power or the losses in an ESA may be caused by the ohmic losses in the conductor of the antenna, ohmic losses in lossy dielectrics or polarization losses. These conduction and dielectric losses may come from the antenna, the antenna support and the device structures nearby. As the dimensions of the ESA decrease the radiation efficiency also decreases. The second challenge of the antenna miniaturization is that the antenna must be efficient to maximize the radiated power.

The Radiation Pattern
The radiation pattern is a numerical or graphical representation of the spatial distribution of the characteristics of the antenna radiated field. It may be expressed in terms of the far-field pattern, near-field pattern, gain pattern and directivity pattern, etc. The radiation of an ESA is sensitive to the nearby structures such as the human head and the devices that the antenna is integrated into. Thus, the third challenge of the antenna miniaturization is that the antenna must provide a proper radiation pattern to function correctly.

1.3.3 Research Challenges in Small Antenna Measurements

Nowadays the performances of antennas are verified with cable measurements in anechoic chambers, which work very well for most traditional antennas. However, the input impedance and radiation efficiency measurements of ESAs represent great challenges. Typically, there exist two mechanisms that introduce errors in the measurements.

First, the feed line causes a significant influence on the measured radiation efficiency for ESAs, due to leaking current on the outer surface of the feed line. The measured radiation efficiency can be strongly overestimated due to this effect. Although a balun can be used to avoid the leaking current, it is typically a narrow-band device. Several baluns are thus required for different frequency bands. Also, the dimensions of the balun need to be tuned carefully at the specified frequency. In addition, the balun may have a size comparable to or even larger than that of the small antenna; thus it may give rise to the scattering. Ferrite cores are also commonly used in the small antenna measurements. However, this method may not be an appropriate approach. It is because the ferrite cores are placed in the reactive field region

of the ESAs; thus the leaking current on the feed line is partially reflected back and partially absorbed by the ferrite cores. The working mechanism of adding ferrite cores is to provide a very high reactive impedance along the feed line so that the leaking current is forced to reflect back. Several pieces of ferrite cores are required to make sure the impedance is high enough. This method is only valid up to 1 GHz in the radiation measurement.

Second, the feed line represents a large scattering structure even if the leaking current is avoided. Measurements of the small antenna characteristics without the use of the feed line is therefore highly desirable.

1.4 Summary of Main Contributions

During this Ph.D. project, the main contributions to the research field of antenna miniaturizations and small antenna measurement techniques are listed as follows.

Journal Paper

- **Jiaying Zhang**, Pivnenko Sergey and Olav Breinbjerg, "Theory and Practice of a Cable-Free Impedance and Gain Measurement Technique for Electrically Small Antennas", *Preparing in Submission to Transactions on Antennas and Propagations*.

Conference Paper(s)

- **Jiaying Zhang** and Olav Breinbjerg, "Self-Resonant Electrically Small Loop Antennas for Hearing-Aids Application", *Proceedings of the Fourth European Conference on Antennas and Propagation (EuCAP 2010)*, Barcelona, Spain, April 2010.
- S. Pivnenko, **J. Zhang**, A. Khatun, T. Laitinen and J. Carlsson, "Characterization of Small Antennas for Hearing-aids by Several Measurement Techniques", *Proceedings of the Fourth European Conference on Antennas and Propagation (EuCAP 2010)*, Barcelona, Spain, April 2010.
- **Jiaying Zhang**, Pivnenko Sergey and Olav Breinbjerg, "A Modified Wheeler Cap Method for Radiation Efficiency Measurement of Balanced Electrically Small Antennas", *Proceedings of the Fourth European*

Conference on Antennas and Propagation (EuCAP 2010), Barcelona, Spain, April 2010.

- **Jiaying Zhang** and Olav Breinbjerg, "Miniaturization of Multiple-Layer Folded Patch Antennas", *Proceedings of the Third European Conference on Antennas and Propagation (EuCAP 2009)*, Berlin, Germany, April 2009, pp. 3502-3506.

- **Jiaying Zhang**, Pivnenko Sergey and Olav Breinbjerg, " A Cable-Free Impedance and Gain Measurement Technique for Electrically Small Antennas", *Proceedings of the 32nd Annual Symposium of Antenna Measurement Techniques Association (AMTA 2010)*, Atlanta, US, October 2010.

- **Jiaying Zhang**, Pivnenko Sergey and Olav Breinbjerg, " Application of the Modified Wheeler Cap Method for the Radiation Efficiency Measurement of Balanced Electrically Small Antennas", *Proceedings of the 32nd Annual Symposium of Antenna Measurement Techniques Association (AMTA 2010)*, Atlanta, US, October 2010.

- **Jiaying Zhang**, Pivnenko Sergey and Olav Breinbjerg, "Electromagnetic Model of a Near-Field Cable-Free Impedance and Gain Measurement Technique for Electrically Small Antennas", *Proceedings of the Fifth European Conference on Antennas and Propagation (EuCAP 2011)*, Rome, April 2011.

1.5 Dissertation Outline

This dissertation is divided into five chapters.

Chapter 1 gives a brief background introduction of this project. In this chapter, the background, justifications, purpose and outline of this Ph.D. project are provided.

Chapter 2 presents several novel designs of electrically small loop antennas for the hearing-aid application which is summarized as follows. The first antenna design is a two-dimensional (2-D) planar differential-fed electrically small loop antenna. An analytical model, simulation results, fabrication and measurement results are presented. The idea of this design is based on the capacitive loading and the inductive coupling between the two small loops. The second antenna design is a planar two-turn electrically small loop antenna. The working mechanism of this antenna is based on the capacitive loading, and both the capacitive and inductive coupling between the two

small loops that are of a comparable size are taken into account. An analytical model is provided to give guidance in the impedance tuning. In addition, several designs of three-dimensional (3-D) folded electrically small loop antennas are proposed, the properties of which are significantly improved compared to the 2-D electrically small loop antennas.

Chapter 3 presents several novel measurement techniques for ESAs. First, the effectiveness of ferrite cores and design of a tunable sleeve balun are investigated. Second, a modified Wheeler cap method for the radiation efficiency measurement of balanced electrically small antennas are introduced. Moreover, the modified Wheeler cap method for measurements of small antennas in complex environments is further developed. Third, a cable-free impedance and gain measurement technique for ESAs is proposed. An electromagnetic model, simulation results, as well as measurement results are presented.

Chapter 4 investigates the influence of complex environments on the characteristics of ESAs. First, the sensitivity analysis of the head phantom parameters on the antenna characteristics is presented, including the influence of the head permittivity and conductivity. Second, the sensitivity analysis of the positions of the ESAs on the antenna characteristics is presented, including the orientations and locations of the ESAs and the distance between the ESA and head. Third, the influence of the hearing-aid shell material on the antenna characteristics is investigated.

Chapter 5 gives the conclusion and future work of this project.

1.6 Chapter Summary

This chapter starts with a background introduction of the antenna miniaturization and small antenna measurement techniques. After introducing the background, the research challenges are presented, including the theoretical limitations on antenna properties versus the antenna size. Then the tasks of this project are identified. In the end, the major contributions and the outline of this dissertation are provided.

CHAPTER

TWO

Antenna Miniaturizations: Electrically Small Loop Antennas

In this chapter, several novel designs of electrically small loops are proposed for the hearing-aid application. Considering the specified application, several requirements in antenna specifications that need to be satisfied are introduced briefly as follows. First, since the power that is provided by the hearing-aid battery is in the μW range, a low frequency of operation may be preferred, for instance lower than 1 GHz; thus in this project the small antennas are designed and evaluated at 400 MHz, 900 MHz and 1000 MHz, respectively. Second, the communication distance between the hearing-aids and external devices is set to 10 meters and the corresponding communication link budget must be fulfilled. Third, the demand for compact systems with stringent specifications makes the antenna size reduction a significant challenge. Therefore the antenna miniaturization is one of the key technologies in designing successful wireless hearing-aids. Hence, the above requirements lead us to the research area of designing highly miniaturized antennas for the ultra low power and short-range wireless communication.

2.1 Differential-Fed Planar Electrically Small Loop Antennas for the Hearing-Aid Application

Electrically small loop antennas are popularly used in short-range wireless communications. However, the small loop antenna itself is inefficient and badly matched in the impedance. An additional matching network may be required to make the antenna resonant, in which lumped components may be used. Moreover, the tolerance and aging problems of lumped components

result in the changes in antenna properties. The small antenna designs without using the lumped components will be desired; thus the loop antenna designs by using the inductively-coupled feed mechanism or the capacitively-coupled feed mechanism is considered in this project.

The coupled feed mechanisms have been used in the designs of antennas [55–59]. Moreover, a metamaterial-inspired small loop antenna was proposed recently in [40], where a small loop is covered by a simple mu-negative (MNG) shell. However, a large ground plane is present in the design of [40], which is not suitable for ultra small devices. Differential feed electrically small antennas will be desired in ultra small devices, such as sensors, hearing-aids and RFIDs. This is because the fact that a ground plane required for proper operation of unbalanced antennas is not existing in these small devices. Moreover, the differential feed is also commonly used in the RF transmitters because of its stability to the pin inductance which may result in the power immunity of the battery; thus for low power application such as the heading-aid, using the differential feed provides higher power supply than using the unbalanced single-end feed. Hence, the differential feed electrically small antennas are adopted in this project.

We are aiming at designing miniaturized antennas for the hearing-aid application around 900 MHz, which are not only geometrically small but also electrically small. In this section, a differential-fed self-resonant electrically small loop antenna, by using an inductively coupled feed, is presented. The working mechanism of this antenna is based on the capacitive loading and the inductive coupling between the two loops, which are the primary loop (the small one) and the secondary loop (the large one). An analytical circuit model is also derived to account for the antenna structure and explain the working mechanism of the inductively-coupled loops, by using which the design rules are illustrated. The impedance matching is realized by this proposed model. In this model, the inductive feed is coupled to the loop antenna through the magnetic flux linkage, and the magnetic flux due to the large loop is approximated by the flux due to two infinitely long wires that carry currents with equal amplitudes and opposite directions. The proposed model is valid through the comparison between the calculations and the numerical simulations. It is noted that the primary and secondary loops share a small piece of path segment in this design. The only effect of the contact of the two loops is that it combines the currents from the two loops in the shared path segment. This does not give any significant changes in the analytical model, compared to the cases that the primary and secondary loops are separated placed. It is because the fundamental working mechanism and the mutual inductance still play the dominate roles in the designs, which are

confirmed by HFSS simulation. Moreover, several three-dimensional (3-D) folded electrically small loop antennas are further developed in the following subsections, the properties of which are significantly improved compared to the two-dimensional (2-D) planar electrically small loop antennas.

The geometry and design variables of the loop antenna design are illustrated in Figure 2.1. In this antenna, there exist two loops, the small one and the large one, which are connected together. The large loop is effectively closed by the capacitive loading that is formed by two closely spaced wires. The small loop is covered by the large loop and is excited by a differential feed. The working mechanism of this antenna is based on the inductive coupling between two small loops. The antenna impedance is matched to 50 ohm without any additional matching network and lumped components.

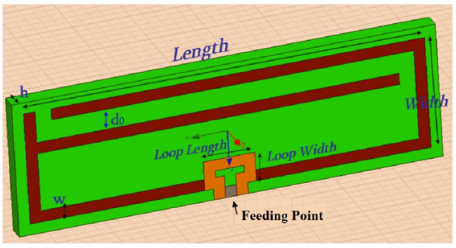

Figure 2.1: Geometry and design variables of the self-resonant electrically small loop antenna. (The loop is designed around 900 MHz, with the dimensions being 35 mm×10 mm×1.524 mm.)

2.1.1 Analytical Model of the Proposed Antenna

The antenna working mechanism and the physical model are explained in this subsection. For the loop antenna presented in Figure 2.1, it is noted that the antenna system is fed on the small loop. The large loop is coupled to the small loop through the magnetic flux linkage, and the magnetic flux due to the large loop can be approximated by the flux due to two infinitely long wires that carry currents with equal amplitudes and opposite directions. The antenna impedance is matched to a specific value without using any additional matching network and lumped components by tuning the antenna as follows.

- First, the imaginary part of the antenna impedance is tuned to zero because the loop inductance is compensated by the loading capacitance involved in the large loop.

- Second, the real part of the antenna impedance, resistance, is matched to 50 ohm by tuning the small loop dimensions.

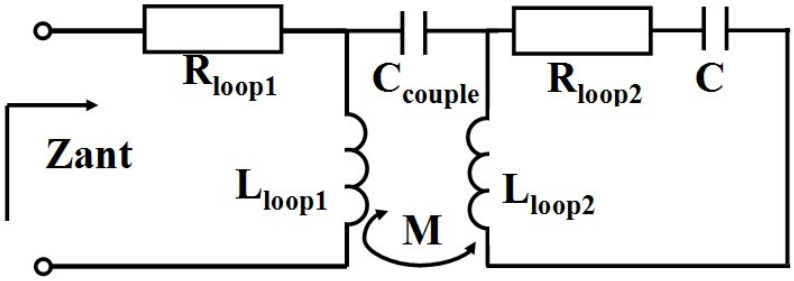

Figure 2.2: Analytical model of the self-resonant electrically small loop antenna.

The two loops contained in this antenna can be located on the same layer or opposite layers of the PCB board depending on the specific designs. On the same layer, the small loop can be placed inside or outside of the large loop, as shown in Figure 2.3-2.4. However, the mutual inductance is different for these two cases which plays an import role in the impedance matching. The analytical formulas of the antenna input impedance versus the antenna parameters will be derived to illustrate the design rules. Additionally, the antenna shape also has its influence. The hearing-aid application requires the shape of the large loop to be rectangular. While for the small loop, the influence of its shape on the impedance matching will be analyzed in the following subsections which are the rectangular and circular, respectively .

The analytical model that is used to explain the antenna working mechanism is illustrated in Figure 2.2. The details of the antenna parameters are presented in Figure 2.3-2.4, respectively. The dimensions of the small loop are L_1 and W_1, and those of the large loop are L_2 and W_2. The distance between the two loops is d. The antenna system is fed on the small loop. R_{loop1} and L_{loop1} are the resistance and inductance of the small loop, and R_{loop2} and L_{loop2} are the resistance and inductance of the large loop, respectively. R_{loop2} can be further expressed to be the sum of the antenna radiation resistance R_{rad} and ohmic loss resistance R_{loss}, that is $R_{loop2} = R_{rad} + R_{loss}$. C is the capacitance of the loading element that is existing in the large loop. C_{couple} and M are the mutual capacitance and mutual inductance between the two loops. C_{couple} is influenced by the relative position between the two loops. For the antenna design shown in Figure 2.1, the size of the small loop is much less than that of the large loop, and therefore C_{couple} is approximated to be negligibly small and only the mutual inductance M contributes to the working mechanism.

In the circuit model illustrated in Figure 2.2, the resistance and reactance of the input impedance Z_{ant} of this antenna are determined from

$$R_{ant} = R_{loop1} + (\omega M)^2 \frac{R_{loop2}}{R_{loop2}^2 + (\omega L_{loop2} - \frac{1}{\omega C})^2} \quad (2.1)$$

$$X_{ant} = \omega L_{loop1} - \frac{(\omega M)^2 (\omega L_{loop2} - \frac{1}{\omega C})}{R_{loop2}^2 + (\omega L_{loop2} - \frac{1}{\omega C})^2}. \quad (2.2)$$

Near the resonance condition where $\omega L_{loop2} = \frac{1}{\omega C}$, the resistance and reactance becomes

$$R_{ant} = R_{loop1} + (\omega M)^2 \frac{1}{R_{loop2}} \quad (2.3)$$

$$X_{ant} = j\omega L_{loop1} \simeq 0, \quad (2.4)$$

In the above equations, the resistance R_{loop2} of the secondary loop is determined from

$$R_{loop2} = R_{loop2}^{RAD} + R_{loop2}^{LOSS} = 31171 \frac{A_{loop2}^2}{\lambda^4} + \frac{l_{loop2}}{p} \sqrt{\frac{\pi f \mu}{\sigma}} \quad (2.5)$$

where R_{loop2}^{RAD} is the radiation resistance of the loop antenna, R_{loop2}^{Loss} is the loss resistance of the loop conductor, A_{loop2} is the loop area, l_{loop2} is the total length of the loop conductor, p is the perimeter of the cross section of the loop conductor. The inductance L_{loop2} of the secondary loop is determined from

$$L_{loop2} = L_{loop2}^A + L_{loop2}^I = 2\mu \frac{a_{loop2}}{\pi} [\ln(\frac{a_{loop2}}{b_{loop2}}) - 0.774] + \mu \frac{A_{loop2}}{2a_{loop2}}, \quad (2.6)$$

where L_{loop2}^A is the inductance of the loop antenna, L_{loop2}^I is the inductance of the loop conductor. a_{loop2} is the equivalent quadratic side of a rectangular loop, which is $a_{loop2} = \sqrt{L_2 W_2}$ with L_2 and W_2 being the length and width of the secondary loop, respectively. b_{loop2} is the equivalent circular radius of a tube conductor which is given by $b_{loop2} = 0.35h + 0.24w$, with h being the thickness of the loop conductor and w being the width of the conductor [60]. C is the capacitance of the loading element that exists in the large loop (the secondary loop). For the loop design using a loaded capacitor the initial estimation of C is determined from

$$C = \frac{1}{\omega_0^2 L_{loop2}}, \quad (2.7)$$

where ω_0 is the frequency of operation. This loaded capacitor will be inserted in the analytical model. For the loop design using the finger printed capacitive loading the initial estimation of C is tuned by changing the distance between the conductors to search the desired resonance.

Mutual Inductance M and Antenna Resistance R_{ant} when the Excitation Loop (Small Loop) is Rectangular

The small excitation loop can be placed inside or outside the large loop. For the case where the small loop is located outside the large one, as shown in Figure 2.3, the magnetic flux due to the large loop is approximated by that due to two infinitely long wires that carry currents with equal amplitudes and opposite directions. Hence the magnetic flux due to these two infinitely long wires are opposite, and the mutual inductance M is then determined from

$$M = \frac{\mu_0}{2\pi} L_1 ln \frac{(W_2+d)(W_1+d)}{d(W_1+W_2+d)}, \tag{2.8}$$

and the antenna input resistance R_{ant} at resonance is

$$R_{ant} = \frac{1}{R_{loop2}} \{2\pi f \frac{\mu_0}{2\pi} L_1 ln \frac{(W_1+d)(W_2+d)}{d(W_1+W_2+d)}\}^2 \tag{2.9}$$

When the small loop is placed inside the large one, as shown in Figure 2.4,

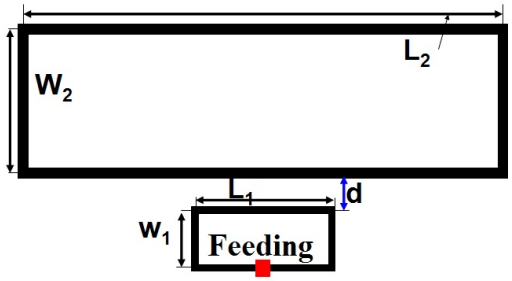

Figure 2.3: Configuration of the self-resonant electrically small loop antenna, with the small loop being **rectangular** and placed **outside** the large loop.

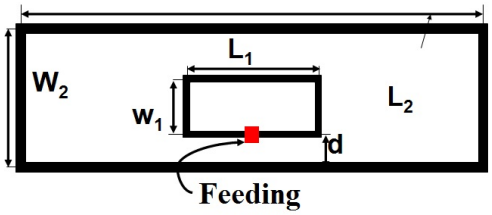

Figure 2.4: Configuration of the self-resonant electrically small loop antenna, with the small loop being **rectangular** and placed **inside** the large loop.

again the magnetic flux due to the large loop can be approximated by that

due to two infinitely long wires that carry currents with equal amplitudes and opposite directions. Since the small loop is in-between these two wires, the magnetic flux contributions from the two infinitely long wires are the same; thus the mutual inductance M is much stronger than the situation when the small loop is placed outside. The mutual inductance M is determined from

$$M = \frac{\mu_0}{2\pi} L_1 ln \frac{(W_1 + d)(W_2 - d)}{d(W_2 - W_1 - d)}, \tag{2.10}$$

and the antenna input resistance at resonance is

$$R_{ant} = \frac{1}{R_{loop2}} \{2\pi f \frac{\mu_0}{2\pi} L_1 ln \frac{(W_1 + d)(W_2 - d)}{d(W_2 - W_1 - d)}\}^2 \tag{2.11}$$

Mutual Inductance M and Antenna Resistance R_{ant} when the Excitation Loop (Small Loop) is Circular

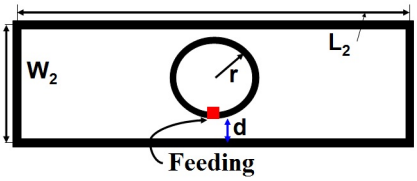

Figure 2.5: Configuration of the self-resonant electrically small loop antenna, with the small loop being **circular** and placed **inside** the large loop.

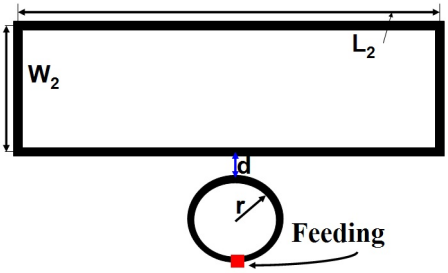

Figure 2.6: Configuration of the self-resonant electrically small loop antenna, with the small loop being **circular** and placed **outside** the large loop.

As shown in Figure 2.5-2.6, the small circular loop can be placed inside or outside the large loop. The dimensions of the large loop are L_2 and W_2. The radius of the small loop is r. The distance between the two loops is d. Again the magnetic flux due to the large loop can be approximated by that due to two infinitely long wires that carry currents with equal amplitudes and

opposite directions. When the small loop is outside the large one, the mutual inductance M is then determined from

$$M = \mu_0[\sqrt{(W_2+d+2r)(W_2+d)} - \sqrt{(d+2r)d} - W_2] \quad (2.12)$$

and the antenna input resistance at resonance is

$$R_{ant} = \frac{1}{R_{loop2}}\{2\pi f\mu_0[\sqrt{(W_2+d+2r)(W_2+d)} - \sqrt{(d+2r)d} - W_2]\}^2 \quad (2.13)$$

When the small loop is inside the large one, the mutual inductance M is determined from

$$M = \mu_0\{W_2 - \sqrt{(d+2r)d} - \sqrt{(W_2-d)(W_2-2r-d)}\}. \quad (2.14)$$

and the antenna input resistance at resonance is

$$R_{ant} = \frac{1}{R_{loop2}}\{2\pi f\mu_0[W_2 - \sqrt{(d+2r)d} - \quad (2.15)$$

$$\sqrt{(W_2-d)(W_2-2r-d)}]\}^2 \quad (2.16)$$

2.1.2 Simulation Results and Discussions

Simulation results of the electrically small loop antenna are presented in this subsection, based on the loop design shown in Figure 2.1. For our application, we are aiming at designing ESAs around 900 MHz. The dimensions of the large loop is fixed to be 35 mm $\times$ 10 mm, which is limited by the maximum size of the hearing-aids. Thus, the resistance and inductance of the large loop are calculated analytically, which are R_{loop2} and L_{loop2}. Then by using equation (2.11) in the circuit model, the dimensions of small loop can be calculated accordingly.

Based on this starting point, the antenna is designed and simulated using the commercial software package HFSS [53]. The antenna dimensions are illustrated in Table 2.1. The simulated resonance frequency is found to be 906 MHz. The impedance bandwidth reference to -10 dB and -15 dB are 3.3 MHz and 1.3 MHz, respectively. The radiation efficiency is found to be 17%. The simulated antenna reflection coefficient ($|S_{11}|$) and antenna input impedance are presented in Figure 2.7-2.8. Moreover, the simulated antenna reflection

Table 2.1: Dimensions and performances of the self-resonant electrically small loop antenna, designed around 900MHz.

Electrically Small Loop	Antenna Performances
Antenna Dimension	$Length$=35mm=0.105λ_0 $Width$=10mm=0.03λ_0 $LoopLength$=4.5mm $LoopWidth$=1.5mm W=1mm, d_0=1.8mm Substrate: Rogers 5870 (thickness=1.5mm)
Frequency of Operation	906 [MHz]
Impedance Bandwidth @ -10 dB	3.3 [MHz]
Impedance Bandwidth @ -15 dB	1.7 [MHz]
Radiation Efficiency [%]	17%
Maximum Directivity [dBi]	1.74 [dBi]
Maximum Gain [dBi]	-5.9 [dBi]

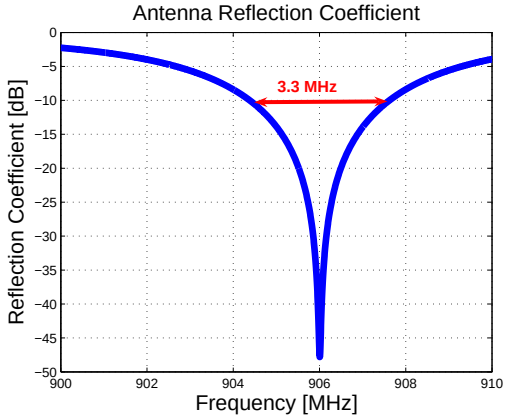

Figure 2.7: Antenna Reflection Coefficient.

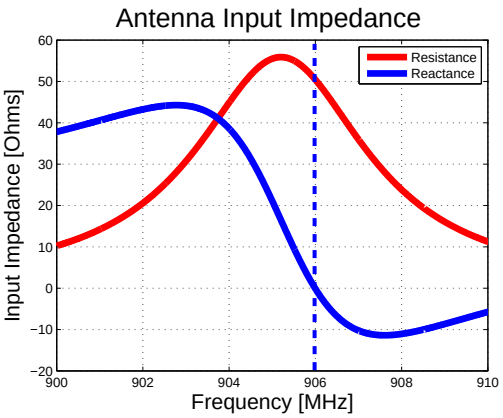

Figure 2.8: Antenna Input Impedance.

coefficient and impedance are compared to the analytical results by the proposed circuit model, which are presented in Figure 2.9-2.10, respectively. A good agreement is observed. From the previous analysis, it shows that the antenna impedance is related to the dimensions of the small loop that are its length and width. Figure 2.11 presents how the antenna resistance changes with the small loop length, when its width is fixed, and a comparison with the HFSS simulation result is presented. Figure 2.12 presents how the antenna resistance changes with the small loop width, when its length is fixed.

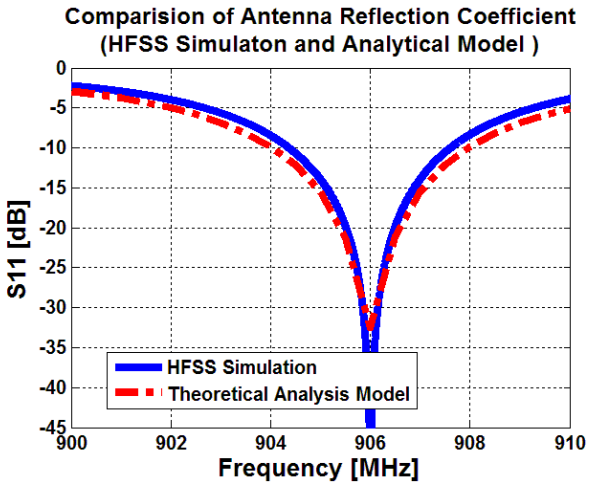

Figure 2.9: The comparison of antenna reflection between the HFSS simulation and analytical results.

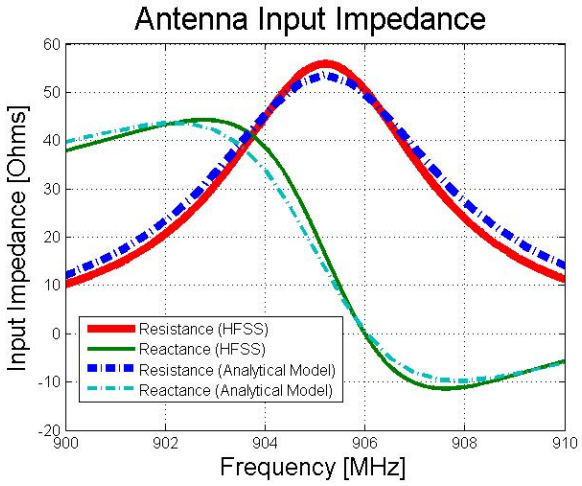

Figure 2.10: The comparison of input impedance between the HFSS simulation and analytical results.

2.1.3 Measurement Results and Discussions

This self-resonant small loop antenna was fabricated on a piece of dielectric substrate, Rogers 5870, with the dielectric constant being 2.33 and loss tangent being 0.0012. The overall antenna dimensions are 35mm $\times$ 10 mm $\times$ 1.5 mm, and the electric size of the antenna length is ka = 0.33, which is shown in Figure 2.13.

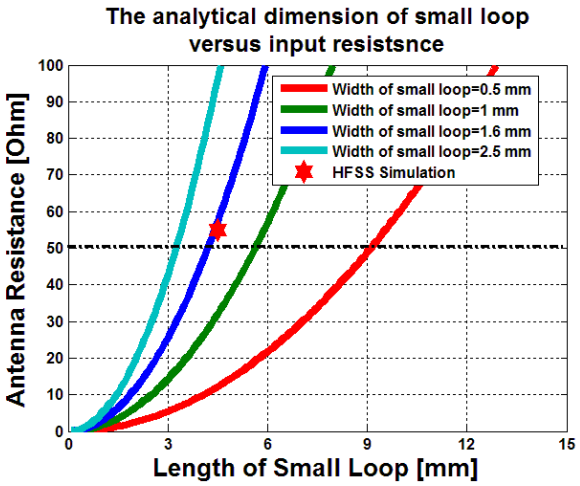

Figure 2.11: The analytical antenna input resistance versus **the length of small loop**, and a comparison between the analytical results and HFSS simulation.

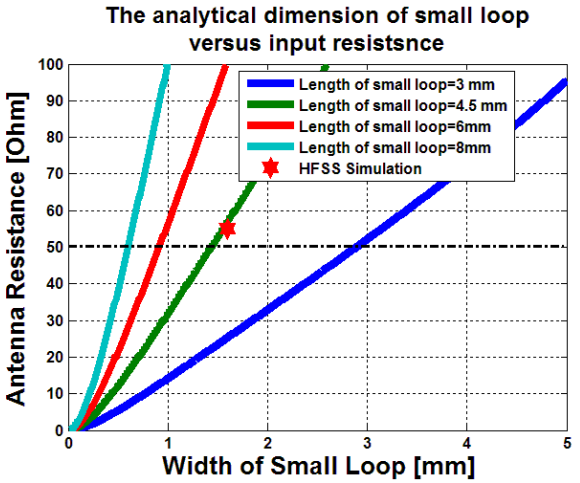

Figure 2.12: The analytical antenna input resistance versus **the width of small loop**, and a comparison between the analytical results and HFSS simulation.

The magnitude of the scattering parameter $|S_{11}|$ was measured first by using the network analyzer HP 8753, with an absorber placed in front of the antenna. A tunable quarter-wave sleeve balun is added to avoid the leaking current along the cable. The sleeve balun used in this measurement was illustrated in Figure 2.13. Since an ordinary balun is a narrow band device, a tunable balun is designed for this measurement which allows us to choose the optimal parameters for the balun. First, in order to suppress the leaking current efficiently, the diameter of the sleeve balun should be fairly large

compared to that of the coaxial cable [61]. Based on HFSS simulation results,

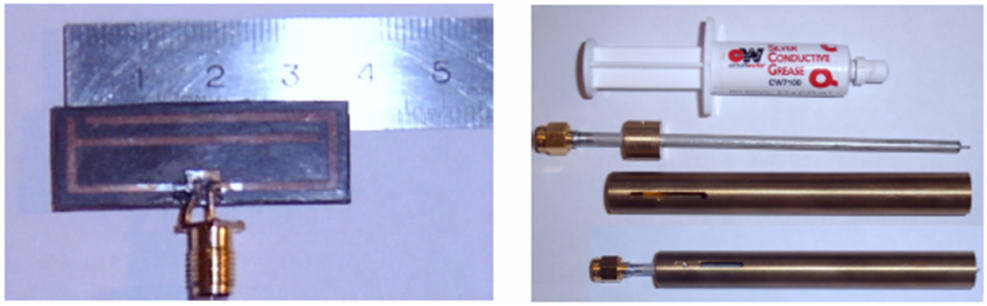

Figure 2.13: Illustration of the fabricated electrically small loop antenna, the sleeve balun and the conductive glue.

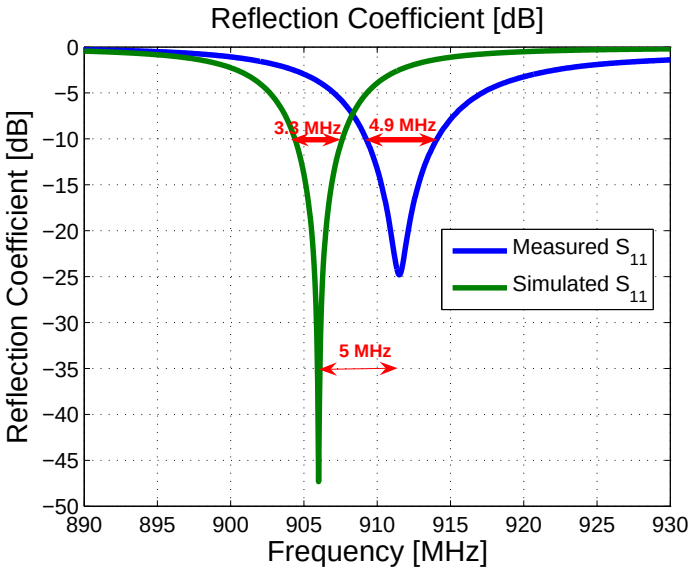

Figure 2.14: The simulated and measured $|S_{11}|$ for the electrically small loop antenna which is designed to operate at 906 MHz.

a diameter of 11 mm is chosen. Second, due to the fringing field effect, a gap is suggested between the antenna and the open end of the balun. Moreover, a conductive glue is necessary to provide a perfect shorting wall. Then the simulated and measured $|S_{11}|$ of this small loop are compared in Figure 2.14. While the simulated resonance frequency is 906 MHz, the measured resonance frequency is 911 MHz, and the deviation is 5 MHz, that is 0.6%. The simulated and measured -10 dB impedance bandwidth are 3.3 MHz and 4.9 MHz respectively, and the difference is thus 1.6 MHz. The difference in the resonance frequency is due to the sensitivity in the capacitance loading in the

large loop as well as the fabrication precision.

The radiation efficiency measurement of ESA is of a great challenge. The small antenna is a balanced device, and using an unbalanced coaxial cable to feed the antenna results in a leaking current along the cable, which may give a significant error in the radiation efficiency. For this measurement, the small antenna is measured by using two different techniques as follows, and in both of them a quarter-wavelength sleeve balun was added. First, the

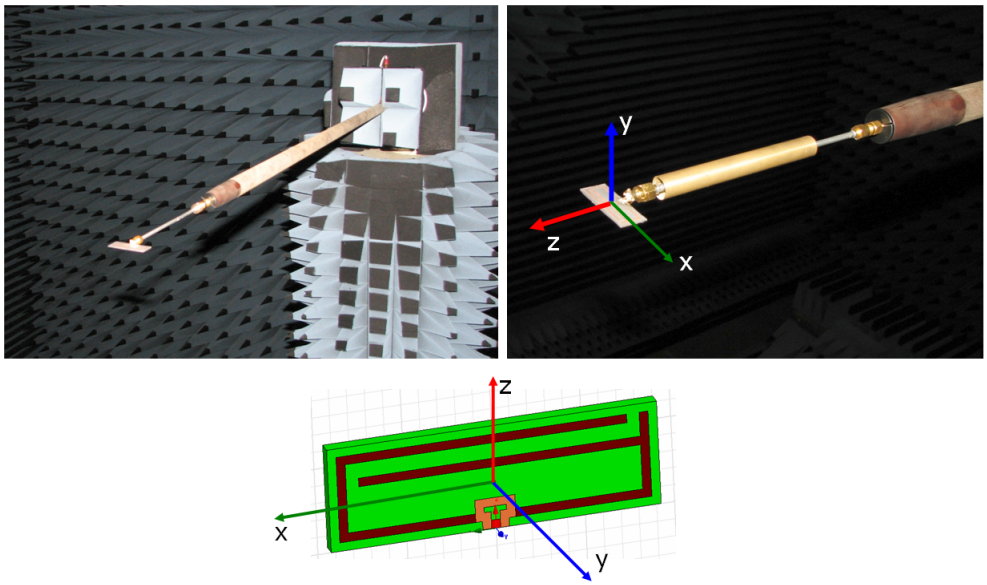

Figure 2.15: Illustration of the measurement setup of the electrically small loop, in the DTU spherical near field antenna test facility.

antenna is measured by using the Wheeler's Cap method, and the radiation efficiency is found to be 21%, which is reasonably close to the simulated radiation efficiency 17%. The gain is acceptable for the antenna of such small dimensions. The difference in the radiation efficiency can be explained by that the loss in the dielectric material may be not exactly the same as the value used in the simulations, which is provided by the manufacturer. Second, this small antenna was also measured in the DTU spherical near field antenna test facility, illustrated in Figure 2.15. The simulated and measured directivity versus θ scan are compared, for the cases of $\phi = 0^o$ and $\phi = 90^o$, respectively, which are shown in Figure 2.16- 2.17. A good agreement is observed when the quarter-wavelength balun is added. Then the radiation efficiency of this antenna was obtained by using the substitution method, and is found to be 20%. It agrees very well with the measured result by the Wheeler's cap method.

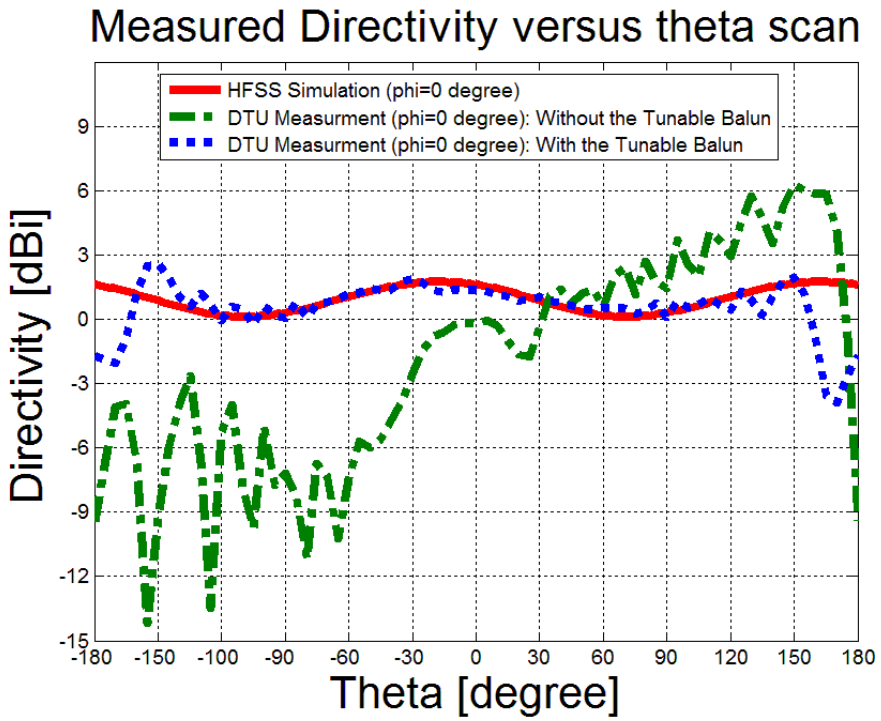

Figure 2.16: The simulated and measured directivity versus θ for the electrically small loop antenna when $\phi = 0^o$. The antenna is designed to operate around 906 MHz.

2.2 Two-Turn Planar Electrically Small Loop Antenna

It is known that the radiation efficiency of a loop antenna is improved significantly when the multiple-turn loop is used. For the loop design presented in previous section, although there exist two loops which are the large one and small one, only the large loop contributes to the radiation because the dimensions of the small loop are much smaller than that of the large one, as illustrated in Figure 2.1. The working mechanism of that self-resonant electrically small antenna is based on the inductive coupling between the two loops. Only the mutual inductance M contributes to the working mechanism, and C_{couple} is approximated to be negligibly small.

Furthermore, if the dimensions of the two loops become comparable as illustrated in Figure 2.18, both the mutual capacitance C_{couple} and mutual inductance M must be taken into account. The same analytical model can still be applied by considering the capacitive coupling together with the inductive coupling between the two loops, as shown in Figure 2.2. This is viewed as the

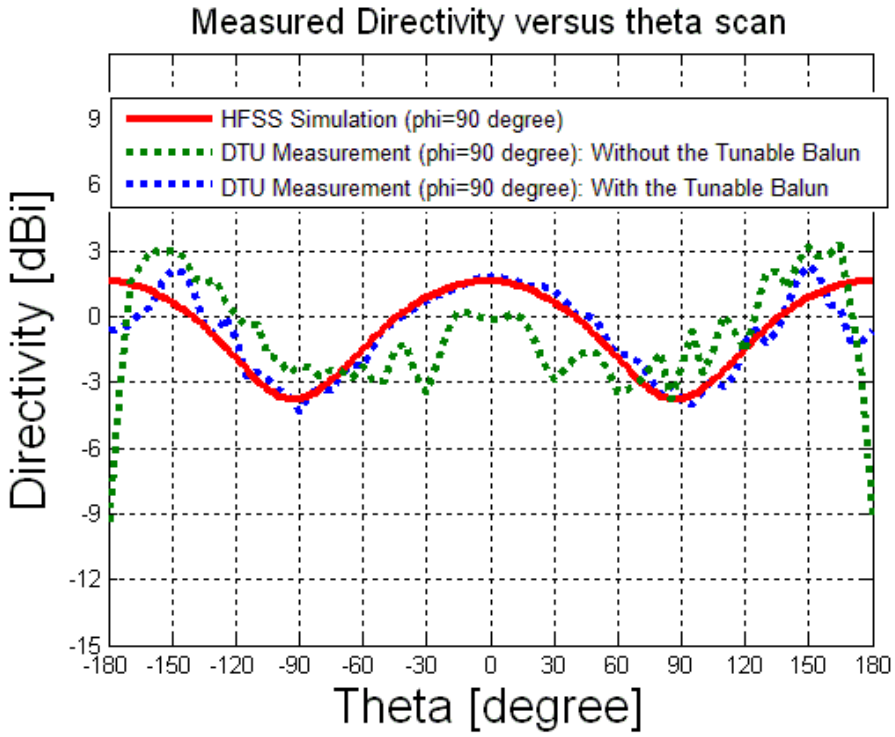

Figure 2.17: The simulated and measured directivity versus θ for electrically small loop antenna when $\phi = 90^o$. The antenna is designed to operate around 906 MHz.

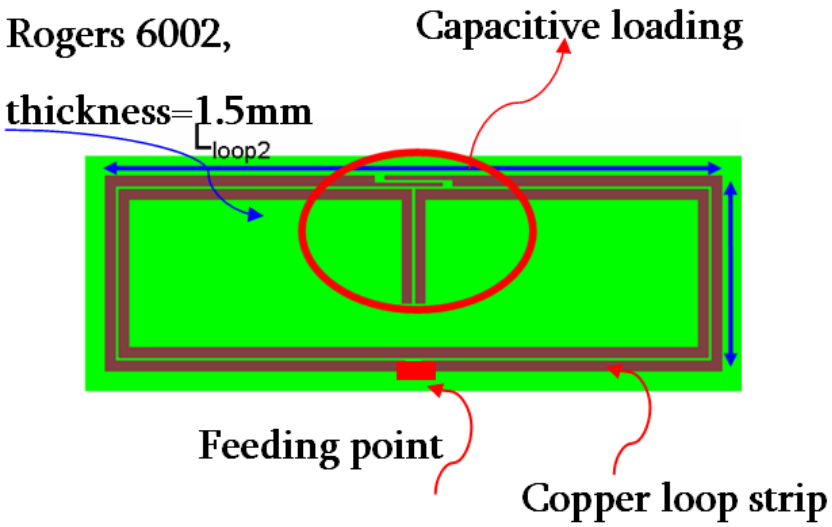

Figure 2.18: Illustration of the two -turn electrically small loop antenna.

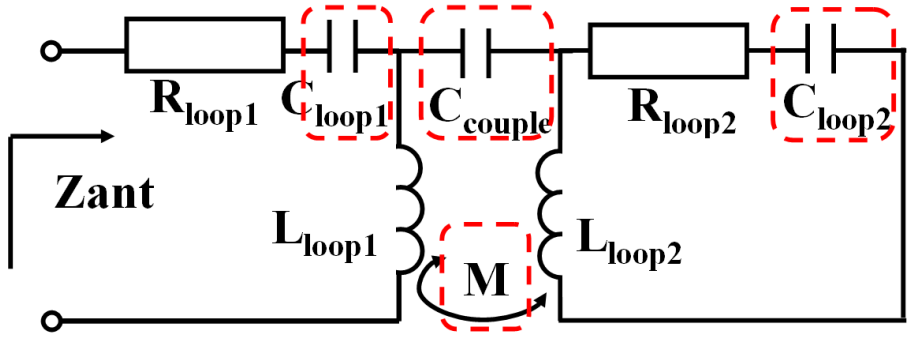

Figure 2.19: Analytical model of the two-turn self-resonant electrically small loop antenna.

main difference between the designs illustrated in Figure 2.1 and Figure 2.18. For the design in Figure 2.18, it is noted that the capacitive loading elements are used in both two loops, for the purpose of compensating the inductance in each loop. Then the equivalent model is modified, as shown in Figure 2.19, where C_{loop1} and C_{loop2} represent the capacitive loading in each loop. Since both of the two loops in this antenna contribute to the radiation mechanism, the radiation efficiency of this antenna is improved significantly compared the previous loop design, but the impedance tuning becomes complicated.

In the circuit model illustrated in Figure 2.19, the resistance and reactance of the input impedance Z_{ant} for this antenna are determined from

$$R_{ant} = R_{loop1} + (\omega M)^2 \frac{R_{loop2}}{R_{loop2}^2 + (\omega L_{loop2} - \frac{1}{\omega C_2})^2} \tag{2.17}$$

$$X_{ant} = j(\omega L_{loop1} - \frac{1}{\omega C_1}) - j\frac{(\omega M)^2(\omega L_{loop2} - \frac{1}{\omega C_2})}{R_{loop2}^2 + (\omega L_{loop2} - \frac{1}{\omega C_2})^2}. \tag{2.18}$$

where

$$C_1 = C_{loop1} + C_{couple} \tag{2.19}$$

$$C_2 = C_{loop2} + C_{couple} \tag{2.20}$$

The antenna impedance is tuned to resonance by tuning the capacitance C_{loop1}, C_{loop2}, C_{couple} and the mutual inductance M. The equation (2.17) and (2.18) provide guidance in the tuning of the antenna input impedance.

The geometry and design variables of this two-turn self-resonant electrically small loop is illustrated in Figure 2.20 and its dimensions are provided in Table2.2. The simulated resonance frequency is 903.2 MHz. The impedance

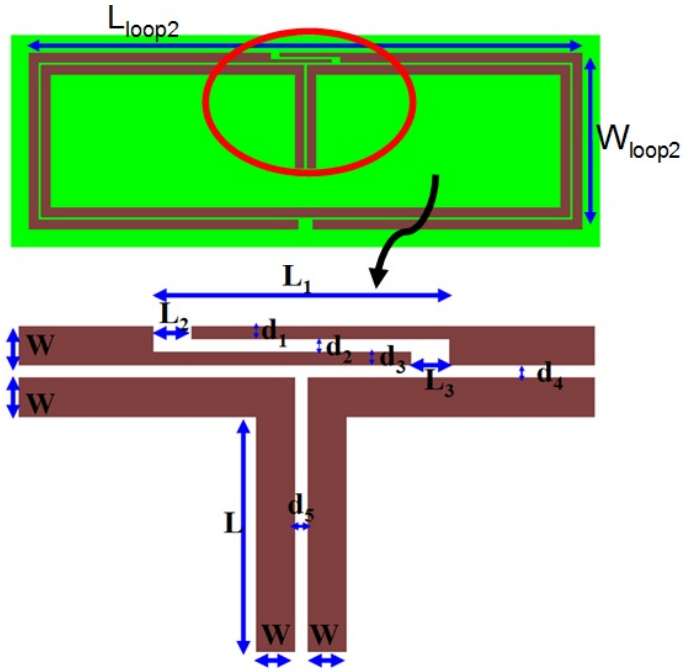

Figure 2.20: Geometry and design variables of the two-turn self-resonant electrically small loop antenna.

bandwidth reference to -10 dB is 4.5 MHz. The simulated radiation efficiency is found to be 35 %. The magnitude of the antenna reflection coefficient and the antenna input impedance are given in Figure 2.21 and Figure 2.22, respectively. The magnitude of the simulated surface current vector provided by HFSS is presented in Figure 2.23. It is seen that the current flow in each loop are in the same direction, which shows both of the two loops contribute to the radiation; thus the radiation efficiency is improved compared to the previous loop design.

2.3 Three-Dimensional (3-D) Folded Electrically Small Loop Antennas

Since the antenna size is limited by the dimensions of hearing-aids, the performances of the two-dimensional (2-D) planar loop antenna are restricted and thus the performances are difficult to be improved further. In this section, several 3-D folded electrically small loops are proposed, and they are configured so that the hearing-aids will be embedded inside the folded loop

Table 2.2: Dimensions and performances of the planar two-turn self-resonant electrically small loop antenna, designed around 900MHz.

Two-Turn Electrically Small Loop	Antenna Performances
Antenna Dimension	L_{loop2}=36.6mm=0.109λ_0 W_{loop2}=11.6mm=0.03λ_0 $d_1 = d_2 = d_3 = d_4 = d_5$=0.2mm L=6.2mm, W=0.6mm L_1=4.6mm,$L_2 = L_3$=0.6mm Substrate: Rogers 5870 (thickness=1.5mm)
Center Frequency of Operation	903.2 [MHz]
Impedance Bandwidth @ -10 dB	4.5 [MHz]
Impedance Bandwidth @ -15 dB	2.5 [MHz]
Radiation Efficiency [%]	35%
Maximum Directivity [dBi]	1.64 [dBi]
Maximum Gain [dBi]	-2.89 [dBi]

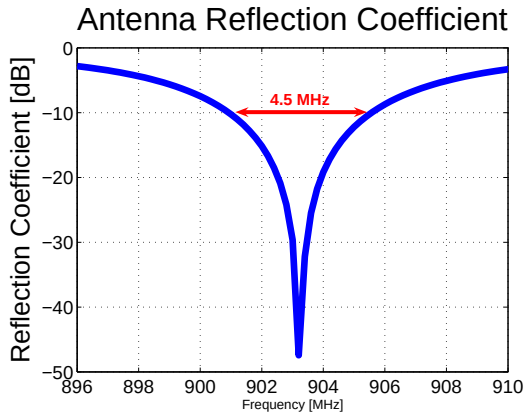

Figure 2.21: Magnitude of the Antenna reflection coefficient.

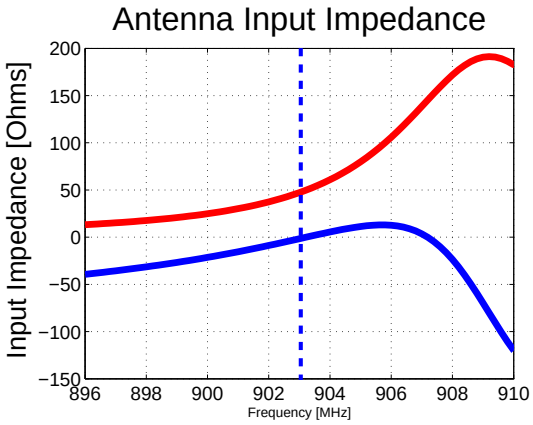

Figure 2.22: Antenna input impedance.

antenna. These antennas are designed to make better use of the volume of hearing-aids so that the antenna performances are improved.

Similarly, the 3-D loop antenna is formed by two small loops, the small one and large one, and the working mechanism is also based on the inductive coupling between the two loops. The dimensions of the small loop are much less that of the large one, and the large loop is folded in a proper way to form the 3-D antenna design. The capacitive loading is also added to compensate the loop inductance and make the antenna resonant.

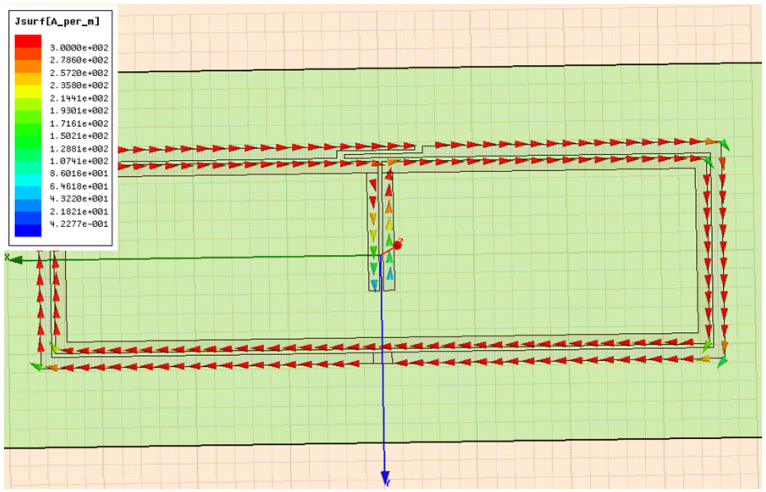

Figure 2.23: The magnitude of the simulated surface current vectors for the two-turn electrically small loop at 900 MHz, predicted by HFSS.

Figure 2.24 presents the configuration of this 3-D loop folded loop antenna, which is designed at 1000 MHz. The antenna is mainly formed by a copper strip of the width 1 mm and of the thickness 35 μm. The antenna occupies a volume of 25 mm$\times$9 mm$\times$6 mm, with ka=0.28. In the design illustrated in Figure 2.24 (a) a capacitor of 0.17 μF is used as the loading element, while in the design illustrated in Figure 2.24 (b) a distributed printed capacitive element is used as the loading element. The advantage of the latter case is that it avoids using the lumped components which face the aging and tolerance problems.

At the initial design phase, no substrate is present in the antenna design. This is because the material permittivity and conductivity of the hearing-aid shell are unknown. The permittivity measurement of this material faces a difficulty because the manufacturer can not provide a sample for measurements with a suitable size. Hence, we will first design the antenna insolated to understand its working mechanism and investigate its performances, and later on this antenna will be adjusted to fit the surface of hearing-aids and will be tuned together with the device.

The geometry and design variables of these 3-D folded self-resonant electrically small loops are illustrated in Figure 2.25 and their dimensions are provided in Table 2.3. For antenna design (a), a lossless capacitor of 0.17 μF is used as the loading element. The simulated resonance frequency is 1003.5 MHz. The impedance bandwidth reference to -10 dB and -15 dB are 2.3 MHz and 1.0 MHz, respectively. The simulated radiation efficiency is found to be

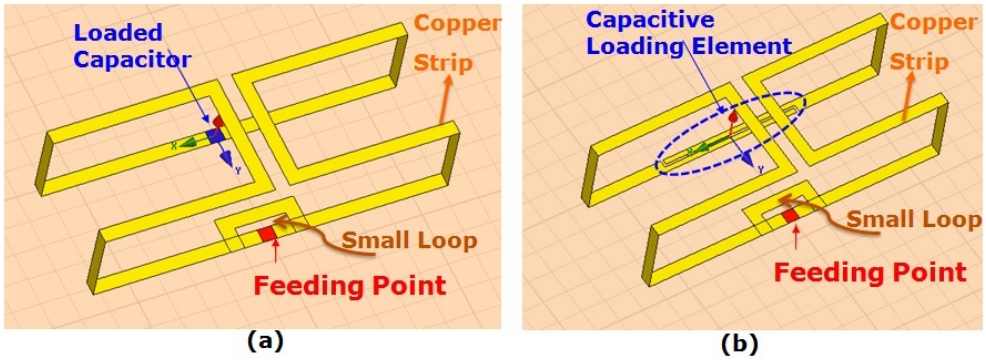

Figure 2.24: The 3-D folded loop antenna designed at 1000 MHz. (a) and (b) present different types of the loading element which is a capacitor and the distributed printed capacitive element.

41.23%. For antenna design (b), the distributed printed capacitive element, of a finger shape, is used as the loading element. The simulated resonance frequency is 999 MHz. The impedance bandwidth reference to -10 dB and -15 dB are 2.3 MHz and 1 MHz, respectively. The simulated radiation efficiency is found to be 40%. The radiation pattern and the magnitude of the simulated surface current vector for the antenna design in Figure 2.25 (a) are presented in Figure 2.26, which is predicted by HFSS.

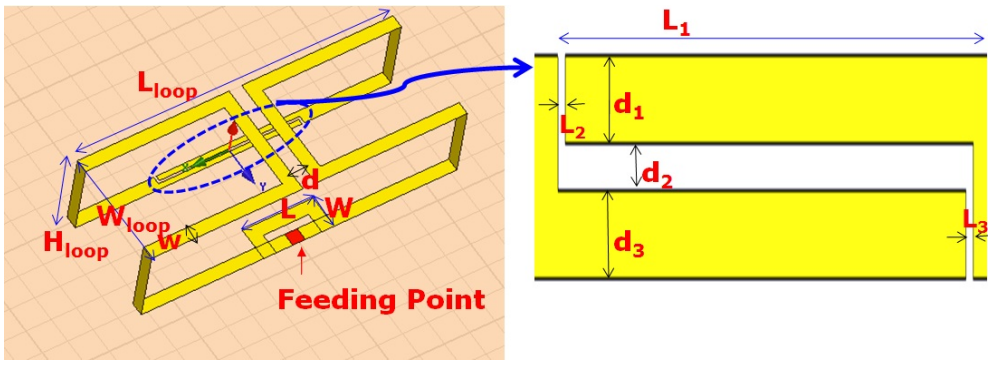

Figure 2.25: The geometry and design variables of the 3-D folded self-resonant electrically small loops, designed at 1000 MHz.

Moreover, there are several ways to fold the large loop, as illustrated in Figure 2.27. This results in the differences in antenna radiation pattern and other performances. The geometry and design variables of the 3-D folded loop antennas are given in Table2.4 for designs presented in Figure 2.27 (c) and (d), respectively.

For antenna design in Figure 2.27 (c) , a lossless capacitor of 0.17 μF is used

Table 2.3: Dimensions and performances of the 3-D folded self-resonant electrically small loop antennas, designed around 1000 MHz.

3-D Folded Electrically Small Loops	Antenna (a)	Antenna (b)
Antenna Dimensions	L_{loop}=25mm=0.083λ_0 W_{loop}=9mm=0.03λ_0 H_{loop}=6mm=0.028λ_0 $L = 5.6mm, W = 2.5mm$ Substrate: no C=0.17μ F	L_{loop}=25mm=0.083λ_0 W_{loop}=9mm=0.03λ_0 H_{loop}=6mm=0.028λ_0 $L = 5.6mm, W = 2.5mm$ Substrate: no $d_1 = d_3$=0.4mm d_2=0.2mm,L_1=11.3mm L_1=11.3mm
ka	0.28	0.28
Center Frequency	1003.5 [MHz]	999 [MHz]
Impedance Bandwidth @ -10 dB	2.3 [MHz]	2.3 [MHz]
Impedance Bandwidth @ -15 dB	1.0 [MHz]	1.0 [MHz]
Radiation Efficiency	41.23%	40%
Maximum Directivity	2.136 [dBi]	2.134 [dBi]
Maximum Gain	-1.71 [dBi]	-1.89 [dBi]

as the loading element. The simulated resonance frequency is 1001 MHz, and the impedance bandwidth reference to -10 dB and -15 dB are 2.3 MHz and 1.0 MHz, respectively. The simulated radiation efficiency is found to be 43.5%. For antenna design in Figure 2.27 (d), a lossless capacitor of 0.02 μF is used as the loading element. The simulated resonance frequency is 998 MHz, and the impedance bandwidth reference to -10 dB and -15 dB are 2.3 MHz and 1.0 MHz, respectively. The simulated radiation efficiency is found to be 41.8%. The simulated radiation pattern and magnitude of the simulated surface current vectors of these two designs are presented in Figure 2.28 and Figure 2.29, respectively, from which the difference in antenna radiation pattern is presented. It is seen that the bandwidth for these antenna designs are almost the same, but the design shown in Figure 2.27 (c) gives the highest radiation efficiency among these designs which is 43.5%.

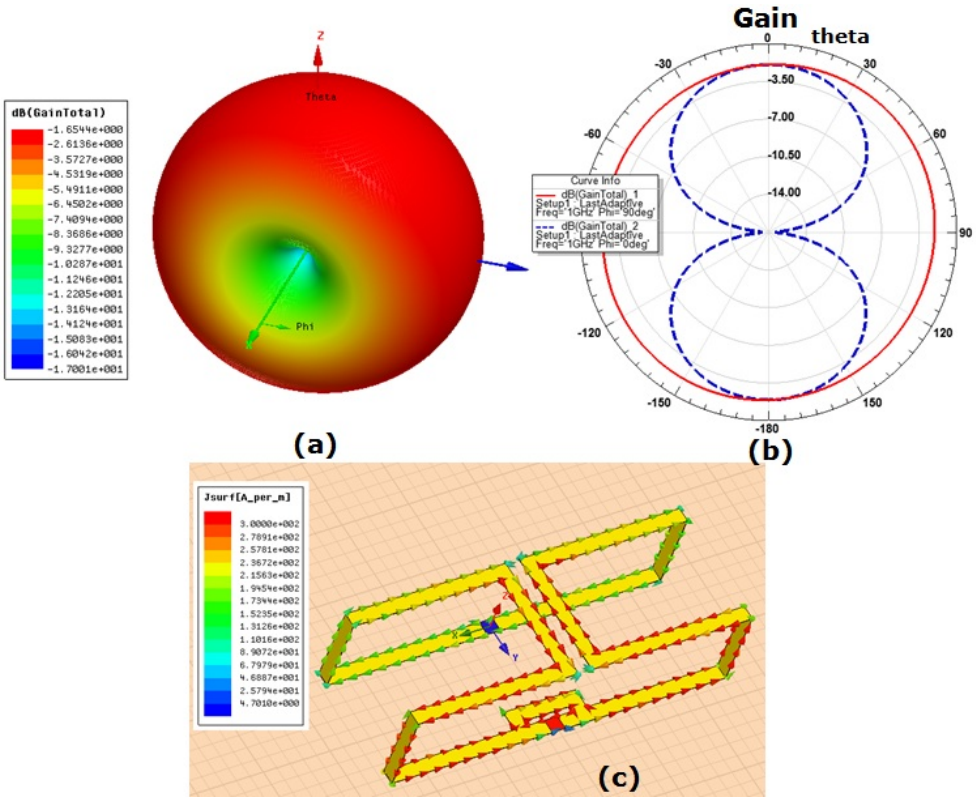

Figure 2.26: The radiation pattern and magnitude of the simulated surface current vectors of the 3-D folded self-resonant electrically small loop, designed at 1000 MHz. (a) presents the 3-D polar gain pattern, (b) presents the 2-D gain pattern in $\phi = 0^o$ and $\phi = 90^o$ plane and (c) presents the simulated surface current vectors.

2.4 Chapter Summary

In this chapter, several novel designs of the self-resonant electrically small loop antennas are presented for the hearing-aid application. The working mechanisms of these designs are explained. These antennas are

- **2-D planar electrically small loop antenna, evaluated at 900 MHz.** The working mechanism is based on the capacitive loading and the inductive coupling between the two small loops. The measured radiation efficiency is found to be 21% with ka being 0.33, and the impedance bandwidth reference to -15 dB is 1.7 MHz.
- **2-D planar two-turn electrically small loop antenna, evaluated at 900 MHz.**

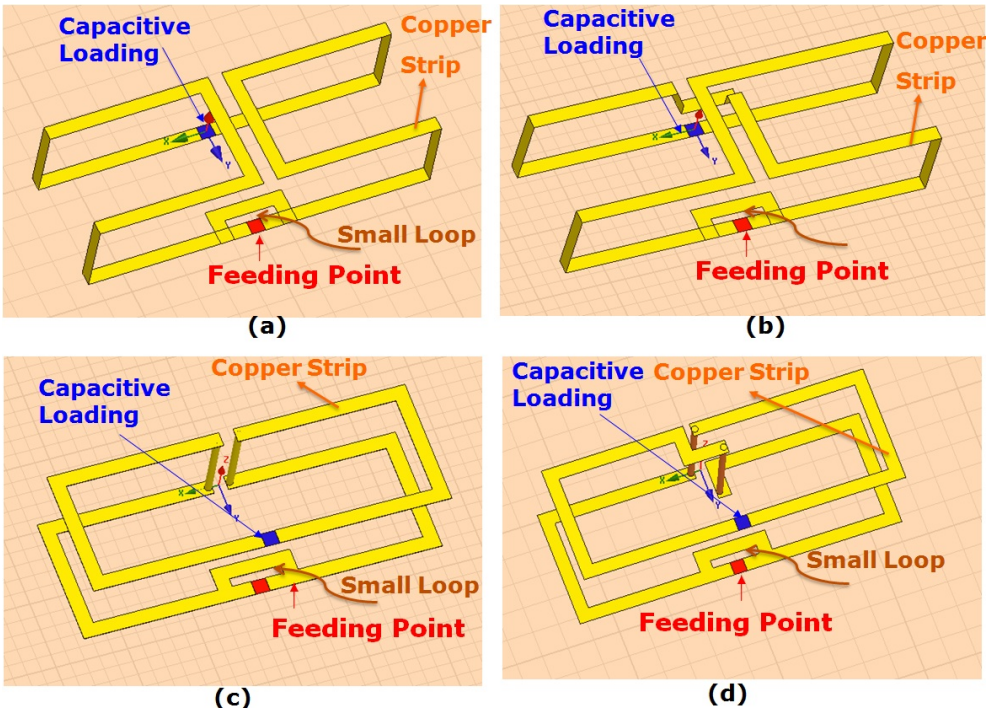

Figure 2.27: The 3-D folded loop antenna designed at 1000 MHz. Several different folding methods are presented.

Table 2.4: Dimensions and performances of the 3-D folded self-resonant electrically small loop antennas, for designs shown in Figure 2.27 (c) and (d).

3-D Folded Electrically Small Loops	Antenna Figure 2.27(c)	Antenna Figure 2.27 (d)
Antenna Dimensions	L_{loop}=25mm=0.083λ_0 W_{loop}=9mm=0.03λ_0 H_{loop}=6mm=0.028λ_0 L=5.4mm, W=2.4mm	L_{loop}=25mm=0.083λ_0 W_{loop}=9mm=0.03λ_0 H_{loop}=6mm=0.028λ_0 L=5.4mm, W=2.4mm
ka	0.28	0.28
Center Frequency	1001 [MHz]	998 [MHz]
Impedance Bandwidth @ -15 dB	1.0 [MHz]	1.0 [MHz]
Radiation Efficiency	43.5%	41.8%

The working mechanism of this antenna is based on the capacitive loading, and both the capacitive and inductive coupling between the two small loops that are of a comparable size are taken into account. The simulated radiation efficiency is found to be 34% with ka being 0.33,

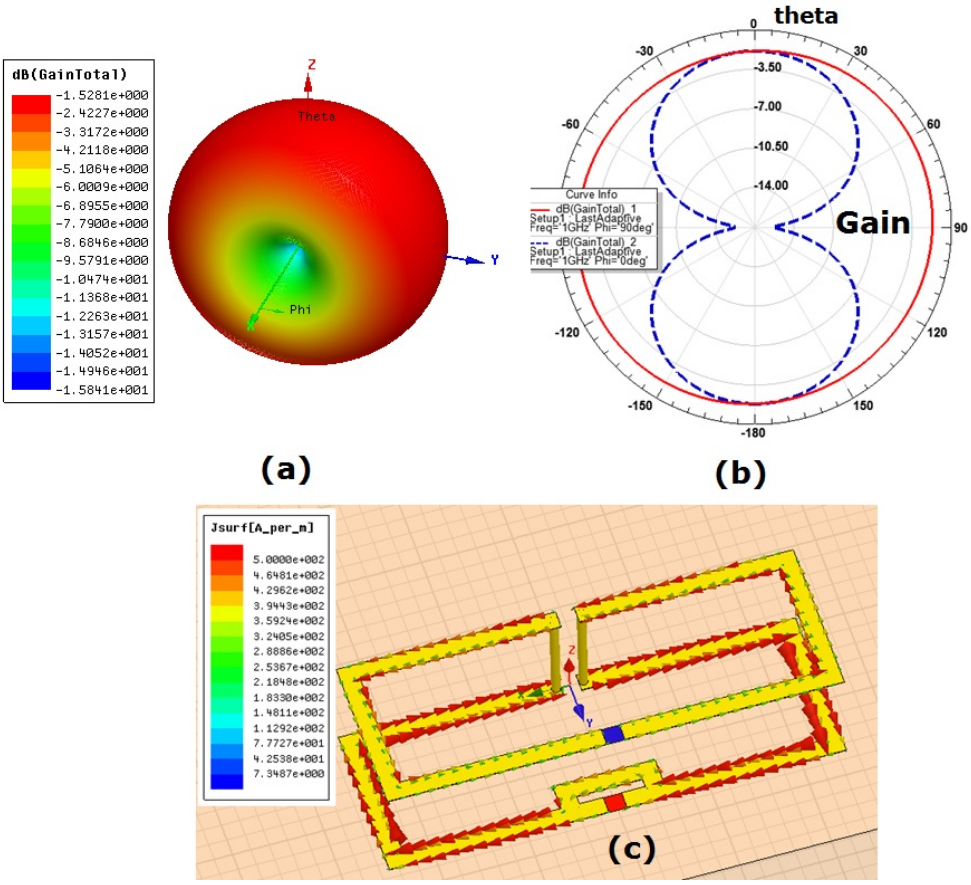

Figure 2.28: The radiation pattern and magnitude of the simulated surface current vectors of the 3-D folded self-resonant electrically small loop, for design shown in Figure 2.27 (c). (a) presents the 3-D polar gain pattern, (b) presents the 2-D gain pattern in $\phi = 0^o$ and $\phi = 90^o$ plane and (c) presents the simulated surface current vectors.

and the impedance bandwidth reference to -15 dB is 2.5 MHz.

- **3-D electrically small loop antennas, evaluated at 1000 MHz**
  The working mechanism is based on the capacitive loading and the inductive coupling between the two loops. The large loop is folded in a proper way to make better use of the device volume. There exist several ways to fold the large loop, and this results in a difference in the antenna radiation pattern. The maximum radiation efficiency of the folded loop is found to be 43% with ka being 0.28, and the impedance bandwidth reference to -15 dB is 1.0 MHz.

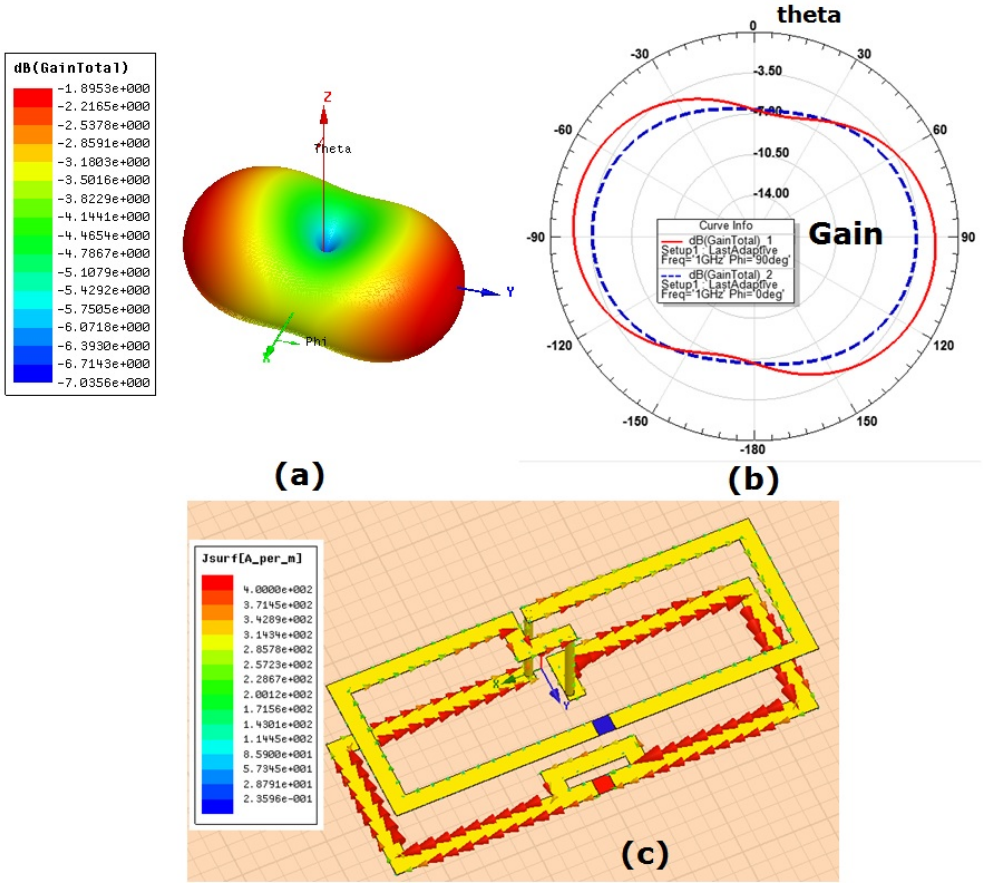

Figure 2.29: The radiation pattern and magnitude of the simulated surface current vectors of the 3-D folded self-resonant electrically small loop, for design shown in Figure 2.27(d). (a) presents the 3-D polar gain pattern, (b) presents the 2-D gain pattern in $\phi = 0^o$ and $\phi = 90^o$ plane and (c) presents the simulated surface current vectors.

During this project, several frequencies are evaluated for the hearing-aid application, including 405 MHz, 900 MHz and 1000 MHz, respectively. It is noted the optimization in the antenna radiation efficiency is only performed for the loop designs at 1000 MHz. In this dissertation, we mainly discuss the antenna designs at the frequency of 1000 MHz. In summary, the following observations are obtained in this chapter, which are

- **Impedance Matching**
  These antenna designs show that the impedance can be matched to the system characteristic impedance by using the self-resonant electrically

small loops, without the use of any external matching circuit. The use of the lumped components is avoided by replacing the loaded capacitors with the distributed printed loading element. The difficulty in the impedance matching is thus overcome.

- **Impedance Bandwidth**
  The specification in the impedance bandwidth is 1.0 MHz reference to -15 dB, as required in the link budget. Although the impedance bandwidth of these ESAs are narrow, the specification in the impedance bandwidth can still be satisfied, either for the 2-D planar loops or the 3-D folded loops.

- **Radiation Efficiency**
  The specification in the radiation efficiency can be satisfied. The radiation efficiency is improved to as high as 43% for the 3-D folded loop antenna, which occupies a volume of 25 mm$\times$9 mm$\times$6 mm.

CHAPTER

THREE

Measurement Techniques for Electrically Small Antennas

Nowadays the performances of antennas are verified with cable measurements in the anechoic chamber. This measurement technique works very well for most of the traditional antennas with the electrical size being lager than one half of a wavelength at least. However, the input impedance and radiation efficiency measurements for ESAs represent a great challenge, and typically there exist two mechanisms that introduce errors in the measurements.

First, the feed line causes a significant influence on the measured radiation efficiency for ESAs, due to leaking current on the outer surface of the feed line. The measured radiation efficiency can be strongly overestimated up to +10 dB due to this effect [61]. Although a sleeve balun can be added to suppress the leaking current, it is typically a narrow-band device. Several baluns are thus required for different frequency bands. Also, the dimension of a balun needs to be tuned carefully at the specified frequency. In addition, the balun may have a size that is comparable to or even larger than that of the ESA; thus it may give rise to scattering. Ferrite cores are also commonly used in the small antenna measurements, but this method may not be an appropriate solution either. It is because the ferrite cores are placed in the reactive field region of the ESAs. The leaking current on the feed line is partially reflected back and partially absorbed by the ferrite cores.

Second, the feed line contributes a large scattering structure even if the leaking current is suppressed. Measurements of antenna characteristics without the feed line is therefore highly desirable.

In this chapter, first, the effectiveness of adding ferrite cores and tunable sleeve-balun are investigated. Second, a modified Wheeler cap method for the radiation efficiency measurement of balanced electrically small antennas is introduced. Moreover, the application of this modified Wheeler cap method for antenna measurements in complex environments is further investigated. Third, a cable-free impedance and gain measurement technique for electrically small antennas is proposed. The electromagnetic model, simulation results, as well as measurement results are presented.

3.1 Ferrite Cores and Tunable Sleeve Balun

Ferrite cores are commonly used in small antenna measurements, but this method may not be an appropriate solution. It is because that ferrite cores are placed in the reactive field region of the ESAs; thus the leaking current on the feed line is partially reflected back and partially absorbed by the ferrite cores. The working mechanism of adding ferrite cores is to provide a very high reactive impedance along the feed line so that the leaking current can be forced to reflect back. Hence several pieces of ferrite cores are required to make sure the impedance is high enough. This solution is only valid up to 1 GHz for the radiation measurements. In this section, we focused on the application of the tunable sleeve balun. To start this analysis, the antenna under test (AUT) is described first.

A balanced electrically small loop is used as the AUT in this investigation. The miniature, self-resonant, capacitively loaded loop antennas were designed to operate around 400 MHz and around 900 MHz, respectively. The loop and the capacitor strips were printed on a 1.5 mm thick Rogers 5870 substrate with ε_r = 2.33 and $\tan\delta$ = 0.0012. The parameters of the capacitor and the feeding part were optimized with the HFSS software. An example of the loop antenna for operation around 900 MHz is shown in Figure 3.1 (a).

It was discovered soon after obtaining first measurement results that simple feeding of this almost symmetric antenna with a bare coaxial cable produced clearly wrong results. For example, not only the measured radiation pattern was strongly asymmetric, but also the measured radiation efficiency was strongly overestimated, for some techniques by as much as 3 times, as it will be shown below. It was clear that due to the asymmetric feeding, the leaking currents on the feed cable can be very strong and they contribute significantly to the antenna radiation. Therefore, it was decided to apply a standard solution to this problem using a sleeve balun. However, in order

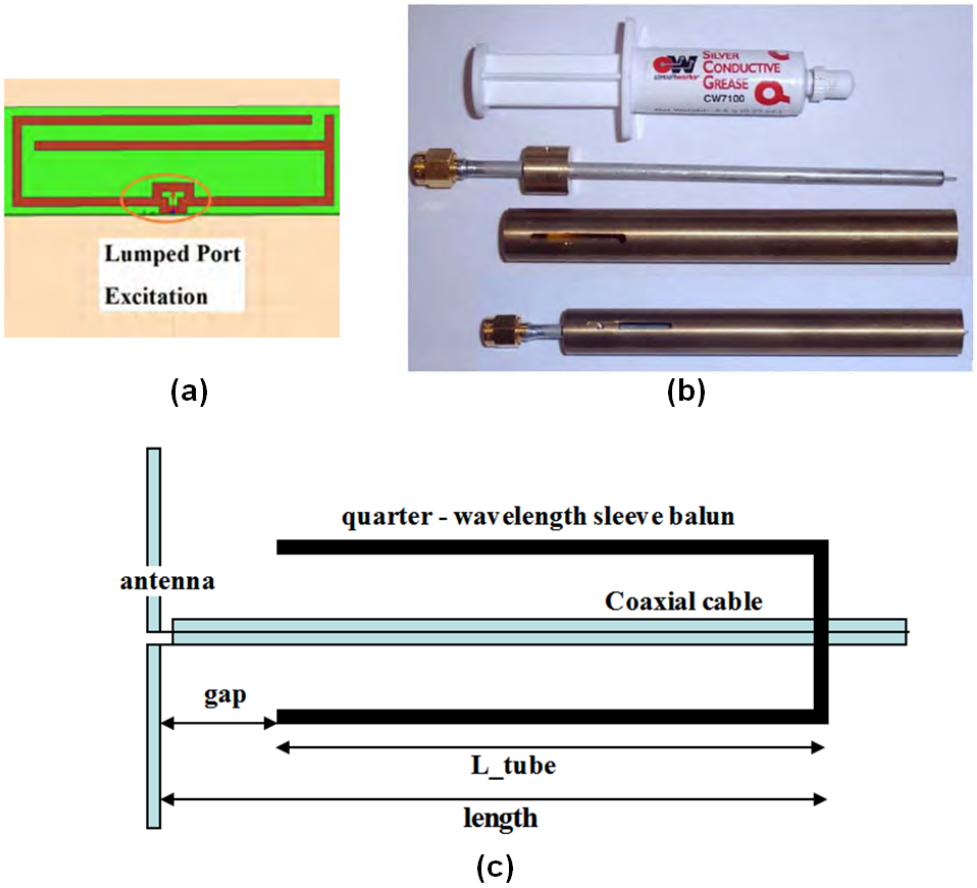

Figure 3.1: Illustrations of the AUT and the tunable sleeve balun. (a) presents the antenna under test (AUT). (b) presents the fabricated tunable sleeve balun. (c) illustrates the parameters of the tunable sleeve balun.

to have the flexibility of adjusting the balun characteristics, it was decided to manufacture a tunable balun with the possibility to change and optimize its length and the gap between the open end of the balun and the antenna. The details of the used tunable balun are presented in Figure 3.1 (b) and (c).

The illustration of the importance of a balun in the radiation efficiency measurements is presented at first in Figure 3.2. The radiation efficiency of the small loop antenna was measured without the balun for different lengths of the feeding cable. It is seen from Figure 3.2 that the measured values can increase more than 2 times, as compared to the expected value of about 20%, depending on the relative length of the cable. This effect is found to be weaker for free-space measurements, where the cable goes through the ab-

sorbers covering the support structure, and stronger for the measurements in a reverberation chamber, where the cable goes into the metallic wall. The latter apparently increases the effect of the leaking current by working as a reflecting surface and creating a standing wave.

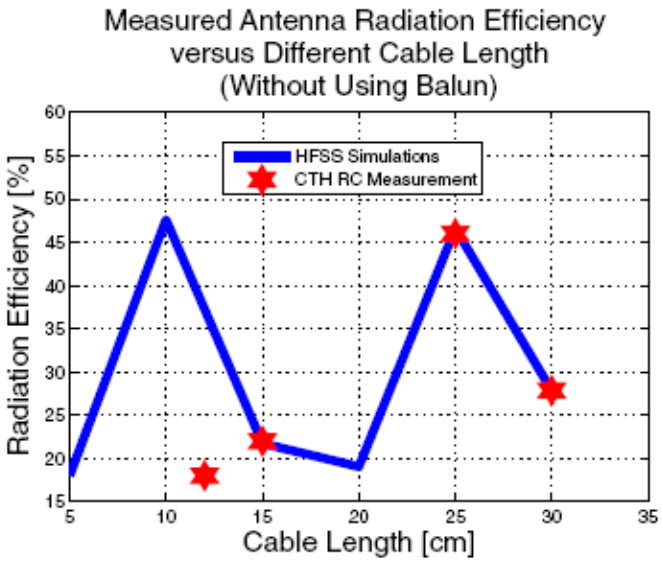

Figure 3.2: Dependence of the simulated and measured radiation efficiency on the feed cable length, without using a balun.

The measured radiation pattern of the loop antenna with and without the sleeve balun is shown in Figure 3.3 together with the simulated pattern from HFSS. It is clearly seen that improper feeding leads to a significant distortion of the radiation pattern, especially in the E-plane, where the error is +4/-9 dB. On the other hand, application of the properly tuned balun provides very good results with very small deviations up to the angle $\theta = 140^o$, after which the tower shadow gives pattern deviation within a couple of dBs. The tower shadow effect is minimized by using a 1 meter long dielectric tube as the mechanical support interface.

It should also be noted that careful tuning of the balun is also very important, both for the radiation pattern and for the radiation efficiency measurements. The optimum balun parameters are investigated and the measured radiation efficiency versus the balun gap length are presented in Figure 3.4 (a), (b) and (c) for the balun length being 83mm, 88mm and 93mm, respectively. Figure 3.4 (d) presents the measured radiation efficiency versus the lengths of the feed line, for three cases with a perfectly tuned balun. It is

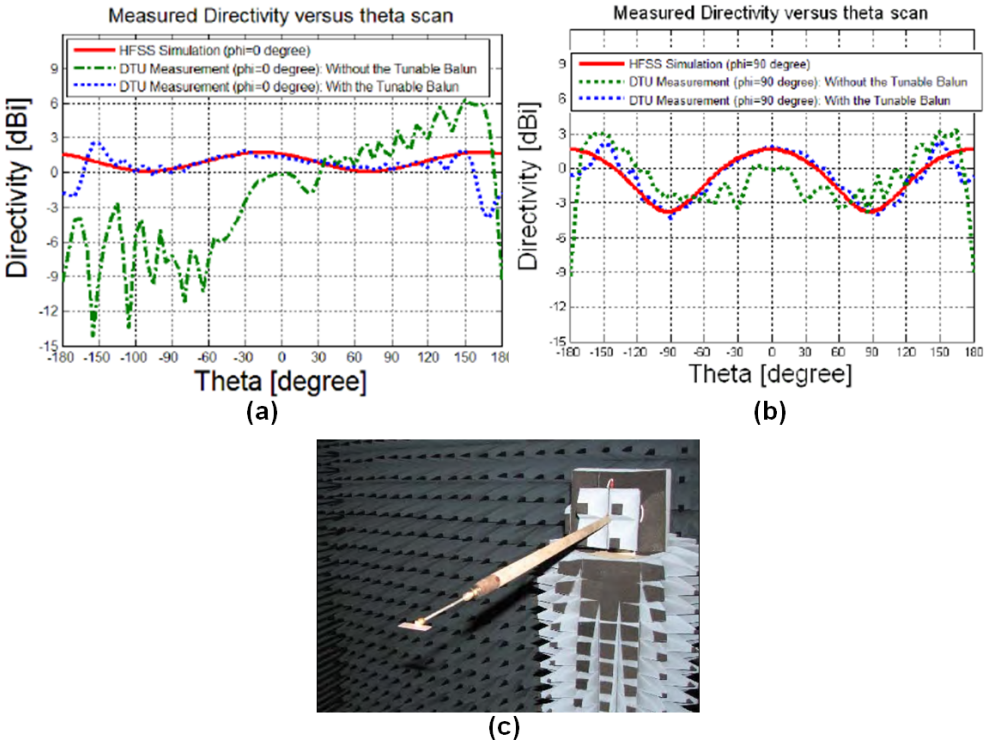

Figure 3.3: The measured radiation pattern of the loop antenna with and without the sleeve balun. (a) presents the measured directivity in the E-plane ($\phi = 0^o$) at DTU, with and without the tunable balun. (b) presents the measured directivity in the H-plane ($\phi = 90^o$) at DTU, with and without the tunable balun.

seen that the measurement result changes versus the gap length. By examining the expected radiation efficiency that is 20%, the optimum parameter L_{tube} is thus obtained which is approximated to be 68 mm for all the three cases. The gap length is better chosen to be 10 mm-20 mm from our experiences. Though it is called a quarter-wave sleeve balun, it was found that the optimum length of the short-circuited sleeve (air-filled) should be about 0.2 wavelength, while the optimum gap between the open end of the sleeve balun and the antenna should be between 0.06-0.1 wavelength. It was noted from numerous experiments that even small deviation from these optimum parameters, e.g. decreasing or increasing the gap, results in strong overestimate of the radiation efficiency, in our case up to twice as much. The found optimum parameters of the balun generally agree with those found in the literature, but the increased sensitivity to the balun parameter deviations, to our knowledge, was not reported before.

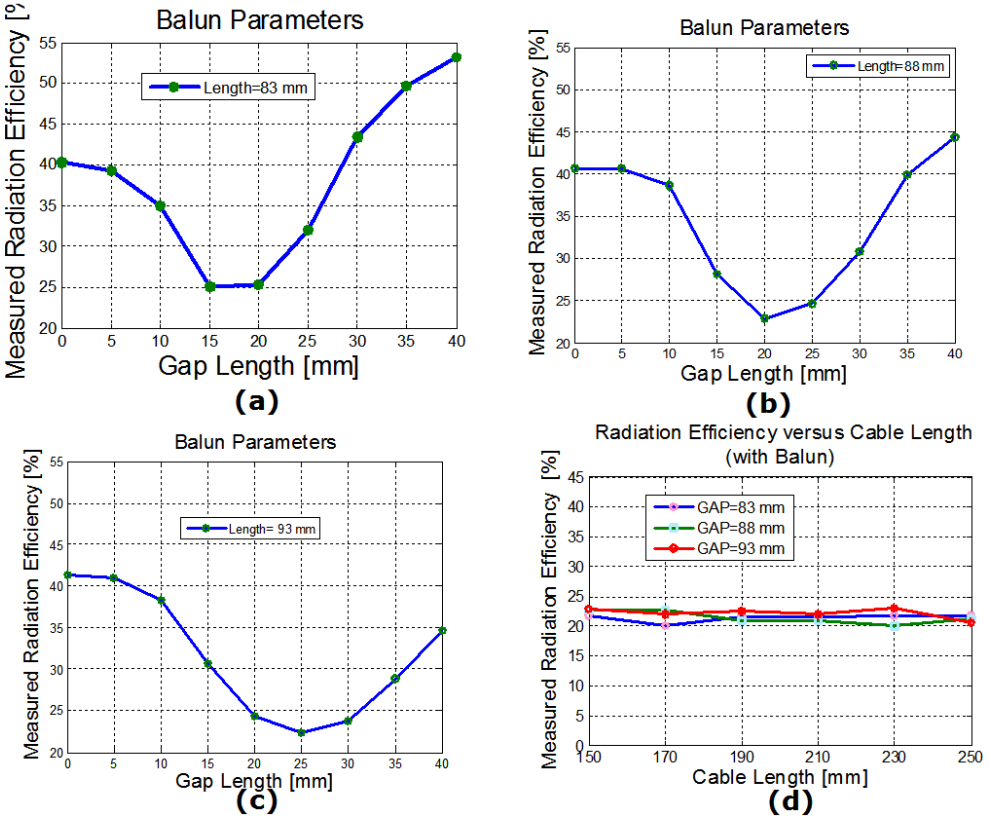

Figure 3.4: Illustrations of the balun parameter investigations. (a) presents the measured radiation efficiency versus the gap length, for the balun length being 83 mm. (b) presents the measured radiation efficiency versus the gap length, for the balun length being 88 mm. (c) presents the measured radiation efficiency versus the gap length, for the balun length being 93 mm. (d) presents the measured radiation efficiency versus the length of the feed-line, for three cases with a perfectly tuned balun.

3.2 Modified Wheeler Cap Method for the Radiation Efficiency Measurement of Balanced Electrically Small Antennas

For small antenna measurements, the Wheeler cap method is a well known and widely used method for the radiation efficiency measurement. However, this method possesses several limitations [62–64]. First, while being applied for unbalanced antennas on a ground plane, it presents a challenge for balanced antennas like loops or dipoles. Balanced electrically small antennas, such as dipoles and loops, have many applications, especially in ultra small devices like sensors, hearing-aids and RFIDs. Wide use of balanced anten-

nas in these applications is caused by the fact that the ground plane required for proper operation of unbalanced antennas, such as monopoles or inverted F antennas, is not existing in the ultra small devices. The performances of unbalanced antennas are then very sensitive to the changes in the working environment, while the balanced antennas are less sensitive to these. For electrically small antennas, the antenna impedance and radiation efficiency are two important parameters that characterize their performances and are of particular interest. However, proper measurement of these two parameters represents great challenges. Unless a carefully adjusted balun is used, the feeding coaxial cable has a significant influence on the measured performances due to the leaking current on the outer conductor and the scattering effects. Accurate measurement techniques for balanced small antennas need to be addressed, especially for the radiation efficiency measurements. Second, the presence of the cavity resonances and their influence on the measurement results impose certain limitations on the cavity dimensions. Thus measurements of different small antennas working at different frequencies may require several cavities of different dimensions, since measurements in a wide frequency band represent a great challenge. Moreover, limited dimensions of the cavity also impose limitations on small antenna measurements in a complex environment. For instance, measurements in the presence of a human hand or head phantom or antenna-on-body measurements are not possible.

In this section, we propose a modification of the Wheeler cap method for the radiation efficiency measurement of balanced ESAs which can be symmetric or asymmetric balanced antennas. A new three-port network model is then proposed for this modified Wheeler cap technique. In order to confirm the validity of the proposed method, an electrically small loop antenna and a wideband dipole were simulated and measured using this method and the obtained results are compared. These results are also compared to the measurement results obtained in an anechoic chamber, with a balun added in front of the AUT.

3.2.1 Three-Port Model of the Wheeler Cap Method

The original Wheeler cap method [62] was further developed in [63–65], in which a two-port network model is proposed by assuming that the antenna is operated in a single mode, and the two ports are defined as the antenna input terminal and the transition between the antenna and free space, respectively. Two measurements are involved in this method, which are the measurement of the antenna input reflection coefficients in free space and in a Wheeler cap,

respectively. The antenna radiation efficiency can be calculated from these two measurements. However, this method is well applied only for antennas on a ground plane, while for balanced antennas the influence of the feed cable represents a severe problem.

In this work, a three-port network model is proposed for the Wheeler cap method for measuring the radiation efficiency of small balanced antennas. As shown in Figure 3.5, the three ports are two excitation ports and one radiation port. A differential-fed antenna is viewed as a linear two-port model, and a virtual ground plane is assumed in the middle of the excitation terminal.

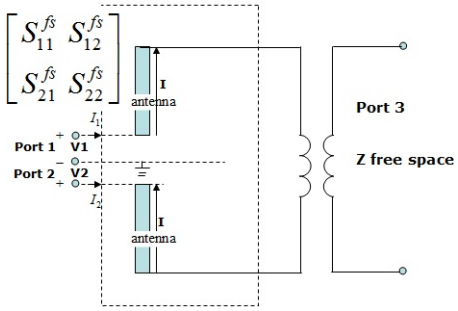

Figure 3.5: An electrically small balanced antenna with the two-port excitation in free space.

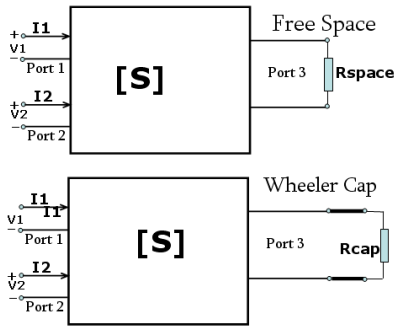

Figure 3.6: The three-port network model of the Wheeler cap measurement for balanced small antennas.

Determination of the differential impedance by using the scattering parameter (s-parameter) based measurements has been studied previously [66–68]. In the method reported in [66], two microstrip lines mounted back to back are used as the test fixture. Then several home-made non-standard calibration tools are used at the end of two microstrip lines in the calibration. The accuracy is found to be acceptable up to 1 GHz. Later, further development of this method was proposed in [67]. It was suggested doing the calibration

by using standard calibration tools, which is performed at the end of the cables of the vector network analyzer (VNA). Instead of using microstrip lines, two pieces of extra coaxial cables are used as the test fixture, whose outer conductors are soldered together. The test fixture parameters need to be extracted from the measurement data in the de-embedding. Then the antenna impedance can be calculated. Recently, Qing et al. suggested to use the port extension function of the VNA to find the antenna impedance, instead of the above calculations [68].

In this work, we apply the s-parameter based method in combination with the Wheeler cap method to determine the antenna radiation efficiency for balanced small antennas. An electrically small dipole antenna with the two-port excitation in free space is illustrated in Figure 3.5. Inside the Wheeler cap, Figure 3.6, the port 3 is loaded with the impedance of the Wheeler cap, with the reflection coefficient being Γ_L, and we obtain the scattering equations for the two ports

$$\begin{bmatrix} S_{11}^{wc} & S_{12}^{wc} \\ S_{21}^{wc} & S_{22}^{wc} \end{bmatrix} = \begin{bmatrix} S_{11} + \frac{S_{13}S_{31}\Gamma_L}{1-S_{33}\Gamma_L} & S_{12} + \frac{S_{13}S_{32}\Gamma_L}{1-S_{33}\Gamma_L} \\ S_{21} + \frac{S_{23}S_{31}\Gamma_L}{1-S_{33}\Gamma_L} & S_{22} + \frac{S_{23}S_{32}\Gamma_L}{1-S_{33}\Gamma_L} \end{bmatrix} \tag{3.1}$$

where S_{nm}^{wc} are the s-parameters of the model obtained inside the Wheeler cap. While in free space, $\Gamma_L = 0$, and the scattering equations are simplified to

$$\begin{bmatrix} S_{11}^{fs} & S_{12}^{fs} \\ S_{21}^{fs} & S_{22}^{fs} \end{bmatrix} = \begin{bmatrix} S_{11} & S_{12} \\ S_{21} & S_{22} \end{bmatrix}. \tag{3.2}$$

where S_{nm}^{fs} are the s-parameters of the model obtained in free space, as shown in Figure 3.6. For symmetric electrically small antennas, the antenna input impedance Z_{ant} in free space and in the Wheeler cap can be determined from

$$\begin{aligned} Z_{ant}^{fs} &= 2Z_0 \frac{1-(S_{11}^{fs})^2+(S_{21}^{fs})^2-2S_{21}^{fs}}{(1-S_{11}^{fs})^2-(S_{21}^{fs})^2} \\ &= 2Z_0 \frac{(1+S_{11}^{fs}-S_{21}^{fs})}{(1-S_{11}^{fs}+S_{21}^{fs})} \end{aligned} \tag{3.3}$$

$$\begin{aligned} Z_{ant}^{wc} &= 2Z_0 \frac{1-(S_{11}^{wc})^2+(S_{21}^{wc})^2-2S_{21}^{wc}}{(1-S_{11}^{wc})^2-(S_{21}^{wc})^2} \\ &= 2Z_0 \frac{(1+S_{11}^{wc}-S_{21}^{wc})}{(1-S_{11}^{wc}+S_{21}^{wc})} \end{aligned} \tag{3.4}$$

Here, Z_0 is the characteristic impedance of the feed cable. As shown in equations (3.3) and (3.4), the simplified formulas are used to avoid the singularity

for the case $1 - S_{11}^{fs} - S_{21}^{fs} = 0$ or $1 - S_{11}^{wc} - S_{21}^{wc} = 0$. For asymmetric electrically small antennas, the antenna input impedance Z_{ant} in free space and in the Wheeler cap are

$$Z_{ant}^{fs} = \frac{2Z_0(1 - S_{11}^{fs}S_{22}^{fs} + S_{12}^{fs}S_{21}^{fs} - S_{12}^{fs} - S_{21}^{fs})}{(1 - S_{11}^{fs})(1 - S_{22}^{fs}) - S_{21}^{fs}S_{12}^{fs}}, \tag{3.5}$$

$$Z_{ant}^{wc} = \frac{2Z_0(1 - S_{11}^{wc}S_{22}^{wc} + S_{12}^{wc}S_{21}^{wc} - S_{12}^{wc} - S_{21}^{wc})}{(1 - S_{11}^{wc})(1 - S_{22}^{wc}) - S_{21}^{wc}S_{12}^{wc}}. \tag{3.6}$$

In order to determine the antenna radiation efficiency, two measurements are necessary, which are the full two-port s-parameter measurement in free space and in the Wheeler cap, respectively. Then the antenna input reflection coefficients in free space Γ_{ant}^{fs} and in the Wheeler cap Γ_{ant}^{wc} can be determined, and the antenna radiation efficiency e_{rad} is calculated using

$$e_{rad} = \frac{1}{1 - |\Gamma_{ant}^{fs}|^2} \times \frac{2}{(\Delta S_{max})^{-1} + (\Delta S_{min})^{-1}} \tag{3.7}$$

where ΔS_{max} and ΔS_{min} are the maximum and minimum of $\Delta S = |\Gamma_{ant}^{fs} - \Gamma_{ant}^{wc}|$ [65]. In (3.7), the cavity is assumed to be lossless. However, the cavity loss may needs to be compensated for frequencies that are higher than 2 GHz. A modified radiation efficiency formula that includes the cavity loss is now introduced, that is

$$e_{rad} = \frac{1}{e_{cavity}(1 - |\Gamma_{ant}^{fs}|^2)} \times \frac{2}{(\Delta S_{max})^{-1} + (\Delta S_{min})^{-1}} \tag{3.8}$$

where the term e_{cavity} represents the cavity efficiency ' and $e_{cavity} = 1$ represents a lossless cavity. The cavity efficiency can be obtained from a Wheeler cap measurement by using a reference antenna with a known radiation efficiency.

3.2.2 Simulation Results and Discussions

Balanced Electrically Small Loop Antenna

An electrically small capacitively-loaded loop antenna was designed to be operated around 900 MHz for the hearing-aid application. The loop is printed on the Rogers 5870 substrate, with the dielectric constant being 2.33 and loss tangent being 0.0012. The overall dimensions of the antenna are $35 \times 10 \times 1.5$ mm^3.

First, the loop antenna itself is simulated with HFSS software by using a lumped port excitation in free space, as shown in Figure 3.7. For this configuration, the input impedance and radiation efficiency are obtained directly and represent reference results.

Second, according to the proposed modified Wheeler cap method, the loop antenna with two extra cables is simulated in free space and in the Wheeler cap, respectively. The outer conductors of the test cables are connected in-between to provide a common ground. These two cables are properly taken into account in the simulation. The so-called waveports are used as the excitation ports, as illustrated in Figure 3.8, which are located at the end of each coaxial cable. In order to find the full two-port scattering matrix at the antenna terminal, the port de-embedding is applied on each waveport. It is noted that the lossless cables are used in this simulation.

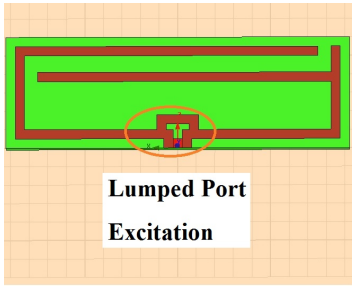

Figure 3.7: Lumped port excitation of the small loop antenna: HFSS model.

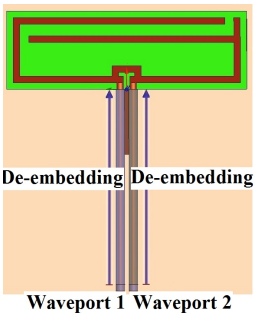

Figure 3.8: Two waveport excitations and port de-embedding: HFSS model.

An aluminum cylindrical cavity with a diameter of 26 cm and a height of 35 cm is used in this simulation as the Wheeler cap. Then the simulated full two-port scattering matrix of the loop antenna are obtained in free space and inside the Wheeler cap, respectively. From these results, the antenna input impedance, the reflection coefficient and the radiation efficiency are calculated.

The properties of the small loop antenna which are calculated from the full two-port scattering matrix are compared to the reference simulation results with a lumped port excitation. The input impedance, reflection coefficient and the radiation efficiency of the loop antenna are illustrated in Figs. 3.9-3.12. It is seen that the results are in a good agreement and the small difference is explained by the finite simulation precision. All simulation results show that the cable effects on the radiation efficiency is avoided by using the proposed method.

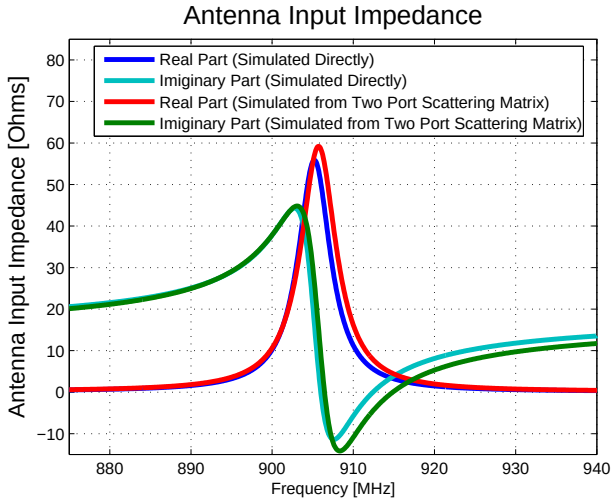

Figure 3.9: Antenna input impedance obtained from a direct simulation and calculated from the simulated full two-port scattering matrix.

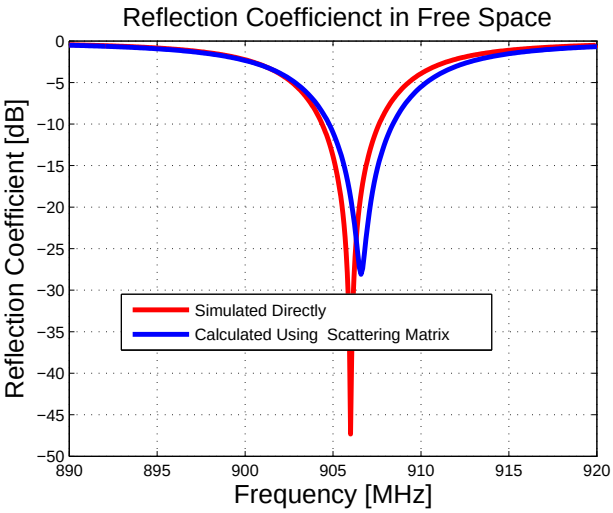

Figure 3.10: Antenna reflection coefficient obtained from a direct simulation and calculated from the simulated full two-port scattering matrix.

Broadband Dipoles

In order to prove that the proposed method is broadband, a differential-fed wideband dipole is simulated to show the possibility of the radiation efficiency measurement over a broad frequency band. Here we use a wideband dipole with two arms made of thin metallic discs without any substrate, as shown in Figure 3.13 and Figure 3.14. The radius of each disc is 3 cm and the

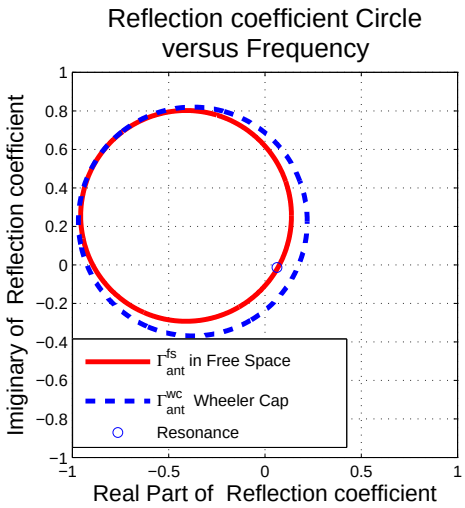

Figure 3.11: Antenna reflection coefficient circle versus frequency in free space and in a Wheeler cap, respectively.

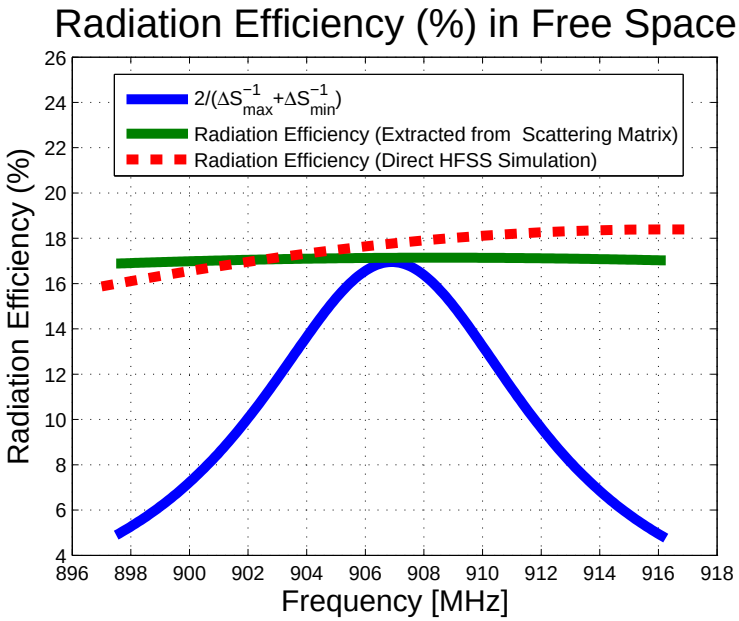

Figure 3.12: Antenna radiation efficiency obtained from a direct simulation and calculated from the simulated full two-port scattering matrix.

gap between the two discs is 2 mm. The radiation efficiency of this wideband dipole is expected to be very close to 100%, since the loss in this antenna is determined only by the finite conductivity of the metal, which is set to 5.8×10^7

S/m to represent the copper. Although this antenna is not electrically small, we prefer to use, both in simulation and in measurement, a broadband antenna with well known radiation efficiency. The radiation efficiency of the dipole which is determined from the simulated scattering matrix is almost a constant over the frequency band from 500 MHz to 2000 MHz and it is equal to 99.7%. This result shows that the radiation efficiency measurement by using the three-port Wheeler cap method is valid over a wide frequency band.

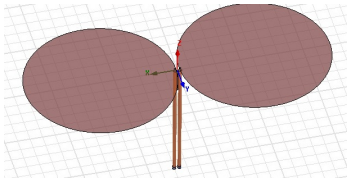

Figure 3.13: Full two-port scattering matrix simulation in free space (HFSS).

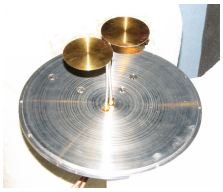

Figure 3.14: Fabricated Broadband Antenna.

3.2.3 Measurement Results and Discussions

Several electrically small loop antennas were manufactured according to the design parameters and measured using the modified Wheeler cap technique. The Wheeler cap used in this measurement was originally designed for measurements of the small antennas down to 400 MHz, but later it was found that it can also be used at higher frequencies by the generalized Wheeler cap method [65], which avoids the influence of cavity resonances.

The full two-port scattering matrix was measured for the loop antenna in free space and in the Wheeler cap, by using the network analyzer HP 8753D, as illustrated in Figure 3.15. The extracted antenna radiation efficiency is shown in Figure 3.16. The measured radiation efficiency is also compared to the result obtained from a spherical near-field antenna facility, where the antenna was measured with a sleeve balun. It is seen from Figure 3.16 that very good agreement is observed between all the results. This confirms the validity of the proposed modified Wheeler cap method.

The measured radiation efficiency for the broadband dipole antenna in the frequency range of 1-3 GHz is illustrated in Figure 3.17. It is seen that the measured efficiency has an average of about 99% and the ripples are explained by the finite calibration accuracy of the VNA. Again, this result clearly shows that the proposed method works very well also in a wide frequency band; thus it can be used for the input impedance and radiation effi-

ciency measurements for wideband antennas.

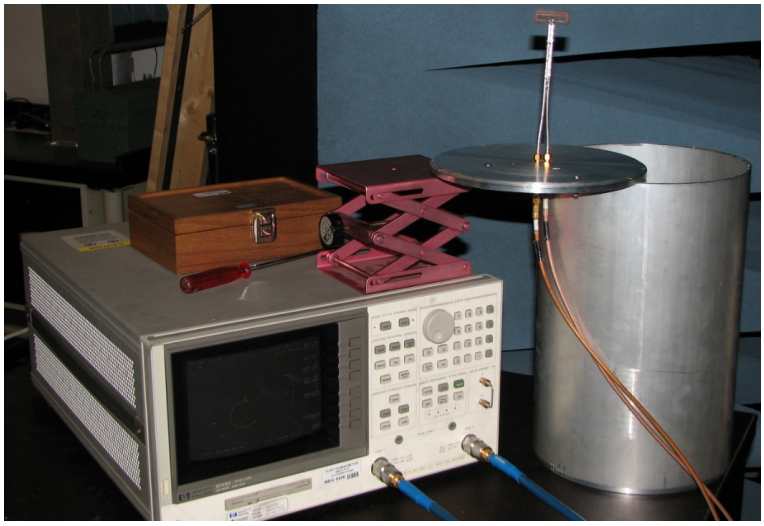

Figure 3.15: The measurement setup of the modified Wheeler cap technique.

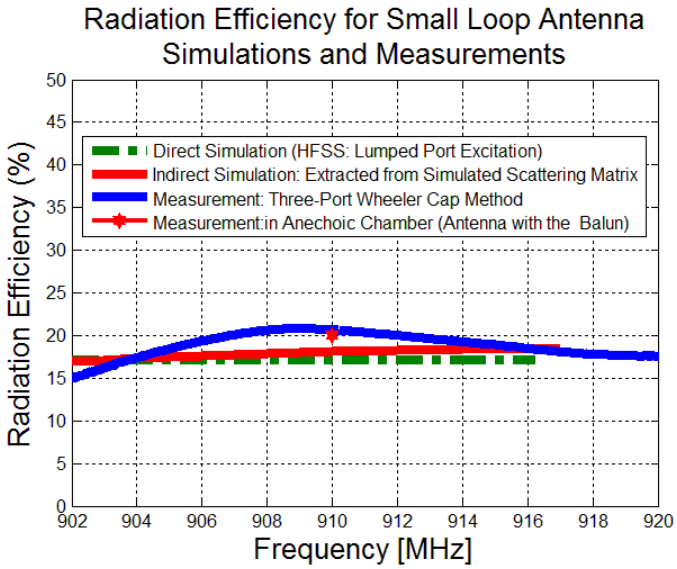

Figure 3.16: The simulated and measured radiation efficiency for the small loop antenna.

In summary, a modified Wheeler cap method was proposed for accurate measurements of input impedance and radiation efficiency of small balanced antennas. The advantages of the proposed method are summarized as follows. First, no balun is required during the measurement and thus the problems of narrow impedance bandwidth and extra scattering caused by the balun

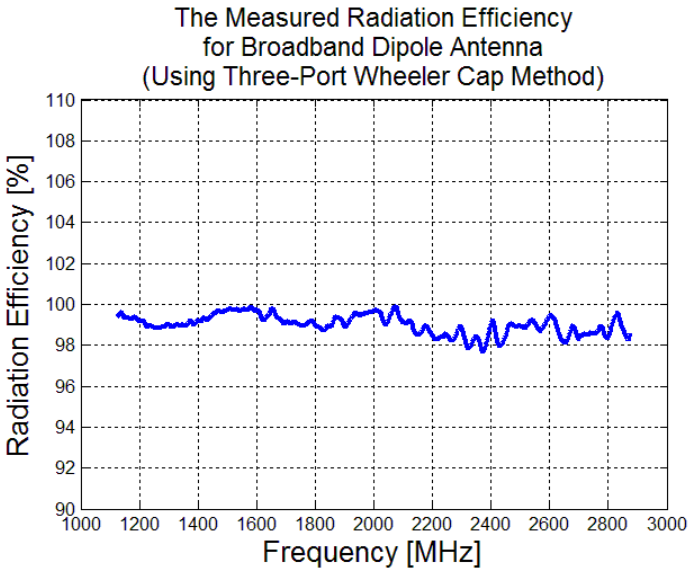

Figure 3.17: The measured radiation efficiency for the broadband dipole antenna.

are avoided. As a result, the proposed method is valid in a broad frequency band. Second, the application of the proposed method and the proper use of the circle fitting for the measured s-parameters ensure that the cavity resonances do not have any significant effect on the measurement results. By using the Wheeler cap method in the proposed way, most of its limitations and disadvantages are avoided. The method is, therefore, suitable for the input impedance and radiation efficiency measurements for most types of antennas in a broad frequency band. The antennas under test are not limited to be electrically small which can be balanced or unbalanced, symmetric or asymmetric antennas.

3.3 Modified Wheeler Cap Method in Complex Environments

A modified Wheeler cap method, proposed recently in [64] and applied in [69] for balanced antennas, gives significant improvements on this method and allows the radiation efficiency measurements for different kinds of small antennas, including balanced, unbalanced, symmetric and asymmetric types. Measurements in a wide frequency band are also possible, which thus removes the limitation on the cavity size. Therefore, the method allows the measurement using a large cavity and it provides the potential to include the antenna working environment. In this section, this modified Wheeler

cap method is applied for the radiation efficiency measurement of balanced electrically small antennas, with particular focus on the involvement of the complex environment: a human head phantom.

In traditional applications of the Wheeler cap method, the presence of cavity resonances in a large cavity requires the use of a small cavity which prevents the antenna measurement in their working environment. This is viewed as a serious disadvantage of this method. In this section, the determination for the AUT radiation efficiency in a complex environment by the Wheeler cap method is investigated. The measurement is performed in a large cavity and uses a proper circle fitting technique to reconstruct the reflection coefficients disturbed by the cavity resonances.

$$e_{rad,ant} = \frac{R_{rad,ant}}{R_{rad,ant} + R_{loss,ant} + R_{loss,head}}. \tag{3.9}$$

$R_{rad,ant}$ and $R_{loss,ant}$ represent the radiation resistance and loss resistance in presence of the head, and $R_{loss,head}$ represents the loss caused by the head phantom.

The losses obtained from the measurement inside the Wheeler cap represent a sum of the terms $R_{loss,ant}$, $R_{loss,cavity}$ and $R_{loss,head(wc)}$. Here, $R_{loss,cavity}$ is the loss in the cavity walls, and considering the high conductivity of the metal cavity this loss is typically very small. $R_{loss,head(wc)}$ represents the loss in the head phantom when it is inside the Wheeler cap. Two effects are involved in $R_{loss,head(wc)}$ which are the absorption losses due to the antenna and the cavity, respectively. Hence, the difference between the loss caused by the head phantom in free space and in the Wheeler cap is the absorption loss inside the cavity. This difference and the cavity loss must be found out in the determination of the radiation efficiency. A calibration of the cavity loss and phantom absorption due to the cavity will be performed using a reference antenna with known radiation efficiency. The calibration is the key feature for the radiation efficiency measurement in a complex environment by using the Wheeler cap method.

3.3.1 Simulation Results and Discussions

The same loop antenna that is used in the previous section is also used as the AUT in this simulation. In the previous section, the simulations for the determination of the AUT radiation efficiency were presented by using an aluminum cylindrical cavity as the Wheeler cap, with a diameter of 26 cm and a height of 35 cm. In this section, we focus on the simulation results by the

proposed method versus different cavity sizes which will show the possibility of the Wheeler cap measurement in a large cavity. First, the loop antenna itself is simulated with HFSS software by using a lumped port excitation in free space. In this configuration, the radiation efficiency is obtained directly and represents reference results. Second, according to the proposed modified Wheeler cap method, the loop antenna with two extra cables is simulated in free space and in the Wheeler cap, respectively. The outer conductors of the test cables are connected in-between to provide a common ground. These two cables are properly taken into account in the simulation. The so-called waveports in HFSS are used as the excitation ports. In order to find the full two-port scattering matrix at the antenna terminal, the port de-embedding is applied on each waveport. It is noted that lossless cables are used. In this simulation, several aluminum cavities are evaluated as the Wheeler cap, which are an aluminum cylindrical cavity with a diameter of 26 cm and a height of 35 cm and two rectangular cavities with the dimensions being $40 \times 40 \times 40$ cm^3 and $60 \times 60 \times 60$ cm^3, respectively. The first cavity was originally designed for measurements of small antennas down to 400 MHz, but later on it was found that it can also be used at higher frequencies by the generalized Wheeler cap method and proper circle fitting techniques which avoids the influence of cavity resonances. The simulated full two-port scattering matrix of the loop antenna are obtained in free space and inside the Wheeler cap, respectively. From these results, the radiation efficiency of the loop antenna is calculated.

Figure 3.18 shows the radiation efficiency obtained from a direct HFSS simulation and that is extracted from the simulated full two-port scattering matrix in different cavities. At the resonance frequency, 906.5 MHz, the direct HFSS simulation gives a radiation efficiency of 17.7%, while the radiation efficiency extracted from the proposed method are 17.2%, 17.9% and 17.8% for the cylindrical cavity, $40 \times 40 \times 40$ cm^3 rectangular cavity and $60 \times 60 \times 60$ cm^3 cavity, respectively. The difference between the direct free space simulation and the proposed method are therefore 0.5%, 0.2% and 0.1%. Hence, a good agreement is clearly observed. Decreasing the convergence parameter in HFSS, which is the maximum delta for s-parameters, results in an improvement in the agreement, but at the expense of long simulation time.

3.3.2 Measurement Results and Discussions

The measurement results by the proposed method are presented for an electrically small loop antenna in this subsection, which is placed close to a head phantom. An aluminum cavity of the dimension $40 \times 40 \times 40$ cm^3 was built

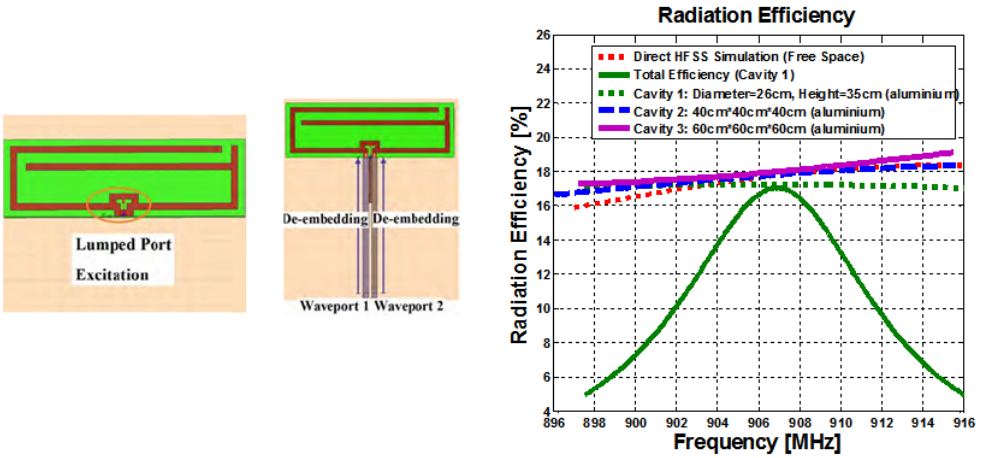

Figure 3.18: Antenna radiation efficiency, obtained from a direct HFSS simulation and extracted from the simulated full two-port scattering matrix in different cavities.

and used as the Wheeler cap in the experiments. The full two-port scattering matrix was measured for the loop antenna together with the head phantom, in free space and in the Wheeler cap, as illustrated in Figure 3.19 (a). The simulated and measured antenna radiation efficiency are presented in Figure 3.19 (b). Due to the presence of the head, the antenna resonance frequency is shifted from 910 MHz to 901 MHz. At the resonance, the measured radiation efficiency is 16%, while the simulated radiation efficiency is 15.2%. The deviation is 0.8%. However, the deviation becomes as large as 4% at 910 MHz, and this is due to the worse impedance matching at that frequency.

In summary, the steps for this measurement are given as follows.

- The VNA calibration is performed at the SMA connectors of the test fixture by using the standard calibration kits.
- The de-embedding calculation of the test fixture is performed. The parameters of the coaxial cable are extracted from a short circuit measurement.
- The calibration of the cavity loss and head phantom loss is performed by using a calibrated reference antenna with known radiation efficiency.
- The full two port S-parameters of a balanced small antenna, together with the head phantom, are measured in free space.
- The full two port S-parameters of a balanced small antenna, together with the head phantom, are measured inside the Wheeler cap.

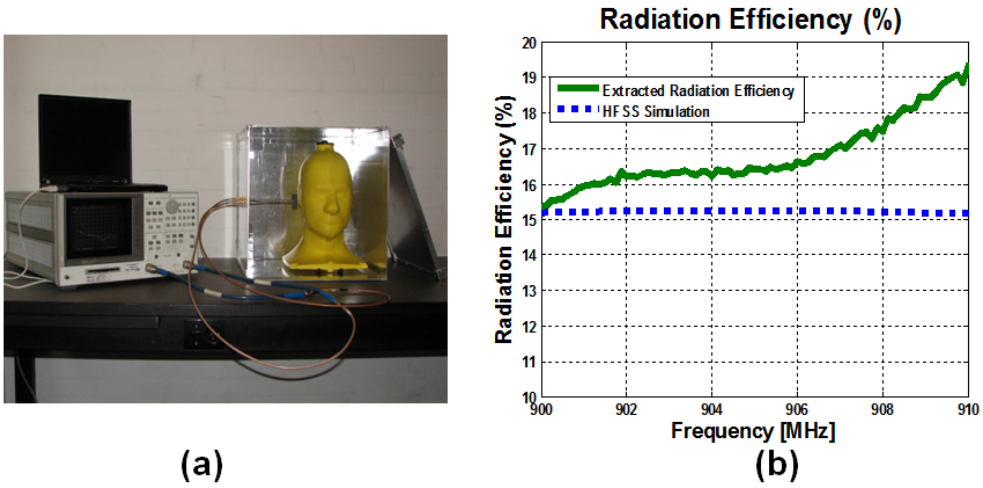

Figure 3.19: Measurement results. (a) presents the measurement setup. (b) presents the simulated and measured radiation efficiency for the small loop antenna, in the presence of a head phantom.

- The circle fitting technique is used to re-construct the antenna reflection coefficient inside the Wheeler cap.
- The antenna impedance and radiation efficiency are extracted together with the compensation of the losses in the test fixture, cavity and head phantom.

In summary, the proposed radiation efficiency measurement technique is a further development of the modified Wheeler cap method that is presented in the previous section, by taking the complex environments into account in the measurement. It is shown that the limitation on the cavity size is overcome with this method and the influence of the cavity resonances are removed by a proper circle fitting technique. Hence, it is possible to perform the radiation efficiency measurement inside a large cavity. The proposed method can also be applied for broadband antennas. Finally, the measurement results for electrically small antennas in complex environments are presented to show the validity of this technique. A calibration technique for the losses in the cavity and phantom is introduced. The device, in which the antenna is integrated, can be involved in the measurement, as well as the human body or human head phantom. Hence, the antenna on-body measurements may become possible by using the proposed modified Wheeler cap method, which is inexpensive, fast and able to provide accurate results. Different circle re-constructing techniques can be compared, aiming at an accuracy improvement. One of the planned improvements to be tested is using a new test-fixture with two

pieces of very thin cables and ultra small connectors, which is expected to reduce the structural scattering influence of the test fixture. Future development is the investigation on the antenna-on-body measurement in a cavity that is larger than the one presented now. Another future development is the measurements of ultra wideband antennas in a complex environment.

3.4 A Cable-Free Impedance and Gain Measurement Technique for Electrically Small Antennas

In this section, we propose a novel cable-free measurement technique to measure the input impedance and gain for ESAs. It is formulated slightly differently from the RCS method [70]- [71]. A complete electromagnetic model is established for the measurement system by using spherical wave expansion (SWE) for the AUT, the probe and the transmission formula to account for the propagation between these. Then the measurement system is modeled by a cascade of three coupled multiple-port networks which represent the probe, AUT and the propagation in-between, respectively.

3.4.1 Theory and Electromagnetic Modeling

In this model the mono-static configuration is described where the probe is both transmitting and receiving, while the AUT is located at a finite distance from the probe. The time convention e^{-iwt} is used in the following derivations.

Model of the Probe and AUT
The electric field $\vec{E}(\vec{r})$ around an antenna, enclosed by the minimum sphere of radius r_0, can be expressed by a spherical wave expansion for $r > r_0$ [72] as

$$\vec{E}(\vec{r}) = \frac{k}{\sqrt{\eta}} \sum_{s=1}^{2} \sum_{n=1}^{N} \sum_{m=-n}^{n} \{a_{smn} \vec{F}_{smn}^{(4)}(\vec{r}) + b_{smn} \vec{F}_{smn}^{(3)}(\vec{r})\} \qquad (3.10)$$

where the superscript $c = 3, 4$ denotes outward and inward propagating waves, respectively. a_{smn} and b_{smn} are the expansion coefficients. $\vec{F}_{smn}^{(c)}$ are the power-normalized spherical vector wave functions. k is the wave number, η is the intrinsic admittance of the medium and $\vec{r}$ is the position vector for a point with (r, θ, ϕ) spherical coordinates. For practical measurements only a finite number of spherical modes are needed to represent the fields. A truncation number N is used for the n summation to make sure the fields

are converged. An antenna can be modeled as a multi-port network with one excitation port that is connected to the generator/load and the radiation ports. Each radiation port represents one spherical wave outside the antenna minimum sphere. The total scattering matrix expression for an antenna is expressed as

$$\begin{bmatrix} w \\ \bar{\mathbf{b}}_{smn} \end{bmatrix} = \underbrace{\begin{bmatrix} \Gamma & \bar{\mathbf{R}}_{s'm'n'} \\ \bar{\mathbf{T}}_{smn} & \bar{\bar{\mathbf{S}}}^{smn}_{s'm'n'} \end{bmatrix}}_{[\bar{\bar{\mathbf{S}}}]} \cdot \begin{bmatrix} v \\ \bar{\mathbf{a}}_{s'm'n'} \end{bmatrix} \tag{3.11}$$

where v and w are the complex amplitudes of the incoming and outgoing waves on the excitation port of an antenna. $\bar{\mathbf{a}}_{s'm'n'}$ and $\bar{\mathbf{b}}_{smn}$ are column vectors that represent the complex amplitudes of the incoming and outgoing spherical modes, respectively. $\bar{\mathbf{R}}_{s'm'n'}$ is a row vector describing the antenna receiving coefficients. $\bar{\mathbf{T}}_{smn}$ is a column vector representing the antenna transmitting coefficients. $\bar{\bar{\mathbf{S}}}^{smn}_{s'm'n'}$ is a square matrix that represents the antenna structural scattering coefficients. $[\bar{\bar{\mathbf{S}}}]$ is the antenna scattering matrix. If there is no incoming wave, $\bar{\mathbf{a}}_{s'm'n'} = 0$, it leads to

$$w = \Gamma v. \tag{3.12}$$

$$\bar{\mathbf{b}}_{smn} = v\bar{\mathbf{T}}_{smn}, \tag{3.13}$$

Both the probe and AUT are modeled by a scattering matrix $[\bar{\bar{\mathbf{S}}}]$ in the form as given in (3.11), which are denoted as $[\bar{\bar{\mathbf{S}}}^{Probe}]$ and $[\bar{\bar{\mathbf{S}}}^{AUT}]$, respectively.

Transmission Formula and Model of the Propagation

We define the coordinates (x, y, z) with respect to the probe, and the primed coordinates (x', y', z') with respect to the AUT. The primed coordinate system of the AUT is related to the unprimed coordinate system of the probe by 3 rotations - through the so-called Euler angles φ, θ, χ and one translation of the distance A, see [72]. The transmission formula describes the complex signal received by the AUT in terms of the transmission coefficients of the probe, the receiving coefficients of the AUT, the 3 rotation angles and the translation distance A [72], that is

$$\begin{aligned} w(A, \chi, \theta, \phi) &= \frac{v}{2} \sum_{\substack{smn \\ \sigma'\mu'\nu'}} T^{Probe}_{smn} e^{im\phi} e^{i\mu'\chi} d^{n}_{\mu' m}(\theta) \\ &\quad \cdot C^{sn(3)}_{\sigma'\mu'\nu'}(kA) R^{AUT}_{\sigma'\mu'\nu'}, \end{aligned} \tag{3.14}$$

where

$$s = 1, 2; m = -n, -n+1, ..., n; n = 1, 2...$$

$$\sigma' = 1, 2; \mu' = -\nu', -\nu' + 1, ..., \nu'; \nu' = 1, 2... \tag{3.15}$$

where smn and $\sigma'\mu'\nu'$ are the SWE indices of the transmitting and receiving antennas, respectively. T^{Probe}_{smn} are the transmitting coefficients of the probe and $R^{AUT}_{\sigma'\mu'\nu'}$ are the receiving coefficients of the AUT. $e^{im\phi}$, $e^{i\mu'\chi}$ and $d^{n}_{\mu' m}(\theta)$ are the rotation coefficients and $C^{sn(3)}_{\sigma'\mu'\nu'}(kA)$ are the translation coefficients.

Model of the Entire Measurement System

The measurement system of the proposed cable-free technique is presented in Figure 3.20. In this model, the entire measurement setup is analyzed by the cascade of three coupled multiple-port networks which represent the probe, the free space propagation and the AUT, respectively. The scattering matrix equations for the AUT and probe are formulated as

$$\begin{bmatrix} w^{AUT} \\ \bar{\mathbf{b}}^{AUT}_{\sigma\mu\nu} - \bar{\mathbf{a}}^{AUT}_{\sigma'\mu'\nu'} \end{bmatrix} = \begin{bmatrix} \Gamma^{AUT} & \bar{\mathbf{R}}^{AUT}_{\sigma'\mu'\nu'} \\ \bar{\mathbf{T}}^{AUT}_{\sigma\mu\nu} & (\bar{\bar{\mathbf{S}}}^{AUT}_{\sigma\mu\nu\,\sigma'\mu'\nu'} - \bar{\bar{\mathbf{I}}}^{AUT}) \end{bmatrix} \cdot \begin{bmatrix} v^{AUT} \\ \bar{\mathbf{a}}^{AUT}_{\sigma'\mu'\nu'} \end{bmatrix} \tag{3.16}$$

and

$$\begin{bmatrix} w^{Probe} \\ \bar{\mathbf{b}}^{probe}_{smn} - \bar{\mathbf{a}}^{Probe}_{s'm'n'} \end{bmatrix} = \begin{bmatrix} \Gamma^{Probe} & \bar{\mathbf{R}}^{Probe}_{s'm'n'} \\ \bar{\mathbf{T}}^{Probe}_{smn} & (\bar{\bar{\mathbf{S}}}^{Probe}_{s'm'n'\,smn} - \bar{\bar{\mathbf{I}}}^{Probe}) \end{bmatrix} \cdot \begin{bmatrix} v^{Probe} \\ \bar{\mathbf{a}}^{Probe}_{s'm'n'} \end{bmatrix}, \tag{3.17}$$

where $\bar{\bar{\mathbf{I}}}^{Probe}$ and $\bar{\bar{\mathbf{I}}}^{AUT}$ denote the unit matrices of an appropriate matrix size. The mode index smn and $s'm'n'$ represent outgoing and incoming spherical waves in the coordinate system of the probe, respectively. The mode index $\sigma\mu\nu$ and $\sigma'\mu'\nu'$ represent outgoing and incoming spherical waves in the coordinate system of the AUT, respectively.

The scattering matrix modeling the free space propagation is expressed as

$$\begin{bmatrix} \bar{\mathbf{a}}^{Probe}_{s'm'n'} \\ \bar{\mathbf{a}}^{AUT}_{\sigma'\mu'\nu'} \end{bmatrix} = \begin{bmatrix} 0 & \bar{\bar{\mathbf{G}}}^{-} \\ \bar{\bar{\mathbf{G}}}^{+} & 0 \end{bmatrix} \cdot \begin{bmatrix} \bar{\mathbf{b}}^{probe}_{smn} \\ \bar{\mathbf{b}}^{AUT}_{\sigma\mu\nu} \end{bmatrix}, \tag{3.18}$$

where the elements of matrix $\bar{\bar{\mathbf{G}}}^{+}$ and $\bar{\bar{\mathbf{G}}}^{-}$ are obtained from (3.14).

On the other hand, the overall measurement system can also be modeled by a two-port network $[\bar{\bar{\mathbf{S}}}^{T}]$, the scattering matrix of which is given by

$$\begin{bmatrix} w^{Probe} \\ w^{AUT} \end{bmatrix} = \begin{bmatrix} S^{T}_{11} & S^{T}_{12} \\ S^{T}_{21} & S^{T}_{22} \end{bmatrix} \cdot \begin{bmatrix} v^{Probe} \\ v^{AUT} \end{bmatrix}. \tag{3.19}$$

where S_{11}^T, S_{12}^T , S_{21}^T and S_{22}^T can be obtained by eliminating the parameters $\bar{\mathbf{b}}_{smn}^{probe}$, $\bar{\mathbf{a}}_{s'm'n'}^{Probe}$, $\bar{\mathbf{b}}_{\sigma\mu\nu}^{AUT}$ and $\bar{\mathbf{a}}_{\sigma'\mu'\nu'}^{AUT}$ using the equations (3.16) - (3.18) as follows. S_{11}^T and S_{21}^T are obtained by setting $v^{AUT} = 0$ and solving for w^{Probe}/v^{Probe} and w^{AUT}/v^{Probe}, respectively. Similarly, S_{12}^T and S_{22}^T are obtained by setting $v^{Probe} = 0$ and solving for w^{Probe}/v^{AUT} and w^{AUT}/v^{AUT}, respectively. For increasing distance between the probe and AUT the influence of the multiple scattering and reflections decreases due to the spatial attenuation of the free space propagation. We assume that the multiple scattered terms are negligibly small, and only the first interaction is taken into account. The scattering parameters S_{11}^T, S_{12}^T , S_{21}^T and S_{22}^T are found to be

$$\begin{aligned} S_{11}^T &\simeq \Gamma^{Probe} + \bar{\mathbf{R}}^{Probe}\bar{\bar{\mathbf{G}}}^{-}(\bar{\bar{\mathbf{S}}}^{AUT} - \bar{\bar{\mathbf{I}}}^{AUT}) \\ &\quad \cdot\bar{\bar{\mathbf{G}}}^{+}\bar{\mathbf{T}}^{Probe} \end{aligned} \tag{3.20}$$

$$S_{12}^T \simeq \bar{\mathbf{R}}^{Probe}\bar{\bar{\mathbf{G}}}^{-}\bar{\mathbf{T}}^{AUT} \tag{3.21}$$

$$S_{21}^T \simeq \bar{\mathbf{R}}^{AUT}\bar{\bar{\mathbf{G}}}^{+}\bar{\mathbf{T}}^{Probe} \tag{3.22}$$

$$\begin{aligned} S_{22}^T &\simeq \Gamma^{AUT} + \bar{\mathbf{R}}^{AUT}\bar{\bar{\mathbf{G}}}^{+}(\bar{\bar{\mathbf{S}}}^{Probe} - \bar{\bar{\mathbf{I}}}^{Probe}) \\ &\quad \cdot\bar{\bar{\mathbf{G}}}^{-}\bar{\mathbf{T}}^{AUT} \end{aligned} \tag{3.23}$$

The second term on the right side of (3.23) represents the influence of the structural scattering from the probe on S_{22}^T of the AUT. This term can be assumed negligibly small compared to the first term for two reasons. First, because a minimum scattering probe is employed, and, second, because of the spatial attenuation in $\bar{\bar{\mathbf{G}}}^{+}$ as well as $\bar{\bar{\mathbf{G}}}^{-}$. Thus (3.23) is approximated by

$$S_{22}^T \simeq \Gamma^{AUT}. \tag{3.24}$$

Determination of the Total Scattering Matrix $[\bar{\bar{\mathbf{S}}}^T]$
The measurement setup is described as follows. There are two antennas involved in this cable-free measurement setup, as illustrated in Figure 3.20, which are the transmitting and receiving probe and the AUT. Their scattering matrices are $[\bar{\bar{\mathbf{S}}}]^{Probe}$ and $[\bar{\bar{\mathbf{S}}}]^{AUT}$, respectively.

For the total measurement setup, a two-port scattering matrix $[\bar{\bar{\mathbf{S}}}^T]$ can be established for reference planes at the input terminal of the probe and AUT. The total scattering matrix $[\bar{\bar{\mathbf{S}}}^T]$ is expressed as

$$[\bar{\bar{\mathbf{S}}}^T] = \begin{bmatrix} S_{11}^T & S_{12}^T \\ S_{21}^T & S_{22}^T \end{bmatrix}. \tag{3.25}$$

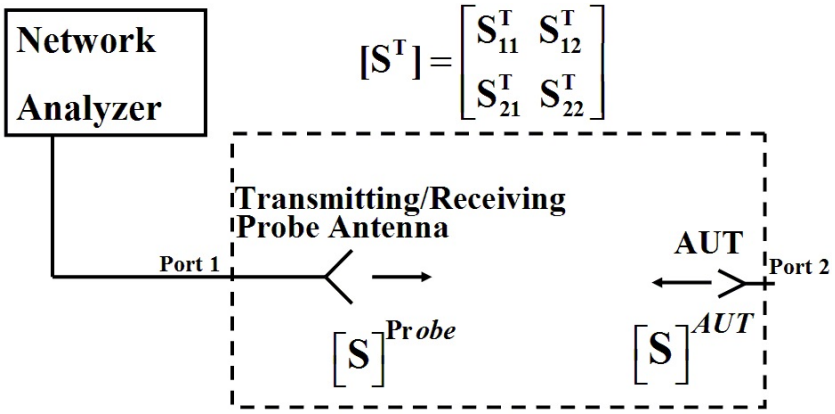

Figure 3.20: Setup of the mono-static measurement of the reflection coefficient and gain of electrically small antennas.

When the AUT is loaded, the measured scattering parameter at the input terminal of the probe is denoted by $S_{11}^{T'}$ which is related to the two-port scattering parameter $[\bar{\bar{\mathbf{S}}}^T]$ as

$$S_{11}^{T'} = S_{11}^{T} + \frac{S_{12}^{T} S_{21}^{T} \Gamma_L}{1 - S_{22}^{T} \Gamma_L} \tag{3.26}$$

where Γ_L is the reflection coefficient of the loads on the AUT.

In the measurement setup that is illustrated in Figure 3.20, the AUT is loaded in turn by a short-circuit, an open-circuit and a known load. The input reflection coefficient of the transmitting probe, $S_{11}^{T'}$, is measured for these three cases. Then the scattering parameters S_{11}^{T}, S_{22}^{T} and $S_{12}^{T} S_{21}^{T}$ of the total scattering matrix are extracted, respectively, and these can be related to the input reflection coefficient and gain of the AUT later. S_{11}^{T} and S_{22}^{T} are determined from

$$\begin{bmatrix} S_{11}^{T} \\ S_{22}^{T} \end{bmatrix} = \begin{bmatrix} (\frac{1}{\Gamma_L^{(1)}} - \frac{1}{\Gamma_L^{(2)}}) & (S_{11}^{T',(1)} - S_{11}^{T',(2)}) \\ (\frac{1}{\Gamma_L^{(1)}} - \frac{1}{\Gamma_L^{(3)}}) & (S_{11}^{T',(1)} - S_{11}^{T',(3)}) \end{bmatrix}^{-1} \cdot \begin{bmatrix} \frac{S_{11}^{T',(1)}}{\Gamma_L^{(1)}} - \frac{S_{11}^{T',(2)}}{\Gamma_L^{(2)}} \\ \frac{S_{11}^{T',(1)}}{\Gamma_L^{(1)}} - \frac{S_{11}^{T',(3)}}{\Gamma_L^{(3)}} \end{bmatrix} \tag{3.27}$$

where $\Gamma_L^{(1),(2),(3)}$ are the measured reflection coefficient of each load, and $S_{11}^{T',(1),(2),(3)}$ are the measured reflection coefficient of the transmitting probe

when the AUT is loaded in three cases. $S_{12}^T S_{21}^T$ is then extracted after S_{11}^T and S_{22}^T are determined, that is

$$S_{12}^T S_{21}^T = (S_{11}^{T',(i)} - S_{11}^T)(1 - S_{22}^T \Gamma_L^{(i)})/\Gamma_L^{(i)}, \tag{3.28}$$

where i=1,2,3. It is noted that there are three sets of data available to be used in this equation, which are obtained from the above three measurements, and they should lead to the same results of $S_{12}^T S_{21}^T$. Taking an average of these results from different sets will result in an improvement in the accuracy.

Antenna Impedance and Gain Determination without the structural scattering and multiple reflections
The impedance of the AUT, Z^{AUT}, is determined from

$$Z^{AUT} = Z_0 \frac{1 + \Gamma^{AUT}}{1 - \Gamma^{AUT}}, \tag{3.29}$$

where Z_0 is the characteristic impedance and Γ^{AUT} is determined from the equation (3.24). The AUT gain is determined by expressing the transmission formula in terms of a gain product of the probe and AUT which is

$$G^{Probe} G_p^{AUT} = \frac{4(kA)^2 |S_{12}^T|^2}{(1 - |\Gamma^{Probe}|^2)(1 - |\Gamma^{AUT}|^2)} \tag{3.30}$$

Here, G_p^{AUT} is the partial gain of the AUT which is parallel to the polarization of the probe. The characteristics of the transmitting probe are assumed known to us from a separate calibration, which are G^{Probe} and S_{11}^{Probe}. Hence, G_p^{AUT} can be extracted by using the equation (3.27), (3.28) and (3.30). (3.30) is the key relation that is used in this cable-free gain measurement technique. It must be mentioned that the probe is assumed to be linearly polarized while the polarization of the AUT is arbitrary. The total gain of the AUT is determined by two orthogonal partial gain measurements.

3.4.2 Simulation Results and Discussions

Two simulation examples of the proposed measurement technique are presented in this subsection, obtained from the commercial software package Ansoft HFSS [53]. A half-wavelength dipole and an electrically small loop antenna are used as the AUT, respectively. In both of these two simulations, the probe is modeled by a half-wavelength dipole. It is noted that the multiple scattering between the probe and AUT is included in the numerical simulations. The first example shows the validation of the proposed method

in a general sense, while the second example shows the validation of this technique for ESAs which may have the characteristics of narrow impedance bandwidth and low radiation efficiency.

Half-Wavelength Dipole

In this example, two identical half-wavelength dipoles are simulated as the probe and AUT, respectively. The length of the half-wavelength dipole is 152 mm and the diameter is 2 mm, which is designed to be resonant around 910 MHz. The material of the dipole is copper. The procedures for this simulation are given as follows. First, the half-wavelength dipole itself (AUT) is simulated in free space by using a lumped-port excitation. At this step, the input impedance and gain of the AUT are obtained directly and will represent the reference results which will be compared to the extracted impedance and gain by the proposed cable-free technique. Second, the measurement setup based on the proposed cable-free measurement method is then simulated, as shown in Figure 3.21 (a). The separation distance between the two dipoles is approximated to be two wavelengths at 910 MHz. The probe is excited using a lumped port. The input reflection coefficient of the probe is recorded, when the AUT is loaded in turn by an open, short and 50 ohms impedance, respectively. Third, in order to investigate the noise influence in a real measurement environment, a random noise at -60 dB level is added to the measured reflection coefficient of the probe $S_{11}^{T'}$, which is denoted by $S_{11,noise}^{T'}$ and is given by

$$S_{11,noise}^{T'} = S_{11}^{T'} + \{max_{1,2,3}|S_{11}^{T'}|\} \cdot 10^{NL_{dB}/20}\alpha e^{j\beta}, \tag{3.31}$$

where NL_{dB} is the noise level to be estimated, α is a random real-valued number between 0 and 1, and β is a random real-valued number between 0 and 2π. It is noted that a new set of random noise is created for every measurement.

Then the antenna reflection coefficient, input impedance and gain product of two half-wavelength dipoles are extracted from the three simulation sets of $S_{11}^{T'}$, by solving the equations (3.24), (3.27), (3.28) and (3.30). (3.30) is the key relation that is used in this cable-free gain measurement technique. Since two identical antennas are used, the gain for each half-wavelength dipole is determined by taking the square root of (3.30). It is noted that a smoothing function is then used on the extracted antenna reflection coefficient, impedance and gain to remove the random noise influence, which uses a sliding average over the samples within a rectangular window.

The extracted antenna reflection coefficient of the AUT by using the cable-free

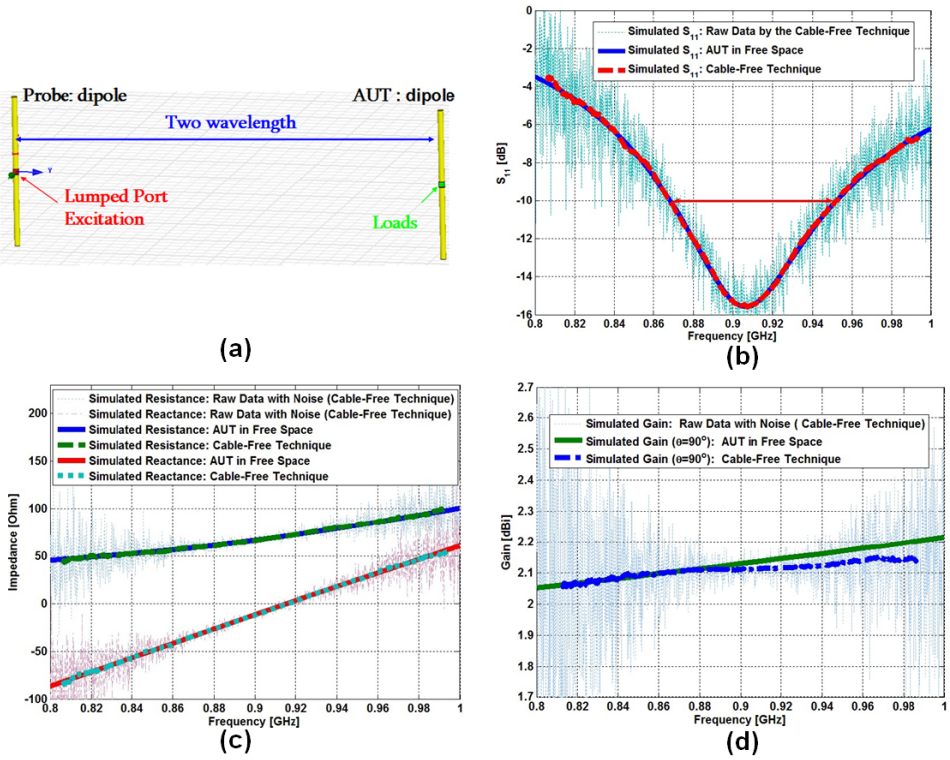

Figure 3.21: Simulations of the cable-free measurement technique, for the AUT being a half-wavelength dipole at 910 MHz. (a) presents the configuration of the simulation setup used in HFSS. (b) presents the comparison of the antenna reflection coefficient versus frequency by using the cable-free technique (with and without smoothing) and by using the direct simulation in free space. (c) presents the comparison of the antenna impedance versus frequency by using the cable-free technique (with and without smoothing) and by using the direct simulation in free space. (d) presents the comparison of the dipole gain (at $\theta = 90^o$) versus frequency by using the cable-free technique (with and without smoothing) and by using the direct simulation in free space.

technique is presented in Figure 3.21 (b), and after the reflection coefficient is calculated, a smoothing function is used on the extracted reflection coefficient to remove the random noise. Then the obtained result is also compared to the direct simulation of the same AUT in free space. It is seen that the maximum deviation in the reflection coefficient doesn't exceed 0.2 dB. The comparison of the extracted antenna input impedance (with smoothing) versus frequency by using the proposed cable-free method and by using the direct simulation in free space is presented in Figure 3.21 (c). A good agreement can be observed. The extracted antenna gain (with smoothing) versus frequency is shown in Figure 3.21 (d) and the result is also compared to the direct simu-

lation result in free space. The deviation in antenna gain is less than 0.05 dB. This example shows that the proposed cable-free technique works well in a real measurement environment with noise, and accurate input impedance and gain are obtained. It is noted that the dynamic range of the modern VNA can well exceed 60 dB which is the value used in the above simulations, and values less than 100 dB can also be easily obtained.

Electrically Small Loop Antenna

In this subsection, the simulation of the proposed cable-free measurement technique is presented for an electrically small loop antenna. An electrically small loop antenna that is resonant at 910 MHz is used as the AUT. It is a self-resonant balanced electrically small loop antenna by using a distributed capacitive loading element. The working mechanism is based on the capacitive loading and inductive coupling between the two small loops. It is printed on the Rogers 5870 substrate with a thickness of 1.5 mm. The dielectric constant of the substrate is 2.33 and the loss tangent is 0.0012. The overall dimensions of this antenna are 35 x 10 mm^2, and the electric size of this antenna is $ka = 0.33$, where k is the wave number and a is the radius of the minimum sphere enclosing the antenna.

The configuration of the measurement setup used in the HFSS simulation is presented in Figure 3.22 (a). Again, the half-wavelength dipole used in the previous example is also used as the probe here and the small loop is modeled as the AUT. The simulation procedures are similar to the previous example of the half wavelength dipole. Again, a random noise level of -60 dB is added to the measured reflection coefficient of the probe, $S_{11}^{T'}$, to represent a real measurement environment. The extracted antenna reflection coefficient of the AUT by the cable-free technique is presented in Figure 3.22 (b), and after the reflection coefficient is calculated, a smoothing function is used on the extracted reflection coefficient to remove the random noise. Then the obtained result is compared to the direct simulation of the AUT in free space. It is seen that the maximum deviation in the reflection coefficient does not exceed 0.5 dB. The comparison of the simulated antenna input impedance (with smoothing) versus the frequency by using the proposed cable-free method and by using the direct simulation in free space is presented in Figure 3.22 (c). The extracted antenna gain (with smoothing) versus the frequency is shown in Figure 3.22 (d), and the result is compared to the direct simulation in free space. The deviation in the antenna gain is less than 0.05 dB. A good agreement is clearly observed.

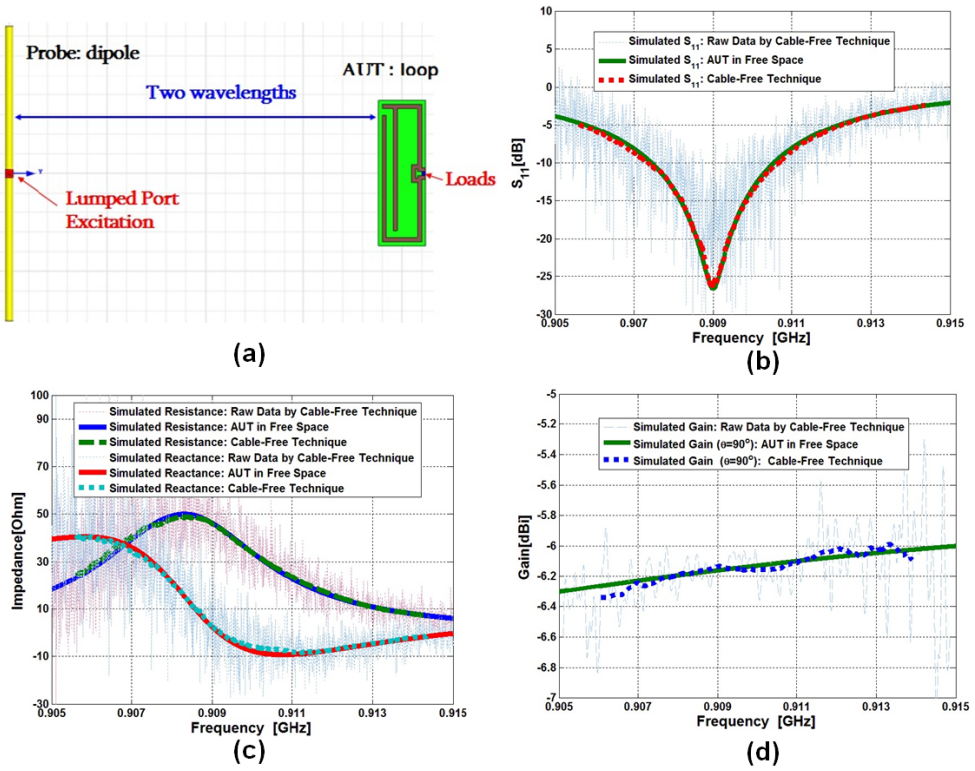

Figure 3.22: Simulations of the cable-free measurement technique, for the AUT being an electrically small loop antenna at 910 MHz. (a) presents the configuration of the simulation setup used in HFSS. (b) presents the comparison of the loop antenna reflection coefficient versus frequency by using the cable-free technique (with and without smoothing) and by using the direct simulation in free space. (c) presents the comparison of the loop antenna impedance versus frequency by using the cable-free technique (with and without smoothing) and by using the direct simulation in free space. (d) presents the comparison of the loop antenna gain (at $\theta = 90^o$) versus frequency by using the cable-free technique (with and without smoothing) and by using the direct simulation in free space.

3.4.3 Measurement Results and Discussions

Three measurement examples by the proposed technique are presented in this subsection. A standard gain horn antenna, a monopole antenna and an electrically small loop antenna are tested as the AUT, respectively. A commercial available standard gain horn antenna is used as the probe for all of these measurements.

Measurements for the Standard Gain Horn

In order to verify the proposed method, two identical commercially available horn antennas are measured first by the proposed method, which are tested as the probe and AUT, respectively, as shown in Figure 3.23 (c). First, the input reflection coefficient of the probe is measured by using the vector network analyzer (VNA) HP 8753D, when the AUT is connected to a short, open and 50 ohm load, respectively. Second, the reflection coefficients of the three loads are measured. Then the antenna input reflection coefficient and the gain product of the two antennas are extracted from the measurement data by using equations (3.24), (3.27), (3.28) and (3.30). (3.30) is the key relation that is used in this cable-free gain measurement technique. Since two identical horn antennas are used, the gain for each horn antenna is determined by taking the square root of (3.30).

In this measurement, the frequency range is selected to be 800 MHz-1000 MHz. The following settings in the VNA are performed to ensure a sufficient dynamic range and accuracy. The number of points used in this frequency range is selected to be 1601 points. The power level is set to the maximum value of the VNA that is +10 dBm. A narrow IF bandwidth is desired which is set to 30 Hz in this measurement. As shown in Figure 3.23 (c), the measurement is performed in a partial anechoic environment. The absorbers are placed on the ground floor and around the antennas, but not on the ceiling and walls. The distance between the probe and AUT is 7 wavelengths at 1 GHz. The measured antenna gain versus the frequency is shown in Figure 3.23 (a) and the result is also compared to the antenna gain given in the datasheet. The deviation in the gain is less than 0.5 dB. The comparison of the antenna input reflection coefficient versus the frequency by using the cable-free method and by using the direct VNA measurement is presented in Figure 3.23 (b). The small deviation in the reflection coefficient may be because that the structural scattering of the probe is ignored. The noise in the measurement environment also has influence.

Measurement Results for the Monopole Antenna

The measurement of the input reflection coefficient for a monopole antenna is presented as follows. The horn antenna is also used as the probe, while the monopole is treated as the AUT, as shown in Figure 3.24 (a). The length of the monopole is 80 mm and the wire diameter is 2 mm, which is made of copper and placed over an aluminum ground plane of dimensions 40 cm x 40 cm. It is designed to be resonant around 870 MHz. Two measurements are performed at the distances of 1.7 m and 2.1 m, respectively, which are 5.5 wavelengths and 7 wavelengths at 1 GHz. Several pieces of foam are used to

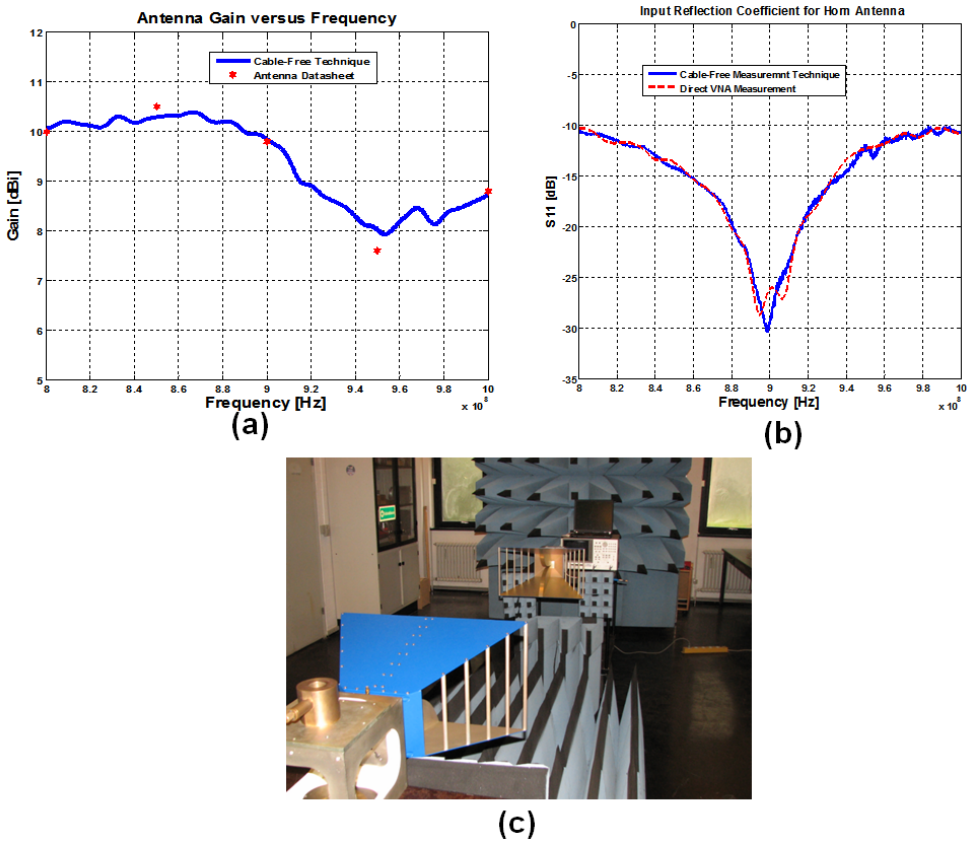

Figure 3.23: The cable free measurements for the standard gain horn antenna. (a) presents the comparison of the antenna gain versus the frequency, by the proposed technique and by the datasheet. (b) presents the comparison of antenna input reflection coefficient versus the frequency, by using the proposed technique and by using direct VNA measurement. (c) presents the setup of the cable-free measurement technique, for two identical horn antennas.

support the monopole antenna.

The reflection coefficients for the monopole antenna are presented in Figure 3.24 (b), compared to the direct VNA measurement. It is noted that a smoothing function was performed on the extracted reflection coefficient to remove the noise. It is seen that the maximum deviation in the reflection coefficient is 0.7 dB, which is at 930 MHz. A good agreement is observed at other frequencies.

Measurement Results for the Electrically Small Loop Antenna

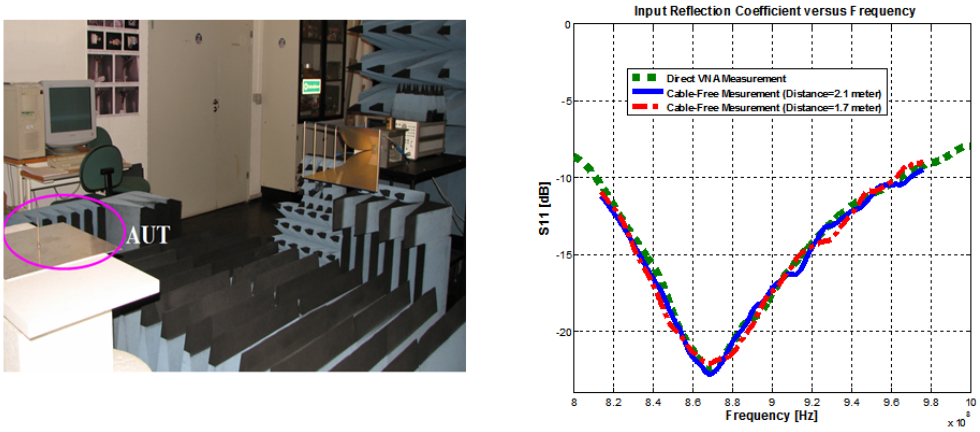

Figure 3.24: The cable free measurements for the monopole, around 910 MHz. (a) presents setup of the cable-free measurement technique, with the probe being a standard gain horn antenna and the AUT being a monopole antenna. (b) presents the antenna input reflection coefficient versus the frequency.

The measurements for an electrically small loop antenna are presented in this subsection. As illustrated in Figure 3.25 (a), an electrically small loop antenna that is resonant at 910 MHz is used as the AUT in this measurement. It is a self-resonant balanced electrically small loop antenna by using a distributed capacitive loading element. The working mechanism is based on the inductive coupling between the two small loops. It is printed on the Rogers 5870 substrate with a thickness of 1.524 mm. The dielectric constant of the substrate is 2.33 and the loss tangent is 0.0012. The overall dimensions of this antenna are 35 mm x 10 mm, and the electric size of this antenna is ka=0.33, where k is the wave number and a is the radius of the minimum sphere enclosing the antenna.

Different from the normal size antennas such as horn antennas, the ultra small connectors and loads are desired for the electrically small antennas. The dimensions of the connectors and loads are required to be much smaller than that of the antennas to avoid the extra scattering effects. Several ultra small connectors and loads that are used in the measurements are illustrated in Figure 3.25 (b).

In this measurement, the distance between the probe and AUT is 5.1 wavelengths at 900 MHz. The measured gain of the small loop antenna by using the proposed cable-free technique, the spherical near-field facility and the Wheeler cap method are presented in Figure 3.25 (c), together with the sim-

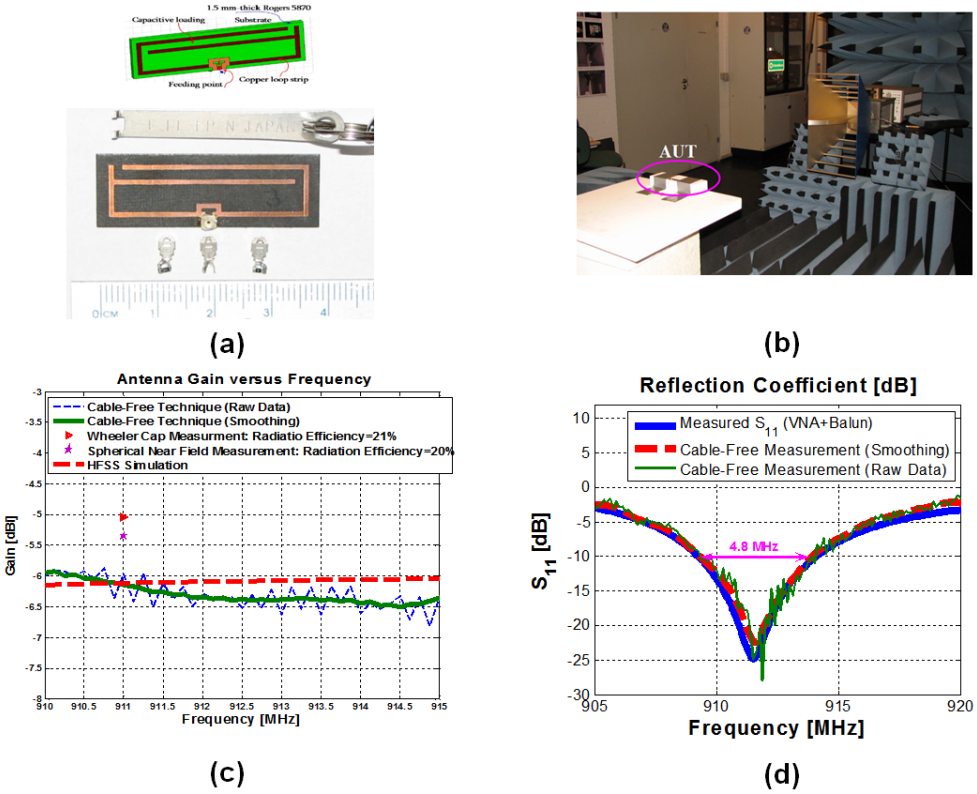

Figure 3.25: The cable-free measurement results for the electrically small loop antenna that is resonant around 910 MHz. (a) presents the fabricated electrically small loop antenna, the ultra small connector and the loads used in the measurement. (b) presents the setup of the cable-free measurement technique, with the probe being a standard gain horn antenna and the AUT being an electrically small loop. (c) presents the comparison of the antenna gain versus the frequency by different techniques. (d) presents the comparison of the antenna input reflection coefficients versus the frequency by different techniques.

ulated gain from HFSS. Comparisons of the measured antenna gain for this small loop antenna at the resonance frequency by different techniques show that the maximum deviation is up to 1.05 dB. The deviation in the antenna gain indicates there is the effect due to the feeding cable.

The measured reflection coefficients for the small loop antenna are shown in Figure 3.25 (d). A comparison of the raw data, the smoothing result of the cable-free measurement, and the direct VNA measurement are presented. In the direct VNA measurement, a balun is used in front of the loop antenna to avoid the leaking current on the cable. At the resonance frequency, the measured $|S_{11}$ from the direct VNA measurement is -24.5 dB, while the measured

$|S_{11}$ from the proposed cable-free method is -22.5 dB. Thus there is a deviation of 2 dB. This deviation indicates there is the scattering effect due to the feeding cable or the balun.

In summary, the electromagnetic model of a cable-free impedance and gain measurement technique for electrically small antennas is proposed by using the spherical wave expansion, which is valid for arbitrary AUT at arbitrary distances between the probe and AUT. The whole measurement setup is modeled by the cascade of three coupled multiple-port networks. Three measurements by the proposed methods are presented. Comparison of the antenna measurement techniques, with and without the feeding cable, has shown that there exist the scattering effects from the cable in both the reflection coefficient measurement and gain measurement.

3.5 Summary

The input impedance and radiation efficiency measurements for ESAs represent a great challenge due to the leaking current on the feeding cable as well as the scattering effects caused by the cable. The development of the input impedance, radiation efficiency and gain measurement techniques and instruments for ESAs is one of the main tasks in this work. In this chapter, we proposed several novel measurement techniques for electrically small antennas. These measurement techniques are

- **Investigations of the Tunable Sleeve Balun**

  The effectiveness of the tunable sleeve balun are investigated. Since an ordinary balun is a narrow band device, a tunable balun is designed for this measurement; thus allows us to choose the optimal parameters for the balun. It is noted that a careful tuning of the balun is very important, both for the radiation pattern and for the efficiency measurements. The optimum balun parameters are investigated. Though it is called a quarter-wave sleeve balun, it was found that the optimum length of the short-circuited sleeve (air-filled) should be about 0.2 wavelength, while the optimum gap between the open end of the balun and the antenna should be between 0.06-0.1 wavelength.

- **The Modified Wheeler Cap Technique**

  A modified Wheeler cap technique for the radiation efficiency measurement of balanced electrically small antennas is proposed. This method

provides the following advantages. First, no balun is required during the measurements; thus the problems of narrow impedance bandwidth and extra scattering effects caused by the balun are avoided. As a result, the proposed method is valid in a broad frequency band. Second, the application of proposed method and the proper use of the circle fitting technique for the measured scattering parameters ensure that the cavity resonances do not have any significant effect on the measurement results. By using the Wheeler cap method in the proposed way, most of its limitations and disadvantages are avoided. The method is, therefore, suitable for the input impedance and radiation efficiency measurements for most types of antennas in a broad frequency band. The antennas under test are not limited to be electrically small and the AUT can be balanced or unbalanced, symmetric or asymmetric antennas.

- **The Modified Wheeler cap Method for the ESA Measurement in Complex Environments**

  Moreover, the modified Wheeler cap method for measurements of small antennas in complex environments is further investigated. It is shown that the limitation on the cavity dimensions can be overcome by this method because the influence of cavity resonances is removed by a proper circle fitting technique. Hence, it is possible to perform the radiation efficiency measurement inside a large cavity. Finally, the measurement results for electrically small antennas in complex environments are presented to show the validity of this technique.

- **A Cable-Free Impedance and Gain Measurement Technique for Electrically Small Antennas**

  A cable-free impedance and gain measurement technique for electrically small antennas is proposed. The electromagnetic model, simulation results, as well as measurement results are presented and discussed. The electromagnetic model of this technique is derived by using the spherical wave expansion. It is valid for arbitrary electrically small AUT at arbitrary distances between the probe and AUT. The whole measurement setup is modeled by the cascade of three coupled multiple-port networks. Three measurement examples by the proposed cable-free technique are presented, in which a standard gain horn antenna, a monopole antenna and an electrically small loop are tested as the AUT, respectively. Comparison of the antenna measurement techniques, with and without the feeding cable, shows that there exist the scattering effects from the cable in both the reflection coefficient measurement and gain measurements.

CHAPTER

FOUR

Complex Environments

The antennas are to function in very complex environments that significantly influence the performance of the antennas. It is necessary to take into account this influence in the design of the antennas. For an antenna integrated into a hearing-aid, this means that the influence of the hearing-aid itself, the human head and ear must be included in the analysis. It is known that the electromagnetic properties of body tissues change significantly with the tissue type and the frequency. Thus, the modeling of human head is a necessary task, and the determination of the accurate dielectric parameters of head tissues at the desired frequency is also important. Mobile phone communication faces a similar challenge, and much of the experience gained in this field over the past 10 years can be exploited in the present work [73,74]. However, previous work for mobile phone antennas is focused on the Specific Absorption Rate (SAR). Moreover, the electrical size of the mobile phone antennas is also not as small as the ESAs in the hearing-aids.

For the hearing-aid application, there exist many sources in the complex environments that can affect the antenna performance. An overview of these sources is provided briefly as follows. These sources are classified into three categories which are

- **Human Head Parameters**
  In this category, the head permittivity and conductivity, which are functions of the frequencies, are the parameters that affect the antenna performance. Moreover, the shape and dimension of a human head also play their roles in the determination of the antenna performance.
- **Types, Positions, and Orientations of the ESAs**
  This category deals with the parameters that are related to antenna de-

signs. For instance, what type of ESAs is employed, and how the ESA interferes with the surroundings. It also includes the factors such as the orientation and feeding position of an ESA, as well as the relative position and distance between the ESA and human head.

- **Hearing-aid Device**
  The dielectric and metal materials in a small device are the sources that influence the antenna performance, such as the plastic shell and the battery. If an ESA is located on the surface of an ultra small device, the electromagnetic properties of the shell are important which must be taken into account in the antenna designs.

In this chapter, the influence of complex environments on the characteristics of electrically small antennas is investigated, including the influence of the human head, the hearing-aid and the antenna locations. First, the sensitivity analysis of the head influence on the antenna performance is presented, including the influence of the head permittivity and conductivity. Second, the sensitivity analysis of the positions of the electrically small antennas is presented, including the orientations and locations of the antennas and the distance between the small antenna and head. Third, the influence of the hearing-aid shell material is investigated. In the end, a summary on the influence of environments is provided.

4.1 Sensitivity Analysis of the Head Phantom Parameters: Permittivity and Conductivity

To start the analysis, the determination of the electromagnetic parameters of head tissues at the desired frequency will be the first task, and the modeling of the human head for both simulations and measurements will be described in detail.

4.1.1 Human Head Permittivity and Conductivity versus Frequency and the Head Modeling

High resolution anatomically human head and body models are available from the medical imaging data. The electromagnetic properties of more than 30 tissue types have been identified [75–79], which can be used in electromagnetic simulations. The dielectric properties of various body tissues change

with the frequency, and thus they need to be determined at every single frequency of operation for simulations. In this project, we evaluated the ESA designs at three frequencies which are 405 MHz, 900 MHz and 1017.66 MHz, respectively, and thus we mainly investigated the head permittivity and conductivity at these three frequencies. Several human head models have been used in this evaluation, as illustrated in Figure 4.1, which are explained as follows.

- **Simple Six-Layer Head Model**
  To model the human head, we mainly consider six types of tissues that are skin, fat, bone, dura, CSF and brain, respectively [80–82]. In this way, the human head is modeled by a sphere or ellipsoid with six layers, as illustrated in Figure 4.1 (a) and (b). This simple model is used for simulations, at the beginning step of the parameter investigations. The advantage of this model is that it takes less simulation time, compared to the so-called SAM model (see below).

- **Simple Homogeneous Head Model**
  Alternatively, we can use a homogeneous head model for simulations, in which the averaged permittivity and conductivity are employed, and again the shape can be modeled by a sphere or ellipsoid for simplicity. This simple model is also used for simulations, at the beginning step of the parameter investigations. The advantage of this model is that it takes the least simulation time, among all these head models.

- **SAM Model**
  The SAM (Standard Anthropomorphic Model) is a head shell phantom intended primarily for use in the measurement of exposure from mobile phones. It is also suitable for radio radiation pattern testing which provides a precise shape representation of a real head. This standard SAM model is used for both simulations and measurements, as illustrated in Figure 4.1 (c) and (d). The head is modeled by a shell filled with a liquid which represents a conservative estimate of the head material properties.

  A standard CAD file of the SAM head is available for the simulation purpose. It can be imported into electromagnetic simulation software packages like HFSS and CST. A commercially available SAM head phantom is also available to be ordered for the measurement purpose. The advantage of this model is that the measurements can be carried out in reality with it, and thus a comparison between the simulations and measurements is possible. Another advantage is that it provides a more precise head representation for the simulation than the above two

models, but at the expense of very long simulation time. This model is useful in antenna tuning at the finalized step. However, for the hearing-aid application the inclusion of human ears is also of great importance, especially for the hearing-aids that are behind the ears (BTE). A disadvantage of this model is that it is initially proposed for the application of mobile phone antennas, and thus the human ears are not included.

It is noted that the head phantom illustrated in Figure 4.1 (d) was ordered for our measurements from the company SPEAG (*www.speag.com/products/*), which is named SAM Head V4.5BS (Broadband Solid) [83]. It has been designed for assessment of the radiation pattern or total radiated power. Its geometry complies with the SAM data as defined by IEEE SCC34 and 3GPP TR25.914, Release 6, CTIA test plan for mobile station over the air performance, Revisions 2.2 and 3.0. High precision casting ensures accurate shape, thickness and tolerances in the relevant areas. The head is filled with a broadband GEL material, with dielectric specifications of the head tissue being valid from 300 MHz - 6 GHz, according to the IEC 62209 and CTIA test plan for mobile station over the air performance, revisions 3.0 standards. Typical deviation of the used material with respect to the target dielectric head parameters is also provided by SPEAG, as shown in Figure 4.2 [84].

- **Accurate Head Model including Ears for Hearing-Aid Application**

  We prefer an accurate head model with the ears being included, for both simulation and measurements. The inclusion of ears into the head model is necessary. However, as far as we know, the human ears are not included in most of commercially available head phantoms. Hence, a real head phantom is fabricated at Danish Technological Institute (Teknologisk Institut). By using the 3-D plastic printing techniques from a CAD head file, a plastic shell with the shape being suitable for our measurements is fabricated, as illustrated Figure 4.1 (e) and (f). This plastic shell is filled with the commercially available equivalent liquid to represent the averaged head tissue. The liquid filled into this shell is also ordered from the company SPEAG, which is named HSL 900. This liquid is a mixture of water and sugar, with the tolerances from the target being less than 5%.

In this project, we investigate the ESA performance at three frequencies which are 405 MHz, 900 MHz and 1017.66 MHz, respectively. The dielectric constant and conductivity of head tissues are computed according to the so-called 4-Cole-Cole Model described in "Compilation of the dielectric prop-

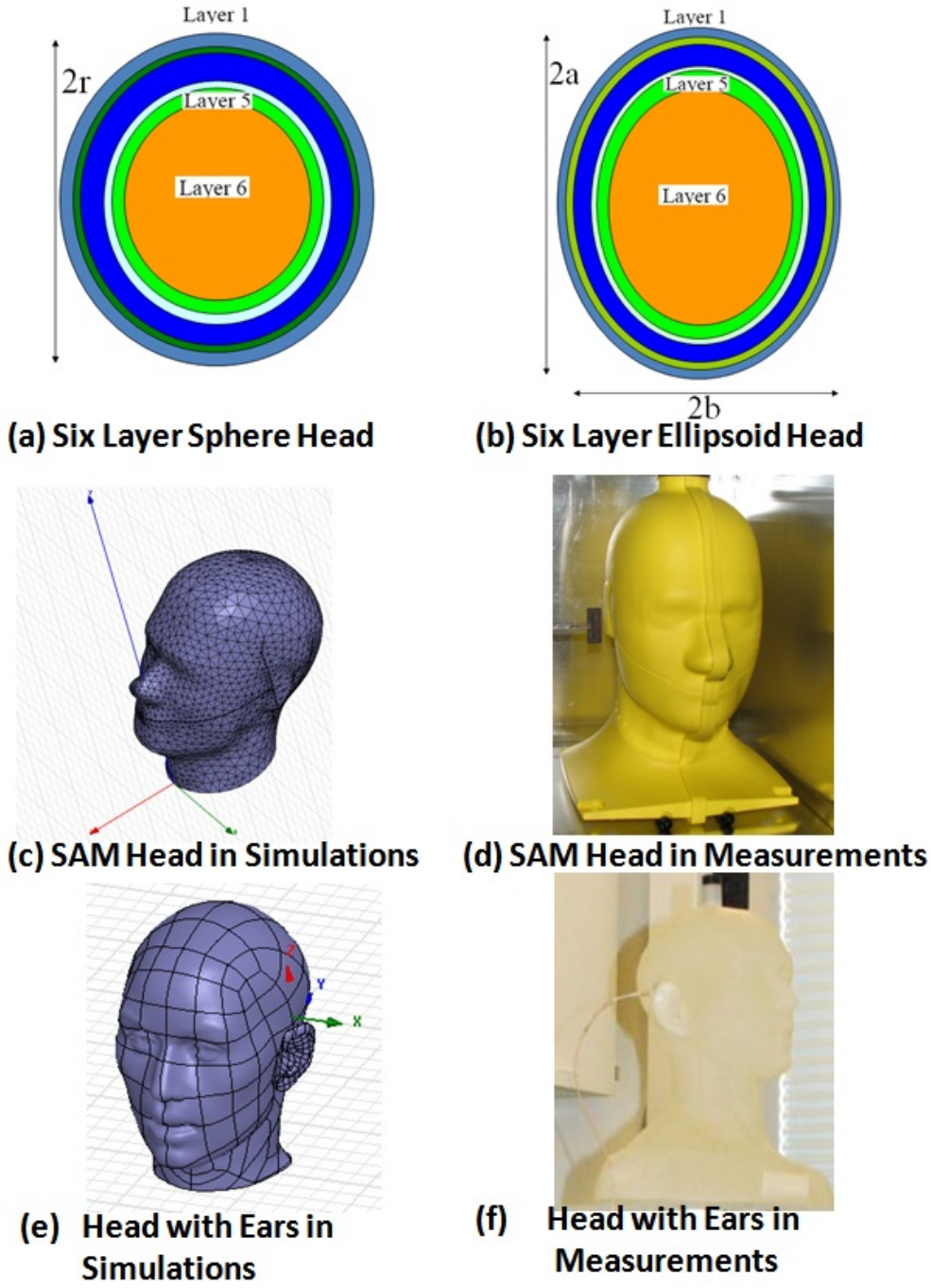

Figure 4.1: Illustrations of the human head phantom used for simulations and measurements. (a) and (b) represent the sixer-layer sphere or ellipsoid head which is used for simulations. (c) and (d) represent the SAM head model for simulations and measurements, respectively. (e) and (f) represent the head model with ears for simulations and measurements, respectively.

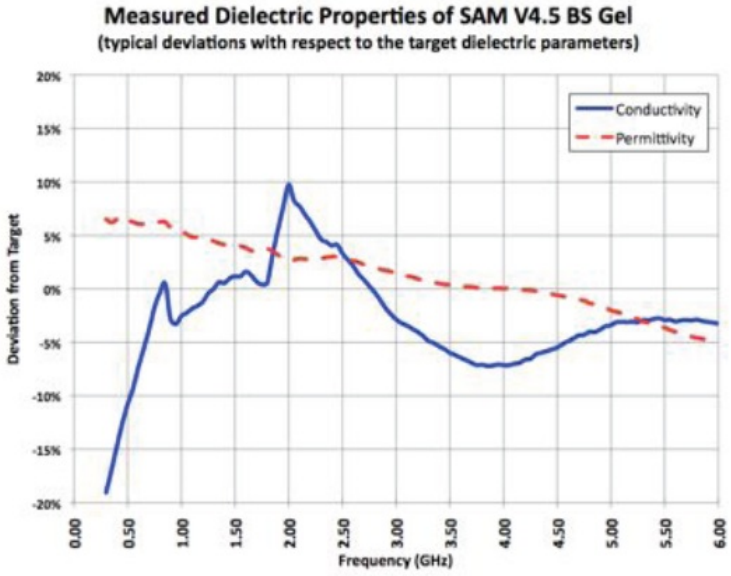

Figure 4.2: Illustrations of the typical deviations in the dielectric constant and conductivity of the used material with respect to the target dielectric constant and conductivity, copied from the phantom datasheet [84].

Table 4.1: Permittivity and conductivity of head tissues at **405 MHz**

Layer	Tissue	Dielectric constant ε_r	Conductivity σ [S/m]
1	Skin	46.67	0.69
2	Fat	5.58	0.04
3	Bone	13.14	0.09
4	Dura	46.62	0.83
5	CSF	70.94	2.25
6	Brain	49.67	0.59

Table 4.2: Permittivity and conductivity of head tissues at **900 MHz**

Layer	Tissue	Dielectric constant ε_r	Conductivity σ [S/m]
1	Skin	41.41	0.87
2	Fat	5.46	0.05
3	Bone	12.45	0.14
4	Dura	44.43	0.96
5	CSF	68.64	2.41
6	Brain	45.81	0.77

Table 4.3: Permittivity and conductivity of head tissues at **1017.66 MHz**

Layer	Tissue	Dielectric Constant ε_r	Conductivity σ [S/m]
1	Skin	40.86	0.91
2	Fat	5.44	0.05
3	Bone	12.35	0.16
4	Dura	44.16	1.00
5	CSF	68.41	2.46
6	Brain	45.81	0.77

Table 4.4: Averaged Permittivity, conductivity and density of brain versus frequencies

Frequencies	Averaged Dielectric Constant ε_r	Averaged Conductivity σ [S/m]	Averaged Density
405 MHz	49.67	0.59	1030.00
900MHz	45.81	0.77	1030.00
1017.66 MHz	45.37	0.81	1030.00
2400 MHz	42.61	1.48	1030.00

erties of body tissues at RF and microwave frequencies" by Camelia Gabriel in the U.S. Air Force Report AFOSRTR-96 and also in [75–79]. The calculated dielectric constant and conductivity for the main tissues in a head are listed in Table 4.1-4.3, at the evaluated frequencies. The calculated averaged dielectric constant, conductivity and density are listed in Table 4.4. It is seen that as the frequency goes up, the dielectric constants decrease while the conductivities increase. Based on the above calculations and the modeling of a human head, now we start the sensitivity analysis on the head parameters.

4.1.2 Sensitivity Analysis of the Human Head Permittivity

The head permittivity changes from people of different ages, genders and races. To make sure the antenna works properly, it is necessary to investigate the influence of the permittivity changes on the performance of the small antennas. This analysis is performed and confirmed by simulations, using the EM simulator Ansoft HFSS. An electrically small loop is used in this simulation which is placed normal to a homogeneous sphere head with a diameter of 17.5 cm, as illustrated in Figure 4.3. The dimensions of this electrically small loop are 35 mm $\times$ 10 mm $\times$ 1.524 mm, and the distance between the loop and the sphere head is set to 1 mm. It is tuned to be resonant in the presence of the head and its resonant frequency of operation is found to be 988

MHz which is obtained from the HFSS simulations. The impedance bandwidth reference to -15 dB is 3.8 MHz, and the simulated radiation efficiency is found to be 22%. These performances will be used as the references which will be compared to the antenna performances as ε_r changes.

It is noted that for this investigation only the head permittivity is changed, with an increasing step of 5% each time. As shown previously, a homogeneous sphere head is employed for simplicity. At the desired frequency, the relative dielectric constant is approximated to be ε_r=45.37. All the other parameters are kept the same as follows.

- The homogeneous head model is used in simulations, and the head dimensions are fixed.
- The head conductivity is fixed.
- The relative position and distance between the ESA and head phantom are fixed.

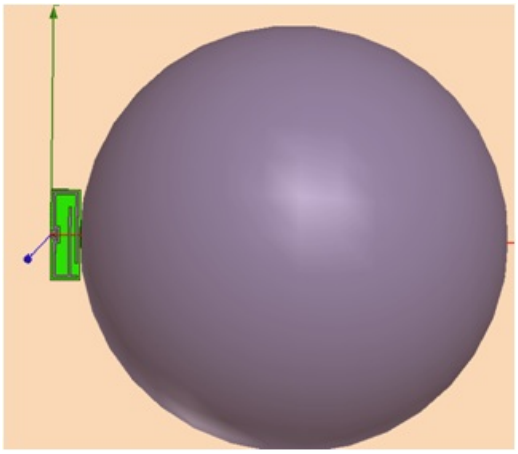

Figure 4.3: Illustrations of the simulation setup for sensitivity investigation of the head permittivity.

The influence of the changes in the head dielectric constant on the loop performance is presented in Figure 4.4. Figure 4.4 (a), (b), (c) and (d) present the simulated $|S_{11}|$, radiation efficiency, antenna resistance and reactance versus the changes in the head dielectric constant ε_r, respectively. As ε_r increases step by step, the antenna resonance frequency, the minimum of $|S_{11}|$, and the shift in the antenna resonance frequency from the reference value are listed in Table 4.5. It is seen that as ε_r increases up to 35%, the frequency shift in

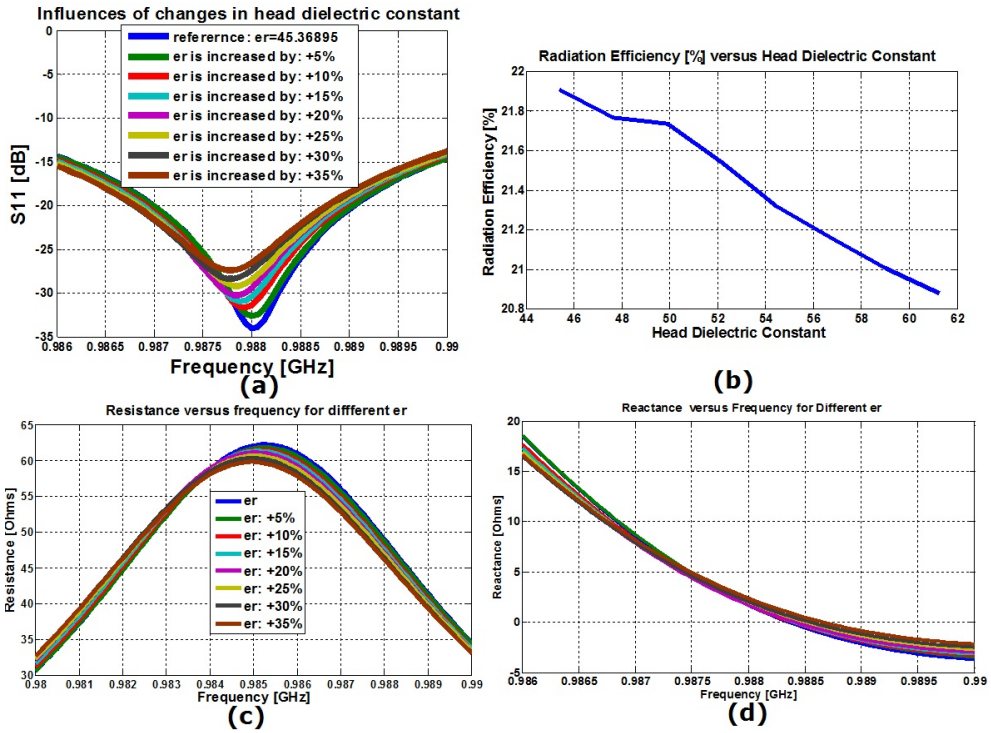

Figure 4.4: Illustrations of the influences of the changes in the head dielectric constant on the loop performance. (a), (b), (c) and (d) present the simulated $|S_{11}|$, the radiation efficiency, antenna resistance and reactance versus the changes in the head dielectric constant ε_r.

the minimum of $|S_{11}|$ is only 0.3 MHz which is negligibly small. Although the minimum $|S_{11}|$ changes from -34 dB to -27.4 dB which gives an increase of 6.6 dB, it still stays within the required impedance bandwidth. It can be concluded that the changes in the head dielectric constant result in very small changes in $|S_{11}|$.

Table 4.6 presents the influence on the antenna impedance bandwidth (BW) versus the changes in the head dielectric constant, as well as the changes in BW. It is seen that as ε_r increases up to 35%, the change in the antenna bandwidth reference to -15 dB is less than 0.1 MHz.

Table 4.7 presents the influence on the radiation efficiency $\mathbf{e}_{rad}$ versus the changes in the head dielectric constant, as well as the changes in $\mathbf{e}_{rad}$. It is found that as ε_r increases up to 35%, the change in the antenna radiation efficiency is 1.05%. For each increasing step in ε_r, the decrease in $\mathbf{e}_{rad}$ is about 0.15% approximately.

It is found that the changes in the head dielectric constant result in very small changes in $|S_{11}|$ and the impedance bandwidth BW. The changes in the head dielectric constant result in a small decrease (not significant) in $\mathbf{e}_{rad}$. These observations show that using a homogenous head model with an averaged dielectric constant is reasonable for fast simulations, compared to the six-layer head model or the SAM head model.

Table 4.5: Influence on $|S_{11}|$ versus the changes in the head dielectric constant

Dielectric constant Changing step=5%	Resonance frequency Freq/min($\|S_{11}\|$)	Shift in frequency and $\|S_{11}\|$ ΔFreq/$\Delta\|S_{11}\|$
ε_r=45.37 (Reference) $\sigma = 0.81$ S/m	988 MHz/-34.0 dB	0 MHz/0 dB
ε_r is increased by : 5%	988 MHz/-32.7 dB	0 MHz/+1.3 dB
ε_r is increased by : 10%	987.9 MHz/-31.7 dB	-0.1 MHz/+2.3 dB
ε_r is increased by : 15%	987.9 MHz/-31.0 dB	-0.2 MHz/+3.0 dB
ε_r is increased by : 20%	987.8 MHz/-30.3 dB	-0.2 MHz/+3.7 dB
ε_r is increased by : 25%	987.8 MHz/-29.2 dB	-0.2 MHz/+4.8 dB
ε_r is increased by : 30%	987.8 MHz/-28.4 dB	-0.2 MHz/+4.6 dB
ε_r is increased by : 35%	987.7 MHz/-27.4 dB	-0.3 MHz/+6.6 dB

Table 4.6: Influence on the impedance bandwidth (BW) versus the changes in the head dielectric constant

Dielectric constant Changing step=5%	Bandwidth BW Reference to -15 dB	Shift in BW ΔBW
ε_r=45.37 (Reference) σ=0.81 S/m	[986.1 MHz-989.9 MHz],BW=3.8 MHz	0 MHz
ε_r is increased by : 5%	[986.1 MHz-989.9 MHz],BW=3.8 MHz	0 MHz
ε_r is increased by : 10%	[986.1 MHz-989.8 MHz],BW=3.7 MHz	-0.1 MHz
ε_r is increased by : 15%	[986 MHz-989.7 MHz],BW=3.7 MHz	-0.1 MHz
ε_r is increased by : 20%	[986 MHz-989.8 MHz],BW=3.8 MHz	0 MHz
ε_r is increased by : 25%	[986 MHz-989.7 MHz],BW=3.7 MHz	-0.1 MHz
ε_r is increased by : 30%	[985.9 MHz-989.7 MHz],BW=3.8 MHz	0 MHz
ε_r is increased by : 35%	[985.9 MHz-989.7 MHz],BW=3.8 MHz	0 MHz

4.1.3 Sensitivity Analysis of the Human Head Conductivity

In this subsection, the influence of the changes in the head conductivity on the antenna performance is investigated. Again, this analysis is performed

Table 4.7: Influence on the antenna radiation efficiency e_{rad} versus the changes in the head dielectric constant

Dielectric constant Changing step=5%	Radiation efficiency Freq/e_{rad}	Shift in frequency and e_{rad} ΔFreq/Δe_{rad}
ε_r=45.37 (Reference) $\sigma = 0.81$ S/m	988 MHz/21.91%	0 MHz/0%
ε_r is increased by : 5%	988 MHz/21.77%	0 MHz/$-$0.14%
ε_r is increased by : 10%	987.9 MHz/21.73%	-0.1 MHz/$-$0.18%
ε_r is increased by : 15%	987.9 MHz/21.54%	-0.2 MHz/$-$0.37%
ε_r is increased by : 20%	987.8 MHz/21.32%	-0.2 MHz/$-$0.59%
ε_r is increased by : 25%	987.8 MHz/21.16%	-0.2 MHz/$-$0.75%
ε_r is increased by : 30%	987.8 MHz/21%	-0.2 MHz/$-$0.91%
ε_r is increased by : 35%	987.7 MHz/20.87%	-0.3 MHz/$-$1.04%

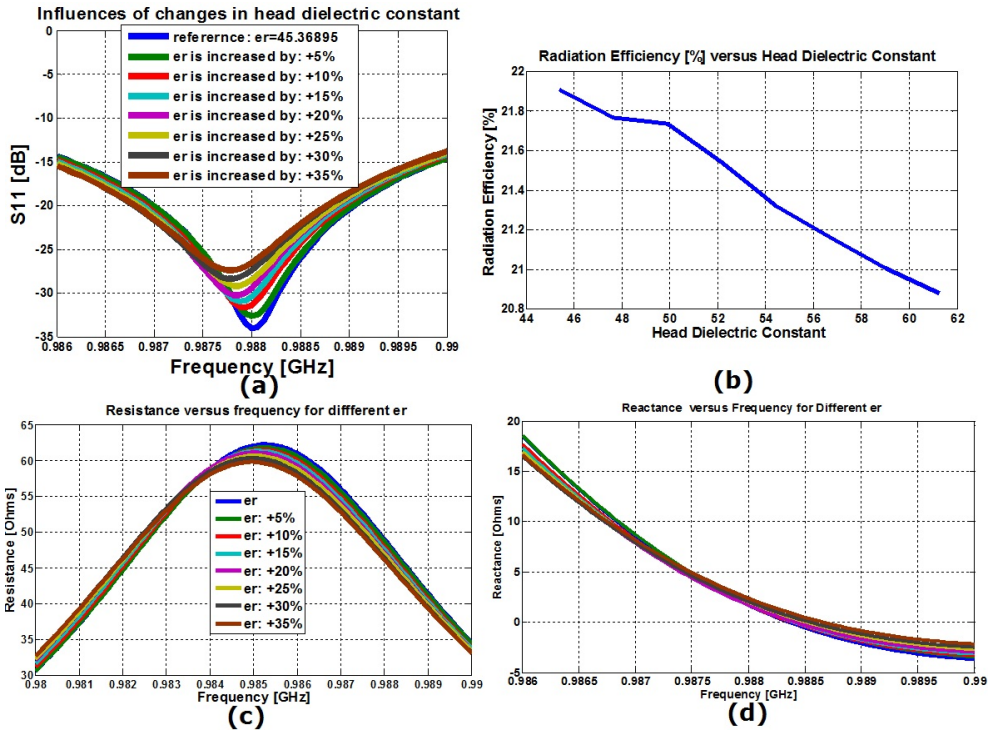

Figure 4.5: Illustrations of the influence of changes in the human head conductivity. (a), (b), (c) and (d) present $|S_{11}|$, the radiation efficiency, the antenna resistance and reactance versus the changes in the head conductivity σ.

and confirmed by simulations, using the EM simulator Ansoft HFSS. The same electrically small loop, the head model and the simulation setup that is used in previous investigations are also used here. As shown previously, a homogeneous sphere head is employed for simplicity. The performance of the same antenna will be used as the reference which will be compared to the antenna performance as σ changes.

It is noted that the head conductivity is the only changed parameter in this investigation, with an increasing step of 5% each time. At the desired frequency, the averaged head conductivity is approximated to be $\varepsilon_r = 0.81$ [S/m]. All the other parameters are kept the same as follows.

- The homogeneous head model is used in simulations and the head dimensions are fixed.
- The head permittivity is fixed.
- The relative position and distance between the ESA and head phantom are fixed.

Table 4.8: Influence of $|S_{11}|$ versus the changes in the head conductivity

Head conductivity Changing step=5%	Resonance frequency Freq/min($|S_{11}|$)	Shift in frequency and $|S_{11}|$ ΔFreq/$\Delta|S_{11}|$
Reference conductivity $\sigma = 0.81$ S/m	987.81 MHz/-48.7 dB	0 MHz/0 dB
σ is increased by 5%: 0.85 S/m	987.81 MHz/-45.3 dB	0 MHz/+3.4 dB
σ is increased by 10%: 0.89 S/m	987.81 MHz/-42.8 dB	0.06 MHz/+5.9 dB
σ is increased by 15%: 0.93 S/m	987.87 MHz/-41.1 dB	0 MHz/+7.6 dB
σ is increased by 20%: 0.97 S/m	987.81 MHz/-39.4 dB	0 MHz/+9.3 dB
σ is increased by 25%: 1 S/m	987.87 MHz/-38.4 dB	0.06 MHz/+10.3 dB

The influence of the changes in the head conductivity on the antenna performance is presented in Figure 4.5. The simulated $|S_{11}|$, radiation efficiency, input resistance and reactance versus the changes in the head conductivity σ are illustrated in Figure 4.5 (a), (b), (c) and (d), respectively. As σ increases step by step, the antenna resonance frequency, the minimum of $|S_{11}|$, and the shift in resonance frequency from the reference are listed in Table 4.8. It is seen that as σ increases up to 25%, the frequency shift in the minimum of $|S_{11}|$ is only 0.06 MHz which is negligibly small. Although the minimum of $|S_{11}|$ changes from -48.7 dB to -38.4 dB which gives an increase of 10.3 dB, it still stays within the required impedance bandwidth. It can be concluded

Table 4.9: Influence of the bandwidth BW versus the changes in the head conductivity

Head conductivity Changing step=5%	Bandwidth BW Reference to -15 dB	Shift in BW ΔBW
Head conductivity $\sigma = 0.81$ S/m	[985.9 MHz-989.8 MHz],BW=3.9 MHz	0 MHz
σ is increased by 5%: 0.85S/m	[985.9 MHz-989.8 MHz],BW=3.9 MHz	0 MHz
σ is increased by 10%: 0.89S/m	[985.9 MHz-989.8 MHz],BW=3.9 MHz	0 MHz
σ is increased by 15%: 0.93S/m	[985.9 MHz-989.8 MHz],BW=3.9 MHz	0 MHz
σ is increased by 20%: 0.97S/m	[985.9 MHz-989.8 MHz],BW=3.9 MHz	0 MHz
σ is increased by 25%:$\sigma = 1$S/m	[985.9 MHz-989.8 MHz],BW=3.9 MHz	0 MHz

Table 4.10: Influence of the antenna radiation efficiency e_{rad} versus the changes in the head conductivity

Head conductivity Changing step=5%	Radiation efficiency Freq/e_{rad}	Shift in frequency and e_{rad} ΔFreq/Δe_{rad}
Head conductivity $\sigma = 0.81$ S/m	987.81 MHz/22%	0 MHz/0%
σ is increased by 5%: 0.85 S/m	987.81 MHz/22.1%	0 MHz/+0.1%
σ is increased by 10%: 0.89 S/m	987.81 MHz/21.9%	0 MHz/−0.1%
σ is increased by 15%: 0.93 S/m	987.9 MHz/21.8%	0.06 MHz/−0.2%
σ is increased by 20%: 0.97 S/m	987.81 MHz/22%	0 MHz/0%
σ is increased by 25%: 1 S/m	987.87 MHz/21.9%	0.06 MHz/−0.1%

that the changes in the head conductivity result in very small changes in the resonant frequency and $|S_{11}|$.

Table 4.9 presents the influence on the antenna impedance bandwidth (BW) versus the changes in the head conductivity, as well as the changes in BW. It is seen that as σ increases up to 25%, the changes in the antenna bandwidth (reference to -15 dB) is very small.

Table 4.10 presents the influence on the radiation efficiency $\mathbf{e}_{rad}$ versus the changes in the head conductivity, as well as the changes in $\mathbf{e}_{rad}$. It is found that as σ increases up to 25%, the change in the antenna radiation efficiency is 0.2% only.

It can be concluded that the changes in the head conductivity result in very small changes in $|S_{11}|$, the impedance bandwidth BW and the radiation efficiency $\mathbf{e}_{rad}$.

4.2 Sensitivity Analysis of the Antenna Related Parameters: Positions and Orientations

The sensitivity analysis of the antenna related parameters on the characteristics of ESAs is presented in this section, including the orientations and locations of the ESA and the distance between the ESA and head. This analysis is carried out at the frequencies of 405 MHz, 900 MHz, and 1000 MHz, respectively.

Sensitivity Analysis of the Antenna Parameters: 405 MHz
A self-resonant electrically small loop antenna which is designed to be resonant at 405 MHz was used in this simulation to investigate the influence of the antenna related parameters, such as the orientation of the ESA and the distance between the ESA and head. The dimensions of this loop are 35 mm $\times$ 10 mm $\times$ 1.524 mm, and a capacitor is loaded in this antenna, as illustrated in Figure 4.7 (a). For the small loop itself in free space, its resonant frequency of operation is 404.6 MHz. The impedance bandwidth reference to -10 dB and -15 dB are 1.6 MHz and 0.8 MHz, respectively. The simulated radiation efficiency is found to be 1.4%. These performances will be used as the reference which will be compared to the antenna performance with the head being present. It is noted that a six-layer sphere head is employed in this simulation, with a diameter of 17.5 cm. At the desired frequency, the dielectric parameters of head tissues are computed according to the 4-Cole-Cole Model, as illustrated in the previous section.

The small loop antenna can be arranged normal or parallel to the head. Figure 4.6 (a) and (b) illustrate the antenna orientation that is normal to the head. Figure 4.6 (d) and (e) illustrate the antenna orientation that is parallel to the head. The distance between the loop and head is d, and the simulated antenna reflection coefficients at different distances d are presented in Figure 4.6 (d) and (e) for the normal and parallel orientations, respectively. It is found that the presence of the head results in a shift in the resonance frequency which is illustrated in Table 4.11 and Table 4.12. The resonance frequencies of the loop for the normal orientation are 403.2 MHz, 403.3 MHz, 403.3 MHz and 403.4 MHz at the distances of 5 mm, 10 mm, 15 mm and 20 mm, respectively. Thus, the shifts in the resonance frequency are 1.4 MHz, 1.3 MHz, 1.3 MHz and 1.2 MHz, respectively. The resonance frequencies of the loop for the parallel orientation are 402.1 MHz, 403.2 MHz, 403.4 MHz and 403.6 MHz at the distances of 5 mm, 10 mm, 15 mm and 20 mm, respectively. Thus, the shifts in the resonance frequency are 2.5 MHz, 1.4 MHz, 1.2 MHz and 1 MHz, respectively. Moreover, it is seen that the presence of the human head results

in very small changes in the antenna impedance bandwidth.

The 3-D gain patterns of the loop antenna versus distances are presented in Figure 4.7, with the loop being placed normal to the human head. Figure 4.7 (a) presents the gain pattern for the loop antenna in free space. Figure 4.7 (b), (c), (d) and (e) present the gain patterns for the cases that the loop is normal to the head, with the distances in-between being 5 mm, 10 mm, 15 mm and 20 mm, respectively. It is seen that the presence of the head results in the changes in the radiation pattern and efficiency, as summarized in Table 4.11. With the head in present, the radiation efficiencies of the loop for the normal orientation are 2.51%, 2.51%, 2.44% and 2.35% at the distances of 5 mm, 10 mm, 15 mm and 20 mm, respectively. Comparing to the radiation efficiency of the loop itself in free space, there is the increases in the antenna radiation efficiency, and the increases are 1.11%, 1.11%, 1.04% and 0.95% for the distances of 5 mm, 10 mm, 15 mm and 20 mm, respectively.

When the loop is placed parallel to the human head, the 3-D gain patterns of the loop antenna versus distances are presented in Figure 4.8. Figure 4.8 (a) presents the gain pattern for the loop antenna itself in free space. Figure 4.8 (b), (c) and (d) present the cases that the loop is placed parallel to the head, with the distances in-between being 5 mm, 10 mm and 15 mm, respectively. It is seen that the presence of the head results in the changes in the radiation pattern and efficiency, as summarized in Table 4.12. With the head in present, the radiation efficiencies of the loop for the parallel cases are 0.18%, 0.26%, 0.34% and 0.42% at the distances of 5 mm, 10 mm, 15 mm and 20 mm, respectively. Comparing to the radiation efficiency of the loop itself in free space, there is the significant decreases in the radiation efficiency, and the decreases are 1.22%, 1.14%, 1.06% and 0.98% for the distances of 5 mm, 10 mm, 15 mm and 20 mm, respectively. It can be concluded that the normal orientation has an advantage over the parallel orientation and the loop needs to be arranged normal to the head in order to get a better radiation efficiency.

Table 4.11: Human head influence versus distances when the loop is **normal** to the head: at **405 MHz**

Distance	Resonance Frequency	Bandwidth (-10 dB)	Bandwidth (-15 dB)	Radiation Efficiency
Loop Only	404.6 MHz	1.6 MHz	0.8 MHz	1.4%
d=5mm	403.2 MHz	1.6 MHz	0.8 MHz	2.51%
d=10mm	403.3 MHz	1.7 MHz	0.9 MHz	2.51%
d=15mm	403.3 MHz	1.7 MHz	0.9 MHz	2.44%
d=20mm	403.4 MHz	1.7 MHz	0.9 MHz	2.35%

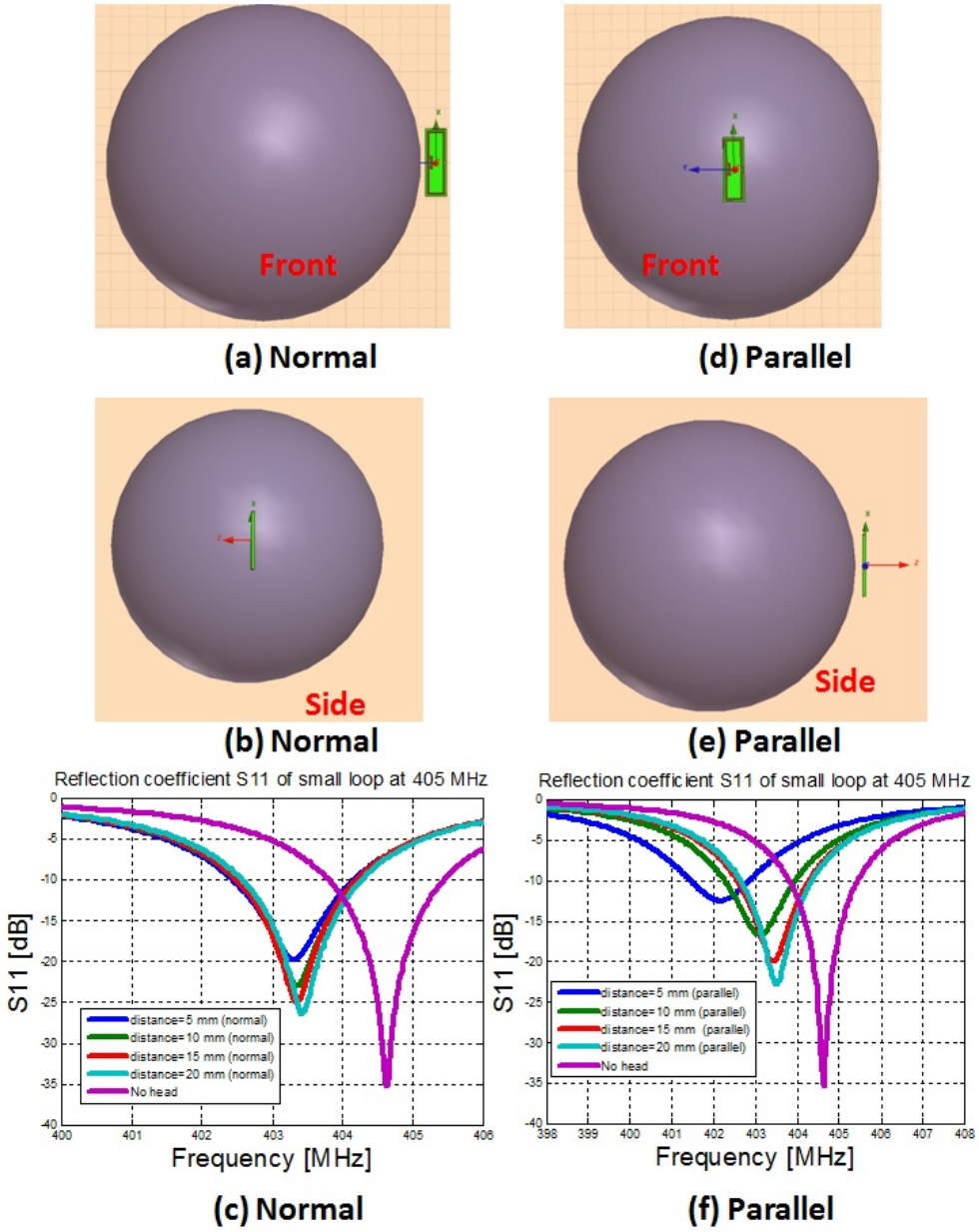

Figure 4.6: The reflection coefficients of the loop antenna (in presence of a human head) versus the distances between the antenna and head. (a) and (b) illustrate the antenna orientation that is normal to the head. (d) and (e) illustrate the antenna orientation hat is parallel to the head. (c) and (f) represent reflection coefficients of the loop antenna versus the distances for the normal and parallel orientations, respectively.

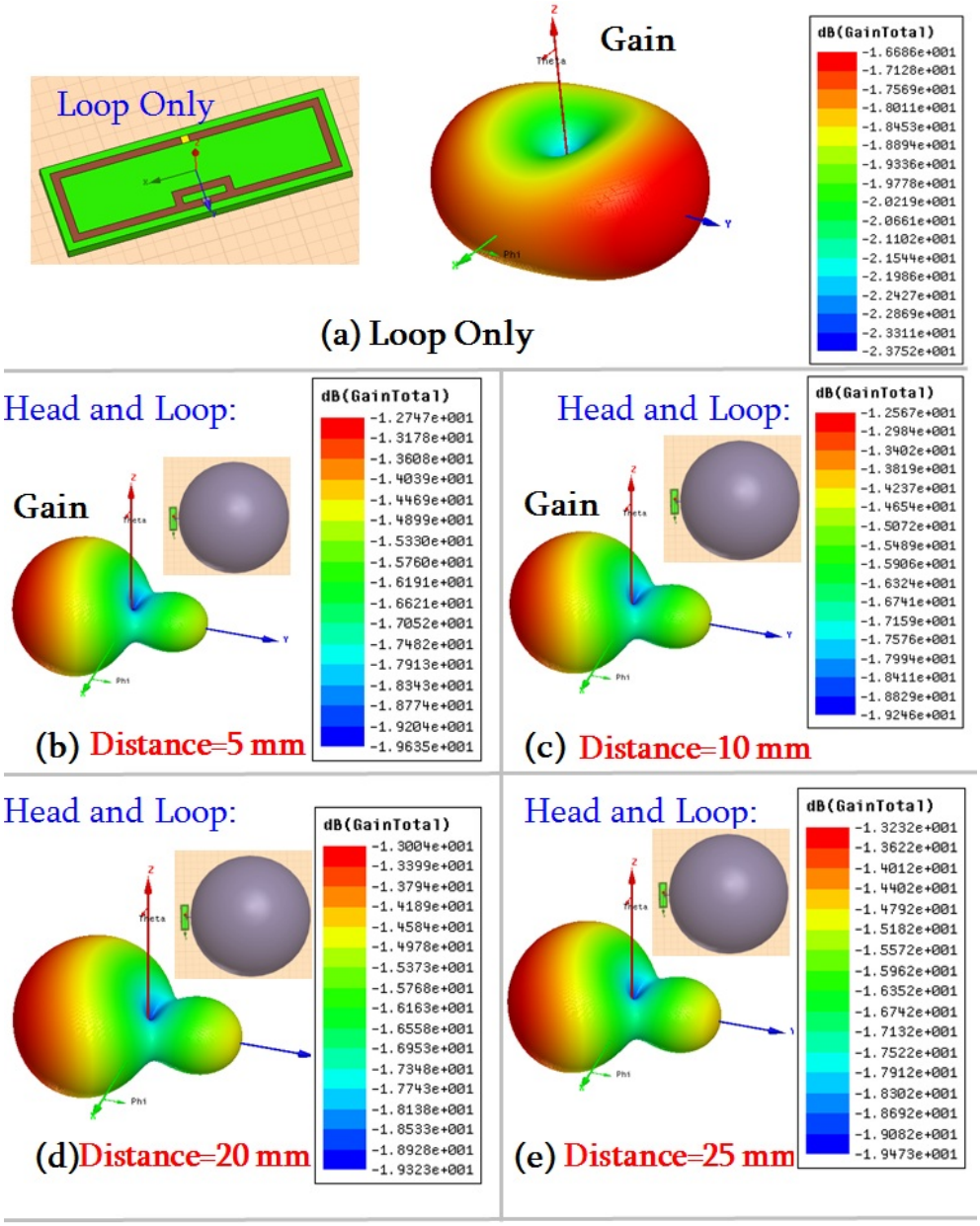

Figure 4.7: The 3-D gain patterns of the loop antenna (normal to a human head) versus the distances between the antenna and head. (a) presents the situation that only the loop antenna is present. (b), (c), (d) and (e) present the cases that the loop is placed normal to the head, with the distances in-between being 5 mm, 10 mm, 15 mm and 20 mm, respectively.

Table 4.12: Human head influence versus distances when the loop is **parallel** to the head: at **405 MHz**

Distance	Resonance Frequency	Bandwidth (-10 dB)	Bandwidth (-15 dB)	Radiation Efficiency
Loop Only	404.6 MHz	0.9 MHz	0.8 MHz	1.4%
d=5mm	402.1 MHz	1.5 MHz	0.6 MHz	0.18%
d=10mm	403.2 MHz	1.7 MHz	0.8 MHz	0.26%
d=15mm	403.4 MHz	1.7 MHz	0.8 MHz	0.34%
d=20mm	403.6 MHz	1.7 MHz	0.8 MHz	0.42%

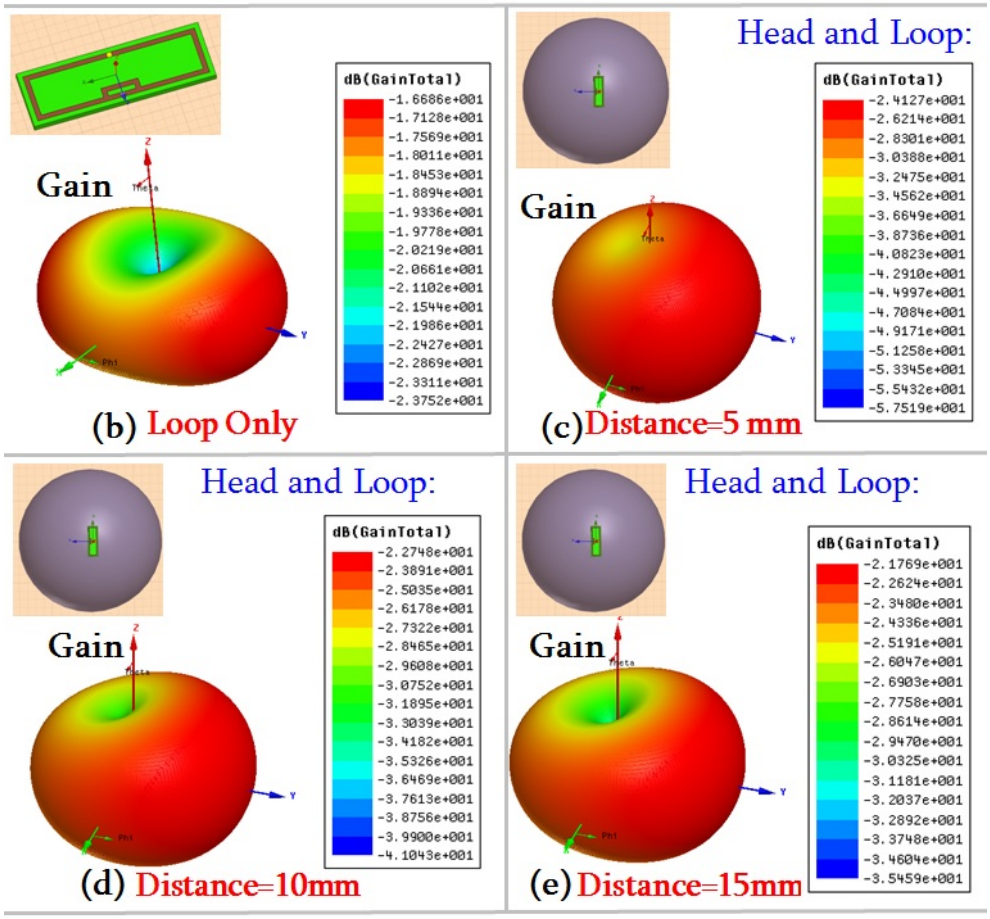

Figure 4.8: The 3-D gain patterns of the loop antenna (parallel to a human head) versus the distances between the antenna and head. (a) presents the situation that only the loop antenna is present. (b), (c) and (d) present the cases that the loop is placed parallel to the head, with the distances in-between being 5 mm, 10 mm and 15 mm, respectively.

Sensitivity Analysis of the Antenna Parameters: 910 MHz

Similar to the previous procedures, a self-resonant electrically small loop antenna, designed to be resonant around 910 MHz, was used in this simulation to investigate the influence of the antenna related parameters, including the ESA orientations and the distance between the ESA and head. The dimensions of the loop antenna are 35 mm $\times$ 10 mm $\times$ 1.524 mm. For the loop itself in free space, its resonant frequency of operation is 912.4 MHz. The impedance bandwidth reference to -10 dB and -15 dB are 3.7 MHz and 1.9 MHz, respectively. The simulated radiation efficiency is optimized to 30%. These performances will be used as the reference which will be compared to the antenna performance with the head being present.

Again, two orientations that the loop is relative to the head are investigated which are the normal and parallel orientations. The simulated antenna reflection coefficients versus the distances are presented in Figure 4.9 (a) and (b) for the normal and parallel orientations, respectively. It is found that the presence of the head results in the shifts in the resonance frequency which are illustrated in Table 4.13 and Table 4.14. The resonance frequencies of the loop antenna for the normal orientation are 909.2 MHz, 910.2 MHz, 910.2 MHz and 910.3 MHz at the distances of 5 mm, 10 mm, 15 mm and 20 mm, respectively. Thus, the shifts in the resonance frequency are 3.2 MHz, 2.2 MHz, 2.2 MHz and 2.1 MHz, respectively. The resonance frequencies of the loop for the parallel orientation are 897.7 MHz, 906.8 MHz, 908.5 MHz and 909.4 MHz at the distances of 5 mm, 10 mm, 15 mm and 20 mm, respectively. Thus, the shifts in the resonance frequency are 14.7 MHz, 5.6 MHz, 3.9 MHz and 3 MHz, respectively. Hence, the parallel orientation of the loop results in a lager shift in the resonance frequency than that of the normal orientation. Moreover, it is seen that the presence of the head causes very small changes in the antenna impedance bandwidth.

The presence of the head results in the changes in the radiation pattern and efficiency, as summarized in Table 4.13. The radiation efficiencies of the loop antenna for the normal orientation are 11.46%, 13.01%, 13.7% and 13.9% at the distances of 5 mm, 10 mm, 15 mm and 20 mm, respectively. Comparing to the radiation efficiency of the loop itself in free space, there are the decreases in the radiation efficiency, and the decreases are 18.54%, 16.99%, 16.3% and 16.1% at the distances of 5 mm, 10 mm, 15 mm and 20 mm, respectively. The radiation efficiencies of the loop antenna for the parallel orientation are 2.03%, 4.02%, 6.43% and 11.37% at the distances of 5 mm, 10 mm, 15 mm and 20 mm, respectively. Comparing to the radiation efficiency of the loop itself

in free space, there are the significant decreases in the radiation efficiency, and the decreases are 27.97%, 25.98%, 23.57% and 18.63% at the distances of 5 mm, 10 mm, 15 mm and 20 mm, respectively. It is concluded that for both the normal and parallel orientations there are the decreases in the radiation efficiency at 910 MHz, but the decreases in the normal orientation is less than that in the parallel orientation. Thus, the normal orientation still has an advantage over the parallel orientation. In order to get a high radiation efficiency, the loop needs to be placed normal to the head.

Table 4.13: Human head influence versus the distances when the loop is **normal** to the head: at **910 MHz**

Distance	Resonance Frequency	Bandwidth (-10 dB)	Bandwidth (-15 dB)	Radiation Efficiency
Loop Only	912.4 MHz	3.7 MHz	1.9 MHz	30%
d=5mm	909.2 MHz	3.5 MHz	/	11.46%
d=10mm	910.2 MHz	3.7 MHz	1.9 MHz	13.01%
d=15mm	910.2 MHz	3.7 MHz	2 MHz	13.7%
d=20mm	910.3 MHz	3.7 MHz	2 MHz	13.9%

Table 4.14: Human head influence versus the distances when the loop is **parallel** to the head: at **910 MHz**

Distance	Resonance Frequency	Bandwidth (-10 dB)	Bandwidth (-15 dB)	Radiation Efficiency
Loop Only	912.4 MHz	3.7 MHz	1.9 MHz	30%
d=5mm	897.7 MHz	/	/	2.03%
d=10mm	906.8 MHz	3.5 MHz	/	4.02%
d=15mm	908.5 MHz	3.9 MHz	1.9 MHz	6.43%
d=20mm	909.4 MHz	3.9 MHz	1.9 MHz	11.37%

Sensitivity Analysis of the Antenna Parameters: 1000 MHz

The frequency of 1000 MHz is interesting for this application, and the sensitivity analysis of the ESA related parameters is also investigated. A self-resonant electrically small loop antenna resonant at 998 MHz is used in this simulation, with the dimensions being 35 mm$\times$10 mm $\times$ 1.524 mm. In the previous investigations, the starting point is that the loop antenna is tuned to be resonant at the desired frequency, when it is placed in free space without a head. A head model is added in the simulations afterwards, and the distance between the loop and the head changes step by step. Then we compare the shifts in the antenna performance for the cases with and without the head,

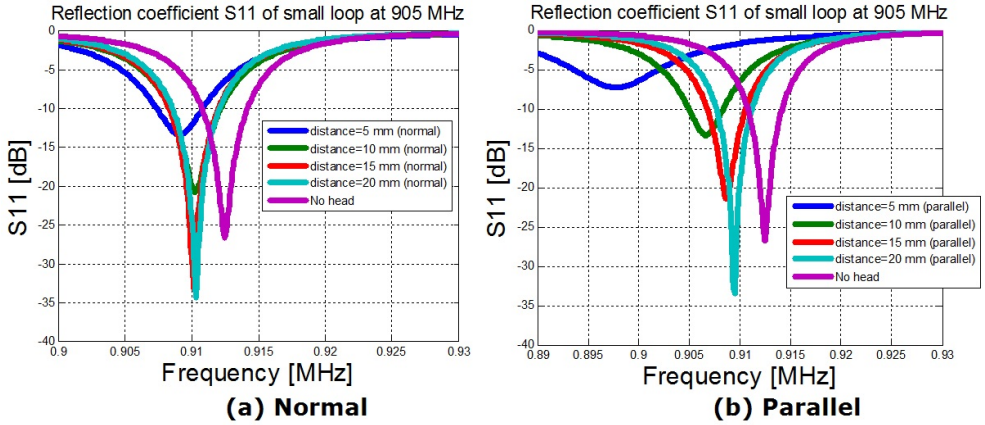

Figure 4.9: Reflection coefficients of the loop antenna (in presence of a human head) versus the distances between the antenna and head. (a) presents the orientation that the antenna is normal to the head. (b) presents the orientation that the antenna is parallel to the head.

and also show the changes in the antenna performance versus the distances.

Different from the previous investigations, in this analysis the loop antenna is tuned to be perfectly matched when it is close to the head with the distance being 1 mm, and this is the starting point of this investigation. Then the distance changes from 1 mm to 13 mm, with an increasing step of 1 mm. Since the normal orientation has an advantage over the parallel orientation which is observed from the previous analysis, we only investigate the cases for the normal orientation.

The performance of the loop antenna, in the presence of a human head, versus the distances between the antenna and head is presented in Figure 4.10. Figure 4.10 (a) presents the changes in the antenna reflection coefficient versus the distances, and Figure 4.10 (b) presents the changes in the antenna radiation efficiency versus the distances. It is seen that as the distance increases from 1 mm to 13 mm, the antenna resonance frequency changes from 988 MHz to 1012 MHz which results in a shift of 24 MHz towards the higher frequencies. The radiation efficiency increases from 22.5% to 35.8%, as the distance increases from 1 mm to 13 mm.

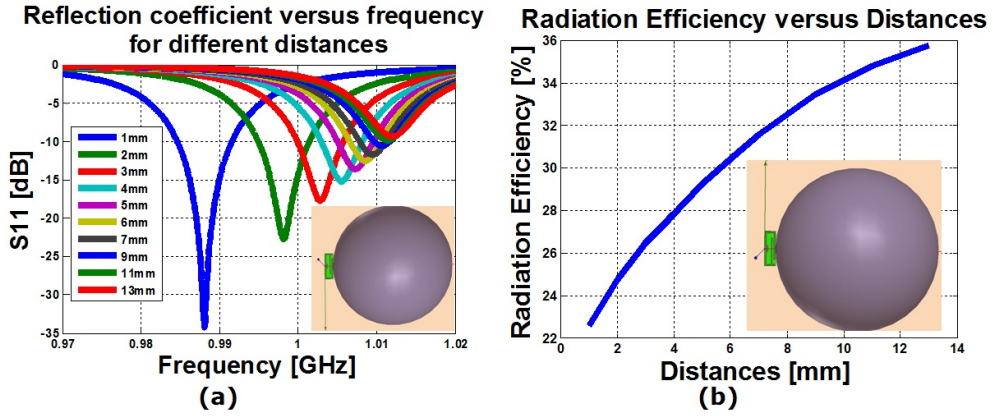

Figure 4.10: The performance of the loop antenna in the presence of a human head, versus the distances between the antenna and head. (a) presents the changes in the antenna reflection coefficient versus the distances. (b) presents the changes in antenna radiation efficiency versus the distances.

4.3 Sensitivity Analysis of the Hearing-Aid Shell Material

The sensitivity analysis of the hearing-aid shell material on the antenna characteristics is investigated in this section. The electromagnetic properties of the hearing-aid shell are unknown at the antenna frequency of operation which is around 1000 MHz. The permittivity of the shell material, which is Polybutylene Terephthalate, is only given at very low frequencies by the manufacturer. The permittivity of this material before the injection molding is 3.1 and 3.0 at 100 Hz and 1 MHz, respectively. The permittivity of this material after the injection molding is 3.9 and 3.7 at 100 Hz and 1 MHz, respectively. It is known that the permittivity of a dielectric material changes with frequencies, and thus the permittivity and conductivity measurements of the hearing-aid shell are necessary. However, these measurements face difficulties and are not performed yet. The material sample under test (SUT) of a suitable size, which is required by the measurement facility, can not be provided by the manufacturer.

Since we may place the antenna on the surface of hearing-aids, an investigation of the permittivity changes on the antenna characteristics is necessary. It can provide guidance in the tuning of antenna impedance for the practical designs. Moreover, the influence of the permittivity changes in the shell material is different for two cases depending on what type of capacitive loading is employed in the loop antenna which are the distributed printed loading element and the loaded capacitors. This analysis is confirmed by the simula-

tions using Ansoft HFSS.

Small Loop Antenna with the Distributed Printed Loading Element

An electrically small loop is used in this simulation to investigate the influence of the substrate permittivity, as illustrated in Figure 4.11. The dimensions of this electrically small loop are 35 mm$\times$10 mm $\times$ 1.524 mm, and the distributed printed loading element is added in this antenna. Figure 4.11 presents the reflection coefficient and input impedance of this antenna. The resonant frequency of operation is tuned to 1001.5 MHz, and the simulated radiation efficiency is found to be 49.7%. The substrate used in this antenna design is Rogers 6002, with the dielectric constant being 2.94 and the loss tangent being 0.0012. The characteristics of this loop antenna, in the case the substrate Rogers 6002 is used, are treated as the reference which will be compared to the antenna characteristics as the substrate permittivity ε_r changes. Thus, in this investigation the initial value of the substrate ε_r is 2.94, and the range of ε_r is selected to be [2, 4], with an increasing step of 0.2 in ε_r. Figure 4.12 presents the magnitude of the antenna reflection coefficient $|S_{11}|$ versus the changes in the permittivity of the heading-aid shell, with ε_r changed in the range [2, 4]. It is seen that as ε_r increases from 2 to 4, the antenna resonance frequency changes from 1095 MHz to 910 MHz which gives a frequency shift of 185 MHz. For each increasing step of the permittivity, that is 0.2 in ε_r, it results in a shift in the resonance frequency of 15-20 MHz, approximately. Although there is a shift in the resonance frequency, the changes in the minimum of $|S_{11}|$ (at the shifted resonance frequency) are less than 5 dB, and the minimum of $|S_{11}|$ still stays within the impedance bandwidth. It is concluded that the changes in the shell dielectric constant result in the shifts in the resonance frequency, but very small changes in the minimum of $|S_{11}|$.

Figure 4.13 and Figure 4.14 present the antenna input resistance and reactance versus the changes in the shell permittivity of the hearing-aids, with ε_r being in the range [2, 3] and [3, 4], respectively. The following observations are made for the changes in the shell permittivity that are

- The resonance frequency is very sensitive to the changes in the shell permittivity. It results in a frequency shift of 15-20 MHz for each increasing step in ε_r, that is 0.2 in ε_r. The reason for this sensitivity is explained by the addition of the distributed capacitive loading element.
- As ε_r increases, the changes in the minimum of $|S_{11}|$ (at the shifted resonance frequency) are very small.
- The measurements of the hearing-aid shell permittivity and conductiv-

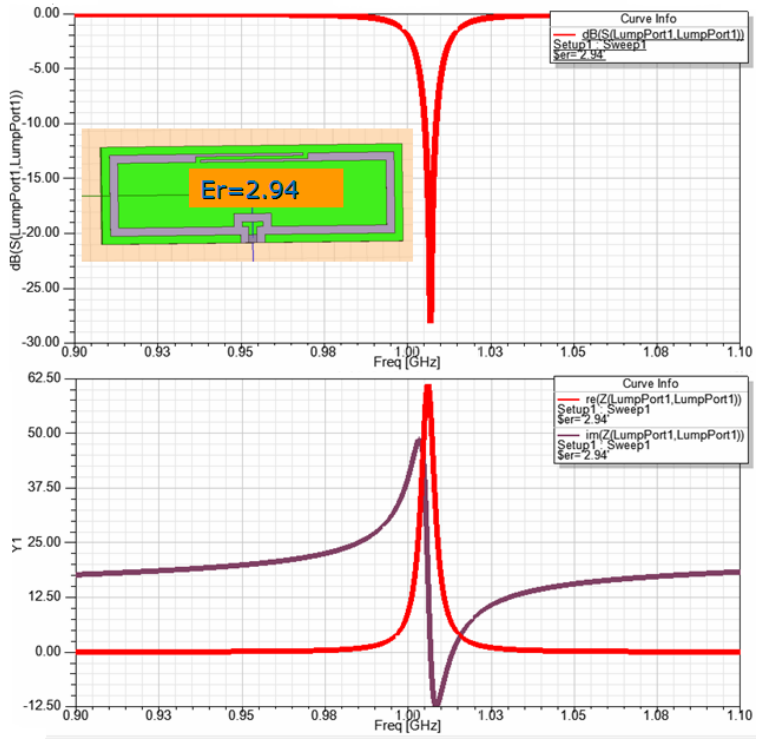

Figure 4.11: The reflection coefficient and input impedance of the electrically small loop antenna at 1000 MHz, obtained from Ansoft HFSS.

ity are necessary.

Small Loop Antenna by Using Lumped Capacitors as the Loading Element

For the small loop antenna by using a distributed printed circuit as the loading element, the advantage is that it avoids using lump capacitors which face aging and tolerance problems, and the disadvantage is that the design is sensitive to the shell permittivity which is unknown. In this subsection, the influence of the shell permittivity on the antenna characteristics is investigated for the loop antenna that uses lumped capacitors as the loading element.

An electrically small loop with its shape fitting to the hearing-aid shell is used in this simulation to evaluate the influence of the shell permittivity, as illustrated in Figure 4.15. The dimensions of this electrically small loop are listed in Figure 4.15, and a capacitor is used to replace the distributed capacitive loading element, see the blue element in Figure 4.15. The substrate used for this antenna is Rogers 6002, with the dielectric constant being 2.94 and the

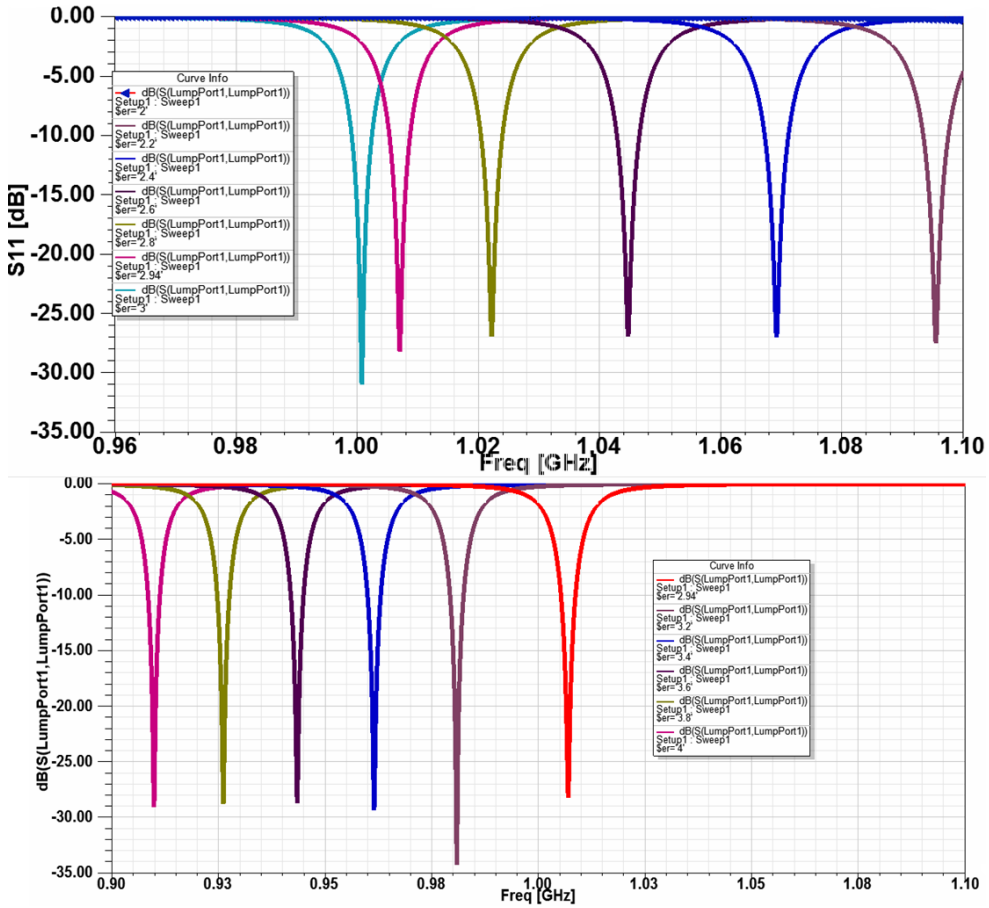

Figure 4.12: The magnitude of the antenna reflection coefficient $|S_{11}|$ versus the changes in the shell permittivity of the heading-aids.

loss tangent being 0.0012. Again, in this investigation the initial value of the substrate ε_r is set to 2.94. The range of ε_r is selected to be [2, 4], with an increasing step of 0.2 in ε_r.

Figure 4.15 presents the antenna reflection coefficient $|S_{11}|$ versus the changes in the heading-aid shell permittivity, with ε_r changed in the range [2, 4]. It is seen that as ε_r increases from 2 to 4, the antenna resonance frequency changes from 1016 MHz to 998 MHz which gives a frequency shift of 18 MHz. For each increasing step of the permittivity, that is 0.2 in ε_r, it only results in a shift of 2 MHz in the resonance frequency, approximately. The changes in the minimum of $|S_{11}|$ (at the shifted resonance frequency) is less than 5 dB, and the minimum of $|S_{11}|$ still stays within the impedance bandwidth. It is concluded that changes in the shell dielectric constant result in a small shift

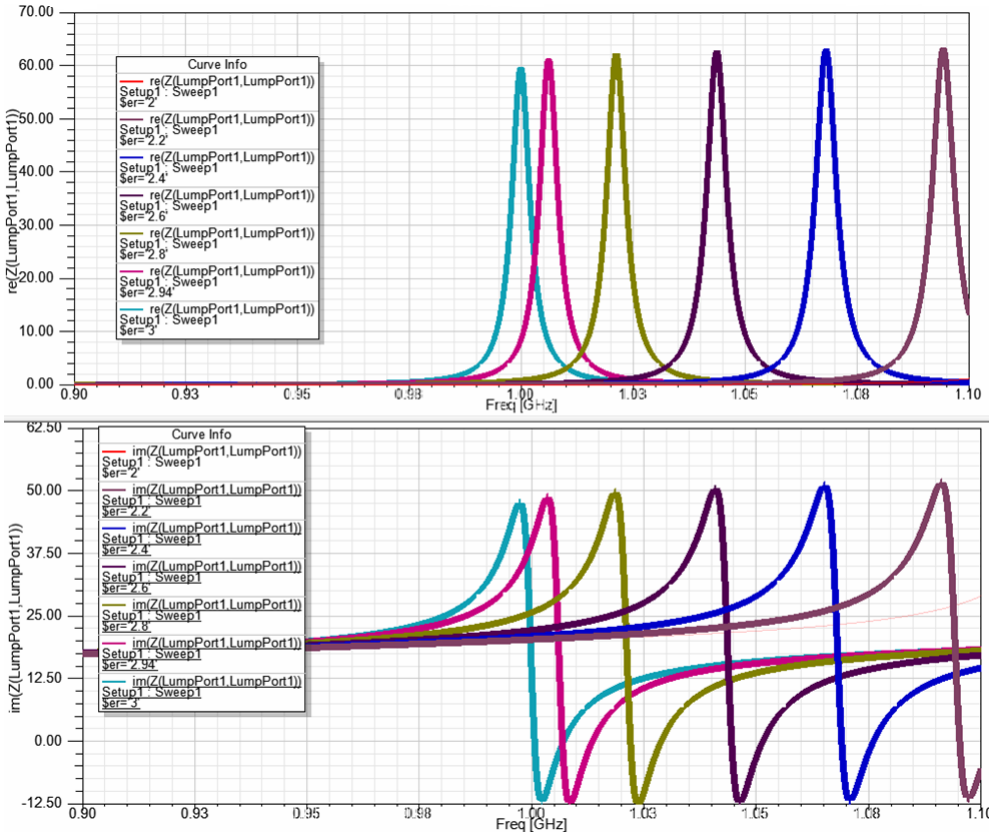

Figure 4.13: The antenna input impedance versus the changes in the shell permittivity of the heading-aids, with ε_r in the range [2, 3].

in the resonance frequency and the minimum of $|S_{11}|$.

4.4 Summary

In summary, the influence of complex environments on the ESA characteristics is investigated in this chapter.

- First, the sensitivity analysis of the head phantom parameters on the antenna characteristics is presented, including the influence of the head permittivity and conductivity. The observations are summarized as follows.

  By keeping all the other parameters fixed, the changes in the head dielectric constant result in very small changes in $|S_{11}|$ and the impedance

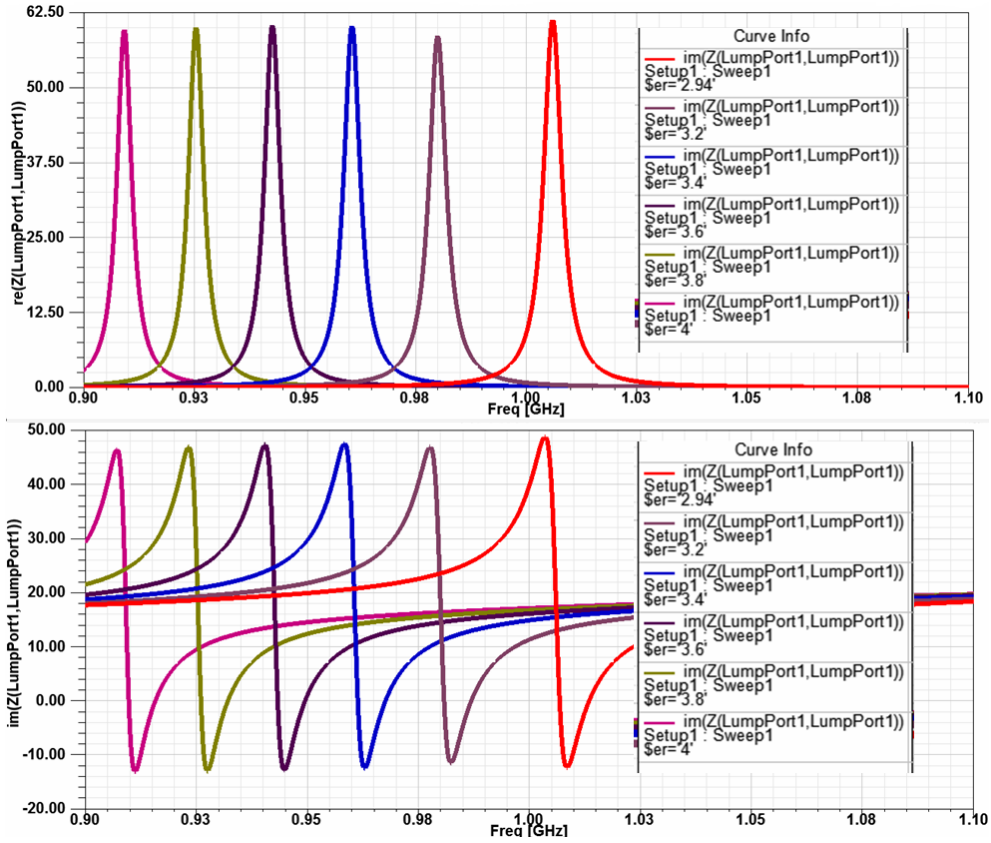

Figure 4.14: The antenna input impedance versus the changes in the shell permittivity of the heading-aids, with ε_r in the range [3, 4].

bandwidth BW. It results in a small decrease in the radiation efficiency $\mathbf{e}_{rad}$. These observations show that using a homogenous head model with an averaged dielectric constant is reasonable for fast simulations, compared to the six-layer head model or the SAM model.

By keeping all the other parameters fixed, the changes in the head conductivity result in very small changes in $|S_{11}|$, impedance bandwidth BW and radiation efficiency $\mathbf{e}_{rad}$.

- Second, the sensitivity analysis of the ESA related parameters is presented, including the orientation and location of the ESAs and the distance between the ESA and head. This analysis is performed at the frequencies of 405 MHz, 905 MHz and 1000 MHz, respectively. Two orientations that the loop antenna is relative to the head are investigated which are the normal and parallel orientations.

  The presence of the head results in a shift in the resonance frequency.

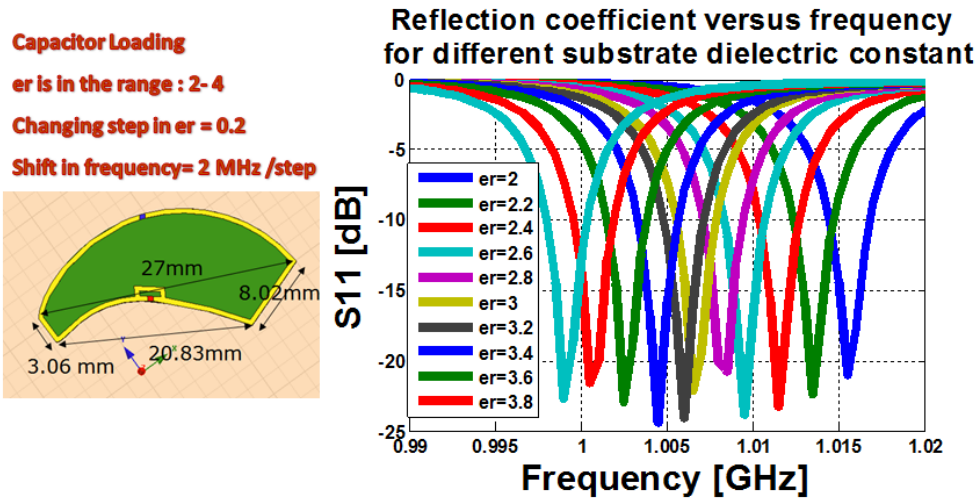

Figure 4.15: The antenna reflection coefficients versus the changes in the shell permittivity of the heading-aids, with ε_r changed in the range [2, 4].

Moreover, the parallel orientation of the loop results in a larger shift in the resonance frequency than that of the normal orientation.

The presence of the head causes very small changes in the antenna impedance bandwidth.

The presence of the head results in significant changes in the radiation pattern and radiation efficiency. The normal orientation has an advantage over the parallel orientation and in order to get a better radiation efficiency, the loop needs to be placed normal to the head.

- Third, the material influence of the hearing-aid shell is investigated. The influence of the permittivity changes in the shell material are different for the two situations depending on what type of capacitive loading is employed in the loop which are the distributed printed element and the loaded capacitors.

  For the loop design using the distributed printed loading element, the resonance frequency is very sensitive to the changes in the shell permittivity. As ε_r increases from 2 to 4, the antenna resonance frequency changes from 1095 MHz to 910 MHz which gives a frequency shift of 185 MHz. Thus, it causes a frequency shift of 15-20 MHz for each changing step in ε_r, that is 0.2 in ε_r. The reason for this sensitivity is explained by the addition of the distributed capacitive loading element. As ε_r increases, the changes in the minimum of $|S_{11}|$ (at the shifted resonance frequency) are very small. The measurements of the hearing-aid shell permittivity and conductivity are necessary.

For the loop design using lumped capacitors as the loading element, as ε_r increases from 2 to 4, the antenna resonance frequency changes from 1016 MHz to 998 MHz which gives a frequency shift of 18 MHz. For each increasing step of the permittivity, that is 0.2 in ε_r, it only results in a shift of 2 MHz, approximately, in the resonance frequency. Thus, the loop antenna using the lumped capacitors as the loading element is less sensitive than that using the distributed printed element as the loading element.

CHAPTER

FIVE

Conclusions

This chapter presents an overview of the major contributions obtained from this work, and summarizes the main results in all previous chapters. To continue the research in the area of antenna miniaturizations for the hearing-aid application, it is also our duty to address research issues in future work.

Antenna Miniaturizations
Designing the highly miniaturized electrically small antennas (ESAs) that are used for the hearing-aid application is a main task in this dissertation. Several novel designs of electrically small loops were presented for the hearing-aid application, which are summarized as follows. First antenna design is a two-dimensional (2-D) planar differential-fed electrically small loop. The working mechanism of this antenna is based on the capacitive loading and the inductive coupling between the two small loops. The analytical model, simulations, fabrications and measurements are presented for this antenna. The measured radiation efficiency is found to be 21% with ka being 0.33. The measured impedance bandwidth reference to -15 dB is 3.0 MHz. Second antenna design is a planar two-turn electrically small loop antenna. The working mechanism of this antenna is based on the capacitive loading, and both the capacitive and inductive coupling between the two small loops that are of a comparable size are taken into account. An analytical model is provided to give guidance in the impedance tuning. The simulated radiation efficiency is found to be 34% with ka being 0.33. The impedance bandwidth reference to -15 dB is 2.5 MHz. Third, several three-dimensional (3-D) folded electrically small loop antennas are proposed, the properties of which are significantly improved compared to the 2-D planar electrically small loop antennas. The working mechanism is based on the capacitive loading and the inductive coupling between the two loops. The large loop is folded in a proper way to make better use of the device volume. There exist several ways to fold the

large loop, which result in different radiation patterns. The maximum radiation efficiency of the folded loop is found to be 43% with ka being 0.28. The impedance bandwidth reference to -15 dB is 1.0 MHz.

These antenna designs show that the antenna impedance can be matched to the system characteristic impedance by using the self-resonant electrically small loops, without adding any external matching circuit. The use of lumped components is avoided, by replacing the capacitors with a distributed printed loading element. The difficulty in the impedance matching is thus overcome. The specification in the impedance bandwidth is 1.0 MHz reference to -15 dB, as required in the link budget. Although the impedance bandwidth of these ESAs is narrow, the specification in the impedance bandwidth can still be satisfied, either for the 2-D planar loops or the 3-D folded loops. The specification in the radiation efficiency can also be satisfied. The radiation efficiency is improved to as high as 43% for the 3-D folded loop antenna, which occupies a volume of 25 mm$\times$9 mm$\times$6 mm.

Measurements Techniques for ESAs
The development of the input impedance, radiation efficiency and gain measurement techniques and instruments for ESAs is another main task in this work. Nowadays the characteristics of antennas are mainly verified with cable measurements in the anechoic chamber, which works very well for most of traditional antennas. However, this measurement technique is not well applicable for ESAs. The input impedance and radiation efficiency measurements of ESAs represent a great challenge. Typically, there exist two mechanisms that introduce errors in the measurements which are the leaking current and the scattering effect caused by the feed line. It is necessary to design and implement new measurement set-ups and techniques for the measurement of ESAs. In this work, several novel measurement techniques are proposed for ESAs, which are summarized as follows.

The effectiveness of adding a tunable sleeve balun in the ESA measurement is investigated and its validity is presented. The optimum balun parameters are studied. It is noted that a careful tuning of the balun is very important, both for the radiation pattern and for the radiation efficiency measurement.

A modified Wheeler cap technique for the radiation efficiency measurement of balanced electrically small antennas is proposed. This method provides the following advantages. First, no balun is required during the measurement and thus the problems of narrow impedance bandwidth and extra scattering effect caused by the balun are avoided. As a result, the proposed method is valid in a broad frequency band. Second, the application of the proposed method and the proper use of the circle fitting for the measured s-parameters

ensure that the cavity resonances do not have any significant effect on the measurement results. By using the Wheeler cap method in the proposed way, most of its limitations and disadvantages are avoided. The method is, therefore, suitable for the input impedance and radiation efficiency measurements for most types of antennas in a broad frequency band. The antennas under test are not limited to be electrically small. They can be balanced or unbalanced, symmetric or asymmetric antennas.

Moreover, the modified Wheeler cap method for measurements of small antennas in complex environments is further developed. It is shown that the limitation on the cavity dimension can be overcome by this method because the influence of the cavity resonances is removed by a proper circle fitting technique. Hence, it is possible to perform the radiation efficiency measurement inside a large cavity. Finally, the measurement results for electrically small antennas in complex environments are presented to show the validity of this technique.

A cable-free impedance and gain measurement technique for electrically small antennas is proposed. The electromagnetic model, simulation results, as well as measurement results are presented and discussed. The electromagnetic model of this technique is derived by using the spherical wave expansion, and it is valid for the arbitrary electrically small AUT at arbitrary distances between the probe and AUT. The whole measurement setup is modeled by the cascade of three coupled multiple-port network. Three measurement examples using the proposed cable-free technique are presented, in which a standard gain horn antenna, a monopole antenna and an electrically small loop are tested as the AUT, respectively. Comparison of the antenna measurement techniques, with and without the feeding cable, shows that there exists the scattering effects from the cable in both the reflection coefficient measurement and gain measurement.

Complex Environments
The influence of complex environments on the characteristics of ESAs is investigated, such as the influence of the human head phantom and hearing-aids.

The sensitivity analysis of the head phantom parameters on the antenna characteristics is presented, including the influence of the head permittivity and conductivity. The following observations are obtained. First, by keeping all other parameters fixed, the changes in the head dielectric constant result in very small changes in $|S_{11}|$ and the impedance bandwidth (BW). It results in a small decrease (not significant) in the radiation efficiency e_{rad}. These observations show that the use of a homogenous head model with an av-

eraged dielectric constant is reasonable for fast simulations, compared to the six-layer head model or the SAM model. Second, by keeping all other parameters fixed, the changes in the head conductivity result in very small change in $|S_{11}|$, the impedance bandwidth BW and the radiation efficiency $\mathbf{e}_{rad}$.

The sensitivity analysis of the ESA related parameters on the antenna characteristics is presented, including the orientations and locations of the ESA and the distance between the ESA and head. This analysis is performed at the frequencies of 405 MHz, 905 MHz and 1000 MHz, respectively. Two orientations that the loop antenna is relative to the head are investigated which are normal and parallel orientations. The observations are summarized as follows. First, the presence of the head results in a shift in the resonance frequency. The parallel orientation of the loop results in a larger shift in the resonance frequency than that of the normal orientation. Second, the presence of the head causes very little change in the antenna impedance bandwidth. Third, the presence of the head results in the significant changes in the radiation pattern and radiation efficiency. The normal orientation has an advantage over the parallel orientation. In order to get a better radiation efficiency, the loop antenna needs to be arranged normal to the head phantom.

The influence of the hearing-aid shell material on the antenna characteristics is also investigated. The influence of the permittivity changes in the shell material is different for the two situations depending on what type of capacitive loading element is employed in the loop antenna, which are the distributed printing element and the lumped capacitors. First, for the loop design using the distributed printed loading element, the resonance frequency is very sensitive to the changes in the shell permittivity. As ε_r increases from 2 to 4, the antenna resonance frequency changes from 1095 MHz to 910 MHz, which gives a frequency shift of 185 MHz. Thus, it causes a frequency shift of 15-20 MHz (approximately) for each changing step in the shell permittivity, that is 0.2 in ε_r. The reason for this sensitivity is explained by the addition of the distributed capacitive loading element. The measurements of the hearing-aid shell permittivity and conductivity are thus necessary. Second, for the loop design using lumped capacitors as the loading element, as ε_r increases from 2 to 4, the antenna resonance frequency changes from 1016 MHz to 998 MHz, which gives a frequency shift of 18 MHz. For each increasing step in the permittivity, that is 0.2 in ε_r, it only results in a shift of 2 MHz (approximately) in the resonance frequency. Thus, the loop antenna using the lumped capacitors as the loading element is less sensitive than that using the distributed printed element as the loading element.

Summary

Based on the research carried out in the above three areas, it can be shown that the difficulties in the designs and measurements of ESAs for the heading-aid application are overcome. The current work is mainly focused on the antenna miniaturization for the BTE (behind the ear) hearing-aid application. The future work is suggested on the further development of the antenna miniaturization for the CIC (completely in the canal) hearing-aid application. Based on the positive results obtained from this project, we believe that the integration of a wireless communication unit into the hearing-aids will become a reality soon in the commercial market.

Paper I

Theory and Practice of a Cable-Free Impedance and Gain Measurement Technique for Electrically Small Antennas

Jiaying Zhang, Pivnenko Sergey and Olav Breinbjerg

Preparing in Submission to IEEE Transactions on Antennas and Propagations

2011 February

Theory and Practice of a Cable-Free Antenna Impedance and Gain Measurement Technique for Electrically Small Antennas

Jiaying Zhang [#1], Sergey Pivnenko [#2] and Olav Breinbjerg [#3]

[#] *Department of Electrical Engineering, Technical University of Denmark*
Ørsteds Plads, Building 348, DK-2800 Kgs. Lyngby, Denmark
[1] jz@elektro.dtu.dk, [2] sp@elektro.dtu.dk, [3] ob@elektro.dtu.dk

***Abstract*—Impedance and gain measurements for electrically small antennas represent a great challenge due to the influence of the feeding cable. In this paper, a novel cable-free antenna impedance and gain measurement technique for electrically small antennas is proposed. In this approach, the antenna properties are extracted by measuring the signal scattered by the antenna under test (AUT) with a probe antenna, when the AUT is loaded with three known loads. The proposed technique is formulated differently from the known radar cross section method. A complete electromagnetic model is derived for a measurement system that includes an arbitrary probe, free space propagation, and an arbitrary AUT. In this model, the probe and AUT are modeled by the spherical wave expansion (SWE) and the whole measurement system is modeled by the cascade of three coupled multiple-port networks of the SWE. The influence of the structural scattering and multiple reflections between the probe and AUT on the measured impedance and gain is included in the model. Moreover, a simple model without the structural scattering and multiple reflections is also introduced for the cable-free measurement at an electrically large distance between the probe and AUT. Simulation and measurement results by the proposed method are presented and discussed.**

I. Introduction

In recent years, there has been a strong interest in antenna miniaturization techniques for numerous applications such as hearing-aids, cell phones, portable wireless equipments, sensors and RFIDs. However, the antenna miniaturization results in performance degradations such as narrow impedance bandwidth and low radiation efficiency. Hence, the performance of electrically small antennas (ESAs) needs to be characterized accurately. Here we focus on the most important parameters that are the input impedance and gain. Nowadays, the performance of antennas is usually tested with cable measurements in an anechoic chamber. This technique works very well for antennas with the electrical size being lager than one half wavelength. However, the traditional techniques are not well applicable to ESAs, the dimensions of which are comparable to the feed line and the support structure. Although several measurement techniques are being used for ESAs, the measurements of the impedance and gain for ESAs represent a great challenge and typically there exist two error mechanisms. First, the feeding cable may have a significant influence on the measured radiation pattern and radiation efficiency due to the leaking current on the outside of the feeding cable [1]. Although a balun can be used to avoid the leaking current, it is typically a narrow-band device. Several baluns are thus required for different frequency bands. Also, the balun needs to be tuned carefully at the specified frequency. In addition, the balun may have a size comparable to or even larger than that of the ESA; thus it gives rise to scattering. Second, the feeding cable presents a large scattering structure even if the leaking current is avoided. Measurement of the small antenna performance without the use of a feeding cable is therefore highly desirable.

The radar cross section (RCS) measurement technique without the use of a feeding cable for traditional antennas has been used for many years. The measurement of the antenna impedance and gain by the RCS method has been described in [2] and later developed in [3] and [4]. The antenna parameters are extracted from measurements of the scattered fields by the AUT, when it is loaded by several known loads. The method is well applicable for antennas with an electric size of several wavelengths, but when it is used for ESAs with a low radiation efficiency the dynamic range of the measured signal becomes rather low, which reduces the measurement accuracy. A complete electromagnetic model that takes into account an arbitrary AUT located at an arbitrary distance from the transmitting and receiving probe antenna needs to be addressed to analyze the scattering mechanism between the probe and AUT. By using such a model the antenna impedance and radiation characteristics may also be obtained from a near-field distance measurement. Another improved measurement approach is proposed in [5], which is a combination of the RCS method and three-antenna method. However, it is only partial cable-free since the feeding cable is used in the reflection coefficient measurement of the AUT. The antenna gain is then determined from the RCS method by taking into account the above reflection coefficients, in which the cable influence is still involved. Recently, an indirect contactless impedance measurement technique for small antennas has been reported in [6]-[7], but it does not provide the gain and radiation efficiency.

In this paper, we propose a cable-free measurement technique for the determination of both the input impedance

and the gain of ESAs. A complete electromagnetic model is proposed for the measurement system by using the Spherical Wave Expansion (SWE), which includes an arbitrary probe, the free space propagation, and an arbitrary AUT. This model is valid for an arbitrary distance (larger than the sum of the radii of the AUT and probe minimum spheres) between the AUT and probe. The probe and AUT are modeled by separate SWEs. Then the SWEs are used to formulate the electromagnetic model of the measurement system by the cascade of three coupled multiple-port networks that represent the probe, the free space propagation, and the AUT, respectively. The antenna gain is extracted from the transmission formula between the probe and AUT. The present work emphasizes this with the theory part and the complete electromagnetic model, together with two simulation results. The experimental application of the proposed measurement technique for an electrically small loop antenna is also presented. More measurement results by the proposed technique were presented in [8].

This paper is organized as follows. The electromagnetic model of the measurement system is derived in Section II. In Section III, the determination of the antenna impedance and gain is presented by deriving the transmission formula using the SWE. In Section IV, two simulation examples by the proposed measurement technique are presented and discussed for a half-wavelength dipole and an electrically small loop antenna, respectively. In Section V, the measurement results for an electrically small loop antenna is presented and discussed. The conclusions and future work are provided in Section VI.

II. Electromagnetic Model of the Measurement System

In this section, the complete electromagnetic model of the measurement system is proposed which is valid for an arbitrary distance between the probe and AUT. The time convention e^{-iwt} is adopted.

A. Model of the Probe and the AUT

While some previous works have assumed just a simple spherical mode for AUT, the model presented here allows for arbitrary AUT and takes into account the complete SWE. The overall transmission system includes the scattering effects and multiple reflections of the probe and AUT which are modeled by scattering matrices with all spherical modes considered. Based on the proposed model, the impedance and far-field characteristics of ESAs may also be extracted from a near-field distance measurement.

The electric field $\vec{E}(\vec{r})$ around an antenna, enclosed by the minimum sphere of radius r_0, can be expressed by using the SWE for $r > r_0$ [9], that is

$$\vec{E}(\vec{r}) = \frac{k}{\sqrt{\eta}} \sum_{s=1}^{2} \sum_{n=1}^{N} \sum_{m=-n}^{n} \{a_{smn} \vec{F}^{(4)}_{smn}(\vec{r}) + b_{smn} \vec{F}^{(3)}_{smn}(\vec{r})\} \tag{1}$$

where the superscript c = 3, 4 denotes outward and inward propagating waves, respectively. a_{smn} and b_{smn} are the expansion coefficients. $\vec{F}^{(c)}_{smn}$ are the power-normalized spherical vector wave functions. k is the wave number, η is the intrinsic admittance of the medium and $\vec{r}$ is the position vector for a point with (r, θ, ϕ) spherical coordinates. For practical measurements only a finite number of spherical modes are needed to represent the field. The truncation number $N$for the n summation must ensure the required convergence. Several truncation rules have been developed, and these depend on the required accuracy of the fields and the electric size of the antennas [10]. In particular, for small antennas with electric size $kr_0 < 1$, the truncation rule $N = [kr_0] + n_1$ can be applied, where n_1 = 2, 3 or 4 depending on the required accuracy. The square brackets in [ ] indicate the largest integer smaller than or equal to kr_0.

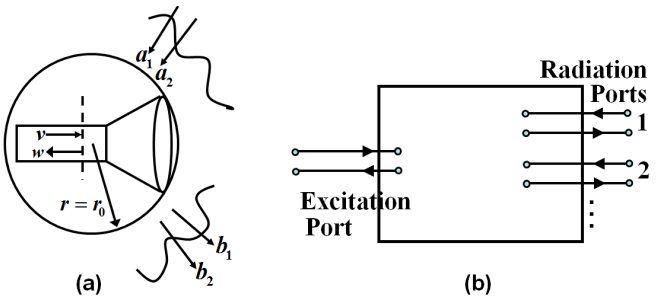

Fig. 1. The network representation of an antenna. (a) presents an antenna with spherical wave modes in its minimum sphere. (b) presents the network representation of the antenna modes. Redrawn from [9].

An antenna can be modeled as a multi-port network with one excitation port that is connected to the generator and the radiation ports each representing one outward and inward spherical mode outside the antenna minimum sphere r_0. The equivalent network is illustrated in Fig. 1(a) and (b). The total scattering matrix of the antenna can be written as [9]

$$\begin{bmatrix} w \\ \bar{\mathbf{b}}_{smn} \end{bmatrix} = \underbrace{\begin{bmatrix} \Gamma & \bar{\mathbf{R}}_{s'm'n'} \\ \bar{\mathbf{T}}_{smn} & \bar{\bar{\mathbf{S}}}^{smn}_{s'm'n'} \end{bmatrix}}_{[\bar{\bar{\mathbf{S}}}]} \cdot \begin{bmatrix} v \\ \bar{\mathbf{a}}_{s'm'n'} \end{bmatrix} \tag{2}$$

where v and w are the complex amplitudes of the incoming and outgoing waves on the excitation port of the antenna. $\bar{\mathbf{a}}_{s'm'n'}$ and $\bar{\mathbf{b}}_{smn}$ are the column vectors that represent the complex amplitudes of the incoming and outgoing spherical modes, respectively. $\bar{\mathbf{R}}_{s'm'n'}$ is a row vector containing the antenna receiving coefficients. $\bar{\mathbf{T}}_{smn}$ is a column vector containing the antenna transmitting coefficients. $\bar{\bar{\mathbf{S}}}^{smn}_{s'm'n'}$ is a square matrix that contains the antenna structural scattering coefficients. The mode index smn and $s'm'n'$ represent the outgoing and incoming spherical waves in the coordinate system of the probe, respectively. $[\bar{\bar{\mathbf{S}}}]$ is the total scattering matrix. Both the probe and AUT can be modeled by a scattering matrix $[\bar{\bar{\mathbf{S}}}]$ in the form (2), which are denoted as $[\bar{\bar{\mathbf{S}}}^{PRB}]$ and $[\bar{\bar{\mathbf{S}}}^{AUT}]$, respectively.

B. Free-Space Propagation Model by One-Way Transmission Formula

In this derivation, we define the un-primed coordinates (x, y, z) with respect to the probe and the primed coordinates

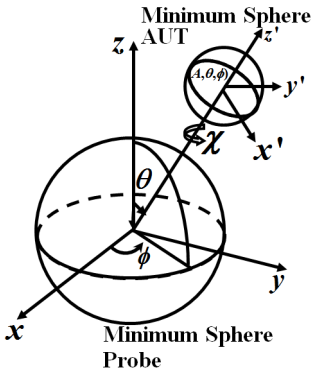

Fig. 2. Coordinates of the transmitting and receiving probe and AUT. Redrawn from [9].

(x', y', z') with respect to the AUT, as illustrated in Fig. 2. The primed coordinate system of the AUT is related to the unprimed coordinate system of the probe by 3 rotations through the angles ϕ, θ, χ and one translation of the distance A, see [9]. The transmission formula describes the complex signal received by the AUT in terms of the transmission coefficients of the probe, the receiving coefficients of the AUT, the 3 rotation angles and the translation distance A [9], that is

$$w^{AUT}(A,\chi,\theta,\phi) = \frac{v^{PRB}}{2} \sum_{\substack{smn \\ \sigma'\mu'\nu'}} T^{PRB}_{smn} e^{im\phi} e^{i\mu'\chi} d^{n}_{\mu' m}(\theta) \cdot C^{sn(3)}_{\sigma'\mu'\nu'}(kA) R^{AUT}_{\sigma'\mu'\nu'}, ... \quad (3)$$

where

$$s = 1,2; m = -n, -n+1, ..., n; n = 1, 2... \\ \sigma' = 1,2; \mu' = -\nu', -\nu'+1, ..., \nu'; \nu' = 1, 2... \quad (4)$$

Here smn and $\sigma'\mu'\nu'$ are the indices of the SWEs of the probe and AUT, respectively. T^{PRB}_{smn} are the transmitting coefficients of the probe and $R^{AUT}_{\sigma'\mu'\nu'}$ are the receiving coefficients of the AUT. $e^{im\phi}$, $e^{i\mu'\chi}$ and $d^{n}_{\mu' m}(\theta)$ are the rotation coefficients. $C^{sn(3)}_{\sigma'\mu'\nu'}(kA)$ is the translation coefficient.

C. Model of the Measurement System

The scattering matrices equation for the AUT and the probe will each be of the form (2). In order to obtain the amplitude of the modes of the scattered fields and not just the outgoing fields, the contribution due to the incident fields must by subtracted from these scattering matrices of the probe and AUT. Hence, these become

$$\begin{bmatrix} w^{AUT} \\ \bar{\mathbf{b}}^{AUT}_{\sigma\mu\nu} - \bar{\mathbf{a}}^{AUT}_{\sigma'\mu'\nu'} \end{bmatrix} = \begin{bmatrix} \Gamma^{AUT} & \bar{\mathbf{R}}^{AUT}_{\sigma'\mu'\nu'} \\ \bar{\mathbf{T}}^{AUT}_{\sigma\mu\nu} & (\bar{\bar{\mathbf{S}}}^{AUT}_{\substack{\sigma\mu\nu \\ \sigma'\mu'\nu'}} - \bar{\bar{\mathbf{I}}}^{AUT}) \end{bmatrix} \cdot \begin{bmatrix} v^{AUT} \\ \bar{\mathbf{a}}^{AUT}_{\sigma'\mu'\nu'} \end{bmatrix} \quad (5)$$

and

$$\begin{bmatrix} w^{PRB} \\ \bar{\mathbf{b}}^{PRB}_{smn} - \bar{\mathbf{a}}^{PRB}_{s'm'n'} \end{bmatrix} = \begin{bmatrix} \Gamma^{PRB} & \bar{\mathbf{R}}^{PRB}_{s'm'n'} \\ \bar{\mathbf{T}}^{PRB}_{smn} & (\bar{\bar{\mathbf{S}}}^{PRB}_{\substack{smn \\ s'm'n'}} - \bar{\bar{\mathbf{I}}}^{PRB}) \end{bmatrix} \cdot \begin{bmatrix} v^{PRB} \\ \bar{\mathbf{a}}^{PRB}_{s'm'n'} \end{bmatrix}, \quad (6)$$

where $\bar{\bar{\mathbf{I}}}^{PRB}$ and $\bar{\bar{\mathbf{I}}}^{AUT}$ denote unit matrices of appropriate sizes.

The measurement setup is modeled by the cascade of three coupled multiple-port networks which represent the probe, the free space propagation, and the AUT, respectively, as illustrated in Fig. 3. There are incoming and outgoing spherical waves for the probe as well as the AUT. The complex amplitude of the incoming spherical waves in the AUT coordinate system can be related to the complex amplitude of the outgoing spherical waves in the probe coordinate as follows,

$$a^{AUT}_{\sigma'\mu'\nu'} = \sum_{smn} g^{smn}_{\sigma'\mu'\nu'}(A,\phi,\theta,\chi) b^{PRB}_{smn} \quad (7)$$

where the $g^{smn}_{\sigma'\mu'\nu'}$ are the combined rotation and translation coefficients

$$g^{smn}_{\sigma'\mu'\nu'} = \frac{1}{2} e^{im\phi} e^{i\mu'\chi} d^{n}_{\mu' m}(\theta) C^{sn(3)}_{\sigma'\mu'\nu'}(kA) \quad (8)$$

Similarly, the amplitude of the incoming spherical waves for the probe can be related to the amplitude of outgoing spherical waves for the AUT,

$$a^{PRB}_{s'm'n'} = \sum_{\sigma\mu\nu} g^{\sigma\mu\nu}_{s'm'n'}(-A,-\phi,-\theta,-\chi) b^{AUT}_{\sigma\mu\nu}, \quad (9)$$

where $g^{\sigma\mu\nu}_{s'm'n'}(-A,-\phi,-\theta,-\chi)$ are applied for transforming from outgoing waves in the AUT coordinate system to the incoming waves in the probe coordinate system. By application of the equations (A 2.7), (A 3.15), (3.21) and (3.22) in [9], we obtain the following expression

$$g^{\sigma\mu\nu}_{s'm'n'}(-A,-\phi,-\theta,-\chi) = (-1)^{m'+\mu} g^{s',-m',n'}_{\sigma,-\mu,\nu}(A,\phi,\theta,\chi). \quad (10)$$

The scattering matrix modeling the free space propagation can be determined from (7) and (9), that is

$$\begin{bmatrix} \bar{\mathbf{a}}^{PRB}_{s'm'n'} \\ \bar{\mathbf{a}}^{AUT}_{\sigma'\mu'\nu'} \end{bmatrix} = \begin{bmatrix} 0 & \bar{\bar{\mathbf{G}}}^{-} \\ \bar{\bar{\mathbf{G}}}^{+} & 0 \end{bmatrix} \cdot \begin{bmatrix} \bar{\mathbf{b}}^{PRB}_{smn} \\ \bar{\mathbf{b}}^{AUT}_{\sigma\mu\nu} \end{bmatrix}, \quad (11)$$

where the elements of the matrix $\bar{\bar{\mathbf{G}}}^{+}$ and $\bar{\bar{\mathbf{G}}}^{-}$ are $g^{smn}_{\sigma'\mu'\nu'}$ (8) and $g^{\sigma\mu\nu}_{s'm'n'}$ (10), respectively.

The equations (5) - (11) give the network model of the AUT, probe, and the free space propagation. The overall measurement system also can be modeled as a two-port network $[\bar{\bar{\mathbf{S}}}^{T}]$ with the scattering matrix given by

$$\begin{bmatrix} w^{PRB} \\ w^{AUT} \end{bmatrix} = \begin{bmatrix} S^{T}_{11} & S^{T}_{12} \\ S^{T}_{21} & S^{T}_{22} \end{bmatrix} \cdot \begin{bmatrix} v^{PRB} \\ v^{AUT} \end{bmatrix}. \quad (12)$$

where S^{T}_{11}, S^{T}_{12} , S^{T}_{21} , and S^{T}_{22} can be obtained by eliminating the parameters $\bar{\mathbf{b}}^{PRB}_{smn}$, $\bar{\mathbf{a}}^{PRB}_{s'm'n'}$, $\bar{\mathbf{b}}^{AUT}_{\sigma\mu\nu}$, and $\bar{\mathbf{a}}^{AUT}_{\sigma'\mu'\nu'}$ from the equations (5) - (11) as follows. S^{T}_{11} and S^{T}_{21} are obtained by setting $v^{AUT} = 0$ and solving for w^{PRB}/v^{PRB}

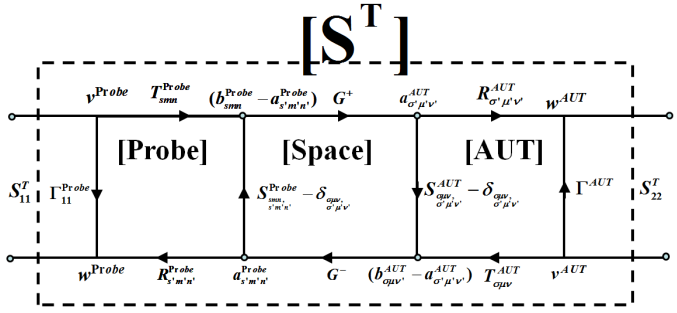

Fig. 3. Scattering matrix for the measurement system, including the probe, free space propagation factor and AUT.

and w^{AUT}/v^{PRB}, respectively. Similarly, S_{12}^T and S_{22}^T are obtained by setting $v^{PRB}=0$ and solving for w^{PRB}/v^{AUT} and w^{AUT}/v^{AUT}, respectively. Thus, the S-parameters S_{11}^T, S_{12}^T , S_{21}^T , and S_{22}^T are found to be

$$\begin{aligned} S_{11}^T &= \Gamma^{PRB}+\bar{\mathbf{R}}^{PRB}[\bar{\bar{\mathbf{I}}}^{PRB}-\bar{\bar{\mathbf{G}}}^{-}(\bar{\bar{\mathbf{S}}}^{AUT}-\bar{\bar{\mathbf{I}}}^{AUT}) \\ &\quad \cdot\bar{\bar{\mathbf{G}}}^{+}(\bar{\bar{\mathbf{S}}}^{PRB}-\bar{\bar{\mathbf{I}}}^{PRB})]^{-1}\bar{\bar{\mathbf{G}}}^{-}(\bar{\bar{\mathbf{S}}}^{AUT}-\bar{\bar{\mathbf{I}}}^{AUT}) \\ &\quad \cdot\bar{\bar{\mathbf{G}}}^{+}\bar{\mathbf{T}}^{PRB} \end{aligned} \tag{13}$$

$$\begin{aligned} S_{12}^T &= \bar{\mathbf{R}}^{PRB}[\bar{\bar{\mathbf{I}}}^{PRB}-\bar{\bar{\mathbf{G}}}^{-}(\bar{\bar{\mathbf{S}}}^{AUT}-\bar{\bar{\mathbf{I}}}^{AUT})\bar{\bar{\mathbf{G}}}^{+} \\ &\quad \cdot(\bar{\bar{\mathbf{S}}}^{PRB}-\bar{\bar{\mathbf{I}}}^{PRB})]^{-1}\bar{\bar{\mathbf{G}}}^{-}\bar{\mathbf{T}}^{AUT}, \end{aligned} \tag{14}$$

$$\begin{aligned} S_{21}^T &= \bar{\mathbf{R}}^{AUT}[\bar{\bar{\mathbf{I}}}^{AUT}-\bar{\bar{\mathbf{G}}}^{+}(\bar{\bar{\mathbf{S}}}^{PRB}-\bar{\bar{\mathbf{I}}}^{PRB})\bar{\bar{\mathbf{G}}}^{-} \\ &\quad \cdot(\bar{\bar{\mathbf{S}}}^{AUT}-\bar{\bar{\mathbf{I}}}^{AUT})]^{-1}\bar{\bar{\mathbf{G}}}^{+}\bar{\mathbf{T}}^{PRB}, \end{aligned} \tag{15}$$

$$\begin{aligned} S_{22}^T &= \Gamma^{AUT}+\bar{\mathbf{R}}^{AUT}[\bar{\bar{\mathbf{I}}}^{AUT}-\bar{\bar{\mathbf{G}}}^{+}(\bar{\bar{\mathbf{S}}}^{PRB}-\bar{\bar{\mathbf{I}}}^{PRB}) \\ &\quad \cdot\bar{\bar{\mathbf{G}}}^{-}(\mathbf{S}^{AUT}-\mathbf{I}^{AUT})]^{-1}\bar{\bar{\mathbf{G}}}^{+}(\bar{\bar{\mathbf{S}}}^{PRB}-\bar{\bar{\mathbf{I}}}^{PRB}) \\ &\quad \cdot\bar{\bar{\mathbf{G}}}^{-}\bar{\mathbf{T}}^{AUT}. \end{aligned} \tag{16}$$

The indices for each antenna are left out for simplicity. The 2 inverse matrices appearing in equations (13) to (16) represent the multiple reflections between the probe and AUT, and they can be expressed in power series. Thus,

$$\begin{aligned} &[\bar{\bar{\mathbf{I}}}^{AUT}-\bar{\bar{\mathbf{G}}}^{+}(\bar{\bar{\mathbf{S}}}^{PRB}-\bar{\bar{\mathbf{I}}}^{PRB})\bar{\bar{\mathbf{G}}}^{-}(\bar{\bar{\mathbf{S}}}^{AUT}-\bar{\bar{\mathbf{I}}}^{AUT})]^{-1} \\ &=\bar{\bar{\mathbf{I}}}^{AUT}+[\bar{\bar{\mathbf{G}}}^{+}(\bar{\bar{\mathbf{S}}}^{PRB}-\bar{\bar{\mathbf{I}}}^{PRB})\bar{\bar{\mathbf{G}}}^{-}(\bar{\bar{\mathbf{S}}}^{AUT}-\bar{\bar{\mathbf{I}}}^{AUT})]+ \\ &[\bar{\bar{\mathbf{G}}}^{+}(\bar{\bar{\mathbf{S}}}^{PRB}-\bar{\bar{\mathbf{I}}}^{PRB})\bar{\bar{\mathbf{G}}}^{-}(\bar{\bar{\mathbf{S}}}^{AUT}-\bar{\bar{\mathbf{I}}}^{AUT})]^2+... \end{aligned} \tag{17}$$

The first term on the right side of the equation (17) represents the direct field, the second term represents a field scattered once by the AUT then the probe, and so on. Similarly,

$$\begin{aligned} &[\bar{\bar{\mathbf{I}}}^{PRB}-\bar{\bar{\mathbf{G}}}^{-}(\bar{\bar{\mathbf{S}}}^{AUT}-\bar{\bar{\mathbf{I}}}^{AUT})\bar{\bar{\mathbf{G}}}^{+}(\bar{\bar{\mathbf{S}}}^{PRB}-\bar{\bar{\mathbf{I}}}^{PRB})]^{-1} \\ &=\bar{\bar{\mathbf{I}}}^{PRB}+[\bar{\bar{\mathbf{G}}}^{-}(\bar{\bar{\mathbf{S}}}^{AUT}-\bar{\bar{\mathbf{I}}}^{AUT})\bar{\bar{\mathbf{G}}}^{+}(\bar{\bar{\mathbf{S}}}^{PRB}-\bar{\bar{\mathbf{I}}}^{PRB})]+ \\ &[\bar{\bar{\mathbf{G}}}^{-}(\bar{\bar{\mathbf{S}}}^{AUT}-\bar{\bar{\mathbf{I}}}^{AUT})\bar{\bar{\mathbf{G}}}^{+}(\bar{\bar{\mathbf{S}}}^{PRB}-\bar{\bar{\mathbf{I}}}^{PRB})]^2+... \end{aligned} \tag{18}$$

By keeping only the first two terms on the right-hand side of equations (17) and (18), equations (13) to (16) become

$$\begin{aligned} S_{11}^T &\simeq \Gamma^{PRB}+\bar{\mathbf{R}}^{PRB}\bar{\bar{\mathbf{G}}}^{-}(\bar{\bar{\mathbf{S}}}^{AUT}-\bar{\bar{\mathbf{I}}}^{AUT})\bar{\bar{\mathbf{G}}}^{+}\bar{\mathbf{T}}^{PRB} \\ &\quad +\bar{\mathbf{R}}^{PRB}\bar{\bar{\mathbf{G}}}^{-}(\bar{\bar{\mathbf{S}}}^{AUT}-\bar{\bar{\mathbf{I}}}^{AUT})\bar{\bar{\mathbf{G}}}^{+}(\bar{\bar{\mathbf{S}}}^{PRB}-\bar{\bar{\mathbf{I}}}^{PRB}) \\ &\quad \cdot\bar{\bar{\mathbf{G}}}^{-}(\bar{\bar{\mathbf{S}}}^{AUT}-\bar{\bar{\mathbf{I}}}^{AUT})\bar{\bar{\mathbf{G}}}^{+}\bar{\mathbf{T}}^{PRB} \end{aligned} \tag{19}$$

$$\begin{aligned} S_{12}^T &\simeq \bar{\mathbf{R}}^{PRB}\bar{\bar{\mathbf{G}}}^{-}\bar{\mathbf{T}}^{AUT}+\bar{\mathbf{R}}^{PRB}\bar{\bar{\mathbf{G}}}^{-}(\bar{\bar{\mathbf{S}}}^{AUT}-\bar{\bar{\mathbf{I}}}^{AUT}) \\ &\quad \cdot\bar{\bar{\mathbf{G}}}^{+}(\bar{\bar{\mathbf{S}}}^{PRB}-\bar{\bar{\mathbf{I}}}^{PRB})\bar{\bar{\mathbf{G}}}^{-}\bar{\mathbf{T}}^{AUT} \end{aligned} \tag{20}$$

$$\begin{aligned} S_{21}^T &\simeq \bar{\mathbf{R}}^{AUT}\bar{\bar{\mathbf{G}}}^{+}\bar{\mathbf{T}}^{PRB}+\bar{\mathbf{R}}^{AUT}\bar{\bar{\mathbf{G}}}^{+}(\bar{\bar{\mathbf{S}}}^{PRB}-\bar{\bar{\mathbf{I}}}^{PRB}) \\ &\quad \cdot\bar{\bar{\mathbf{G}}}^{-}(\bar{\bar{\mathbf{S}}}^{AUT}-\bar{\bar{\mathbf{I}}}^{AUT})\bar{\bar{\mathbf{G}}}^{+}\bar{\mathbf{T}}^{PRB} \end{aligned} \tag{21}$$

$$\begin{aligned} S_{22}^T &\simeq \Gamma^{AUT}+\bar{\mathbf{R}}^{AUT}\bar{\bar{\mathbf{G}}}^{-}(\bar{\bar{\mathbf{S}}}^{PRB}-\bar{\bar{\mathbf{I}}}^{PRB})\bar{\bar{\mathbf{G}}}^{+}\bar{\mathbf{T}}^{AUT} \\ &\quad +\bar{\mathbf{R}}^{AUT}\bar{\bar{\mathbf{G}}}^{+}(\bar{\bar{\mathbf{S}}}^{PRB}-\bar{\bar{\mathbf{I}}}^{PRB})\bar{\bar{\mathbf{G}}}^{-}(\bar{\bar{\mathbf{S}}}^{AUT}-\bar{\bar{\mathbf{I}}}^{AUT}) \\ &\quad \bar{\bar{\mathbf{G}}}^{+}(\bar{\bar{\mathbf{S}}}^{PRB}-\bar{\bar{\mathbf{I}}}^{PRB})\bar{\bar{\mathbf{G}}}^{-}\bar{\mathbf{T}}^{AUT} \end{aligned} \tag{22}$$

It is seen that in the equation (19) and (22), the effects of the scattered fields on S_{11}^T and S_{22}^T are through the second-order propagation ($\propto|\bar{\bar{\mathbf{G}}}^{+}\bar{\bar{\mathbf{G}}}^{-}|$) and the fourth-order propagation ($\propto|\bar{\bar{\mathbf{G}}}^{+}\bar{\bar{\mathbf{G}}}^{-}\bar{\bar{\mathbf{G}}}^{+}\bar{\bar{\mathbf{G}}}^{-}|$). While in the equation (20) and (21), it is seen the effects of the scattered fields on S_{12}^T and S_{21}^T are through the third-order propagation($\propto|\bar{\bar{\mathbf{G}}}^{+}\bar{\bar{\mathbf{G}}}^{-}\bar{\bar{\mathbf{G}}}^{+}|$).

For increasing electrical distance between the probe and AUT the multiple scattered term decreases because of the spatial attenuation of the free space propagation along the forward and backward directions. A minimum scattering probe will reduce the multiple scattered terms even further. We assume this term to be negligibly small and hence, the equations (13) to (16) are further simplified to

$$\begin{aligned} S_{11}^T &\simeq \Gamma^{PRB}+\bar{\mathbf{R}}^{PRB}\bar{\bar{\mathbf{G}}}^{-}(\bar{\bar{\mathbf{S}}}^{AUT}-\bar{\bar{\mathbf{I}}}^{AUT}) \\ &\quad \cdot\bar{\bar{\mathbf{G}}}^{+}\bar{\mathbf{T}}^{PRB} \end{aligned} \tag{23}$$

$$S_{12}^T \simeq \bar{\mathbf{R}}^{PRB}\bar{\bar{\mathbf{G}}}^{-}\bar{\mathbf{T}}^{AUT} \tag{24}$$

$$S_{21}^T \simeq \bar{\mathbf{R}}^{AUT}\bar{\bar{\mathbf{G}}}^{+}\bar{\mathbf{T}}^{PRB} \tag{25}$$

$$\begin{aligned} S_{22}^T &\simeq \Gamma^{AUT}+\bar{\mathbf{R}}^{AUT}\bar{\bar{\mathbf{G}}}^{+}(\bar{\bar{\mathbf{S}}}^{PRB}-\bar{\bar{\mathbf{I}}}^{PRB}) \\ &\quad \cdot\bar{\bar{\mathbf{G}}}^{-}\bar{\mathbf{T}}^{AUT} \end{aligned} \tag{26}$$

Now we start to analyze the effect of the second term on the right side of the equation (26), and its influence on the measured gain and impedance of the AUT. It will be shown in the next sub-section that the measurement is performed by measuring the reflection coefficient at the input terminal of the probe, denoted by $S_{11}^{T'}$, when the AUT is loaded with three known loads. Equation (30) shows this relation between $S_{11}^{T'}$ and the two-port scattering parameters. By using the power series expansion of the term $1/(1-S_{22}^T\Gamma_L)$ in (30), and inserting the expressions of the S_{11}^T, S_{22}^T, and $S_{12}^TS_{21}^T$ from the equations (23) to (26), (30) becomes

$$\begin{aligned} S_{11}^{T'} &\simeq \Gamma^{PRB}+\bar{\mathbf{R}}^{PRB}\bar{\bar{\mathbf{G}}}^{-}(\bar{\bar{\mathbf{S}}}^{AUT}-\bar{\bar{\mathbf{I}}}^{AUT})\bar{\bar{\mathbf{G}}}^{+}\bar{\mathbf{T}}^{PRB}+ \\ &\quad [\bar{\mathbf{R}}^{PRB}\bar{\bar{\mathbf{G}}}^{-}\bar{\mathbf{T}}^{AUT}][\bar{\mathbf{R}}^{AUT}\bar{\bar{\mathbf{G}}}^{+}\bar{\mathbf{T}}^{PRB}][\Gamma_L+\Gamma_L^2\cdot \\ &\quad \Gamma^{AUT}+\Gamma_L^2\bar{\mathbf{R}}^{AUT}\bar{\bar{\mathbf{G}}}^{+}(\bar{\bar{\mathbf{S}}}^{PRB}-\bar{\bar{\mathbf{I}}}^{PRB})\bar{\bar{\mathbf{G}}}^{-}\bar{\mathbf{T}}^{AUT}] \\ &\quad +o(\frac{1}{(ka)^4}). \end{aligned} \tag{27}$$

On the right-hand side of (27), the first term represents the reflection coefficient of the probe, the second term represents the scattered fields from the AUT, and the third term includes the effects of the modulated loads, the reflection coefficient of AUT, and scattered fields due to the probe. Thus, these show

that the second term on the right-hand side of the equation (26) only contributes to the measurement through the fourth-order propagation terms. In fact, the fourth-order propagation terms can be assumed negligibly small compared to the second-order propagation term due to the spatial attenuation of the free space propagation. It can be summarized that the second term on the right-hand side of (26) represents the influence of the structural scattering from the probe on the S_{22}^T of the AUT. This term can be assumed negligibly small compared to the first term for two reasons. First, it is because a minimum scattering probe is employed, and, second, it is because the strong spatial attenuation in $\bar{\bar{\mathbf{G}}}^+$ as well as $\bar{\bar{\mathbf{G}}}^-$, which are approximated to be negligible compared to Γ^{AUT}. Thus, (26) is approximated by

$$S_{22}^T \simeq \Gamma^{AUT}. \tag{28}$$

Furthermore, in the case there is the limited dynamic range for the backscattering measurement for small antennas, the measurement at a finite distance in the near-field region may become necessary. In this case, the formula (28) can still be applied by choosing a probe antenna with minimum structural scattering, as well as the equations (24) and (25). However, in equation (23) the second term on the right-hand side of it represents the scattering due to the AUT. It is not possible to assume that the structural scattering of the AUT, $(\bar{\bar{\mathbf{S}}}^{\mathbf{AUT}} - \bar{\bar{\mathbf{I}}}^{\mathbf{AUT}})$, is small for an arbitrary AUT since the structural scattering is unknown.

In summary, equations (13) to (16) give the general expressions of the matrix element of $[\bar{\bar{\mathbf{S}}}^T]$ for arbitrary probe and AUT, and it is valid for any distance between the probe and AUT. $[\bar{\bar{\mathbf{S}}}^T]$ can be obtained from the measurement. The equations (23) to (26) give the expressions of the matrix element of $[\bar{\bar{\mathbf{S}}}^T]$ when the multiple scattered terms are negligibly small, but in these expressions the lowest order interaction of the scattered field is still taken into account. The equation (28) is valid because first the structural scattering of the probe is small and second the scattered fields of the probe only contribute to the measurement through the high order propagation terms. The conditions for using above formulas are summarized as follows. First, under conditions that the probe and AUT are separated by an electrically large distance, the scattered fields of the probe caused by the structural scattering and multiple reflections are negligibly small. The formula (24), (25), and (28) are applicable. Second, for the measurement at a small distance, the formula (24), (25), and (28) can still be used by choosing a suitable probe with minimum structural scattering.

D. Determination of the Total Scattering Matrix $[\bar{\bar{\mathbf{S}}}^T]$

The measurement setup is described as follows. There are two antennas involved in this monostatic cable-free measurement setup as illustrated in Fig. 4, which are the transmitting and receiving probe and the AUT. Their scattering matrices are $[\bar{\bar{\mathbf{S}}}]^{PRB}$ and $[\bar{\bar{\mathbf{S}}}]^{AUT}$, respectively. For the total measurement setup, a two-port scattering matrix $[\bar{\bar{\mathbf{S}}}^T]$ can be established for reference planes at the input terminal of the probe and AUT. The total scattering matrix $[\bar{\bar{\mathbf{S}}}^T]$ is expressed as

$$[\bar{\bar{\mathbf{S}}}^T] = \begin{bmatrix} S_{11}^T & S_{12}^T \\ S_{21}^T & S_{22}^T \end{bmatrix}. \tag{29}$$

When the AUT is loaded, the measured reflection coefficient at the input terminal of the probe is denoted by $S_{11}^{T'}$, which is related to the two-port scattering parameter $[\bar{\bar{\mathbf{S}}}^T]$ as

$$S_{11}^{T'} = S_{11}^T + \frac{S_{12}^T S_{21}^T \Gamma_L}{1 - S_{22}^T \Gamma_L} \tag{30}$$

where Γ_L is the reflection coefficient of the load of the AUT.

In the measurement setup that is illustrated in Fig. 4, the AUT is loaded in turn by a short-circuit, an open circuit, and a known load, and the reflection coefficient of the transmitting probe is measured. Then the scattering parameters S_{11}^T, S_{22}^T, and $S_{12}^T S_{21}^T$ of the total scattering matrix can be extracted. S_{11}^T and S_{22}^T are determined from

$$\begin{bmatrix} S_{11}^T \\ S_{22}^T \end{bmatrix} = \begin{bmatrix} (\frac{1}{\Gamma_L^{(1)}} - \frac{1}{\Gamma_L^{(2)}}) & (S_{11}^{T',(1)} - S_{11}^{T',(2)}) \\ (\frac{1}{\Gamma_L^{(1)}} - \frac{1}{\Gamma_L^{(3)}}) & (S_{11}^{T',(1)} - S_{11}^{T',(3)}) \end{bmatrix}^{-1} \cdot \begin{bmatrix} \frac{S_{11}^{T',(1)}}{\Gamma_L^{(1)}} - \frac{S_{11}^{T',(2)}}{\Gamma_L^{(2)}} \\ \frac{S_{11}^{T',(1)}}{\Gamma_L^{(1)}} - \frac{S_{11}^{T',(3)}}{\Gamma_L^{(3)}} \end{bmatrix} \tag{31}$$

where $\Gamma_L^{(1),(2),(3)}$ are the measured reflection coefficient of each load, and $S_{11}^{T',(1),(2),(3)}$ are the measured reflection coefficients of the probe when the AUT is loaded in three cases. $S_{12}^T S_{21}^T$ can be extracted after S_{11}^T and S_{22}^T are determined, that is

$$S_{12}^T S_{21}^T = (S_{11}^{T',(i)} - S_{11}^T)(1 - S_{22}^T \Gamma_L^{(i)})/\Gamma_L^{(i)}, \tag{32}$$

where i=1,2,3. It is noted that there are three sets of data

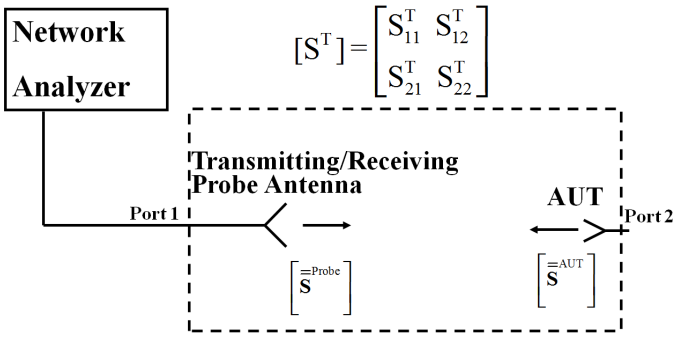

Fig. 4. Setup of the monostatic measurement for the impedance and gain of electrically small antennas.

available to be used in this equation, which are obtained from the three measurements. Taking an average of the results from different sets results in an improvement of the accuracy. The next task is to determine the impedance and gain of the AUT by formulating the relations between these parameters and $[\bar{\bar{\mathbf{S}}}^T]$, which is described in the next section.

III. Antenna Impedance and Gain Determination without the Structural Scattering and Multiple Reflections

In this section, the probe structural scattering and multiple reflections are assumed to be negligibly small, as shown in the equations (24), (25) and (28). The impedance of the AUT will be determined first, and then the determination of the AUT gain is presented.

A. Antenna Impedance Determination

First, S_{22}^T is determined from (31) and, second, Γ_{AUT} is determined from (28). Third, the AUT input impedance Z_{in}^{AUT} can be obtained from

$$Z_{in}^{AUT} = \frac{1+\Gamma^{AUT}}{1-\Gamma^{AUT}} Z_0, \tag{33}$$

where Z_0 is the reference impedance.

B. Determination of the Antenna Gain

Both the probe and AUT are treated as general reciprocal antennas with all the high order spherical modes considered. The only assumption here is that the probe is linearly polarized along $\hat{x}$, while the polarization of AUT is arbitrary. In this derivation, we define the coordinate system (x, y, z) with respect to the probe, and the primed coordinate (x', y', z') system with respect to the AUT so that $\hat{x'} = \hat{x}$, $\hat{y'} = \hat{y}$ and $\hat{z'} = \hat{z}$. Thus, (χ, θ, ϕ) =$(0, 0, 0)$ and

$$e^{im\phi} = 0; e^{i\mu\chi} = 0; d^n_{\mu m}(0) = \delta_{\mu m}. \tag{34}$$

The transmission formula (3) then becomes

$$w^{AUT}(A,0,0,0) = \frac{v^{PRB}}{2} \sum_{smn} \sum_{\sigma m\nu} T^{PRB}_{smn} C^{sn(3)}_{\sigma m\nu}(kA) R^{AUT}_{\sigma m\nu}. \tag{35}$$

For electrically large distances, $kA \gg 1$, the translation coefficient $C^{sn(3)}_{\sigma\mu\nu}(kA)$ becomes ([9], Appendix A3)

$$C^{sn(3)}_{\sigma\mu\nu}(kA) = o(\frac{1}{kA}), \text{ for } \mu \neq \pm 1, \tag{36}$$

$$C^{sn(3)}_{\sigma,\pm1,\nu}(kA) = \frac{\sqrt{(2n+1)(2\nu+1)}}{2} i^{\nu-n-1}(\pm1)^{s+\sigma} \cdot \frac{e^{ikA}}{kA} + o(\frac{1}{kA}), \tag{37}$$

Thus, the modes with $\mu \neq \pm 1$ decay much faster than the modes with $\mu = \pm 1$. It can be approximated that a non-zero translation coefficient $C^{sn(3)}_{\sigma\mu\nu}(kA)$ only exist for the mode $\mu = \pm 1$.

The transmission formula (35) is then

$$w^{AUT}(A,0,0,0) = \frac{v^{PRB}}{2} \frac{e^{ikA}}{kA} \sum_{n\nu} \frac{\sqrt{(2n+1)(2\nu+1)}}{2} i^{\nu-n-1} \cdot (T^P_{2,1,n} + T^{PRB}_{1,1,n})(R^{AUT}_{2,1,\nu} + R^{AUT}_{1,1,\nu} + R^{AUT}_{1,-1,\nu} - R^{AUT}_{2,-1,\nu}) \tag{38}$$

where the relations $R^{PRB}_{2,1,\nu} = -R^{PRB}_{2,-1,\nu}$ and $R^{PRB}_{1,1,\nu} = R^{PRB}_{1,-1,\nu}$ for an x-polarized probe have been used.

The far-field pattern function $\vec{K}_{smn}(\theta,\phi)$ is defined as [9]

$$\vec{K}_{smn}(\theta,\phi) = \lim_{kr\to\infty} [\sqrt{4\pi} \frac{kr}{e^{ikr}} \vec{F}^{(3)}_{smn}(r,\theta,\phi)]. \tag{39}$$

Once the transmission formula is determined, the relations between the transmission formula and the gain of the probe and AUT are established. The far field pattern $\vec{K}^{PRB}(0,\phi)$ in the probe coordinate system in the direction of AUT can be given by

$$\vec{K}^{PRB}(\theta=0,\phi) = \sum_{\substack{smn= \\ s,\pm1,n}} T^{PRB}_{smn} \vec{K}_{smn}(0,\phi) \tag{40}$$

$$= -\sum_n (-i)^n \sqrt{2n+1} [T^{PRB}_{2,1,n} + T^{PRB}_{1,1,n}] \hat{x}$$

The far field pattern of the AUT in the direction of the probe can be determined from

$$\vec{K}^{AUT}(\theta'=\pi,\phi') = \sum_{\substack{\sigma\mu\nu= \\ s,\pm1,\nu}} T^{AUT}_{\sigma\mu\nu} \vec{K}_{\sigma\mu\nu}(\theta'=0,\phi') \tag{41}$$

$$= \sum_\nu i^\nu \frac{\sqrt{2\nu+1}}{2} [R^{AUT}_{1,-1,\nu} + R^{AUT}_{1,1,\nu} + R^{AUT}_{2,1,\nu} - R^{AUT}_{2,-1,\nu}] \hat{x}$$

$$-i^{\nu+1} \frac{\sqrt{2\nu+1}}{2} [R^{AUT}_{1,1,\nu} - R^{AUT}_{1,-1,\nu} + R^{AUT}_{2,-1,\nu} + R^{AUT}_{2,1,\nu}] \hat{y},$$

where the transmission coefficient $T^{AUT}_{\sigma\mu\nu}$ is transformed to the receiving coefficient $R^{AUT}_{\sigma\mu\nu}$ by using the reciprocity relation

$$T^{AUT}_{\sigma,-\mu,\nu} = (-1)^\mu R^{AUT}_{\sigma\mu\nu}. \tag{42}$$

Hence, the transmission formula (38) can be rewritten in terms of $\vec{K}^{PRB}$ and $\vec{K}^{AUT}$ as

$$w^{AUT}(A,0,0,0) = \frac{v^{PRB}}{2} \frac{ie^{ikA}}{kA} \{\vec{K}^{PRB}(\theta=0,\phi)\cdot\hat{x}\} \cdot \{\vec{K}^{AUT}(\theta'=\pi,\phi')\cdot\hat{x}\}, \tag{43}$$

and introducing the gain of the probe, G^{PRB}, and the partial gain of the AUT along $\hat{x}$ direction, G^{AUT}_x, which are

$$G^{PRB} = \frac{1}{1-|\Gamma^{PRB}|^2} |\vec{K}^{PRB}(\theta=0,\phi)\cdot\hat{x}|^2 \tag{44}$$

$$G^{AUT}_x = \frac{1}{1-|\Gamma^{AUT}|^2} |\vec{K}^{AUT}(\theta'=\pi,\phi')\cdot\hat{x}|^2, \tag{45}$$

Combining (43) to (45) gives

$$\frac{|w^{AUT}|^2}{|v^{PRB}|^2} = (1-|\Gamma^{PRB}|^2)(1-|\Gamma^{AUT}|^2) \frac{G^{PRB} G^{AUT}_x}{4(kA)^2}. \tag{46}$$

On the other hand, we have

$$|S^T_{12}|^2 = \frac{|w^{AUT}|^2}{|v^{PRB}|^2} \tag{47}$$

Hence, the gain product of the probe and AUT becomes

$$G^{PRB} G^{AUT}_x = \frac{4(kA)^2 |S^T_{12}|^2}{(1-|\Gamma^{PRB}|^2)(1-|\Gamma^{AUT}|^2)}. \tag{48}$$

Since the characteristics of the probe, G^{PRB} and S_{11}^{PRB}, are assumed known to us from a separate probe calibration, G_x^{AUT} can be extracted.

The equation (48) is the key relation that is used in this cable-free gain measurement technique. In order to determine the total gain for the AUT, two gain measurements are required for two orthogonal orientations of the probe.

In summary, the steps for the determination of the AUT gain can be as follows.

- First, three measurements of the reflection coefficients of the probe are performed, when the AUT is loaded in turn by a short, open, and a known impedance.
- Second, the reflection coefficients of the loads connected to the AUT are measured, which are the short, open, and impedance.
- Third, the parameters $|S_{11}^T|$, $|S_{22}^T|$, and $|S_{12}^T|^2$ can be extracted from the equations (31) and (32). Then the partial gain along $\hat{x}$, G_x^{AUT}, is determined using (48).
- Fourth, since $|S_{11}^T|$ and $|S_{22}^T|$ have been determined from the previous step, only one more measurement is enough to determine another partial gain in the orthogonal direction that is G_y^{AUT}. The reflection coefficients of the probe is measured when the AUT is loaded by any one of the short, the open, and the known impedance.
- Fifth, the total gain of the AUT is determined by adding G_x^{AUT} and G_y^{AUT}. Hence, four measurements are required in total to determine the total AUT gain in one direction.

IV. Simulation Results and Discussions

Two simulation examples of the proposed cable-free measurement technique are presented in this section, which are obtained by the commercial software package Ansoft HFSS [11]. A half-wavelength dipole and an electrically small loop antenna are used as the AUT, respectively. In both of these two simulations, the probe is modeled by a half-wavelength dipole. It is noted that the multiple scattering between the probe and AUT is included in the numerical simulations.

A. Half-Wavelength Dipole

Two identical half-wavelength dipoles are simulated as the probe and AUT, respectively. The length of the half-wavelength dipole is 152 mm and the diameter is 2 mm, which is designed to be resonant around 910 MHz. The material of the dipole is copper. The procedures of this simulation are given as follows. First, the half-wavelength dipole itself (AUT) is simulated in free space by using a lumped-port excitation and no feeding cable is present in the simulation. From this step, the input impedance and gain of the AUT are obtained directly and represent the reference results, which will be compared to the extracted impedance and gain by the proposed cable-free technique. Second, the measurement setup for the proposed cable-free measurement method is simulated, as shown in Fig. 5. The separation between the two dipoles is 2 wavelengths at 910 MHz. The probe is excited by using the lumped-port excitation, and the input reflection coefficient of the probe is recorded, when the AUT is loaded in turn by an open, short, and 50 ohm impedance, respectively. Third, in order to investigate the noise influence in a real measurement environment, a random noise at -60 dB level is added to the measured reflection coefficient of the probe $S_{11}^{T'}$, which is denoted by $S_{11,noise}^{T'}$ and is given by

$$S_{11,noise}^{T'} = S_{11}^{T'} + \{max_{1,2,3}|S_{11}^{T'}|\} \cdot 10^{NL_{dB}/20} \alpha e^{j\beta}, \quad (49)$$

where NL_{dB} is the noise level, α is a random real-valued number between 0 and 1, and β is a random real-valued number between 0 and 2π. It is noted that a new set of random noise is created for every simulated measurement.

Then the antenna reflection coefficient, input impedance and gain product of two half-wavelength dipoles can be extracted from the three simulation sets of $S_{11}^{T'}$, by solving equations (28), (31), (32) and (48). Since two identical antennas are used, the gain for each half-wavelength dipole is determined by taking the square root of (48). It is noted that a smoothing function is then used on the extracted antenna reflection coefficient, impedance, and gain to remove the random noise influence, which uses a sliding average over samples within a rectangular window. Fig. 6 compares the reference and

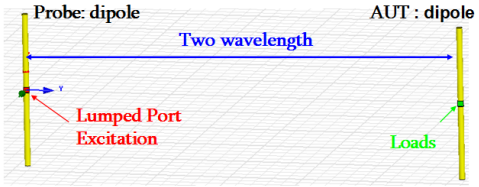

Fig. 5. The configuration of the measurement setup used in HFSS simulation, for the cable-free impedance and gain extraction.

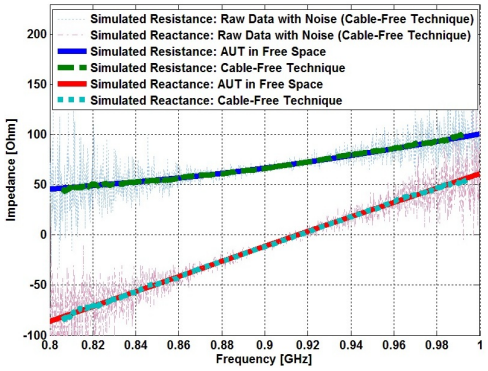

Fig. 6. Comparison of the dipole impedance versus frequency by using the cable-free technique (with and without smoothing) and by using the direct simulation in free space.

extracted antenna input impedances versus frequency. A good agreement can be observed. Fig. 7 presents the reference and extracted antenna gain versus frequency. The deviation in the gain is less than 0.05 dB. This example shows that the proposed cable-free technique works well in a real measurement environment with the noise accounted for. The accurate input

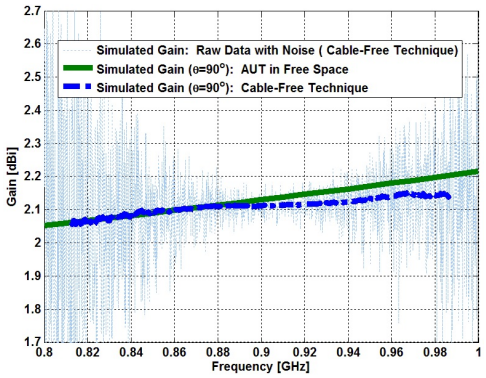

Fig. 7. Comparison of the dipole gain (at $\theta = 90^o$) versus Frequency by using the cable-free technique (with and without smoothing) and by using the direct simulation in free space.

impedance and gain can be obtained. It is noted that the dynamic range of a modern VNA can well exceed 60 dB which is the value used in the above simulations, and the values larger than 100 dB can also be easily obtained.

B. Electrically Small Loop Antenna

The simulation results of the proposed cable-free measurement technique is presented for an electrically small loop antenna, illustrated in Fig. 8, that is resonant at 910 MHz. It is a self-resonant balanced electrically small loop antenna using a distributed capacitive loading element [12]. The working mechanism is based on the capacitive loading and inductive coupling between the two small loops. It is printed on the Rogers 5870 substrate with a thickness of 1.5 mm. The dielectric constant of the substrate is 2.33 and the loss tangent is 0.0012. The overall dimensions of the antenna are 35 x 10 mm^2, and the electrical size of the loop is $ka = 0.33$, where k is the wave number and a is the radius of the minimum sphere enclosing the antenna. The configuration of the measurement

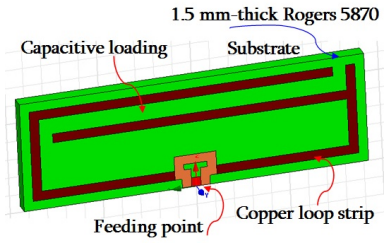

Fig. 8. The AUT: an electrically small loop antenna designed at 910 MHz (not scaled).

setup used in the HFSS simulation is presented in Fig. 9. Again, the half-wavelength dipole is used as the probe and the small loop antenna is modeled as the AUT. The simulation procedures and the noise model are similar to the previous example.

Fig. 10 presents the comparison of the reference and extracted antenna input impedances versus frequency. The reference and extracted antenna gains versus frequency is

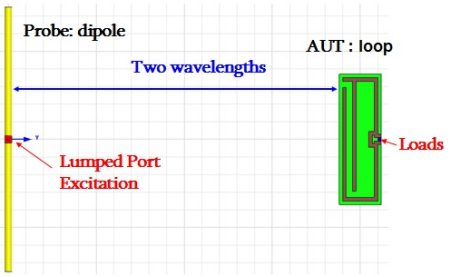

Fig. 9. The configuration of the measurement setup used in HFSS simulation, for the cable-free impedance and gain extraction (not scaled).

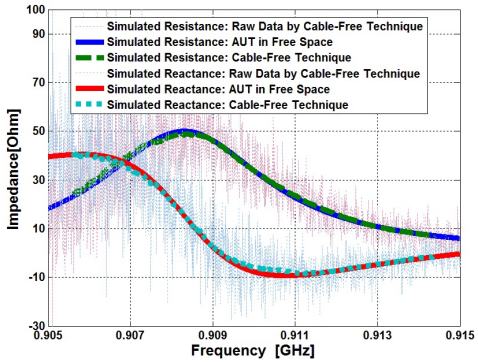

Fig. 10. Comparison of the loop impedance versus frequency by using the cable-free technique (with and without smoothing) and by using the direct simulation in free space.

presented in Fig. 11. The deviation in the loop gain is less than 0.05 dB.

V. Measurement Results and Discussions

The measurement results by the proposed method are presented in this section. In order to verify the proposed method, an electrically small loop antenna that is resonant around 910 MHz is tested as the AUT, and a commercial available standard gain horn antenna is used as the probe for this measurement, as illustrated in shown in Fig. 12. In this measurement, the frequency range is selected to be 900 MHz - 925 MHz. The

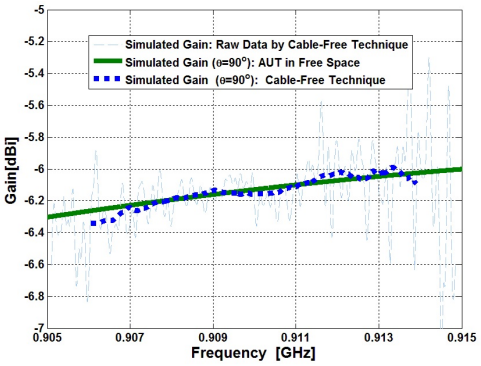

Fig. 11. Comparison of the loop gain (at $\theta = 90^o$) versus frequency by using the cable-free technique (with and without smoothing) and by using the direct simulation in free space.

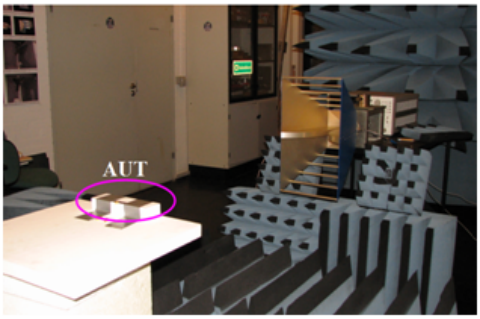

Fig. 12. The setup of the cable-free measurement technique, for the probe and the small loop antenna.

Fig. 13. The ultra small connectors and loads for the electrically small loop antenna.

following settings in the VNA are performed to ensure a sufficient dynamic range and accuracy. The number of points used in this frequency range is selected be to 201 points. The power level is set to the maximum value of the VNA that is +10 dBm. A narrow IF bandwidth is desired which is set to 30 Hz in this measurement. As shown in Fig. 12, the measurement is performed in a partial anechoic environment. The absorbers are placed on the ground floor and around the ESA, but not on the ceiling and walls. Different from the normal size antennas such as horn antennas, the ultra small connectors and loads are desired for electrically small antennas. The dimensions of the connectors and loads are required to be much smaller than that of the antennas to avoid the extra scattering effects. Several ultra small connectors and loads which are used in

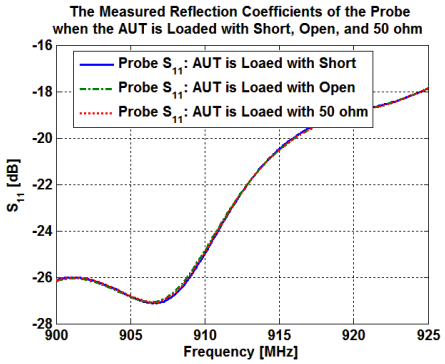

Fig. 14. The measured reflection coefficient of the probe, when the AUT is connected to a short, open, and 50 ohm load, respectively.

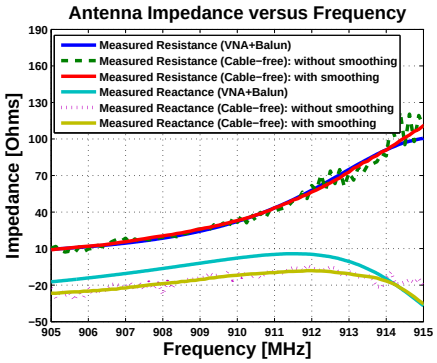

Fig. 15. Comparison of the measured antenna input impedances versus frequency.

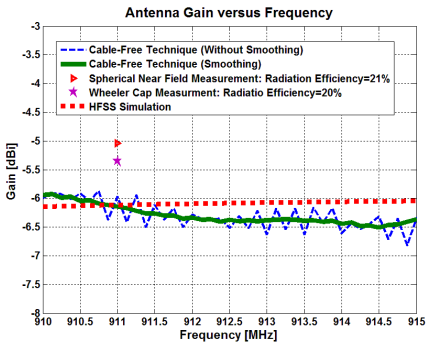

Fig. 16. Comparison of the measured antenna gain versus frequency by different techniques.

the measurements are illustrated in Fig. 13. The measured reflection coefficients of the probe are shown in Fig. 14, when the AUT is connected to a short, open, and 50 ohm load, respectively. It is noted that although the differences among these three curves are very small, the properties of the AUT can still be extracted as presented below. In this measurement, the distance between the probe and the AUT is 5.1 wavelengths at 900 MHz.

The measured impedance for the small loop antenna is shown in Fig. 15. A comparison of the results obtained from the cable-free measurement, with and without smoothing, and the direct VNA measurement are presented. In the direct VNA measurement, a balun is used in front of the loop antenna to avoid the leaking current on the cable. From Fig. 15 it is seen that the frequency variation of the extracted impedance is in good agreement with the reference impedance, but while the level of the extracted resistance agrees well with the reference resistance there is a maximum offset of 15 Ω for the reactance. The measured gain of the small loop antenna by using the proposed cable-free technique, the spherical nearfield facility, and the Wheeler cap technique are presented in Fig. 16, together with the simulated gain predicting by HFSS. Comparisons of the measured antenna gain for the small loop at the resonance frequency by different techniques show that the maximum deviation is 1.05 dB. It is noted that the spherical near-field measurement as well as the Wheeler

cap measurement are carried out with a feeding cable and a balun connected to the AUT, and thus these measurement results may be influenced by the scattering effects of the cable and balun. The HFSS simulation accounts for both the finite conductivity and dielectric losses. On the other hand, the cable-free measurement may be influenced by the structural scattering of the support structure and environment, since it is only partial anechoic. These may be the reasons for the observed differences in gain.

VI. Conclusion

In this paper, an electromagnetic model of a cable-free impedance and gain measurement technique for ESAs is proposed by using the SWE technique, which is valid for an arbitrary AUT at arbitrary distances between the probe and AUT. The probe and AUT are modeled by the SWE and the measurement setup is modeled by the cascade of three coupled multiple-port networks of the SWE. The structural scattering and the multiple reflections between the probe and AUT are included in the model. Disregarding the negligible high-order multiple reflections as the measurement distance becomes electrically large, a simplified model is established that serve as the basis for the practical technique.

Two simulation examples of the proposed measurement technique for a half wavelength dipole and an electrically small loop antenna are presented. The noise in the measurement environments is also taken into account in the simulations. The simulated antenna impedance and gain by using the cable-free technique compares well to the simulation results obtained from a direct HFSS simulation in free space. These results show that the proposed measurement technique works well for the ESA measurements. Moreover, the experimental measurement results for an electrically small loop antenna are also obtained and compared to results from other experimental techniques and from simulations. The comparison of the antenna measurement techniques, with and without the feeding cable, show that there is the scattering effects from the cable in both the reflection coefficient measurement and gain measurement. The leaking current and the scattering effects due to the feeding cable constitutes a significant challenge for ESA measurements. The cable-free measurement technique proposed and implemented here overcome these challenges. Future work will be focused on the cable-free measurement at a near field distance between the probe and AUT.

References

[1] J. Zhang, S. Pivnenko, A.Khatun, T.Laitinen, and J.Carlsson, "Characterization of Small Antennas for Hearing Aids by Several Measurement Technique," *4th European Conference on Antennas and Propagation, EuCAP*, 2010.

[2] R. J. Garbacz, "Determination of antenna parameters by scattering cross section measurements," *Proc. Inst. Elect. Eng.*, vol. 111, no. 10, pp. 1679-1686, Oct. 1964.

[3] J. Appel-Hansen, "Accurate determination of gain and radiation patterns by radar crosssection measurements," *IEEE Trans. Antennas Propagat.*, vol. AP-27, pp. 640-645, Sept. 1979.

[4] W. Wiesbeck and E. Heidrich, "Wide-band multiport antenna characteriztion by polarimetric RCS measurement," *IEEE Trans. AnreMos Propogat.*, vol. AP-46. pp. 341-350, March 1998.

[5] Hsin-Chia Lu and Tah-Hsiung Chu, "Antenna Gain and Scattering Measurement Using Reflective Three-Antenna Method," *Antennas and Propagation Society International Symposium*, 1999.

[6] B. Monsalve, S. Blanch, J.Romeu, and L. Jofre, "A contact-less small antenna characterization through impedance modulation," *3rd European Conference on Antennas and Propagation, EuCAP 2009*, pp. 696-698, 2009.

[7] M. H. Capstick, J. O. Jekkonen, A. C. Marvin, I. D. Flintoft, L. Dawson, "A Novel Indirect Method to Determine the Radiation Impedance of a Handheld Antenna Structure" *IEEE Trans. Instrum. Meas.*, vol. 58, iss. 3, pp. 578-585, March 2009.

[8] J. Zhang, S. Pivnenko, and O. Breinbjerg, "A Cable-Free Impedance and Gain Measurement Technique for Electrically Small Antennas," *Proceedings of the 32nd Annual Symposium of Antenna Measurement Techniques Association , AMTA2010*, Atlanta, US, Oct. 2010.

[9] Hansen J. E., "Spherical Near-Field Antenna Measurements", *Peter Peregrinus Ltd. London*, 1988.

[10] Koivisto, P., "Analytical solution for characteristic modal power distribution and truncation limit for spherical wave expansion of antenna radiation pattern" *Journal of electromagnetic waves and applications* , vol. 16, iss. 9, pp. 1307-1328, 2002.

[11] http://www.ansoft.com/.

[12] J. Zhang and O. Breinbjerg, "Self-Resonant Electrically Small Loop Antennas for Hearing-Aids Application," *Proceedings of the Fourth European Conference on Antennas and Propagation (EuCAP 2010)*, Barcelona, Spain, April 2010.

Paper II

Self-Resonant Electrically Small Loop Antennas for Hearing-Aids Application

Jiaying Zhang and Olav Breinbjerg

Proceedings of the Fourth European Conference on Antennas and Propagation (EuCAP 2010)

Presented in Barcelona, Spain, April 2010.

Self-Resonant Electrically Small Loop Antennas for Hearing-Aids Application

Jiaying Zhang* and Olav Breinbjerg*
*Department of Electrical Engineering, Electromagnetic Systems, Technical University of Denmark
Ørsted Plads, Building 348, DK-2800 Kgs. Lyngby, Denmark
jz@elektro.dtu.dk, ob@elektro.dtu.dk

***Abstract*—Two novel self-resonant electrically small antennas are proposed in this paper, which are designed for hearing-aids applications. They are miniaturized by using the capacitive and inductive coupling mechanism between two loops, and the antenna impedance can be matched to a specific value without using any additional matching network and lumped components. The dimension of the proposed antenna is $0.10\lambda_0 \times 0.03\lambda_0$, and it is designed to be resonant at 900 MHz. Both the analytical model and numerical simulations are discussed and explained. The antenna is also fabricated and measured in an anechoic chamber. The measurement methods for electrically small antennas are reported.**

I. Introduction

Hearing-aids already constitute an advanced technology, and wireless communication integrated in hearing-aids will open for a range of completely new functionalities. For this application, there are several requirements that should be satisfied as follows. First, since the power that can be provided by hearing-aids battery is in the μW range, low frequency would be preferred, and thus in this paper the antenna is designed at 900 MHz. Second, the communication distance from hearing-aids to external devices is set to 10 meters and the according link budget must be fulfilled. Third, the demand for compact systems with stringent specifications makes the antenna size reduction a significant challenge. Therefore antenna miniaturization should be one of the key technologies in designing successful wireless hearing-aids. Hence, the above requirements lead us to the area of compact antenna designs for ultra low power and short range wireless communications. This paper aims at designing the miniaturized antennas for hearing-aids application at 900 MHz, by designing the self-resonant small loop antennas, in which the antennas are not only geometrically small but also electrically small.

Electrically small loop antennas are popularly used in short range wireless communications. However, the small loop antenna itself is inefficient and badly matched, and additional matching network is required to make the antenna resonant, in which lumped components may be included. The tolerance and aging of lumped components can result in the change of antenna properties. Recently, a metamaterial-inspired small loop antenna was proposed in [1], where a small loop is covered by a simple mu-negative (MNG) shell.

In this paper, a differential-fed self-resonant electrically small loop antenna is proposed and developed, and the geometry and design variables of this antenna are illustrated in Fig. 1. The working mechanism is based on the coupling between two loops. In this antenna, there are two loops, the small one and the large one, which are connected together and shown in Fig. 1 in different colors. The large loop is effectively closed by the capacitive loading formed by two closely spaced wires. The small loop is covered by the large loop and is excited by a differential feed. The antenna impedance is matched to 50 ohm without any additional matching network and lumped components. The analytical model will be explained in Section. II.

Moreover, if the dimension of two loops are comparable as illustrated in Fig. 2, the antenna represents a single split ring component. The same analytical model can still be applied by considering the capacitive coupling together with the inductive coupling between loops, and thus by proper tuning an ultra small split ring itself can behave as a small resonant antenna, the radiation efficiency of which can be improved.

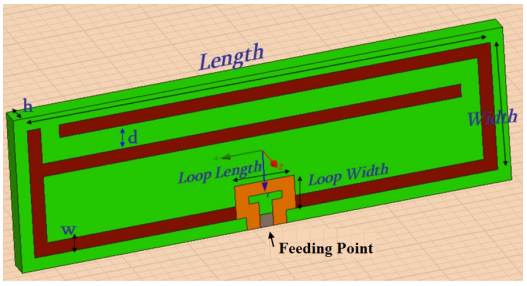

Fig. 1. Geometry of design variables of the self-resonant electrically small loop antenna. (Antenna design 1 for 900 MHz, the dimension is $35mm \times 10mm \times 1.5mm$)

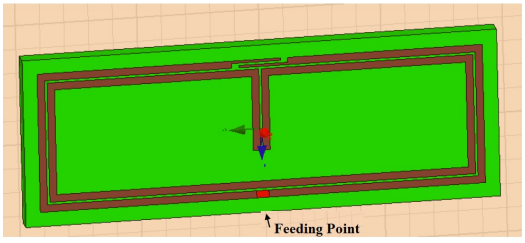

Fig. 2. Geometry of design variables of the self-resonant electrically small split ring antenna. (Antenna design 2 for 900 MHz, the dimension is $36.6mm \times 11.6mm \times 1.5mm$)

II. Antenna Design and Analysis

The antenna working mechanism and the physical model will be explained in this section. For antenna design 1 which is presented in Fig. 1, the antenna system is fed on the small loop. The large loop is coupled to the small loop by the magnetic flux linkage, and the magnetic flux due to the large loop can be approximated by the flux due to two infinitely long wires that carry currents with equal amplitudes and opposite directions. The antenna impedance can be matched to a specific value without using any additional matching network and lumped components by tuning the antenna as follows. First, the imaginary part of the antenna impedance can be tuned to zero since the inductance is compensated by the capacitance involved in the large loop. Second, the real part of the antenna impedance, resistance, can be matched to 50 ohm by tuning the dimension of the small loop.

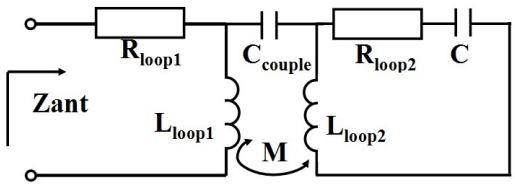

Fig. 3. Analytical Model of Self-Resonant Electrically Small Loop Antenna.

The two loops contained in the antenna can be located on the same layer or opposite layers depending on the specific designs. On the same layer, the small loop can also be placed inside and outside of the large loop, as shown in Fig. 4-5. The mutual inductance is quite different in these two cases, which plays an import role in impedance matching, and the analytical formulas will be derived to illustrate the design rules. Additionally, the antenna shape also has its influence. The hearing-aids application requires the shape of the large loop to be rectangular. While for the small loop, the influence of the shape on impedance matching will be analyzed in the following subsections, which are the rectangular and circular shape respectively .

The analytical model used to explain the working mechanism is illustrated in Fig. 3, and the details of the antenna configuration are presented in Fig. 4-5. The dimension of small loop is L_1 and W_1, and those of the large loop are L_2 and W_2. The smallest distance between the two loops is d. The antenna system is fed on the small loop. R_{loop1} and L_{loop1} are the resistance and inductance of the small loop, and R_{loop2} and L_{loop2} are the resistance and inductance of the large loop respectively. R_{loop2} can be further expressed to be the sum of antenna radiation resistance R_{rad} and ohmic loss resistance R_{loss}, that is $R_{loop2} = R_{rad} + R_{loss}$. C is the capacitive loading existing in the large loop. C_{couple} and M are the mutual capacitance and mutual inductance between two loops. C_{couple} can be influenced by the relative size of two loops. For the antenna design shown in Fig.1, the size of small loop is much less than the large loop, and therefore C_{couple} can be approximated to be negligibly small and only the mutual inductance M contributes to the working mechanism. While for the antenna design 2, illustrated in Fig. 2, the size of the small loop is comparable to the large loop, and both the mutual capacitance C_{couple} and mutual inductance M must be taken into account.

In the circuit model illustrated in Fig. 3, the resistance and reactance of the antenna input impedance Z_{ant} of the antenna can be determined from

$$R_{ant} = R_{loop1} + (\omega M)^2 \frac{R_{loop2}}{R_{loop2}^2 + (\omega L_{loop2} - \frac{1}{\omega C})^2} \quad (1)$$

$$X_{ant} = j\omega L_{loop1} - j\frac{(\omega M)^2(\omega L_{loop2} - \frac{1}{\omega C})}{R_{loop2}^2 + (\omega L_{loop2} - \frac{1}{\omega C})^2}. \quad (2)$$

Near the resonance condition where $\omega L_{loop2} = \frac{1}{\omega C}$, the resistance and reactance becomes

$$R_{ant} = R_{loop1} + (\omega M)^2 \frac{1}{R_{loop2}} \quad (3)$$

$$X_{ant} = j\omega L_{loop1} \simeq 0 \quad (4)$$

A. Mutual Inductance and Antenna Resistance when the Small Loop is Rectangular

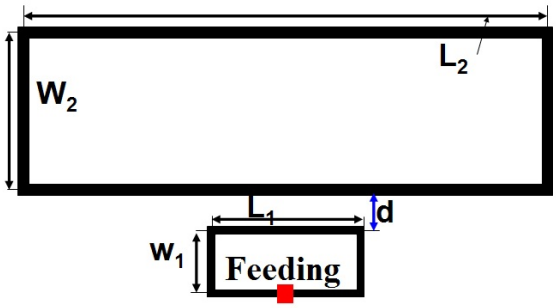

Fig. 4. Rectangular Small Loop Feeding (Small Loop is Outside).

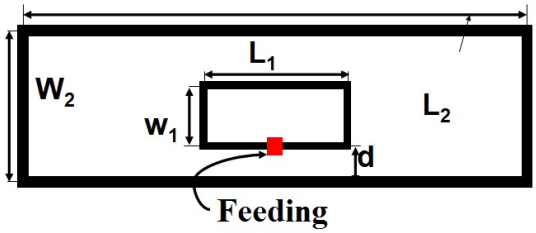

Fig. 5. Rectangular Small Loop Feeding (Small Loop is Inside).

The small rectangular loop can be placed inside or outside the large loop. For the case where the small loop is located outside the large one, as shown in Fig. 4, the magnetic flux due to the big loop is approximated by that due to two infinitely long wires that carry currents with equal amplitudes and opposite directions. Hence the magnetic flux due to two infinitely long wires are opposite, and the mutual inductance M can be determined from

$$M = \frac{\mu_0}{2\pi} L_1 ln \frac{(W_2+d)(W_1+d)}{d(W_1+W_2+d)}, \quad (5)$$

and the antenna input resistance R_{ant} at resonance is

$$R_{ant} = \frac{1}{R_{loop2}} \{2\pi f \frac{\mu_0}{2\pi} L_1 ln \frac{(W_1+d)(W_2+d)}{d(W_1+W_2+d)}\}^2 \quad (6)$$

When the small loop is placed inside the large one, as shown in Fig. 5, again the magnetic flux due to the big loop can be approximated by that due to two infinitely long wires that carry currents with equal amplitudes and opposite directions. But the small loop is in between these two wires, the magnetic flux contributions from two infinitely long wires are the same, and thus the mutual inductance is much stronger than that when the small loop is placed outside. The mutual inductance can be determined from

$$M = \frac{\mu_0}{2\pi} L_1 ln \frac{(W_1+d)(W_2-d)}{d(W_2-W_1-d)}, \quad (7)$$

and the antenna input resistance at resonance is

$$R_{ant} = \frac{1}{R_{loop2}} \{2\pi f \frac{\mu_0}{2\pi} L_1 ln \frac{(W_1+d)(W_2-d)}{d(W_2-W_1-d)}\}^2 \quad (8)$$

B. Mutual Inductance and Antenna Resistance when the Small Loop is Circular

As shown in Fig. 6-7, the small circular loop can be placed inside and outside the large loop. The dimension of the large loop are L_2 and W_2, and the small loop radius is r. The distance between the two loops is d. Again the magnetic flux due to the big loop can be approximated by that due to two infinitely long wires that carry currents with equal amplitudes and opposite directions. When the small loop is outside the large one, the mutual inductance can be determined from

$$M = \mu_0[\sqrt{(W_2+d+2r)(W_2+d)} - \sqrt{(d+2r)d} - W_2] \quad (9)$$

and the antenna input resistance at resonance is

$$R_{ant} = \frac{1}{R_{loop2}} \{2\pi f \mu_0[\sqrt{(W_2+d+2r)(W_2+d)} - \sqrt{(d+2r)d} - W_2]\}^2 \quad (10)$$

When the small loop is inside the large one, the mutual inductance can be determined from

$$M = \mu_0\{W_2 - \sqrt{(d+2r)d} - \sqrt{(W_2-d)(W_2-2r-d)}\}. \quad (11)$$

and the antenna input resistance at resonance is

$$R_{ant} = \frac{1}{R_{loop2}} \{2\pi f \mu_0[W_2 - \sqrt{(d+2r)d} - \quad (12)$$

$$\sqrt{(W_2-d)(W_2-2r-d)}]\}^2 \quad (13)$$

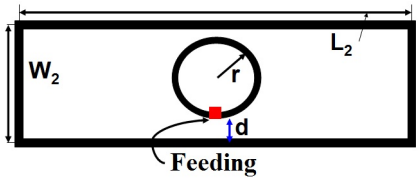

Fig. 6. Circular Small Loop Feeding (Small Loop is Inside).

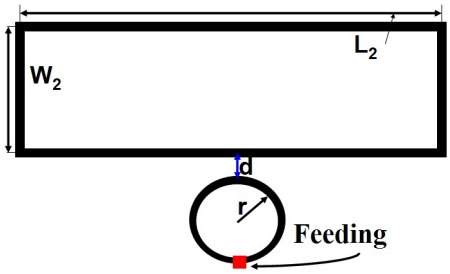

Fig. 7. Circular Small Loop Feeding (Small Loop is Outside).

C. Model Extension to Self-Resonant Split Ring Antennas

The split ring antenna has been recently used in antenna miniaturizations, in which it behaves as the ultra electrically small antenna. However, it has to be excited by an extra small dipole or loop element that contributes to the loss mechanism. In this paper, it was shown by applying this model and tuning properly, a split ring itself can behave as the small resonant antenna, as shown in Fig. 8-9. Therefore the radiation efficiency can be improved.

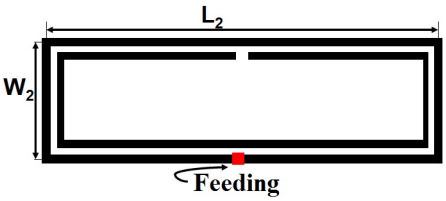

Fig. 8. Self Resonant Split Ring Antenna.

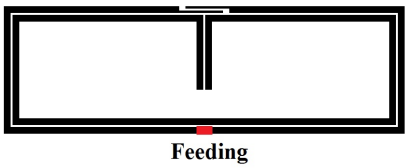

Fig. 9. Self Resonant Split Ring Antenna at 900 MHz.

In our previous analysis, the capacitance between two loops is viewed to be negligibly small, and only the magnetic coupling is considered. While for this self resonance split ring antenna design, both the capacitive and magnetic coupling should be taken into account in the antenna tuning. A design example will be shown in Section. III.

TABLE I
DIMENSION OF SELF RESONANT ELECTRICALLY SMALL ANTENNA DESIGNS (FREQUENCY: AROUND 900MHZ).

	Antenna Dimension	Resonance Frequency	Bandwidth @-10 dB	Bandwidth @-15 dB	Efficiency %	Directivity [dBi]	Gain [dBi]
Design1 Electrically Small Loop Antenna	$Length = 35mm = 0.105\lambda_0$ $Width = 10mm = 0.03\lambda_0$ $LoopLength = 4.5mm, LoopWidth = 1.5mm$ $W = 1mm, d = 1.8mm$ Substrate: Rogers 5870 (thickness=1.5mm)	906 MHz	3.3 MHz	1.75 MHz	17%	1.74 dBi	-5.9
Design2 Electrically Small Split Ring Antenna	$L_{loop2} = 36.6mm = 0.109\lambda_0$ $W_{loop2} = 11.6mm = 0.03\lambda_0$ $d_1 = d_2 = d_3 = d_4 = d_5 = 0.2mm$ $L = 6.2mm, W = 0.6mm$ $L_1 = 4.6mm, L_2 = L_3 = 0.6mm$ Substrate: Rogers 6002 (thickness=1.5mm)	903.2 MHZ	4.5 MHz	2.5MHz	35 %	1.64 dBi	-2.89dBi

III. ANTENNA DESIGNS AND SIMULATIONS

Two electrically small antennas will be presented in this section, based on the designs of Fig. 1-2.

A. Self Resonant Electrically Small Loop Antenna 1

For our application, we are aiming at designing antennas around 900 MHz. The dimension of the big loop is fixed to be $35mm \times 10mm$ from which the resistance and inductance of the large loop can be determined first, which are R_{loop2} and L_{loop2}. Then by using equation (8) in the circuit model, the dimension of small loop can be calculated accordingly. Based on this starting point, the antenna is designed and simulated using the commercial software package HFSS [2]. The antenna dimensions are illustrated in Tab. I. The simulated resonance frequency is 906 MHz, and the bandwidth at -10 dB is 3.3 MHz. The radiation efficiency is found to be 17 %. The antenna reflection coefficient and antenna input impedance are given in Fig. 10-11.

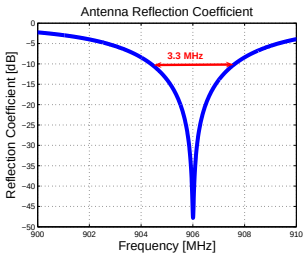

Fig. 10. Antenna Reflection Coefficient.

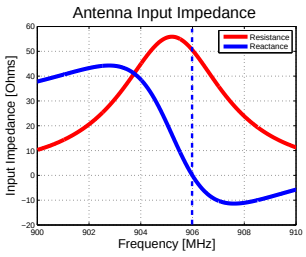

Fig. 11. Antenna Input Impedance.

B. Self Resonant Electrically Small Loop Antenna 2

The geometry and design variables of the self-resonant electrically small split ring antenna is illustrated in Fig. 12 and its dimension are given in Tab.1. The simulated resonance frequency is 903.2 MHz, and the bandwidth at -10 dB is 4.5 MHz. The radiation efficiency is found to be 35 %. The antenna reflection coefficient and antenna input impedance are given in Fig. 13-14.

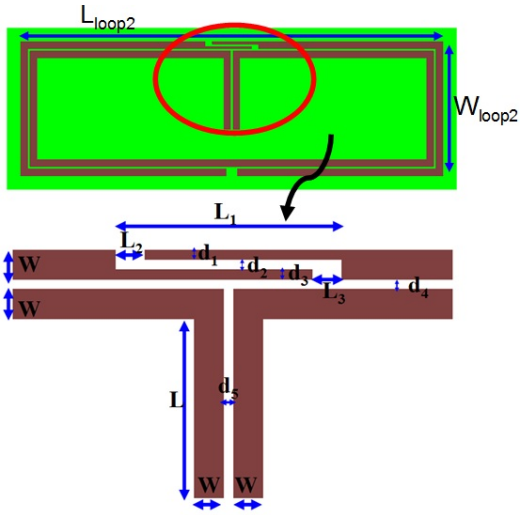

Fig. 12. Geometry of design variables of the self-resonant electrically small split ring antenna.

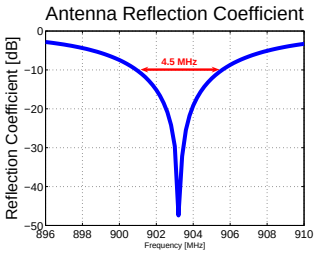

Fig. 13. Antenna Reflection Coefficient.

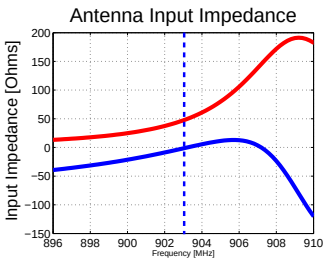

Fig. 14. Antenna Input Impedance.

IV. MEASUREMENT RESULTS

The small loop antenna from design 1 was fabricated on a piece of dielectric substrate, Rogers 5870, with the dielectric constant 2.33 and loss tangent 0.0012. The overall antenna dimension is $35mm \times 10mm \times 1.5mm$, and the electrical size of the antenna length is ka = 0.33, which is shown in Fig. 15.

The S_{11} parameter was measured first by using the network analyzer HP 8753 with an absorber placed in front of the antenna, and a tunable quarter-wave sleeve balun is added

to avoid the leak current along the cable. The sleeve balun used in our measurement is illustrated in Fig. 16, and since an ordinary balun is a narrow band device, a tunable balun is designed, which allows us to choose the optimal parameters for the balun. First, in order to suppress the leaking current efficiently, the diameter of the sleeve balun should be fairly large compared to that of the coaxial cable [3]. Based on HFSS simulation results, a diameter of 11 mm is chosen. Second, due to the fringing field effect, a gap is suggested between the antenna and the open end of balun. Moreover, a conductive glue is necessary to provide a perfect shorting wall. Then the simulated and measured S_{11} of this small loop antenna are compared in Fig. 17. While the simulated resonance frequency is 906 MHz, the measured resonance frequency is 911 MHz, and the deviation is 5 MHz, that is 0.6 %. The simulated and measured -10dB bandwidth are 3.3 MHz and 4.9 MHz respectively, and the difference is thus 1.6 MHz. The difference in resonance frequency is due to the sensitivity in the capacitance loading in the large loop as well as the fabrication accuracy.

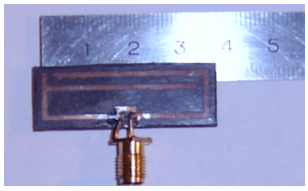

Fig. 15. The fabricated electrically small loop antenna, operated at 906 MHz

Fig. 16. Illustration of the sleeve balun and the conductive glue.

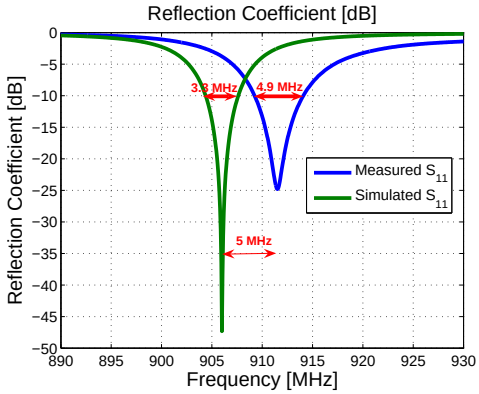

Fig. 17. The simulated and measured S11 values for electrically small loop antenna, which is designed to operate at 906 MHz.

The radiation efficiency measurement is of a great challenge. The small antenna is a balanced device, and using unbalanced coaxial feed line to feed antenna can results in the leak current along the cable, which gives significant change in radiation efficiency. For this measurement, the antenna is measured using two different methods, and in both of them the quarter-wave balun should be added. First, the antenna is measured by using the Wheeler's Cap method, and the radiation efficiency is found to be 21 %, which is reasonably

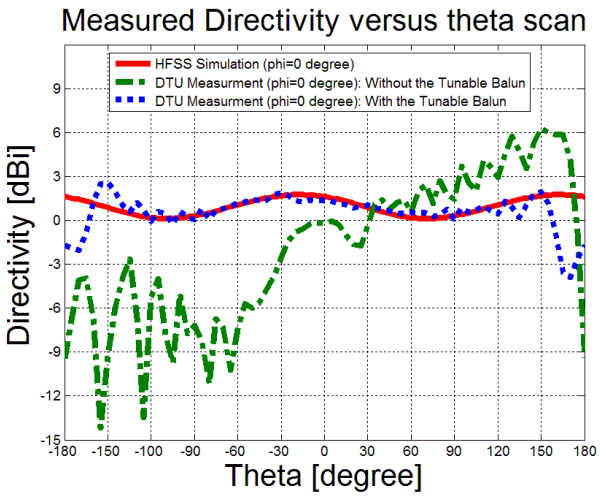

Fig. 18. The simulated and measured directivity versus theta for electrically small loop antenna, which is designed to operate at 906 MHz.

close to the simulated efficiency 17 %. The gain is acceptable for the antenna of such small dimension. The difference in efficiency can be explained that the loss in dielectric material may be not exactly the same as the value in simulations. Second, the antenna was also measured in the DTU-ESA Spherical Near Field Antenna Test Facility. The simulated and measured directivity versus theta scan are compared, and a good agreement can be found when the balun is used, as shown in Fig. 18. The efficiency of the antenna was measured by using the substitution method, and found to be 20 %, which agrees very well with the measured result in the Wheeler's cap.

V. Conclusions

In this paper, two differential-fed self-resonant electrically small loop antennas are proposed. They are miniaturized by using the coupling mechanism between two loops, without using additional matching circuit and lumped components. An analytical model is also proposed to explain the working mechanism and illustrate the design rules. Moreover, one of two antenna designs is simulated, fabricated, and measured. The dimension of this antenna is ka = 0.33, and the measured radiation efficiency is 21 %. The simulated and measured radiation pattern are also compared and presented, and a good agreement is found.

Acknowledgment

Dr. S. Pivnenko is acknowledged for doing the antenna measurement in Anechoic Chamber.

References

[1] Erentok, A. and R. W. Ziolkowski, "Metamaterial-inspired efficient electrically small antennas," *IEEE Trans. Antennas Propag.*, vol. 56, pp. 692-706, March 2008.

[2] http://www.ansoft.com/

[3] C. Icheln, M. Popov, P. Vainikainen, and S. He, "Optimal reduction Of the influence of RF feed cables in small antenna measurements," *Microw Opt. Technol. Lett.*, 2000, 25, (3), pp. 194-196.

Paper III

Characterization of Small Antennas for Hearing-Aids by Several Measurement Techniques

S. Pivnenko, J. Zhang, A. Khatun, T. Laitinen and J. Carlsson

Proceedings of the Fourth European Conference on Antennas and Propagation (EuCAP 2010)

Presented in Barcelona, Spain, April 2010.

Characterization of Small Antennas for Hearing Aids by Several Measurement Techniques

S. Pivnenko*, J. Zhang*, A. Khatun†, T. Laitinen†, and J. Carlsson‡
*Department of Electrical Engineering, Technical University of Denmark
Oersteds Plads, bldg. 348, DK-2800 Kgs. Lyngby, Denmark
jz@elektro.dtu.dk, sp@elektro.dtu.dk
†Aalto University School of Science and Technology, Department of Radio Science and Engineering, SMARAD
P. O. Box 13000, 00076 Aalto, Finland
‡Department of Signals and Systems, Chalmers University of Technology
Chalmersplatsen 1, Gothenburg, Sweden

***Abstract*—Characteristics of electrically small loop antennas were measured by different techniques and the results were compared in-between. The techniques employed were: a single-probe spherical near-field technique, a multi-probe spherical near-field technique, a reverberation chamber, and a Wheeler cap technique. The results were compared with regard to the measurement accuracy, measurement speed, and applicability for characterization of small antennas in complex application environment.**

I. Introduction

Within the project "Antenna miniaturization in complex environments" carried out at the Technical University of Denmark (DTU), several small antennas were developed for the purpose of wireless communication with hearing aids [1], [2]. Due to application constraints, the developed miniature antennas are geometrically very small, with typical dimensions of 1×1 cm^2 or 1×4 cm^2. At the operation frequency of 900 MHz or 400 MHz it implies that these antennas are also electrically very small, from 1/10 to 1/30 of a wavelength. It is also worth noting that in the case of small antennas the influence of the complex environment, e.g. hearing aid and a person's head, on the antenna performance is very significant.

Accurate experimental characterization of small antennas, either alone or in a complex environment, requires reviewing the existing measurement techniques for their applicability for the purpose. In some cases new measurement techniques should be developed and the need for these is justified by the following reasons. First, since the antennas are electrically small, the measurement results will strongly be influenced by the feed cable as well as the mechanical support equipment used during the measurement. Second, since the antennas will eventually operate in a complex environment, it is necessary that a model of the environment is also included in the measurements.

Through cooperation between three Nordic universities within the project "Efficient and accurate characterization techniques for small antennas" [3], the measurements of typical characteristics of different small antennas were carried out by various techniques. In this paper, the characteristics of electrically small loop antennas obtained by different measurement techniques are presented and compared with regard to the measurement speed, the accuracy of the obtained data and overall applicability for measurement of miniaturized antennas in a complex environment.

II. Antenna Under Test

A. Miniature Loop Antenna

The miniature, self-resonant, capacitively loaded loop antennas were designed to operate around 400 MHz and around 900 MHz [2]. The loop and the capacitor strips were printed on 1.5 mm thick Rogers 5870 substrate with ϵ = 2.33 and $\tan\delta = 0.0012$. The parameters of the capacitor and the feed part were optimized with the HFSS software. An example of the loop antenna for operation at 900 MHz is shown in Fig. 1.

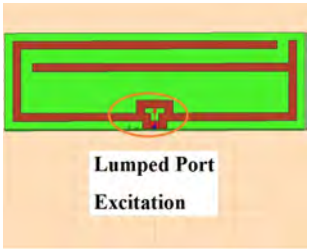

Fig. 1. Capacitively loaded printed loop antenna for hearing aids application.

B. Tunable Balun

It was discovered soon after obtaining first measurement results that simple feeding of this almost symmetric antenna with a bare coaxial cable produced clearly wrong results. For example, not only the measured radiation pattern was strongly asymmetric, but also the measured radiation efficiency was strongly overestimated, for some techniques by as much as 3 times, as it will be shown below. It was clear that due to asymmetric feeding the leak currents on the feed cable can be very strong and contribute significantly to the antenna radiation.

Therefore, it was decided to apply a standard solution to this problem that is use a sleeve balun. However, in order to have the flexibility of adjusting the balun characteristics, it was

decided to manufacture a tunable balun with the possibility to change and optimize its length and the gap between the open end of the balun and the antenna. The details of the used tunable balun are shown in Fig. 2.

Fig. 2. Details of the tunable balun for 900 MHz.

III. Measurement Techniques

A. Spherical Near-Field (SNF) Technique at DTU

The loop antenna radiation pattern and efficiency were measured by traditional spherical near-field technique at the DTU-ESA Spherical Near-Field Antenna Test Facility located at the Technical University of Denmark (DTU) [4]. The antenna under test (AUT) was rotated by a roll-over azimuth positioner and the full-sphere near-field signal was measured on a regular grid by a dual-polarized probe. The measured signal was then transformed to the far-field using the spherical wave expansion and properly correcting for the probe characteristics. The loop antenna attached to the antenna tower at the DTU-ESA Facility is shown in Fig. 3.

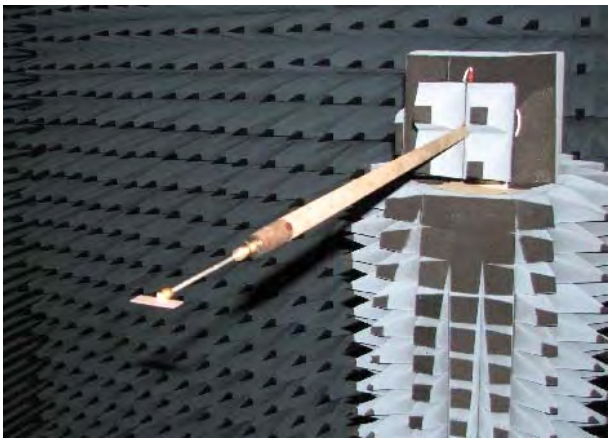

Fig. 3. The loop antenna attached to the antenna tower at the DTU-ESA Facility.

It should be noted that for electrically small antennas, having dimensions less then 0.5 wavelength, a series of simplifications of the spherical near-field technique can be made.

First, since the far field region starts already some 1-2 wavelengths away from the AUT, probe pattern correction can be omitted as the probe is typically located at a distance of several meters from the AUT, e.g. at 6 m distance at the DTU-ESA Facility. Also, probe polarization calibration can be omitted, if the probes are good linearly polarized, e.g. at the DTU-ESA Facility probes have typically better than 40 dB polarization axial ratio. The only probe calibration to be done is the probe channel balance measurement, which takes only some 2 min.

Second, precise mechanical alignment of the measurement setup, typically taking few hours, can be omitted, since in the case of far-field measurement of small antennas located close to the center of rotation small mechanical errors have truly negligible effect.

Third, the angular sampling intervals can be chosen rather large, up to 20° or 30°, without degrading the measurement uncertainty. This results in significant reduction of the scanning time, for example, at the DTU-ESA Facility typical scanning time for presented small antenna is about 15-20 min per configuration. It should also be noted that the measurement time can be further reduced to about 5-10 min, but with some degradation of the accuracy.

The only time consuming part is the total power calibration carried out as full-sphere measurement of a Standard Gain Horn with known radiation efficiency, which takes some 30-45 min. But since the thermal drift of the measurement system is very low, less than 0.1 dB in several days, one total power calibration can be used for many antenna measurements.

As a result, the measurement system can be prepared within 1 hour, including total power calibration, and then used for accurate measurement of small antennas with typical measurement time being some 20 min per antenna configuration.

B. Rapid Antenna Measurement System at Aalto University

The radiation pattern and efficiency of the loop antenna were measured at the Aalto University School of Science and Technology (AALTO) by a Rapid Antenna Measurement System (RAMS), which uses 32 electronically-switched dual-polarized probes located at the radius of 1 m on a spherical grid around AUT [5]. The far field was then also obtained through the spherical wave expansion, but avoiding the mechanical rotation allows reducing the measurement time to about 4 min per antenna configuration. The AUT radiation efficiency was determined by calibrating the measurement system with a reference dipole and then comparing the total radiated power for the AUT and for the dipole.

C. Reverberation Chamber at Chalmers

The impedance and efficiency of the loop antenna were measured in a BlueTest Reverberation Chamber at Chalmers University of Technology (CTH) [6]- [8]. The AUT radiation efficiency is determined by calibrating the measurement system with a reference discone antenna and then comparing the total radiated power for the AUT and for the discone antenna.

Typical measurement time in the BlueTest reverberation chamber is about 3-6 min per antenna configuration depending on the chosen measurement uncertainty. The loop antenna during the measurements in the reverberation chamber is shown in Fig. 4.

Fig. 4. The loop antenna during measurement in the reverberation chamber.

D. Wheeler Cap at DTU

The impedance and efficiency of the antennas were also measured with the Wheeler cap method at DTU. The cylindrical Wheeler cap with inner diameter of 26 cm and the length of 35 cm was manufactured for measurements of small antennas down to 400 MHz. The AUT radiation efficiency is measured according to the generalized Wheeler cap method [9], which allows effectively avoiding cavity resonances. The setup for Wheeler cap measurements at DTU is shown in Fig. 5.

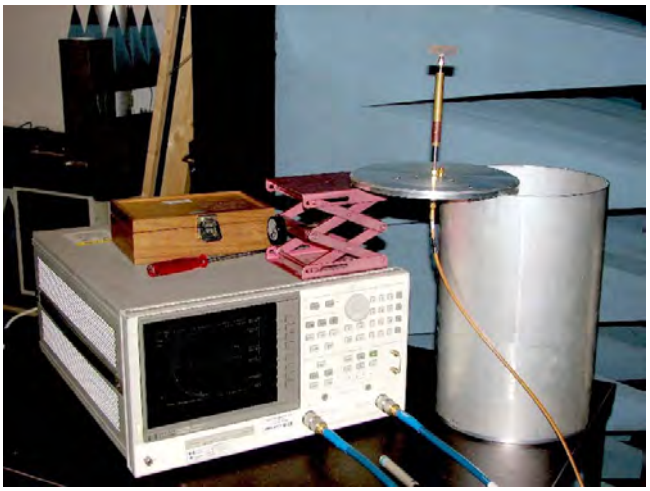

Fig. 5. The Wheeler cap measurement setup at DTU.

IV. Measurement Results

A. Application of the Tunable Balun

The measured radiation pattern of the loop antenna with and without the sleeve balun is shown in Figs. 6-7 together with the simulated pattern from HFSS. It is clearly seen that improper feeding leads to a significant distortion of the radiation pattern, especially in the E-plane, where the error is $+4/-9$ dB. On the other hand, application of the properly tuned balun provides very good results with very small deviations up to angle $\theta = 140°$, after which the tower shadow gives pattern deviation within a couple of dB. The tower shadow effect is minimized by using a 1 m long dielectric tube as the mechanical support interface, as seen in Fig. 3.

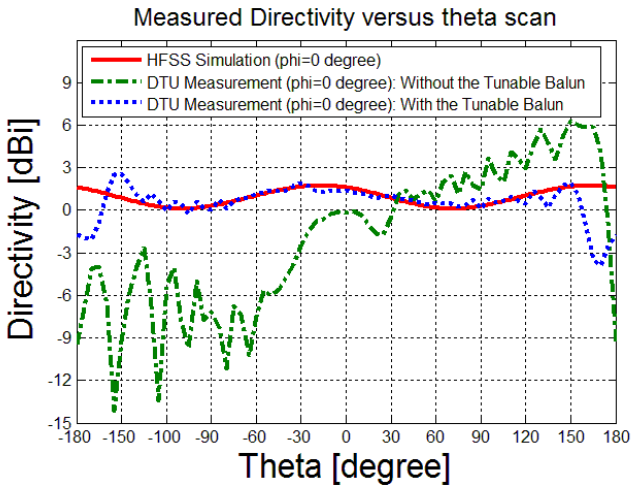

Fig. 6. The measured directivity in the E-plane ($\phi = 0°$) at DTU, with and without the tunable balun.

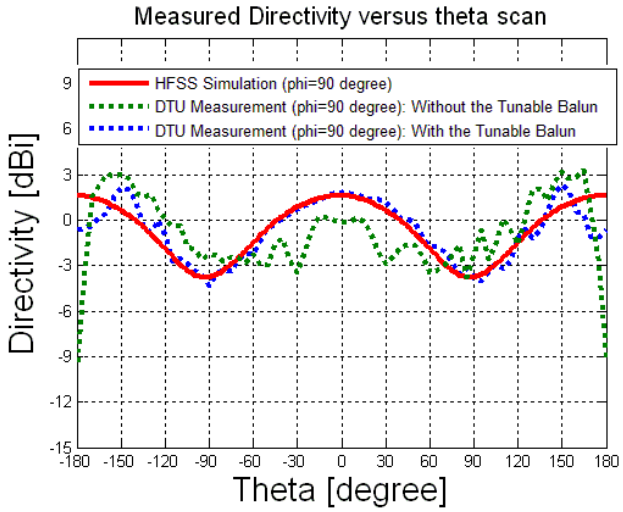

Fig. 7. The measured directivity in the H-plane ($\phi = 90°$) at DTU, with and without the tunable balun.

Another illustration of the importance of a balun in the radiation efficiency measurements is shown in Fig. 8. The radiation efficiency of the small loop antenna was measured

without the balun for different lengths of the feeding cable. It is seen from Fig. 8 that the measured values can increase more than 2 times, as compared to the expected value of about 20%, depending on the relative length of the cable. This effect is found to be weaker for free-space measurements, where the cable goes through the absorbers covering the support structure, and stronger for the measurements in a reverberation chamber, where the cable goes into the metallic wall. The latter apparently increases the effect of the leaking current by working as a reflecting surface and creating a standing wave.

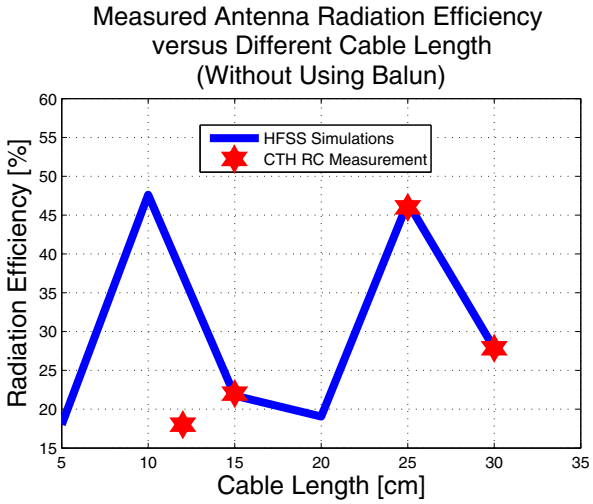

Fig. 8. Dependence of the simulated and measured radiation efficiency on the feed cable length without using balun.

It should also be noted that careful tuning of the balun is also very important, both for the radiation pattern and for the efficiency measurement. Though it is called a quarter-wave sleeve balun, it was found that the optimum length of the short-circuited sleeve (air-filled) should be about 0.2 wavelength, while the optimum gap between the open end of the sleeve and the antenna should be between 0.06-0.1 wavelength. It was noted from numerous experiments that even small deviation from these optimum parameters, e.g. decreasing or increasing the gap, results in strong overestimate of the radiation efficiency, in our case up to twice as much. The found optimum parameters of the balun generally agree with those found in the literature, but the increased sensitivity to the balun parameter deviations, to our knowledge, was not reported before.

B. Comparison Between the Techniques

The radiation pattern of the small loop antenna with the balun measured by SNF technique at DTU and by RAMS at AALTO are shown in Figs. 9-10. It is seen that the patterns agree well, though deviation within few dB can be observed in the E-plane for the RAMS results, which is explained by the lower accuracy of the RAMS setup.

The measured radiation efficiency by using the Wheeler cap method at DTU and by using reverberation chamber at CTH are compared in Fig. 11. It is seen that the results agree quite well, within the estimated measurement accuracy.

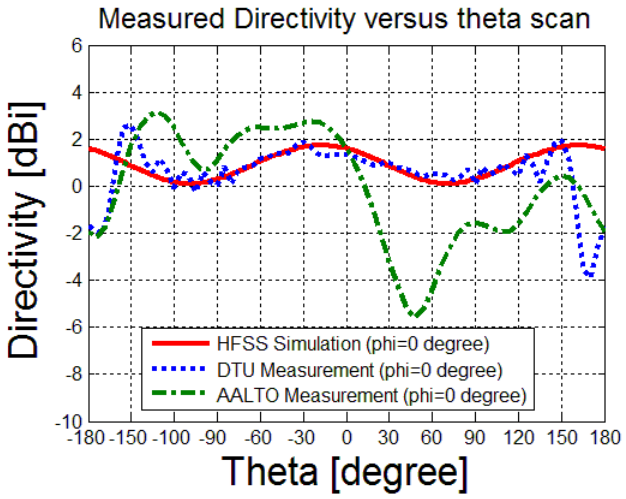

Fig. 9. The measured directivity in the E-plane ($\phi = 0°$), DTU and AALTO results.

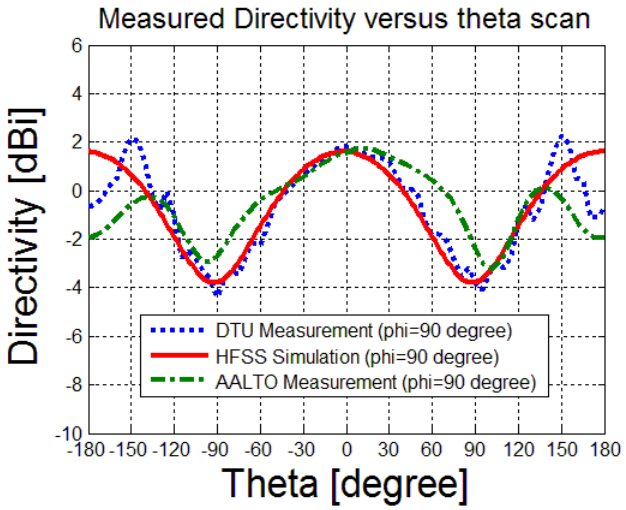

Fig. 10. The measured directivity in the H-plane ($\phi = 90°$), DTU and AALTO results.

Comparison of the measured radiation efficiency of the small loop antenna at the resonance frequency by different techniques is shown in Table I. As it was mentioned in section IV-A, without a balun the measured efficiency values vary a lot depending on the feed cable length and can exceed the expected value by a factor of 2 or even 3. With a properly tuned balun, all techniques show excellent agreement of the measured efficiency values within their uncertainties.

Regarding the measurement speed, the Wheeler cap method is the fastest one, the RAMS and the BlueTest reverberation chamber are a bit slower, but also provide the results within few minutes, while the SNF technique is rather slow, despite all the simplifications mentioned in section III-A.

On the other hand, the SNF technique provides high measurement accuracy and allows measuring all the characteristics, while the radiation pattern cannot be measured in the Wheeler cap and in the reverberation chamber.

TABLE I
COMPARISON OF SMALL ANTENNA RADIATION EFFICIENCY MEASUREMENT BY DIFFERENT TECHNIQUES

Measurements	Different techniques for small antenna measurements			
Radiation Efficiency (%)	DTU: SNF Antenna Test Facility	DTU: Wheeler Cap Method	AALTO: Rapid Antenna Meas. System	CTH: Reverberation Chamber
Antenna without a tunable balun	20% - 25%	21%-27%	20% - 43%	18% - 65%
Antenna with a tunable balun	20%	20%	20%	24%
Measurement time	20 min	2 min	4 min	3-6 min

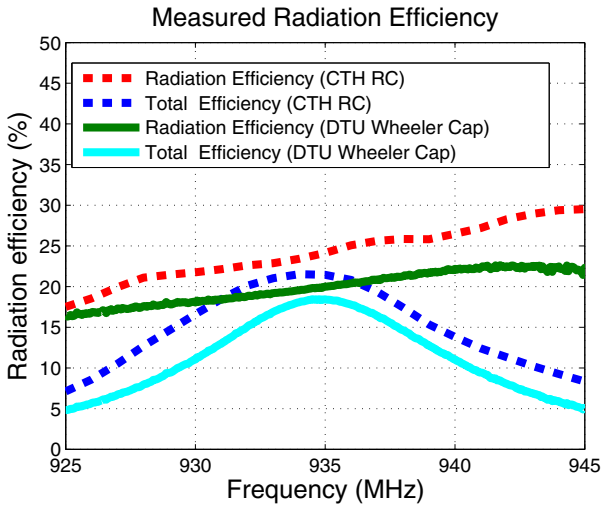

Fig. 11. The measured radiation efficiency by using the Wheeler cap method at DTU and by using the reverberation chamber at CTH.

The Wheeler cap method also provides good accuracy for the measured radiation efficiency, but the dimensions of the AUT are very limited: typically it should be less than about 0.25 wavelength. With this limitation, measurements of the antenna in the presence of a head phantom cannot be made. The other three techniques do not have strict limitations on the size of the AUT and thus measurements of the antenna in a complex environment is clearly possible, perhaps with some increase of the measurement time for the SNF technique in order to maintain high accuracy.

V. CONCLUSIONS

Comparison of the considered antenna measurement techniques has shown that all results are quite close to what has been obtained with the SNF technique, which is expected to be the more accurate one. The Wheeler cap method is very fast, but has limitations on the maximum dimensions of the device under test. The latter, for example, does not allow measurements of an antenna in the presence of a head phantom. The reverberation chamber and the RAMS are both quite fast, but the first (as well as the Wheeler cap) does not allow measuring the radiation pattern.

It was also shown that measuring symmetric antennas like loops or dipoles without proper balun not only results in a distorted radiation pattern, but also lead to a strong overestimate of the radiation efficiency, which gives very significant error, for example, if the expected efficiency is less than 50%. We believe that similar overestimate can happen also for non-symmetric antennas attached to small communication device mock-up and fed with a cable, since the leak currents can also be strong in that case.

ACKNOWLEDGMENT

The authors of this paper would like to thank NordForsk for the financial support of this work. J. Zhang and S. Pivnenko would like to thank X. Chen at Chalmers University of Technology for help with the measurements in reverberation chamber. T. Laitinen would like to thank Academy of Finland (decision notification no. 129055) for the financial support of this work.

REFERENCES

[1] http://www.dtu.dk/centre/ems/English/research/projects/projects/Antenna_Miniaturization.aspx
[2] J. Zhang and O. Breinbjerg, "Self-Resonant Electrically Small Loop Antennas for Hearing-Aids Application", European Conference on Antennas and Propagation, EuCAP2010, Barcelona, Spain, April 2010.
[3] http://www.dtu.dk/centre/ems/English/research/projects/projects/characterization_techniques.aspx
[4] Web-page for the DTU-ESA Spherical Near-Field Antenna Test Facility: http://www.dtu.dk/centre/ems/English/research/facilities.aspx
[5] T. Laitinen, *Advanced spherical antenna measurements*, Doctor′s Thesis, report S 273, Teknillinen korkeakoulu (TKK), Espoo, Finland, 2005, 63p.
[6] P.-S. Kildal and K. Rosengren, "Correlation and capacity of MIMO systems and mutual coupling, radiation efficiency and diversity gain of their antennas: Simulations and measurements in reverberation chamber", *IEEE Comm. Magazine*, vol. 42, no. 12, pp. 102-112, Dec. 2004.
[7] K. Rosengren and P.-S. Kildal, "Radiation efficiency, correlation, diversity gain, and capacity of a six monopole antenna array for a MIMO system: Theory, simulation and measurement in reverberation chamber", *Proceedings IEE, Microwave Antennas Propagat.*, vol. 152, no. 1, pp. 7-16, Feb. 2005. See also Erratum published in August 2006.
[8] M. Andersson, A. Wolfgang, C. Orlenius, J. Carlsson, "Measuring Performance of 3GPP LTE Terminals and Small Base Stations in Reverberation Chambers", chapter in the book by Borko Furht and Syed Ahson (Ed.), *Long Term Evolution – 3GPP LTE Radio and Cellular Technology*, CRC Press, Taylor and Francis Group, New York, 2009.
[9] R. H. Johnston and J. G. McRory, "An improved small antenna radiation efficiency measurement method," *IEEE Antennas Propagat. Magazine*, vol. 40, pp. 40-48, October 1998.

Paper IV

A Modified Wheeler Cap Method for Radiation Efficiency Measurement of Balanced Electrically Small Antennas

Jiaying Zhang, Pivnenko Sergey and Olav Breinbjerg

Proceedings of the Fourth European Conference on Antennas and Propagation (EuCAP 2010)

Presented in Barcelona, Spain, April 2010.

A Modified Wheeler Cap Method for Radiation Efficiency Measurement of Balanced Electrically Small Antennas

Jiaying Zhang*[1], S. Pivnenko*, and Olav Breinbjerg*
*Department of Electrical Engineering, Technical University of Denmark
Ørsteds Plads, Building 348, DK-2800 Kgs. Lyngby, Denmark
[1]jz@elektro.dtu.dk

***Abstract*—Measurement of radiation efficiency for ultra small antennas represents a great challenge due to influence of the feeding cable. The Wheeler cap method is often used to measure the radiation efficiency of small antennas. However, it is well applicable for antennas on a ground plane, but not for balanced antennas like loops or dipoles. In this paper, a modified Wheeler cap method is proposed for the radiation efficiency measurement of balanced electrically small antennas and a three-port network model of the Wheeler cap measurement is introduced. The advantage of the modified method is that it is wideband, thus does not require any balun, and both the antenna input impedance and radiation efficiency can be obtained. An electrically small loop antenna and a wideband dipole were simulated and measured according to the proposed method and the results of measurements and simulations are presented. The obtained results are also compared with the results from a spherical near-field measurements in an anechoic chamber and a good agreement is observed.**

I. Introduction

In recent years, there has been a strong interest for antenna miniaturization, since highly miniaturized electrically small antennas are now being more and more used in short range wireless communication applications, such as in body sensors, hearing-aids, and RFIDs. These miniaturized antennas are not only geometrically small, but also electrically small, and they can be used without or with ground plane, that is being balanced or unbalanced, and also can be symmetric or asymmetric. For small antennas, there are several important parameters that characterize their performance: input impedance, radiation efficiency, and radiation pattern. In particular, the radiation efficiency, which is defined as the ratio of the radiated power to the accepted power, is of great importance in the calculation of the communication link budget.

The radiation efficiency measurement of electrically small balanced antennas represents a great challenge for several reasons. First, the feeding coaxial cable has a significant influence on the measured radiation efficiency for balanced antennas due to leak current and due to scattering from the cable. Although a balun can be used to avoid the leak current, it is typically a narrow-band device and thus several baluns should normally be made to be applied at different frequencies. Second, for electrically small antennas the radiation efficiency can be rather low. Hence the measurement facility should be accurate enough to provide a reasonable accuracy for low efficiency antennas. Third, the antenna under test can be symmetric or asymmetric, and thus the radiation efficiency evaluated from measurement of half of the antenna over a large ground plane is not always a valid approach. There is thus a need for a measurement technique overcoming these challenges.

For small antenna measurements, the Wheeler cap method is a well known and widely used method for measurement of radiation efficiency. However, it is only well applicable for small antennas on a ground plane. In this paper, we propose a modification of the Wheeler cap method aiming at radiation efficiency measurements for balanced small antennas, which can be symmetric or asymmetric. A new three-port network model of the Wheeler cap measurement is proposed. In order to confirm the validity of the proposed modified Wheeler cap method, an electrically small loop antenna and a wideband dipole were simulated and measured using this method and the results compared in-between and to the measurements of the antennas with a balun in an anechoic chamber.

II. Three-Port Model of the Wheeler Cap Method

The original Wheeler cap method [1] was further developed in [2], [3], in which a two-port network model is proposed by assuming that the antenna is operated in a single mode, and the two ports are defined as the antenna input terminal and the transition between the antenna and free space, respectively. Two measurements are involved in this method, which are the measurement of the antenna input reflection coefficients in free space and in a Wheeler cap, respectively. The antenna radiation efficiency can then be extracted. However, this method is well applicable only for antennas on a ground plane, while for balanced antennas influence of the feed cable represents a severe problem.

In this paper, a three-port network model is proposed for the Wheeler cap method for measuring the radiation efficiency of small balanced antennas. As shown in Fig. 1, the three ports are two excitation ports and one radiation port. A differential-fed antenna can be viewed as a linear two port model, and a virtual ground plane in the middle of the excitation terminal can be assumed.

Determination of differential impedance by using S-parameter based measurements has been studied previously

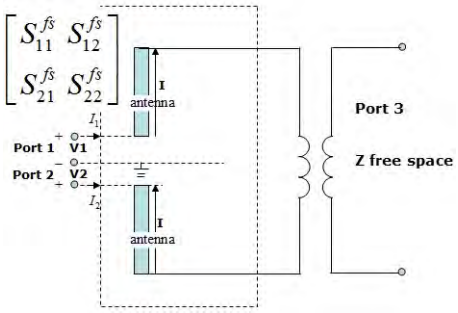

Fig. 1. An electrically small balanced antenna with the two-port excitation in free space.

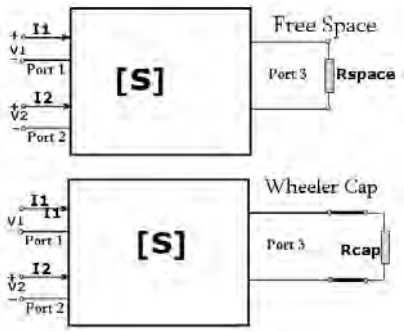

Fig. 2. The three-port network model for Wheeler cap measurement of the balanced small antenna.

[4]- [6]. In the method reported in [4], two microstrip lines mounted back to back are used as the test fixture. Then some home-made non-standard calibration tools are used at the end of two microstrip lines in the calibration. The accuracy is found acceptable up to 1 GHz. Later, further development of this method was proposed in [5] and it was suggested doing the calibration at the end of VNA cables using standard calibration tools. Instead of using microstrip lines, two pieces of extra coaxial cables are used as the test fixture, whose outer conductors are soldered together. The parameters of the test fixture need to be extracted from the measurement data, and then antenna impedance can be calculated. Recently, Qing et al. suggested to use the the port extension function of VNA to find the antenna impedance, instead of the above calculations [6].

In this paper, we apply the S-parameter based method in combination with the Wheeler cap method to determine the antenna radiation efficiency for balanced small antennas. An electrically small dipole antenna with the two-port excitation in free space is illustrated in Fig. 1. Inside the Wheeler cap, Fig. 2, the port 3 is loaded with the impedance of the Wheeler cap, with the reflection coefficient Γ_L, and we can obtain the scattering equations for the two ports

$$\begin{bmatrix} S_{11}^{wc} & S_{12}^{wc} \\ S_{21}^{wc} & S_{22}^{wc} \end{bmatrix} = \begin{bmatrix} S_{11} + \frac{S_{13}S_{31}\Gamma_L}{1-S_{33}\Gamma_L} & S_{12} + \frac{S_{13}S_{32}\Gamma_L}{1-S_{33}\Gamma_L} \\ S_{21} + \frac{S_{23}S_{31}\Gamma_L}{1-S_{33}\Gamma_L} & S_{22} + \frac{S_{23}S_{32}\Gamma_L}{1-S_{33}\Gamma_L} \end{bmatrix} \quad (1)$$

where S_{nm}^{wc} are the S-parameters of the model obtained in the Wheeler cap. While in free space, $\Gamma_L = 0$, and the scattering equations can be further simplified to

$$\begin{bmatrix} S_{11}^{fs} & S_{12}^{fs} \\ S_{21}^{fs} & S_{22}^{fs} \end{bmatrix} = \begin{bmatrix} S_{11} & S_{12} \\ S_{21} & S_{22} \end{bmatrix}. \quad (2)$$

where S_{nm}^{fs} are the S-parameters of the model obtained in free space, as shown in Fig. 2. For symmetric electrically small antennas, the antenna input impedance Z_{ant} in free space and in the Wheeler cap can be determined from

$$\begin{aligned} Z_{ant}^{fs} &= 2Z_0 \frac{1-(S_{11}^{fs})^2+(S_{21}^{fs})^2-2S_{21}^{fs}}{(1-S_{11}^{fs})^2-(S_{21}^{fs})^2} \\ &= 2Z_0 \frac{(1+S_{11}^{fs}-S_{21}^{fs})}{(1-S_{11}^{fs}+S_{21}^{fs})} \quad (3) \\ Z_{ant}^{wc} &= 2Z_0 \frac{1-(S_{11}^{wc})^2+(S_{21}^{wc})^2-2S_{21}^{wc}}{(1-S_{11}^{wc})^2-(S_{21}^{wc})^2} \\ &= 2Z_0 \frac{(1+S_{11}^{wc}-S_{21}^{wc})}{(1-S_{11}^{wc}+S_{21}^{wc})} \quad (4) \end{aligned}$$

Here, Z_0 is the characteristic impedance of the feed cable. As shown in equations (3) and (4), the simplified formulas are used to avoid the singularity for the case $1 - S_{11}^{fs} - S_{21}^{fs} = 0$ or $1 - S_{11}^{wc} - S_{21}^{wc} = 0$. For asymmetric electrically small antennas, the antenna input impedance Z_{ant} in free space and in the Wheeler cap are

$$\begin{aligned} Z_{ant}^{fs} &= \frac{2Z_0(1-S_{11}^{fs}S_{22}^{fs}+S_{12}^{fs}S_{21}^{fs}-S_{12}^{fs}-S_{21}^{fs})}{(1-S_{11}^{fs})(1-S_{22}^{fs})-S_{21}^{fs}S_{12}^{fs}}, \quad (5) \\ Z_{ant}^{wc} &= \frac{2Z_0(1-S_{11}^{wc}S_{22}^{wc}+S_{12}^{wc}S_{21}^{wc}-S_{12}^{wc}-S_{21}^{wc})}{(1-S_{11}^{wc})(1-S_{22}^{wc})-S_{21}^{wc}S_{12}^{wc}}. \quad (6) \end{aligned}$$

In order to determine antenna radiation efficiency, two measurements are necessary, which are the full two-port S-parameter measurement in free space and in the Wheeler cap. Then the antenna input reflection coefficients in free space Γ_{ant}^{fs} and in the Wheeler cap Γ_{ant}^{wc} can be extracted, and the antenna radiation efficiency e_{rad} can be calculated from

$$e_{rad} = \frac{1}{1-|\Gamma_{ant}^{fs}|^2} \times \frac{2}{(\Delta S_{max})^{-1}+(\Delta S_{min})^{-1}} \quad (7)$$

where ΔS_{max} and ΔS_{min} are maximum and minimum of $\Delta S = |\Gamma_{ant}^{fs} - \Gamma_{ant}^{wc}|$ [3].

III. Simulations

A. Balanced Electrically Small Loop Antenna

An electrically small capacitively-loaded loop antenna was designed to be operated around 900 MHz for hearing aid applications. The loop is printed on the Rogers 5870 substrate with the dielectric constant of 2.33 and loss tangent of 0.0012. The overall dimensions of the antenna are $35\times10\times1.5$ mm^3.

First, the loop antenna itself is simulated with HFSS software by using lumped port excitation in free space, as shown in Fig. 3. For this configuration, the input impedance and radiation efficiency are obtained directly and represent reference results.

Second, according to the proposed modified Wheeler cap method, the loop antenna with two extra cables is simulated in free space and in the Wheeler cap, respectively. The outer conductors of the test cables are connected in-between to provide a common ground and these two cables are properly taken into account in the simulation. The waveports are used as the excitation ports, as illustrated in Fig. 4, which are located at the end of each coaxial cable. In order to find the full two-port scattering matrix at the antenna port, the port de-embedding is applied on each waveport. It is noted that lossless cables are used in the simulation.

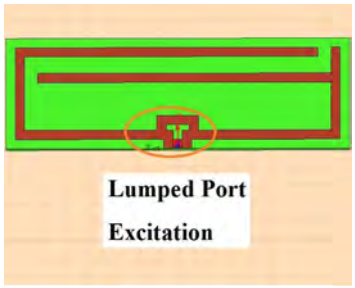

Fig. 3. Lumped port excitation of the small loop antenna: HFSS model.

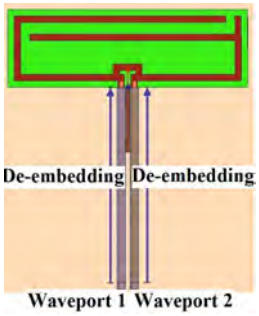

Fig. 4. Two waveport excitations and port de-embedding: HFSS model.

An aluminum cylindrical cavity with the diameter of 26 cm and the height of 35 cm is used in the simulation as the Wheeler cap. Then the simulated full two-port scattering matrix of the loop antenna in free space and inside the Wheeler cap, respectively, are obtained. From these results, the antenna input impedance, the reflection coefficient, and the radiation efficiency are calculated.

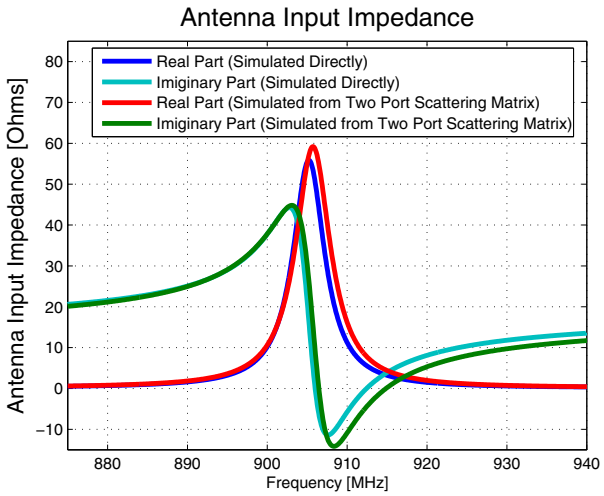

Fig. 5. Antenna input impedance obtained from direct simulation and from scattering matrix.

The small loop antenna properties obtained from the full two-port scattering matrix are then compared to the reference simulation results with the lumped port excitation. The input impedance, reflection coefficient, and the radiation efficiency of the loop antenna are illustrated in Figs. 5-8. It is seen that the results are in a good agreement and the small difference can be explained by finite simulation accuracy. All simulation results show that the cable effects on the radiation efficiency can be avoided by using the proposed method.

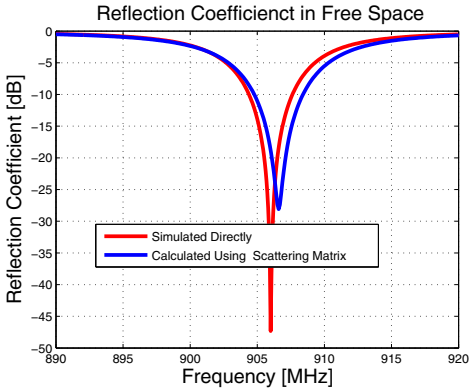

Fig. 6. Antenna reflection coefficient obtained from direct simulation and calculated from scattering matrix.

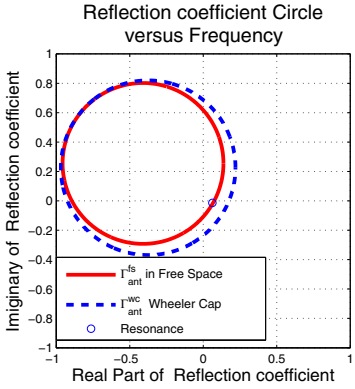

Fig. 7. Antenna reflection coefficient circle versus frequency in free space and in a Wheeler cap.

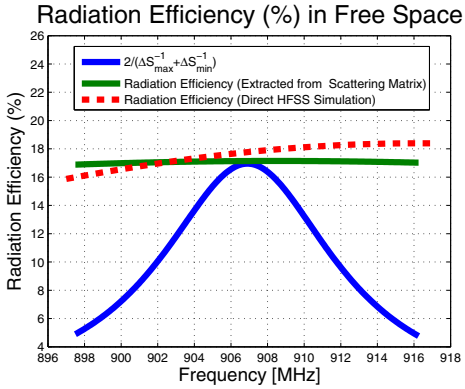

Fig. 8. Antenna radiation efficiency obtained from direct simulation and from full two-port scattering matrix.

B. Broadband Dipole

In order to prove that the proposed method is broadband, a differential-fed wideband dipole is also simulated to show the possibility of the radiation efficiency measurement over a broad frequency band. Here we use a wideband dipole with the arms made of thin metallic discs without any substrate, as shown in Fig. 9 and Fig. 10. The radius of each disc is 3 cm and the gap between the discs is 2 mm. The radiation efficiency of this wideband dipole is expected to be very close to 100%, since the loss in this case is determined only by the finite conductivity of the metal, which is set to 5.8×10^7 S/m to represent copper. Although this antenna is not electrically small, we prefer to use, both in simulation and in measurement, a broadband antenna with well known radiation efficiency. The radiation efficiency of the dipole obtained using the simulated scattering matrix is almost constant over the band from 500 MHz to 2000 MHz and it is equal to 99.7% This result shows that the radiation efficiency measurement by using the three-port Wheeler cap method is valid over a wide frequency bandwidth.

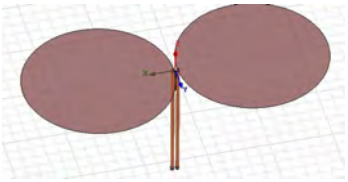

Fig. 9. Full two-port scattering matrix simulation in free space (HFSS).

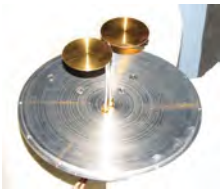

Fig. 10. Fabricated Broadband Antenna.

IV. Measurement Results

Several electrically small loop antennas were manufactured according to the design parameters and measured using the modified Wheeler cap technique. The Wheeler cap used in the measurements was originally designed for measurements of small antenna down to 400 MHz, but later it was found that it also can be used at higher frequencies by the generalized Wheeler cap method [3], which allows avoiding influence of the cavity resonances.

The full two-port scattering matrix was measured for the loop antenna in free space and in the Wheeler cap, by using the network analyzer HP 8753D, as illustrated in Fig. 11. The extracted antenna radiation efficiency is shown in Fig. 12. The measured radiation efficiency is also compared with the result from a spherical near-field antenna facility, where the antenna was measured with a sleeve balun. It is seen from Fig. 12 that very good agreement is observed between all the results that confirms the validity of the proposed modified Wheeler cap method.

The measured radiation efficiency for the broadband dipole antenna in the frequency range 1-3 GHz is illustrated in Fig. 13. It is seen that the measured efficiency is about 99% in average and the ripples can be explained by the finite calibration accuracy of the VNA. Again, this result clearly shows that the proposed method works very well also in a wide frequency band and can be well used for the input impedance and radiation efficiency measurements of wideband antennas.

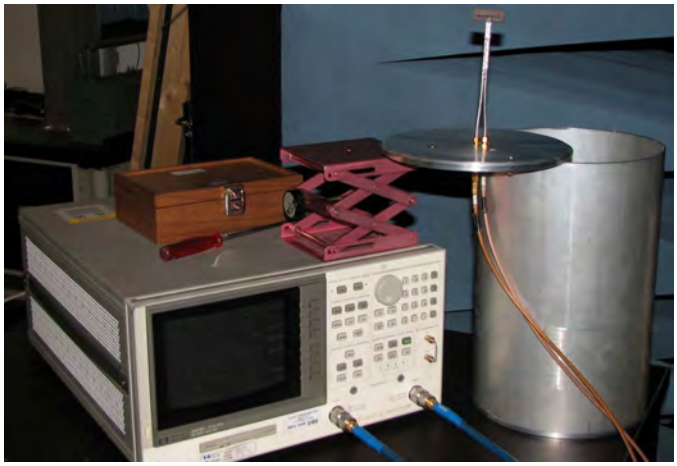

Fig. 11. The measurement setup for modified Wheeler cap technique.

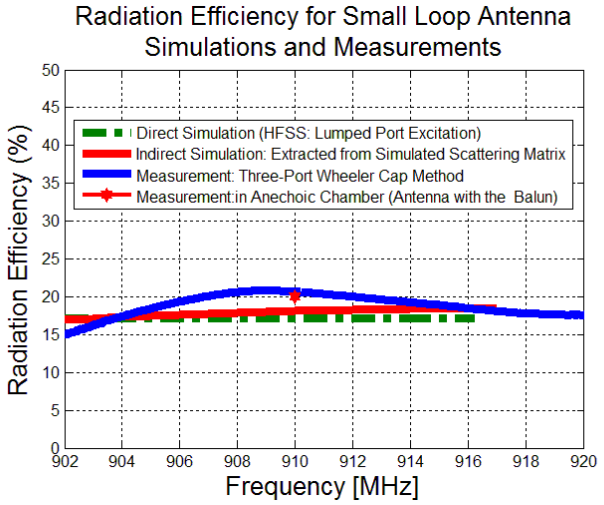

Fig. 12. The simulated and measured radiation efficiency for the small loop antenna.

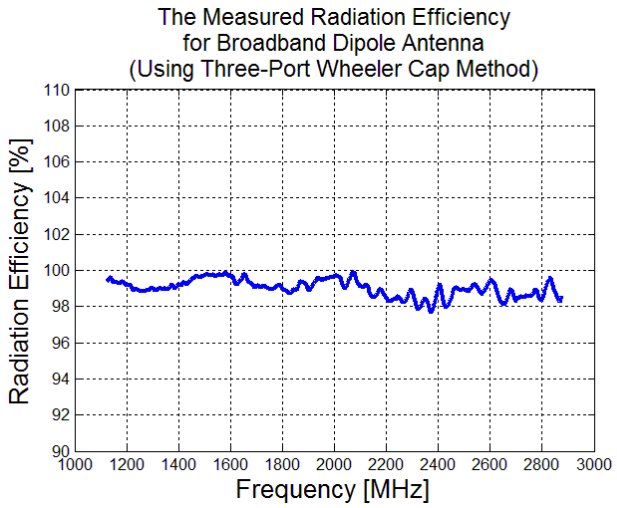

Fig. 13. The measured radiation efficiency for the broadband dipole antenna.

V. Conclusions

A modified Wheeler cap method is proposed for accurate measurements of input impedance and radiation efficiency of small balanced antennas. The advantages of the proposed method can be summarized as follows. First, no balun is required during the measurement, thus the problems of balun bandwidth and extra scattering effects are avoided. Second, it is shown that the proposed method is broadband and the cavity resonances do not have any significant effect of the measurement results with the proper use of the circle fitting for the measured S-parameters. This also means that the cavity size should not necessarily be small as it was commonly considered until now.

In summary, it was shown in this paper that by using the Wheeler cap method in a proper way, most of its limitations and disadvantages can be avoided. The method is, therefore, suitable for input impedance and radiation efficiency measurement for most types of antennas in a broad frequency bandwidth. The antennas are not limited to be electrically small and can be balanced or unbalanced, symmetric or unsymmetric type.

References

[1] H. A. Wheeler, "The radiansphere around a small antenna," *Proceedings of the IRE*, pp. 1325-1331, August 1959.

[2] R. H. Johnston and J. G. McRory, "An improved small antenna radiation efficiency measurement method," *IEEE Antennas Propagat. Mag.*, vol. 40, pp. 40-48, October 1998.

[3] C. Mendes and C. Peixeiro, "Theoretical and experimental validation of a generalized Wheeler cap method," European Conference on Antennas and Propagation, EuCAP2007, Edinburgh, Scotland, UK, November 2007.

[4] R. Meys and F. Janssens, "Measuring the impedance of balanced antennas by an S-parameter method," *IEEE Antennas Propag. Mag.*, vol. 40, pp. 62-65, December 1998.

[5] K. D. Palmer and M. W. V. Rooyen, "Simple broadband measurements of balanced loads using a network analyzer," *IEEE Trans. Microw. Theory Tech.*, vol. 55, no. 2, pp. 266-272, February 2006.

[6] X. Qing, C. K. Goh, and Z. N. Chen, "Impedance characterization of RFID tag antennas and application in tag co-design," *IEEE Trans. Instrum. Meas.*, vol. 57, no. 5, pp. 1268-1274, May 2009.

Paper V

Miniaturization of Multiple-Layer Folded Patch Antennas

Jiaying Zhang and Olav Breinbjerg

Proceedings of the Third European Conference on Antennas and Propagation (EuCAP 2009)

Presented in Berlin, Germany, April 2009, pp. 3502-3506.

Miniaturization of Multiple-Layer Folded Patch Antennas

Jiaying Zhang #1 and Olav Breinbjerg #2

#Department of Electrical Engineering, Electromagnetic Systems, Technical University of Denmark
Ørsted Plads, Building 348, DK-2800 Kgs. Lyngby, Denmark
[1]jz@elektro.dtu.dk
[2]ob@elektro.dtu.dk

***Abstract*—A new folded patch antenna with multiple layers was developed in this paper, by folding the patch in a proper way, and a highly miniaturized antenna can be realized. The multiple layer patch with 4-layer and 6-layer are designed and evaluated at 2.4 GHz, 915 MHz, and 415 MHz respectively. Then a 4 layer patch is fabricated and measured to validate the design method. The theoretical analysis, design and simulations, fabrications, as well as the measurements are presented in this paper. All the results show that the folded patch antenna is a good candidate in making a highly miniaturized compact antenna.**

***Index Terms*—Small antennas.**

I. Introduction

The antenna is an important component in wireless systems, and the demand for compact systems with stringent specifications for bandwidth and gain makes antenna size reduction a significant challenge. It is with no doubt that the antenna miniaturization is one of the key technologies in designing successful wireless networks, and a lot of antenna miniaturization techniques have been developed [1]-[5]. In this paper, the multiple layer folded patch antenna is studied and compact antenna designs are developed. The conventional rectangular patch antenna resonates when its length is half of the wavelength. By adding a shorting wall at the center of the patch, the antenna size can be reduced to a quarter of the wavelength. Moreover, by folding the wall-shorted patch, the overall size of the two layer patch antenna becomes one eighth of the wavelength [6]-[8]. In this paper, the multiple layer folded patch antenna is further developed by folding the patch in a proper way, which results in a highly miniaturized antenna. Multiple layer folded patch antennas with 4 and 6 layers are designed and evaluated at 2.4 GHz, 915 MHz, and 415 MHz respectively, using the commercial software package HFSS [10]. Then a 4-layer patch for 415 MHz is fabricated and measured to validate the design method. The theoretical analysis, numerical simulations, manufacturing issues, as well as measurements will be presented in this paper.

II. Theoretical Analysis: Transmission Line Model

The transmission line model [8]-[9] is used to analyze the multiple layer patch. For an N layer patch, each layer can be viewed as a section of the transmission with length L and the characteristic admittance Y_0, as shown in Fig. 1 and Fig. 2,

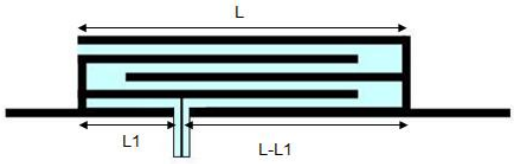

Fig. 1. An example of the multiple-layer folded patch (4 layers).

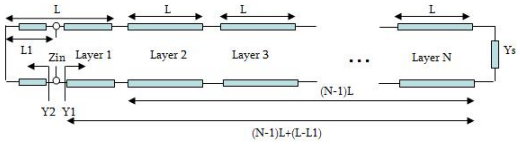

Fig. 2. The transmission line model of the multiple-layer patch antenna.

where N is the numbers of layers, L_1 is the feed position of the antenna, and Y_0 is characteristic admittance of each layer. The input impedance at the feed point can be expressed as

$$Z_{in} = jX_f + Z_A, \tag{1}$$

where X_f is the reactance of the feed probe. X_f is given by

$$X_f = \frac{\omega\mu_0 h}{2\pi}[ln(\frac{2}{\beta r}) - 0.57721], \tag{2}$$

where $\beta = 2\pi/\lambda_0$, r is the radius of the probe, and Z_A is antenna impedance, $Z_A = 1/Y_A$. The admittance Y_A can be found from Y_1 and Y_2, $Y_A = Y_1 + Y_2$, which are

$$\begin{cases} Y_1 = Y_0 \frac{Y_s + jY_0 \tan\beta[(N-1)L+(L-L_1)]}{Y_0 + jY_s \tan\beta[(N-1)L+(L-L_1)]} \\ Y_2 = Y_0 \frac{1}{j\tan(\beta L_1)} \\ Y_A = Y_0 \frac{Y_s + jY_0 \tan\beta[(N-1)L+(L-L_1)]}{Y_0 + jY_s \tan\beta[(N-1)L+(L-L_1)]} + \frac{Y_0}{j\tan(\beta L_1)} \end{cases}, \tag{3}$$

where N is the number of layers, L_1 is the feed position of the antenna, Y_0 is characteristic impedance of each layer, and Y_s is the admittance of the equivalent radiation slot of the patch. We assume that each layer of the folded patch is of equal thickness h, and thus the characteristic impedance of each layer are the same approximately. Y_s can be determined from $Y_s = G_s + jB_s$, and

$$Gs = \begin{cases} \frac{1}{90}(\frac{W}{\lambda_0})^2, & W \le 0.35\lambda_0 \\ \frac{1}{120}(\frac{W}{\lambda_0}) - \frac{1}{60\lambda_0^2}, & 0.35\lambda_0 \le W \le 2\lambda_0 \\ \frac{1}{120}(\frac{W}{\lambda_0}), & 2\lambda_0 \le W \end{cases}, \tag{4}$$

TABLE I
PROBE-FED MULTIPLE LAYER FOLDED PATCH ANTENNA (FREQUENCY= 2400MHZ).

	Antenna Dimension [mm]	Feed Position $L_1[mm]$	Ground Size [mm]	Bandwidth (BW@-10 dB)	Efficiency [%]	Directivity [dBi]	Gain [dBi]
Design1 (2-layer design)	$L_{patch} = 15.5mm = 0.124\lambda_0$ $W_{patch} = 17.5mm = 0.14\lambda_0$ $H_{patch} = 2h = 3mm$ $L_{gap} = 1mm, h = 1.5mm$	2.3 mm	21.5 mm*21.5 mm	12 MHz	89.5%	2.07 dBi	1.59 dBi
Design2 (4-layer design)	$L_{patch} = 8.875mm = 0.071\lambda_0$ $W_{patch} = 8.75mm = 0.07\lambda_0$ $H_{patch} = 4h = 6mm$ $L_{gap} = 1mm, h = 1.5mm$	2 mm	13.8 mm*12.75 mm	12 MHz	87.5%	1.73 dBi	1.16 dBi
Design3 (6-layer design)	$L_{patch} = 5mm = 0.04\lambda_0$ $W_{patch} = 6mm = 0.048\lambda_0$ $H_{patch} = 6h = 3mm$ $L_{gap} = 1.5mm, h = 0.5mm$	0.9 mm	11 mm*10 mm	4 MHz	62%	1.56 dBi	-0.52 dBi

TABLE II
PROBE-FED MULTIPLE LAYER FOLDED PATCH ANTENNA (FREQUENCY= 900MHZ).

	Antenna Dimension [mm]	Feed Position $L_1[mm]$	Ground Size [mm]	Bandwidth (BW@-10 dB)	Efficiency [%]	Directivity [dBi]	Gain [dBi]
Design4 (2-layer design)	$L_{patch} = 39.12mm = 0.117\lambda_0$ $W_{patch} = 41.625mm = 0.125\lambda_0$ $H_{patch} = 2h = 3mm$ $L_{gap} = 2mm, h = 1.5mm$	6.5 mm	45.12 mm*45.625 mm	12 MHz	95.5%	2.2 dBi	2 dBi
Design5 (4-layer design)	$L_{patch} = 22.83mm = 0.069\lambda_0$ $W_{patch} = 21.47mm = 0.065\lambda_0$ $H_{patch} = 4h = 6mm$ $L_{gap} = 1.5mm, h = 1.5mm$	3.5 mm	27.4 mm*25.8 mm	1.2 MHz	58%	2 dBi	-0.4 dBi
Design6 (6-layer design)	$L_{patch} = 13mm = 0.039\lambda_0$ $W_{patch} = 14mm = 0.042\lambda_0$ $H_{patch} = 6h = 3mm$ $L_{gap} = 1.5mm, h = 0.5mm$	1.9 mm	15.6 mm*16.8 mm	1.5 MHz	22.5%	1.9 dBi	-4.6 dBi

where G_s and B_s are the conductance and susceptance respectively, and W is the width of the patch. For the electrically small antenna, Y_s is much smaller than Y_0, and the effect of Y_s is small. For simplicity, we assume that its influence can be ignored, as well as the probe reactance. Hence, at the resonance there is the condition that $Y_A = 0$, which leads to

$$\frac{Y_0}{\tan(\beta L_1)} = Y_0 \tan\beta[(N-1)L + (L - L_1)] \qquad (5)$$

Using the relation that $tan^{-1}(\beta L_1) = tan(\pi/2 - \beta L_1)$, the approximate resonance length L of the N-layer folded patch antenna is found to be

$$L = \frac{\lambda_0}{4N\sqrt{\varepsilon_r}}, \qquad (6)$$

where λ_0 is the wavelength in free space and ε_r is the dielectric constant of the substrate. The Equation (6) is an important result of this paper. For the 4-layer patch, the overall length of the patch is $L = \frac{\lambda_0}{16\sqrt{\varepsilon_r}}$. For the 6-layer patch, the resonance length becomes to $L = \frac{\lambda_0}{24\sqrt{\varepsilon_r}}$.

III. ANTENNA DESIGNS

Our purpose here is to design the highly miniaturized antenna, and folded patch antennas are designed and evaluated at 2400 MHz, 900 MHz, and 415 MHz for different applications. For each frequency, three different versions are designed, which are 2-layer, 4-layer, and 6-layer folded antennas, and the antenna performance is given for each case. The geometry and design variables of the folded patch are illustrated in Fig. 3.

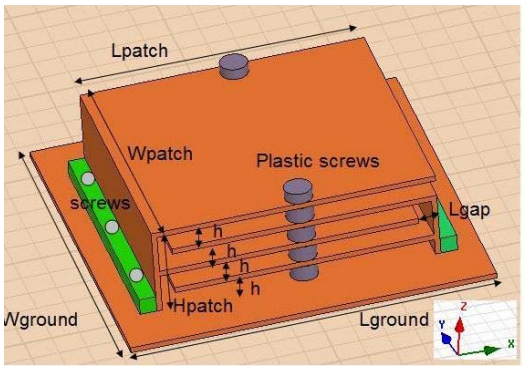

Fig. 3. Geometry of design variables for 4-layer folded patch (in HFSS).

Table I shows the folded patch antennas which are designed to operate at the frequency of 2400 MHz, and also predicts the performance provided by HFSS, including the bandwidth and radiation efficiency. For the four layer case in design 2, the antenna dimension is $8.875mm \times 8.75mm \times 6mm$, and the electrical size of the patch length is reduced to 0.071 λ_0 ($ka = 0.23$), and at the same time the ground plane size is also limited to be as small as possible. The bandwidth is found to be 12 MHz and the radiation efficiency is 87.5%. For the 6-layer case, in design 3, the antenna is of the dimension $5mm \times$

TABLE III
PROBE-FED MULTIPLE LAYER FOLDED PATCH ANTENNA (FREQUENCY= 415MHZ).

	Antenna Dimension [mm]	Feed Position $L_1[mm]$	Ground Size [mm]	Bandwidth (BW@-10 dB)	Efficiency (for ground size 1)	Efficiency (for ground size 2)
Design7 (2-layer design)	$L_{patch} = 50.2mm = 0.069\lambda_0$ $W_{patch} = 46.7mm = 0.065\lambda_0$ $H_{patch} = 4h = 12mm$ $L_{gap} = 2.5mm$, $h = 3mm$	8.6 mm	Ground size 1: 60.25 mm*55.4 mm Ground size 2: 200 mm*200 mm	1.2 MHz	52%	67%

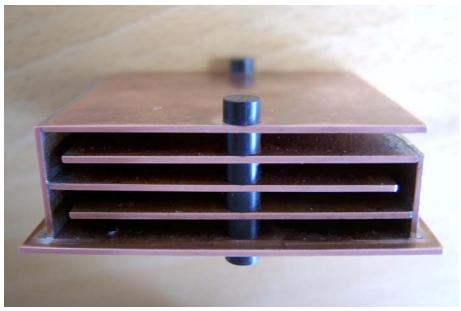

Fig. 4. The fabricated 4-layer patch antenna with a small ground plane, in design 7, operated at 415 MHz

$6mm \times 6mm$. The electrical length of the patch length is 0.04 λ_0 ($ka = 0.126$), and the bandwidth is found to be 4 MHz and the radiation efficiency is 62%. The bandwidth is small in design 3 and this is due to a smaller thickness is used between each layer. The radiated power is reduced as the antenna size decreases, and thus the radiation efficiency for design 3 must be lower than that for design 2. Hence, the ultra small antenna is possible to be realized by this folded patch, and a high fabrication accuracy is required since the antenna is both electrically and mechanically small at this frequency.

Table II gives the folded patch designs at 915 MHz , as well as their bandwidth and radiation efficiency. Similarly, the ground plane size is controlled as small as possible. For the four layer case, design 5, the antenna dimension is $22.83mm \times 21.47mm \times 6mm$, that is the electrical length of the patch is reduced to about 0.068 λ_0 ($ka = 0.21$). The bandwidth is found to be 1.2 MHz and the radiation efficiency is 58%. The maximum gain is -0.4 dBi. For the 6-layer case, in design 6, the antenna dimension is decreased to $13mm \times 14mm \times 6mm$, and the electrical size of the patch length is 0.039 λ_0 ($ka = 0.12$). The bandwidth is found to be 1.5 MHz and the radiation efficiency is 22.5%. The maximum gain is -4.6 dBi. These results shows that the folded patch antenna is a good candidate in making the highly miniaturized compact antenna, while we should also keep in mind that the mechanism of the miniaturization is the tradeoff among antenna size and performance.

Table III illustrates the folded antenna designed to operate at 415 MHz, which is a 4-layer patch antenna. This antenna is of the dimension of $50.2mm \times 46.7mm \times 12mm$, and the electrical size of the patch length is 0.069 λ_0 with ka is equal to 0.22. The bandwidth is 1.2 MHz and the radiation efficiency is 67%.

IV. ANTENNA FABRICATION

In order to validate the above performance predicted by the numerical simulations, the antenna in design 7 which operates at 415 MHz is fabricated at our workshop. As shown in Fig. 4, this antenna uses 1 mm thickness copper plate as its each layer. Several practical issues are involved, which should be solved carefully during the fabrication and steps can be given as follows. First, each layer and the side wall are cut into rectangular pieces accurately, and then these pieces can be combined together by the soldering. In order to control the thickness between each layer, we make several plastic screws in our workshop with its thickness is accurately controlled, and then we put two of them between the each layer. However, its influence on the resonance frequency must be taken into account. Second, another important step is the connection between the antenna and the ground plane. In our design, the antenna is attached to the ground by using the screws rather than the soldering, and we did it in this way because we can replace the ground plane easily, which provides us the convenience to evaluate the size influence of different ground plane. The same 4-layer folded patch antenna but with a different ground is shown in Fig. 5, in which the ground plane is much larger. Since the ground plane has an important influence on the antenna impedance, the feeding point position must be adjusted accordingly when different ground plane is used. Later, the large ground plane is used in the measurement in order to avoid the cable influence. Third, about the antenna feeding, a specially smart SMA connecter is used as the feed probe, whose inner conductor is possible to be taken away from the SMA easily. We first solder the inner conductor to the feed point on the patch, and then attach the antenna and the ground. Then screw the SMA frame to the ground, and combine the inner and the outer of the SMA at the same time. The antenna assembling process is done by the above steps during which the accuracy can be controlled as much as possible.

V. ANTENNA MEASUREMENT

In order to compare the antenna performance with the numerical simulation results, this 4-layer design at 415 MHz is measured with respect to impedance and radiation properties. The s parameter S_{11} was measured first by using the network analyzer HP 8720D, with an absorber placed in front of the antenna. The simulated and measured S_{11} for the 4-layer patch antenna are presented and compared in Fig. 6. While the simulated resonance frequency is 415 MHz, the measured resonance frequency is 416.7 MHz, and the deviation is only

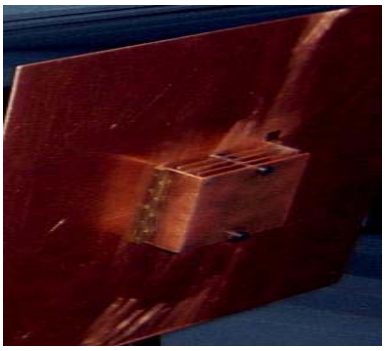

Fig. 5. The fabricated 4-layer patch antenna with a large ground plane, in design 7, operated at 415 MHz

0.4 %. The simulated and measured -10dB bandwidth are 1.12 MHz and 1.08 MHz respectively, and the difference is thus only 0.04 MHz.

The radiation measurement is performed in the Radio Anechoic Chambers at DTU, which is called DTU-ESA Spherical Near Field Antenna Test Facility. The measured directivity versus θ (for $\phi = 0°$ and $\phi = 90°$) at 415 MHz are shown in Fig. 7 and Fig. 8 respectively. The efficiency of the antenna was measured by using the substitution method, and found to be 59%, which is reasonably close to the simulated efficiency 67%. The gain is acceptable for the antenna of such small dimension.

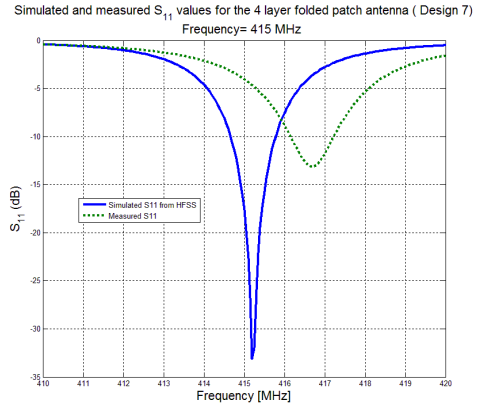

Fig. 6. The simulated and measured S11 for the 4-layer patch antenna, which is designed to operate at 415 MHz.

VI. Conclusions

Multiply layer patch antennas are developed at three frequencies, and the performance of these highly miniaturized antennas are presented. A 4-layer folded patch operated at 415 MHz is fabricated and all practical issues are solved and discussed. Then the antenna measurement is performed, and measured results agree well with numerical simulations.

In this work, the folded patch antennas are designed in the vacuum environment for simplicity, and further development will be focused on the combination of using the high dielectric constant substrate. Moreover, the low loss magneto-dielectric

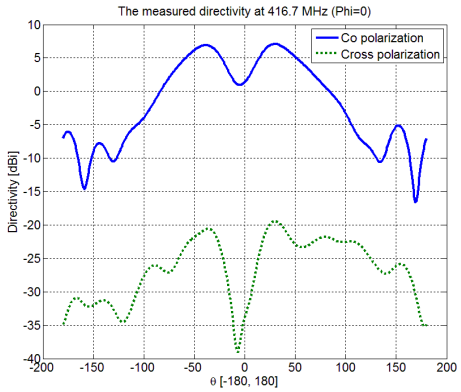

Fig. 7. The measured directivity versus θ (for $\phi = 0°$), which is a 4-layer folded patch antenna at 415 MHz.

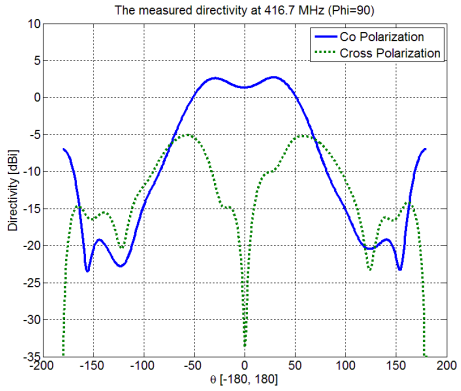

Fig. 8. The measured directivity versus θ (for $\phi = 90°$), which is a 4-layer folded patch antenna at 415 MHz.

material is also a good candidate to be evaluated as the patch substrate, which should result in a bandwidth improvement.

Acknowledgment

This work is supported by the Danish Højteknologifonden from the year 2007 to 2010, within the project "Wireless Coupling in Small Autonomous Apparatus".

References

[1] A.K. Skrivervik, J.F. Zurcher, O. Staub, and J.R. Mosig, "PCS antenna design: the challenge of miniaturization," *IEEE Antennas Propagat. Mag.*, vol. 43, pp. 12-27, Aug, 2001.

[2] K.L. Wong, *Planar Antennas for Wireless Communications*, John Wiley & Sons, Inc., 2003.

[3] R.B. Waterhouse, S.D. Targonski, and D.M. Kokotoff, "Design and performance of small printed antennas," *IEEE Trans. Antennas Propagat.*, vol. 46, pp. 1629-1633, Nov. 1998.

[4] C.R. Rowell, and R.D. Murch, "A capacitively loaded PIFA for compact mobile telephone handsets," *IEEE Trans. Antennas Propagat.*, vol. 45, pp. 837-842, May 1997.

[5] H.K. Kan and R.B. Waterhouse, "Size reduction technique for shorted patches," *Electron. Lett.*, vol. 35, pp. 948-949, June 1999.

[6] R.L. Li, G. DeJean, E. Tsai, E. Tentzeris, and J. Laskar, "Novel Small Folded Shorted-Patch Antennas," *IEEE APS Int. Symp.*, Vol. 4, pp. 26-29, 2002.

[7] P.M. Mendes, A. Polyakov, M. Bartek, J.N. Burghartz, and J.H. Correia, "Design of a Folded-Patch Chip-Size Antenna for Short-Range Communications," *Microwave Conference*, vol. 2, pp. 723-726, 2003.

[8] R.L. Li, G. DeJean, M.M. Tentzeris, and J. Laskar, "Development and Analysis of a Folded Shorted-Patch Antenna With Reduced Size," *IEEE Trans. Antennas Propagat.*, vol. 52, pp. 555-562, 2004.
[9] R. Garg, P. Bhartia, I. Bahl, and A. Ittipiboon, *Microstrip Antenna Design Handbook*, Chapter 4, Norwood, MA: Artech House, 2001.
[10] http://www.ansoft.com/

Paper VI

A Cable-Free Impedance and Gain Measurement Technique for Electrically Small Antennas

Jiaying Zhang, Pivnenko Sergey and Olav Breinbjerg

Proceedings of the 32nd Annual Symposium of Antenna Measurement Techniques Association (AMTA 2010)

Presented in Atlanta, US, Oct. 2010.

A CABLE-FREE IMPEDANCE AND GAIN MEASUREMENT TECHNIQUE FOR ELECTRICALLY SMALL ANTENNAS

Jiaying Zhang[1], Sergey Pivnenko[2], and Olav Breinbjerg[3]
Department of Electrical Engineering, Technical University of Denmark
Ørsteds Plads, Building 348, DK-2800 Kgs. Lyngby, Denmark
[1]jz@elektro.dtu.dk, [2]sp@elektro.dtu.dk, and [3]ob@elektro.dtu.dk

ABSTRACT

Impedance and gain measurements for electrically small antennas represent a great challenge due to influences of the feeding cable. The leaking current along the cable and scattering effects are two main issues caused by the feed line. In this paper, a novel cable-free antenna impedance and gain measurement technique for electrically small antennas is proposed. The antenna properties are extracted by measuring the signal scattered by the antenna under test (AUT), when it is loaded with three known loads. The technique is based on a rigorous electromagnetic model where the probe and AUT are represented in terms of spherical wave expansions (SWEs), and the propagation is accounted for by a transmission formula. In this paper the measurement results by the proposed technique will be presented for several AUTs, including a standard gain horn antenna, a monopole antenna, and an electrically small loop antenna. A comparison of measurement results by using the proposed method and by using other methods will be presented.

Keywords: Impedance Measurement, Gain Measurement, Electrically Small Antennas, Spherical Wave Expansions.

1 Introduction

In recent years, there has been a strong interest in antenna miniaturization for numerous applications. Several measurement techniques are being used for electrically small antennas, but problems still exist. Measurements of the impedance and gain for electrically small antennas represent a great challenge due to the following reasons. First, the feeding cable may have a significant influence on the measured radiation pattern and radiation efficiency due to the leaking current which exists on the outer conductor of the cable. For instance, for electrically small antennas with low radiation efficiency, the measured efficiency can be strongly overestimated due to this effect [1]. Although a balun can be used to avoid the leaking current, it is typically a narrow-band device. Several baluns are thus required for different frequency bands. Also, the dimensions of the balun need to be tuned carefully at the specified frequency. In addition, the balun may have a size comparable to or even larger than that of the small antenna and thus it may give rise to the scattering. Second, the feeding cable contributes a large scattering structure even if the leaking current can be avoided. Measurement of small antenna characteristics avoiding the use of the feeding cable is therefore highly desirable.

In this paper, we propose a novel cable-free measurement technique to measure the input impedance and gain of electrically small antennas. It is formulated slightly differently from the RCS method [2] - [5]. A complete electromagnetic model is established for the measurement system by using the spherical wave expansions for the AUT and probe and the transmission formula to account for the propagation between these. The measurement system is modeled by the cascade of three coupled multiple-port network which represent the probe antenna, AUT, and the propagation in-between, respectively. The full theory and complete electromagnetic model of this measurement technique, together with the simulation results, are given in [7]. The present work emphasizes this with several measurement results.

2 Electromagnetic Model of the Measurement System

In this model the mono-static configuration is described where the probe antenna is both transmitting and receiving, while the AUT is located at a finite distance from the probe. The time convention $e^{-i\omega t}$ is used in this model.

2.1. Model of the Probe and AUT

The electric field $\vec{E}(\vec{r})$ around an antenna, enclosed by the minimum sphere of radius r_0, can be expressed as a spherical wave expansion for $r > r_0$ as [6]

$$\vec{E}(\vec{r}) = \frac{k}{\sqrt{\eta}} \sum_{s=1}^{2} \sum_{n=1}^{N} \sum_{m=-n}^{n} \{a_{smn} \vec{F}_{smn}^{(4)}(\vec{r}) + b_{smn} \vec{F}_{smn}^{(3)}(\vec{r})\} \qquad (1)$$

where the superscript c=3, 4 denotes outward and inward propagating waves, respectively. a_{smn} and b_{smn} are the expansion coefficients. $\vec{F}_{smn}^{(c)}$ is the power-normalized spherical vector wave function. k is the wave number, η is the intrinsic admittance of the medium, and $\vec{r}$ is the position vector for a point with (r, θ, ϕ) spherical coordinates. For practical measurements only a finite number of spherical modes are needed to represent the fields, and truncation number N is for the n summation to make sure the fields are converged.

An antenna can be modeled as a multi-port network with one excitation port that is connected to the generator and the radiation ports. Each radiation port represents one spherical wave outside the antenna minimum sphere r_0. The total scattering matrix expression for the antenna can be expressed as [6]

$$\begin{bmatrix} w \\ \bar{\mathbf{b}}_{smn} \end{bmatrix} = \underbrace{\begin{bmatrix} \Gamma & \bar{\mathbf{R}}_{s'm'n'} \\ \bar{\mathbf{T}}_{smn} & \bar{\bar{\mathbf{S}}}_{s'm'n'}^{smn} \end{bmatrix}}_{[\bar{\bar{\mathbf{S}}}]} \cdot \begin{bmatrix} v \\ \bar{\mathbf{a}}_{s'm'n'} \end{bmatrix} \tag{4}$$

where v and w are the complex amplitudes of the incoming and outgoing waves on the excitation port of the antenna. $\bar{\mathbf{a}}_{s'm'n'}$ and $\bar{\mathbf{b}}_{smn}$ are column vectors that represent the complex amplitudes of the incoming and outgoing spherical modes, respectively. $\bar{\mathbf{R}}_{s'm'n'}$ is a row vector with the antenna receiving coefficients. $\bar{\mathbf{T}}_{smn}$ is a column vector with the antenna transmitting coefficients. $\bar{\bar{\mathbf{S}}}_{s'm'n'}^{smn}$ is a matrix with the antenna structural scattering coefficients. $[\bar{\bar{\mathbf{S}}}]$ is the antenna scattering matrix.

2.2 Transmission Formula and Model of the Propagation

We define the coordinate (x, y, z) with respect to the probe, and the primed coordinate (x', y', z') with respect to the AUT. In general the primed coordinate system of the probe is related to the unprimed coordinate system of the AUT by 3 rotations - through the angles ϕ, θ, χ and one translation of the distance A, see [6]. The transmission formula describes the complex signal received by the AUT in terms of the transmission coefficients of the probe, the receiving coefficients of the AUT, the 3 rotation angles, and the translation distance A [6], which is

$$w(A,\chi,\theta,\varphi) = \frac{v}{2}\sum_{\substack{smn \\ \sigma\mu\nu}} T_{smn}^{Probe} e^{im\varphi} e^{i\mu\chi} d_{\mu m}^{n}(\theta) C_{\sigma\mu\nu}^{sn(3)}(kA) R_{\sigma\mu\nu}^{AUT}, \tag{5}$$

where smn and $\sigma\mu\nu$ are the indices of the SWEs of the transmitting probe and receiving AUT, respectively. T_{smn}^{Probe} is transmitting coefficient of the probe, and $R_{\sigma\mu\nu}^{AUT}$ is the receiving coefficient of the AUT. $e^{im\varphi}$, $e^{i\mu\chi}$, and $d_{\mu m}^{n}(\theta)$ are the rotation coefficients, and $C_{\sigma\mu\nu}^{sn(3)}(kA)$ is the translation coefficient.

2.3 Model of the Entire Measurement System

The measurement system of the proposed cable-free technique is presented in Fig. 1. In this model, the entire measurement setup is analyzed by the cascade of three coupled multiple-port network which represent the probe, the free space propagation, and the AUT respectively. The scattering matrix equations for the AUT and probe can be formulated as

$$\begin{bmatrix} w^{AUT} \\ \bar{\mathbf{b}}_{\sigma\mu\nu}^{AUT} - \bar{\mathbf{a}}_{\sigma'\mu'\nu'}^{AUT} \end{bmatrix} = \begin{bmatrix} \Gamma^{AUT} & \bar{\mathbf{R}}_{\sigma'\mu'\nu'}^{AUT} \\ \bar{\mathbf{T}}_{\sigma\mu\nu}^{AUT} & (\bar{\bar{\mathbf{S}}}_{\sigma\mu\nu}^{\sigma'\mu'\nu'AUT} - \bar{\bar{\mathbf{I}}}^{AUT}) \end{bmatrix} \cdot \begin{bmatrix} v^{AUT} \\ \bar{\mathbf{a}}_{\sigma'\mu'\nu'}^{AUT} \end{bmatrix} \tag{6}$$

and

$$\begin{bmatrix} w^{Probe} \\ \bar{\mathbf{b}}_{smn}^{probe} - \bar{\mathbf{a}}_{s'm'n'}^{Probe} \end{bmatrix} = \begin{bmatrix} \Gamma^{Probe} & \bar{\mathbf{R}}_{s'm'n'}^{Probe} \\ \bar{\mathbf{T}}_{smn}^{Probe} & (\bar{\bar{\mathbf{S}}}_{smn}^{s'm'n'Probe} - \bar{\bar{\mathbf{I}}}^{Probe}) \end{bmatrix} \cdot \begin{bmatrix} v^{Probe} \\ \bar{\mathbf{a}}_{s'm'n'}^{Probe} \end{bmatrix}, \tag{7}$$

where $\bar{\bar{\mathbf{I}}}^{Probe}$ and $\bar{\bar{\mathbf{I}}}^{AUT}$ denote the unit matrices of appropriate matrix sizes. The mode index smn and $s'm'n'$ represent outgoing and incoming spherical waves in the coordinate system of the probe, respectively. The mode index $\sigma\mu\nu$ and $\sigma'\mu'\nu'$ represent outgoing and incoming spherical waves in the coordinate system of the AUT, respectively.

The scattering matrix modeling the free space propagation can be expressed as

$$\begin{bmatrix} \bar{\mathbf{a}}_{s'm'n'}^{Probe} \\ \bar{\mathbf{a}}_{\sigma'\mu'\nu'}^{AUT} \end{bmatrix} = \begin{bmatrix} 0 & \bar{\bar{\mathbf{G}}}^{-} \\ \bar{\bar{\mathbf{G}}}^{+} & 0 \end{bmatrix} \cdot \begin{bmatrix} \bar{\mathbf{b}}_{smn}^{probe} \\ \bar{\mathbf{b}}_{\sigma\mu\nu}^{AUT} \end{bmatrix}, \tag{8}$$

where the element of the matrix $\bar{\bar{\mathbf{G}}}^{+}$ and $\bar{\bar{\mathbf{G}}}^{-}$ are obtained from the transmission formula (5).

On the other hand, the entire system also can be modeled by a two-port network with a scattering matrix $[\bar{\bar{\mathbf{S}}}^{T}]$. It is established for reference planes at the input terminal of the probe antenna and AUT. The scattering matrix $[\bar{\bar{\mathbf{S}}}^{T}]$ is expressed as

$$[\bar{\bar{\mathbf{S}}}^{T}] = \begin{bmatrix} S_{11}^{T} & S_{12}^{T} \\ S_{21}^{T} & S_{22}^{T} \end{bmatrix}, \tag{9}$$

and the entire measurement system is given by

$$\begin{bmatrix} w^{Probe} \\ w^{AUT} \end{bmatrix} = \begin{bmatrix} S_{11}^{T} & S_{12}^{T} \\ S_{21}^{T} & S_{22}^{T} \end{bmatrix} \cdot \begin{bmatrix} v^{Probe} \\ v^{AUT} \end{bmatrix}. \tag{10}$$

General expressions for S_{11}^{T}, S_{12}^{T}, S_{21}^{T}, and S_{22}^{T} can be obtained by eliminating the parameters $\bar{\mathbf{b}}_{smn}^{probe}$, $\bar{\mathbf{a}}_{s'm'n'}^{Probe}$, $\bar{\mathbf{b}}_{\sigma\mu\nu}^{AUT}$, and $\bar{\mathbf{a}}_{\sigma'\mu'\nu'}^{AUT}$. For increasing distance between the probe and the AUT the influence of the multiple scattering and reflection decreases because of the spatial attenuation of the free space propagation. We assume that the multiple scattered terms are negligibly small, and only the first interaction is taken into account, the s-parameters S_{11}^{T}, S_{12}^{T}, S_{21}^{T}, and S_{22}^{T} can then be simplified to

$$S_{11}^{T} \cong \Gamma^{Probe} + \bar{\mathbf{R}}^{Probe} \bar{\bar{\mathbf{I}}}^{Probe} \bar{\bar{\mathbf{G}}}^{-} (\bar{\bar{\mathbf{S}}}^{AUT} - \bar{\bar{\mathbf{I}}}^{AUT}) \bar{\bar{\mathbf{G}}}^{+} \bar{\mathbf{T}}^{Probe} \tag{11}$$

$$S_{12}^{T} \cong \bar{\mathbf{R}}^{Probe} \bar{\bar{\mathbf{I}}}^{Probe} \bar{\bar{\mathbf{G}}}^{-} \bar{\mathbf{T}}^{AUT} \tag{12}$$

$$S_{21}^{T} \cong \bar{\mathbf{R}}^{AUT} \bar{\bar{\mathbf{I}}}^{AUT} \bar{\bar{\mathbf{G}}}^{+} \bar{\mathbf{T}}^{Probe} \tag{13}$$

$$S_{22}^{T} \cong \Gamma^{AUT} + \bar{\mathbf{R}}^{AUT} \bar{\bar{\mathbf{I}}}^{AUT} \bar{\bar{\mathbf{G}}}^{-} (\bar{\bar{\mathbf{S}}}^{Probe} - \bar{\bar{\mathbf{I}}}^{Probe}) \bar{\bar{\mathbf{G}}}^{+} \bar{\mathbf{T}}^{AUT} \tag{14}$$

The second term on the right side of (14) represents the influence of the structural scattering from the probe on the S_{22}^T of the AUT. This term can be assumed negligibly small compared to the first term for two reasons. First, if a minimum scattering probe is employed, and, second, due to the spatial attenuation in $\bar{\bar{\mathbf{G}}}^+$ as well as $\bar{\bar{\mathbf{G}}}^-$. Thus (14) is approximated by

$$S_{22}^T \cong \Gamma^{AUT}. \tag{15}$$

2.4 Determination of the Total Scattering Matrix $[\bar{\bar{\mathbf{S}}}^T]$ from Measurements

The measurement setup is described as follows. There are two antennas involved in this cable-free measurement setup, as illustrated in Fig. 1, which are the transmitting and receiving probe and the AUT. Their scattering matrices are $[\bar{\bar{\mathbf{S}}}]^{Probe}$ and $[\bar{\bar{\mathbf{S}}}]^{AUT}$, respectively.

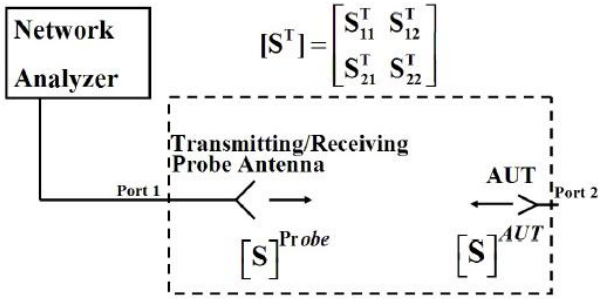

Figure 1 – Setup of cable-free technique for the impedance and gain measurement of small antennas.

When the AUT is loaded, the measured reflection coefficient at the input terminal of the probe antenna is denoted noted by $S_{11}^{T'}$, which is related to the two-port scattering parameter $[\bar{\bar{\mathbf{S}}}^T]$ as

$$S_{11}^{T'} = S_{11}^T + \frac{S_{12}^T S_{21}^T \Gamma_L}{1 - S_{22}^T \Gamma_L} \tag{16}$$

where Γ_L is the reflection coefficient of the loads.

In the measurement setup which is illustrated in Fig. 1, the AUT is loaded in turn by a short-circuit, an open circuit, and a known load, and the input reflection coefficients of the transmitting probe are measured. Then the scattering parameters S_{11}^T, S_{22}^T, and $S_{12}^T S_{21}^T$ of the total scattering matrix can be extracted respectively, which are related to the input reflection coefficient and gain of the AUT. S_{11}^T and S_{22}^T are determined from

$$\begin{bmatrix} S_{11}^T \\ S_{22}^T \end{bmatrix} = \begin{bmatrix} (\frac{1}{\Gamma_L^{(1)}} - \frac{1}{\Gamma_L^{(2)}}) & (S_{11}^{T',(1)} - S_{11}^{T',(2)}) \\ (\frac{1}{\Gamma_L^{(1)}} - \frac{1}{\Gamma_L^{(3)}}) & (S_{11}^{T',(1)} - S_{11}^{T',(3)}) \end{bmatrix}^{-1} \cdot \begin{bmatrix} \frac{S_{11}^{T',(1)}}{\Gamma_L^{(1)}} - \frac{S_{11}^{T',(2)}}{\Gamma_L^{(2)}} \\ \frac{S_{11}^{T',(1)}}{\Gamma_L^{(1)}} - \frac{S_{11}^{T',(3)}}{\Gamma_L^{(3)}} \end{bmatrix} \tag{17}$$

where $\Gamma_L^{(1),(2),(3)}$ are the measured reflection coefficient of each load, and $S_{11}^{T',(1),(2),(3)}$ are the measured reflection coefficient of the transmitting probe antenna when the AUT is loaded in three cases. $S_{12}^T S_{21}^T$ can be extracted after S_{11}^T and S_{22}^T are determined, that is

$$S_{12}^T S_{21}^T = (S_{11}^{T',(i)} - S_{11}^T)(1 - S_{22}^T \Gamma_L^{(i)}) / \Gamma_L^{(i)}, \tag{18}$$

where i=1, 2, 3. It is noted that there are three sets of data are available to be used in this equation, which are obtained from three measurements, and they should lead to the same results of $S_{12}^T S_{21}^T$. Taking an average of the results from different sets will result in an improvement in the accuracy.

2.5. Antenna Impedance and Gain Determination

The impedance of the AUT, Z^{AUT}, can be determined from S_{22}^T using the formula (15), which is

$$Z^{AUT} = Z_0 \frac{1 + \Gamma^{AUT}}{1 - \Gamma^{AUT}}, \tag{19}$$

where Z_0 is the characteristic impedance. The gain of the AUT can be determined by expressing the transmission formula in terms of the gain product of the probe and AUT, which are

$$G^{Probe} G_p^{AUT} = \frac{4(kA)^2 \mid S_{12}^T \mid^2}{(1 - \mid \Gamma^{Probe} \mid^2)(1 - \mid \Gamma^{AUT} \mid^2)}. \tag{20}$$

Here, G_p^{AUT} is the partial gain of the AUT which is parallel to the polarization of the probe. The characteristics of the transmitting probe antenna are assumed known to us from a separate calibration, which are G^{Probe} and Γ^{Probe}. Hence, G_p^{AUT} can be extracted by using the equation (17), (18), and (20). (20) is the key relation that is used in this cable-free gain measurement technique. It must be mentioned that the probe is assumed to be linearly polarized while the polarization of AUT is arbitrary. The gain of the AUT is determined by two orthogonal partial gain measurements.

3. Measurement Results and Discussions

Three measurement examples by the proposed method will be presented in this section. A standard gain horn antenna, a monopole antenna, and an electrically small loop antenna will be tested as the AUT, respectively. A commercial available standard gain horn antenna will be used as the probe for all these measurements.

3.1. Measurements for the Standard Gain Horn

In order to verify the proposed method, two identical commercial available horn antennas are measured first by the proposed method, which are tested as the probe and AUT, respectively, as shown in Fig. 2. First, the input reflection coefficient of the probe is measured by using the vector network analyzer (VNA) HP 8753D, when the AUT is connected to a short, open, and 50 ohm load, respectively. Second, the reflection coefficients of three loads are measured. Then the antenna input reflection coefficient and the gain product of two antennas can be extracted from the measurement data by using the equations (15), (17), (18), and (20). Since two identical horn antennas are used, the gain for each horn antenna can be determined by taking the square root of (20).

In this measurement, the frequency range is set to 800 MHz-1000 MHz. The following settings in the VNA are performed to ensure a sufficient dynamic range and accuracy. The number of points used in this frequency range is selected be to 1601 points. The power level is set to the maximum value of the VNA that is +10 dBm. A narrow IF bandwidth is desired which is set to 30 Hz in this measurement.

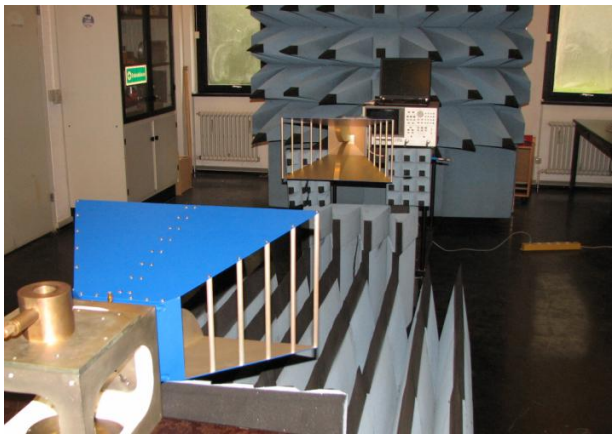

Figure 2 –The setup of the cable-free measurement technique, for two identical horn antennas.

As shown in Fig. 2, the measurement is performed in a partial anechoic environment. The absorbers are placed on the ground floor and around the antennas, but not on the ceiling and walls. The distance between the probe and AUT is 7 wavelengths at 1 GHz. The measured antenna gain versus frequency is shown in Fig. 3, and the result is also compared to the antenna gain given in the datasheet. The deviation in the gain is less than 0.5 dB. The comparison of antenna input reflection coefficient versus frequency by using the cable-free method and by using the direct VNA measurement is presented in Fig. 4. The small deviation in the reflection coefficient may be because the structural scattering of the probe is ignored. The noise in the measurement environment also has the influence.

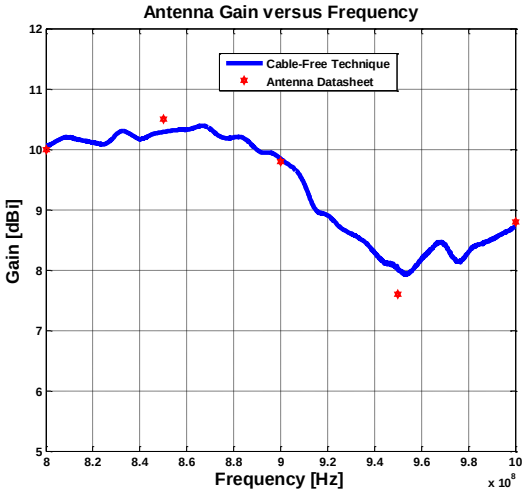

Figure 3 –Comparison of the antenna gain versus frequency, by the proposed method and datasheet.

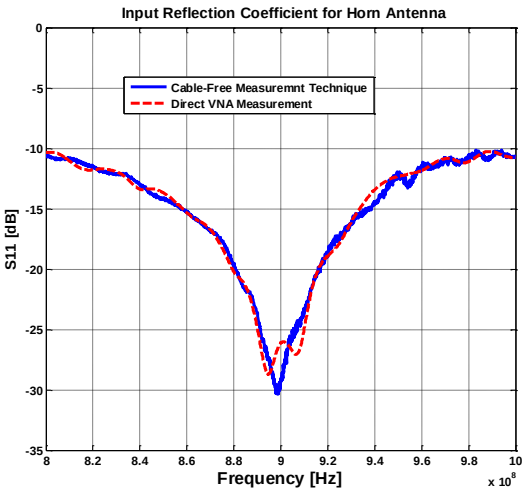

Figure 4 –Comparison of antenna input reflection coefficient versus frequency, by using the proposed method and by using direct VNA measurement.

3.2. Measurement Results for the Monopole Antenna

The measurement of the input reflection coefficient for a monopole antenna will be presented. The horn antenna will be used as the probe, while the monopole is treated as the AUT, as shown in Fig. 5. The length of the monopole is 80 mm and the wire diameter is 2 mm, which is made of copper and placed over an aluminum ground plane of the dimensions 40cm x 40cm. It is designed to be resonant around 870 MHz. Two measurements are performed at the distances of 1.7 m and 2.1 m, respectively, which are 5.5 wavelengths and 7 wavelengths at 1 GHz. Several pieces of foam are used to support the monopole antenna.

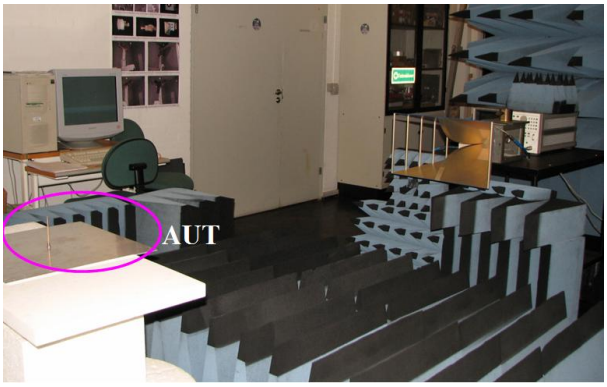

Figure 5 –The setup of the cable-free measurement technique, for the probe versus monopole antenna.

The reflection coefficients for the monopole antenna are presented in Fig. 6, compared to the direct VNA measurement. It is noted that a smoothing function was performed on the raw data to remove the noises. It is seen that the maximum deviation in the reflection coefficient is 0.7 dB, which is at 930 MHz. A good agreement can be observed at other frequencies.

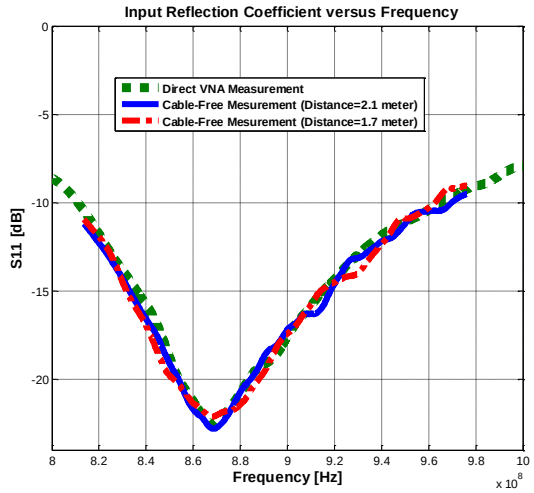

Figure 6 –Antenna input reflection coefficient versus frequency.

3.3. Measurement Results for the electrically small loop antenna

The measurements for an electrically small loop antenna will be presented in this section. As illustrated in Fig. 7 and Fig. 8, an electrically small loop antenna that is resonant at 910 MHz will be used as the AUT in this measurement. It is a self-resonant balanced electrically small loop antenna by using a distributed capacitive loading element. The working mechanism is based on the inductive coupling between two small loops. It is printed on the Rogers 5870 substrate with the thickness of 1.524 mm. The dielectric constant of the substrate is 2.33 and the loss tangent is 0.0012. The overall dimensions of the antenna are 35 mm x 10 mm, and the electric size of the antenna is ka=0.33, where k is the wave number and a is the radius of the minimum sphere enclosing the antenna.

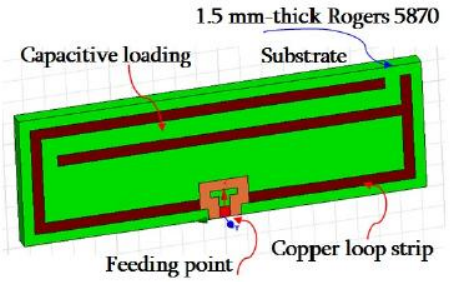

Figure 7 –The AUT: an electrically small loop antenna at 910 MHz (not scaled).

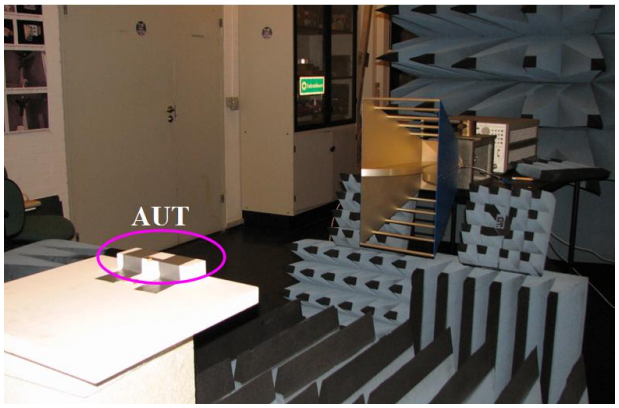

Figure 8 –The setup of the cable-free measurement technique, for the probe and the small loop antenna.

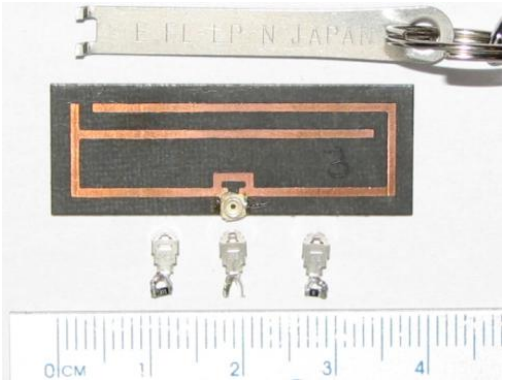

Figure 9 –The ultra small connector and loads for the electrically loop small antenna.

Different from the normal size antennas such as horn antennas, the ultra small connectors and loads are desired for electrically small antennas. The dimensions of the connectors and loads are required to be much smaller than that of the antennas to avoid the extra scattering effects. Several ultra small connectors and loads which are used in the measurements are illustrated in Fig. 9.

In this measurement, the distance between the probe and the AUT is 5.1 wavelengths at 900 MHz. The measured gain of the small loop antenna by using the proposed cable-free technique, the spherical near-field facility and the Wheeler cap are presented in Fig. 10, together with the simulated gain from HFSS. Comparisons of the measured antenna gain for the small loop antenna at the resonance frequency by different techniques show that the maximum deviation is up to 1.05 dB. The deviation in the gain indicates there is the effect due to the feeding cable. However, further analysis is underway to reach a full conclusion on this.

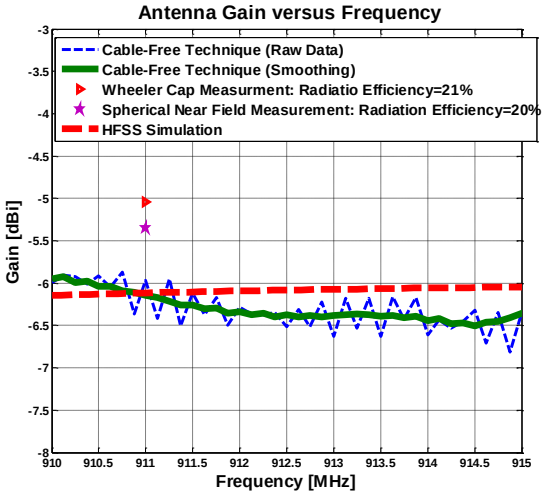

Figure 10 –Comparison of the antenna gain versus frequency by different techniques.

The measured reflection coefficients for the small loop antenna are shown in Fig. 11. A comparison of the raw data, the smoothing result of the cable-free measurement, and the direct VNA measurement are presented. In the direct VNA measurement, a balun is used in front of the loop antenna to avoid the leaking current on the cable. At the resonance frequency, the measured S_{11} from the direct VNA measurement is -24.5 dB, while the measured S_{11} from the proposed cable-free method is -22.5 dB. Thus there is a deviation of 2 dB. This deviation indicates there is the scattering effect due to the feeding cable or the balun.

6. Conclusions

In this paper, the electromagnetic model of a cable-free impedance and gain measurement technique for electrica-

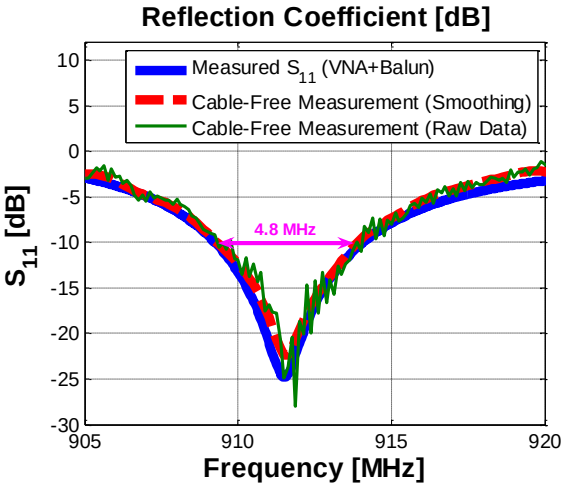

Figure 11 –Comparison of the antenna input reflection coefficients versus frequency.

lly small antennas is proposed by using the spherical wave expansion technique, which is valid for arbitrary AUT at arbitrary distances between the probe and AUT. The whole measurement setup is modeled by the cascade of three coupled multiple-port network. Three measurements by the proposed methods are presented. Comparison of the antenna measurement techniques, with and without the feeding cable, has shown that the there is the scattering effect from the cable in both the reflection coefficient measurement and gain measurement.

8. REFERENCES

[1] J. Zhang, S. Pivnenko, A. Khatun, T. Laitinen, and J. Carlsson, "Characterization of Small Antennas for Hearing Aids by Several Measurement Technique," 4th European Conference on Antennas and Propagation, 2010.

[2] J. Appel-Hansen, ”Accurate determination of gain and radiation patterns by radar crosssection measurements,” IEEE Trans. Anrennas Propagat.,vol. AP-27, pp. 640-645, Sept. 1979.

[3] W. Wiesbeck and E. Heidrich, "Wide-band multiport antenna characteriztion by polarimetric RCS measurement," IEEE Trans. AnreMos Propogat., vol. AP-46. pp. 341-350, March 1998.

[4] Hsin-Chia Lu and Tah-Hsiung Chu, "Antenna Gain and Scattering Measurement Using Reflective Three-Antenna Method," Antennas and Propagation Society International Symposium, 1999.

[5] B. Monsalve, S. Blanch, J.Romeu, and L. Jofre, "A contact-less small antenna characterization through impedance modulation," EuCAP 2009.

[6] Hansen J. E., "Spherical Near-Field Antenna Measurements", Peter Peregrinus Ltd. London, 1988.

[7] J. Zhang, S. Pivnenko, and O. Breinbjerg, "Electromagnetic Modeling of a Cable-Free Antenna Gain and Impedance Measurement Technique for Electrically Antenans Small Antennas ", in writing.

Paper VII

Application of the Modified Wheeler Cap Method for the Radiation Efficiency Measurement of Balanced Electrically Small Antennas

Jiaying Zhang, Pivnenko Sergey and Olav Breinbjerg

Proceedings of the 32nd Annual Symposium of Antenna Measurement Techniques Association (AMTA 2010)

Presented in Atlanta, US, Oct. 2010.

APPLICATION OF THE MODIFIED WHEELER CAP METHOD FOR RADIATION EFFICIENCY MEASUREMENT OF BALANCED ELECTRICALLY SMALL ANTENNAS IN COMPLEX ENVIRONMENT

Jiaying Zhang[1], Sergey Pivnenko[2], and Olav Breinbjerg[3]
Department of Electrical Engineering, Technical University of Denmark
Ørsteds Plads, Building 348, DK-2800 Kgs. Lyngby, Denmark
[1]jz@elektro.dtu.dk, [2]sp@elektro.dtu.dk, and [3]ob@elektro.dtu.dk

ABSTRACT

In this paper, application of a modified Wheeler cap method for the radiation efficiency measurement of balanced electrically small antennas is presented. It is shown that the limitations on the cavity dimension can be overcome and thus measurement in a large cavity is possible. The cavity loss is investigated, and a modified radiation efficiency formula that includes the cavity loss is introduced. Moreover, a modification of the technique is proposed that involves the antenna working complex environment inside the Wheeler Cap and thus makes possible measurement of an antenna close to a hand or head phantom. The measurement procedures are described and the key features of the technique are discussed. The results of simulations and measurements by the proposed method are presented and compared.

Keywords: Radiation Efficiency Measurement, Wheeler Cap Method, Balanced Antennas, Electrically Small Antennas, Antenna-on-Body Measurements

1 Introduction

Balanced electrically small antennas, such as dipoles and loops, have many applications, especially in ultra small devices like sensors, hearing-aids, and RFIDs. Wide use of balanced antennas in these applications is caused by the fact that a ground plane required for proper operation of unbalanced antennas, such as monopoles or inverted F antennas, is not existing in the ultra small devices. The performance of unbalanced antennas is then very sensitive to the changes in working environment, while the balanced antennas are less sensitive to these.

For electrically small antennas, the antenna impedance and radiation efficiency are two important parameters that characterize their performance and are of particular interest. However, proper measurement of these two parameters represents great challenges. Unless a carefully adjusted balun is used, the feeding coaxial cable has a significant influence on the measured performance due to leaking current on the outer conductor and the scattering effects. Accurate measurement methods for balanced small antennas need to be addressed, especially for measurement of the radiation efficiency.

The Wheeler cap method is widely used for the radiation efficiency measurement of electrically small antennas [1], [2]. However, this method possesses several limitations. First, it is only well applicable for small antennas with a ground plane, while for balanced small antennas a properly adjusted balun is required. Typically used sleeve balun is a narrowband device and its careful adjustment complicates the measurement. Second, presence of the cavity resonances and their influence on the measurement results imposes certain limitations on the dimensions of the cavity. Thus measurements of different small antennas working at different frequencies may require several cavities of different dimensions, since measurements in a wide frequency band represent great challenge. Moreover, limited dimensions of the cavity also impose limitations on measurement of antennas in complex environment, for instance, measurements in the presence of human hand or head phantoms or antenna-on-body measurements are not possible.

A modified Wheeler cap method, proposed recently in [3] and applied in [4] for balanced antennas, gives significant improvements on this method and allows the radiation efficiency measurements for different kind of small antennas, including balanced, unbalanced, symmetric, and asymmetric types. Measurements in a wide frequency band are also possible, which thus removes the limitation for the cavity size. Therefore, the method allows the measurement using a large cavity and thus it provides the potential to involve the complex environment. In this paper, this modified Wheeler cap method is applied for radiation efficiency measurement of balanced electrically small antennas, with particular focus on involvement of the complex environment: a human head phantom.

2. Model of the Three-Port Wheeler Cap Method

The original Wheeler cap method was first proposed in [1], by using an assumption that the antenna impedance can be modeled by the series of the radiation resistance and loss resistance. Then this method was further developed in [2] and [3], in which a two-port network model is proposed by assuming that the antenna is operated in a single radiation mode, and the two ports are defined as the antenna input terminal and the transition between the antenna and free space, respectively. Two measurements

are involved in this method, which are the measurement of the antenna input reflection coefficient in free space and in a Wheeler cap, respectively. The antenna radiation efficiency can then be extracted. However, the method is still applied to measurements in a small cavity.

In this paper, it is proposed to apply the Wheeler cap method for measurement in a large cavity. In addition, a three-port network model is proposed for the Wheeler cap method for measuring the radiation efficiency of small balanced antennas.

As shown in Fig. 1, the three ports are two excitation ports and one radiation port. A balanced (differential-fed) antenna can be viewed as a linear two port model with a virtual ground plane assumed in the middle of the excitation terminal. Determination of differential impedance by using the S-parameter based measurements has been studied previously [5]-[6]. In this paper, we apply the determination of the differential impedance based on the S-parameters measurements in combination with the Wheeler cap method to determine the radiation efficiency for balanced small antennas.

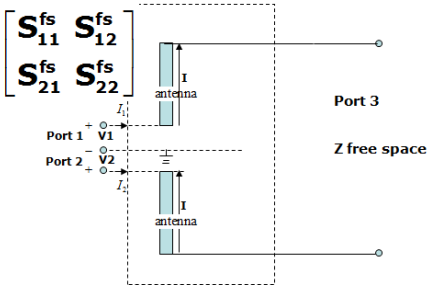

Figure 1 - An electrically small balanced antenna with the two-port excitation in free space.

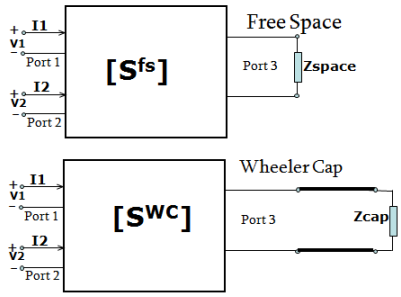

Figure 2 - The three-port network model for Wheeler cap measurement of the balanced small antenna.

An electrically small dipole antenna with the two-port excitation in free space is illustrated in Fig. 1. Inside the Wheeler cap, Fig. 2, the port 3 is loaded with the impedance of the Wheeler cap, with the reflection coefficient Γ_L, and we can obtain the scattering equations for the two ports

$$\begin{bmatrix} S_{11}^{wc} & S_{12}^{wc} \\ S_{21}^{wc} & S_{22}^{wc} \end{bmatrix} = \begin{bmatrix} S_{11} + \dfrac{S_{13}S_{31}\Gamma_L}{1-S_{33}\Gamma_L} & S_{12} + \dfrac{S_{13}S_{32}\Gamma_L}{1-S_{33}\Gamma_L} \\ S_{21} + \dfrac{S_{23}S_{31}\Gamma_L}{1-S_{33}\Gamma_L} & S_{22} + \dfrac{S_{23}S_{32}\Gamma_L}{1-S_{33}\Gamma_L} \end{bmatrix}, \quad (1)$$

where S_{nm}^{wc} are the S-parameters of the model obtained in the Wheeler cap. While in free space, $\Gamma_L = 0$, and the scattering equations can be simplified to

$$\begin{bmatrix} S_{11}^{fs} & S_{12}^{fs} \\ S_{21}^{fs} & S_{22}^{fs} \end{bmatrix} = \begin{bmatrix} S_{11} & S_{12} \\ S_{21} & S_{22} \end{bmatrix}. \quad (2)$$

where the S_{nm}^{fs} are the S-parameters of the model obtained in free space, as shown in Fig. 2. In order to determine the antenna radiation efficiency, two measurements are required, which are the full two-port S-parameter measurement in free space and in the Wheeler cap. For symmetric electrically small antennas, the antenna input impedance Z_{ant} in free space and in the Wheeler cap can be determined from

$$Z_{ant}^{fs} = \frac{2Z_0(1+S_{11}^{fs}-S_{21}^{fs})}{(1-S_{11}^{fs}+S_{21}^{fs})} \quad (3)$$

$$Z_{ant}^{wc} = \frac{2Z_0(1+S_{11}^{wc}-S_{21}^{wc})}{(1-S_{11}^{wc}+S_{21}^{wc})} \quad (4)$$

Here, Z_0 is the characteristic impedance of the feed cable. For geometrically asymmetric electrically small antennas, the antenna input impedance Z_{ant} in free space and in the Wheeler cap are

$$Z_{ant}^{fs} = \frac{2Z_0(1-S_{11}^{fs}S_{22}^{fs}+S_{12}^{fs}S_{21}^{fs}-S_{12}^{fs}-S_{21}^{fs})}{(1-S_{11}^{fs})(1-S_{22}^{fs})-S_{21}^{fs}S_{12}^{fs}} \quad (5)$$

$$Z_{ant}^{wc} = \frac{2Z_0(1-S_{11}^{wc}S_{22}^{wc}+S_{12}^{wc}S_{21}^{wc}-S_{12}^{wc}-S_{21}^{wc})}{(1-S_{11}^{wc})(1-S_{22}^{wc})-S_{21}^{wc}S_{12}^{wc}} \quad (6)$$

The equations (3) and (5) give the input impedance of the balanced small antennas, for the symmetric and asymmetric type, respectively. Then antenna radiation efficiency e_{rad} can be calculated from

$$e_{rad} = \frac{1}{1-|\Gamma_{ant}^{fs}|^2} \times \frac{2}{(\Delta S_{max})^{-1}+(\Delta S_{min})^{-1}} \quad (7)$$

where ΔS_{max} and ΔS_{min} are maximum and minimum of $\Delta S = |\Gamma_{ant}^{fs} - \Gamma_{ant}^{wc}|$. In (7), the cavity is assumed to be lossless. However, the cavity loss may need to be compensated for frequencies that are higher than 2 GHz. A modified radiation efficiency formula that includes the cavity loss is now introduced,

$$e_{rad} = \frac{2}{e_{cavity}(1-|\Gamma_{ant}^{fs}|^2)[(\Delta S_{max})^{-1}+(\Delta S_{min})^{-1}]}, \quad (8)$$

where the term e_{cavity} represents the cavity efficiency and $e_{cavity}=1$ represents a lossless cavity. The cavity efficiency can be obtained from a Wheeler cap measurement by using a reference antenna with known radiation efficiency.

3. Key Features of the Modified Wheeler Cap Method

Proper treatment of several issues related to this method is critical for obtaining a good accuracy of the determined radiation efficiency. Several important features of the method are explained in this section.

3.1. The Circle Fitting Technique

The measured complex values Γ_{ant}^{fs} and Γ_{ant}^{wc} versus frequency should represent a set of points located on a curve approximating a circle in a complex plane. Due to presence of the cavity resonances, some points of the Γ_{ant}^{wc} are disturbed. In order to remove the disturbance, the measured reflection coefficient Γ_{ant}^{wc} is replaced by a corresponding circle, which is reconstructed by the circle fitting technique using the least squares minimization algorithm. For a given set of measured points, the sum of the squares of the offsets of the points from the curve is minimized, from which the curve best-fitting to the measurement data will be found. A clear advantage of this approach is the robustness with respect to the measurement errors. By using the method in [3] and by using a proper circle fitting technique, the influence of the cavity resonances can be effectively suppressed.

The coordinates of the extracted reflection coefficient Γ_{ant}^{wc} inside the Wheeler cap are denoted by (Γ_x^i, Γ_y^i), where *i* represents the number of the point. At least three points are required for the circle fitting, but the optimum number of points depends on several parameters. The chosen set of points is then fitted to the circle $(\Gamma_x^i-a)^2+(\Gamma_y^i-b)^2=r^2$, where r is the radius of the circle and (a,b) are the coordinates of the center of the circle. The error function that to be minimized is

$$\mathrm{F(a,\ b,\ r)}=\sum_{i=1}^{m}(L_i-r)^2;\text{and } L_i=\sqrt{(\Gamma_x^i-a)^2+(\Gamma_y^i-b)^2}. \quad (9)$$

Taking partial derivatives of the function F with respect to the variable *r*, *a*, and *b*, respectively, and setting these three derivatives to zero, the radius and the coordinates of the center of the circle can be determined from

$$r_{j+1}=\frac{1}{m}\sum_{i=1}^{m}\sqrt{(\Gamma_x^i-a_j)^2+(\Gamma_y^i-b_j)^2};(j\geq 0) \quad (10)$$

$$a_{j+1}=\frac{1}{m}\sum_{i=1}^{m}\Gamma_x^i+[\frac{1}{m}\sum_{i=1}^{m}L_i][\frac{1}{m}\sum_{i=1}^{m}\frac{a_j-\Gamma_x^i}{L_i}];(j\geq 0) \quad (11)$$

$$b_{j+1}=\frac{1}{m}\sum_{i=1}^{m}\Gamma_y^i+[\frac{1}{m}\sum_{i=1}^{m}L_i][\frac{1}{m}\sum_{i=1}^{m}\frac{b_j-\Gamma_y^i}{L_i}];(j\geq 0) \quad (12)$$

where $a_0=\frac{1}{m}\sum_{i=1}^{m}\Gamma_x^i$ and $b_0=\frac{1}{m}\sum_{i=1}^{m}\Gamma_y^i$ are used as the initial estimate to solve the above equations by using a sets of points iteratively.

Using this approach the circle for Γ_{ant}^{wc} can be reconstructed from the above equations and this new curve will be used in the determination of the antenna radiation efficiency. Other circle reconstructing techniques will be investigated and compared in our future work.

3.2 The Port De-embedding Technique

A test fixture has to be employed for the impedance and radiation efficiency measurements for the balanced small antennas. As shown in Fig. 3, the test fixture is formed by two identical coaxial cables, with the outer conductors of the cables soldered together to provide a common ground. For each coaxial cable, one end is connected to a standard SMA connector, while the other end is left open with a small tip of the inner conductor, which is used to connect to the AUT. The full two-port calibration of the VNA is performed as usual, at the end of its cables.

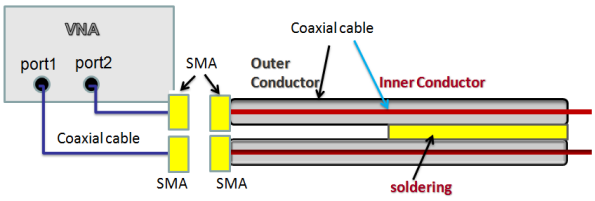

Figure 3 – The configuration of the test fixture.

In order to remove the effect of the test fixture, its de-embedding should be performed. The port extension function of VNA is used to perform the de-embedding calculation automatically from a short circuit measurement. However, in the port extension function of the VNA, it is assumed that the coaxial cable of the test fixture is the lossless transmission line and thus only the phase changes are removed from the measured s-parameter. The losses in the cables of the test fixture and impedance discontinuities in the SMA connectors are not compensated. Hence, the losses in the test fixture should be properly considered in the extraction of the radiation efficiency.

3.3 Antennas Working in a Complex Environment and Calibration of the Cavity and Phantom Losses

In the traditional application of the Wheeler cap method, the presence of the resonances in a large cavity enforces

using small cavities that also prevents measurement of antennas in their working environment. This can be seen as a serious disadvantage of this method. In this paper, the determination for the AUT radiation efficiency in complex environment with the Wheeler cap method is evaluated. The measurements are performed in a large cavity and using the proper circle fitting technique to reconstruct the reflection coefficients disturbed by the cavity resonances.

The antenna radiation efficiency is defined as the ratio of the radiated power to the accepted power, and it also can be presented in terms of the radiation resistance $R_{rad,ant}$ and ohmic loss resistance $R_{loss,ant}$, which is

$$e_{rad,ant} = \frac{R_{rad,ant}}{R_{rad,ant} + R_{loss,ant}} \tag{13}$$

This expression is used to represent the radiation efficiency of the antenna only when in free space. When the working environment is involved, and in this paper the presence of the head phantom is of particular interest, the radiation efficiency becomes

$$e_{rad} = \frac{R'_{rad,ant}}{R'_{rad,ant} + R'_{loss,ant} + R_{loss,head}} \tag{14}$$

$R'_{rad,ant}$ represents the radiation resistance in presence of the head, and $R_{loss,head}$ represents the loss in the head phantom, in free space.

While the losses obtained from the measurement inside the Wheeler cap represent a sum of the terms $R_{loss,ant}$, $R_{loss,cavity}$ and $R_{loss,head(wc)}$. Here, $R_{loss,cavity}$ is the loss in the cavity walls, and considering the high conductivity of the metal cavity this loss is typically very small. $R_{loss,head(wc)}$ represents the loss in the head phantom when it is inside the Wheeler cap. Two effects are involved in $R_{loss,head(wc)}$, which are the absorption losses due to the antenna and the cavity, respectively. Hence, the difference between the loss in the head phantom in free space and in Wheeler cap is the absorption loss inside the cavity. This difference and the cavity loss must be found out to determine the radiation efficiency. A calibration of the cavity losses and phantom absorption due to the cavity will be performed using a reference antenna with the known radiation efficiency. The calibration is the key feature for the radiation efficiency measurement in complex environments by using the Wheeler cap method.

4. Simulation Results and Discussions

An electrically small capacitive-loaded loop antenna was designed to be operated around 900 MHz. The loop is printed on the Rogers 5870 substrate with the dielectric constant of 2.33 and loss tangent of 0.0012. The overall dimensions of the antenna are $35\times10\times1.5$ mm^3. The simulation results for the radiation efficiency of this loop antenna by using an aluminum cylindrical cavity with the diameter of 26 cm and the height of 35 cm as the Wheeler cap have been presented in [4]. In this section, we focus on simulation results of the proposed method versus different cavity sizes, which will show the possibility of the Wheeler cap measurement in the large cavity.

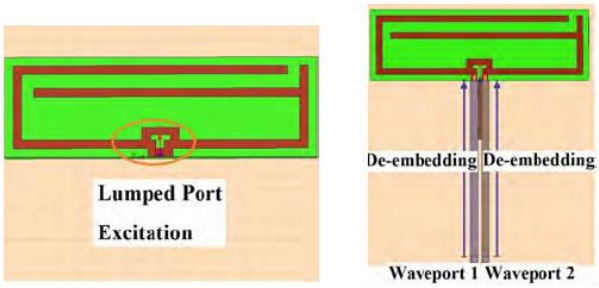

(a) **(b)**

Figure 4 - (a) Lumped port excitation of the small loop antenna (HFSS model). (b) Two waveport excitations and port de-embedding (HFSS model).

First, the loop antenna itself is simulated with HFSS software [7] by using lumped port excitation in free space, as shown in Fig. 4(a). For this configuration, the radiation efficiency is obtained directly and represents reference result.

Second, according to the proposed modified Wheeler cap method, the loop antenna with two extra cables is simulated in free space and in the Wheeler cap, respectively. The outer conductors of the test cables are connected in-between to provide a common ground and these two cables are properly taken into account in the simulation. The waveports are used as the excitation ports, as illustrated in Fig. 4(b), which are located at the end of each coaxial cable. In order to find the full two-port scattering matrix at the antenna port, the port de-embedding is applied on each waveport. It is noted that lossless cables are used in the simulation.

Several aluminum cavities are evaluated as the Wheeler cap, which are an aluminum cylindrical cavity with the diameter of 26 cm and the height of 35 cm and two rectangular cavities with the dimensions $40*40*40$ cm^3 and $60*60*60$ cm^3, respectively. The first cavity was originally designed for measurements of small antenna down to 400 MHz, but later it was found that it also can be used at higher frequencies by the generalized Wheeler cap method and proper circle fitting techniques, which allows avoiding influence of the cavity resonances. The simulated full two-port scattering matrix of the loop an-

tenna in free space and inside the Wheeler cap, respectively, is obtained. From these results, the radiation efficiency of the loop antenna is calculated.

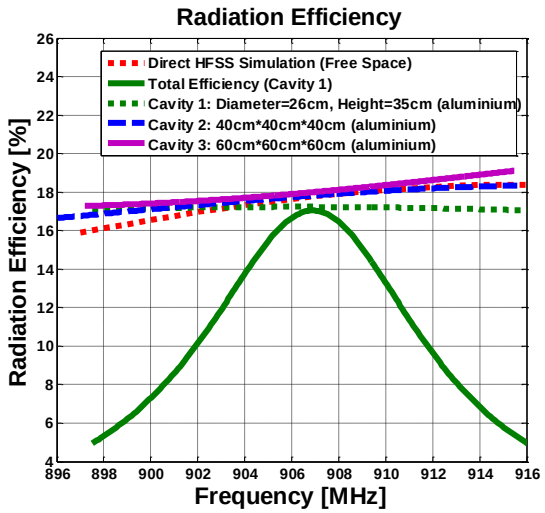

Figure 5 – Antenna radiation efficiency, obtained from a direct HFSS simulation and from full two-port scattering matrix in different cavities.

Fig.5 shows the radiation efficiency obtained from a direct HFSS simulation and that obtained from the full two-port scattering matrix in different cavities. At the resonance frequency, 906.5 MHz, the direct HFSS simulation gives a radiation efficiency of 17.7%, while the radiation efficiency obtained by the proposed method are 17.2%, 17.9%, and 17.8% for the cylindrical cavity, the $40\times40\times40$ cm^3 rectangular cavity, and the $60\times60\times60$ cm^3 cavity, respectively. The difference between the direct free space simulation and the proposed method are therefore 0.5%, 0.2%, and 0.1%. Hence, a good agreement is clearly observed. Decreasing the convergence parameter, which is the maximum delta for the S-parameters in HFSS, can result in an improvement in the agreement, but at the expense of long simulation time.

5. Measurement Results and Discussions

Two measurement examples by the proposed method will be presented in this section. First, the radiation efficiency of an electrically small loop antenna, which is used in the previous simulations, will be presented and compared to the results from other methods. Second, the radiation efficiency for the small loop antenna, close to the head phantom, will be shown. An aluminum cavity of the dimension $40\times40\times40$ cm^3 was build and used as the Wheeler cap in the experiments.

First, the full two-port scattering matrix was measured for the loop antenna in free space and in the Wheeler cap, by using the vector network analyzer HP 8753D. The extracted antenna radiation efficiency is shown in Fig. 6. The measured radiation efficiency is compared to the result obtained from a spherical near-field antenna facility, where the antenna was measured with a sleeve balun. It is seen from Fig. 6 that the measured radiation efficiency by using the anechoic chamber and by using the proposed method are 20% and 21%, respectively. The deviation by two different methods is only 1%. Hence a good agreement is observed and thus it confirms the validity of the proposed modified Wheeler cap method.

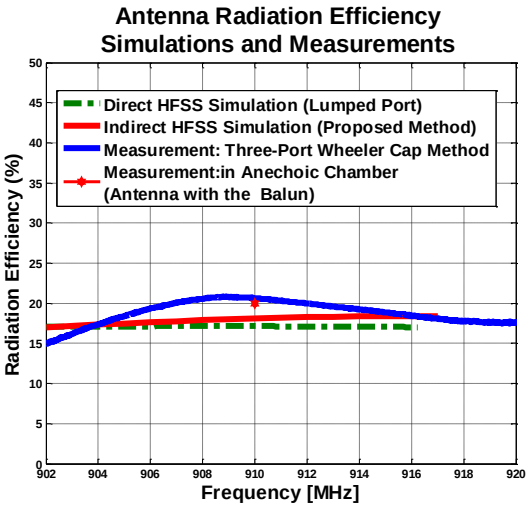

Figure 6 –The simulated and measured radiation efficiency for the small loop antenna only.

Second, the full two-port scattering matrix was measured for the loop antenna together with the head phantom, in free space and in the Wheeler cap, as illustrated in Fig. 7. The simulated and measured antenna radiation efficiency is presented in Fig. 8. Due to the presence of the head, the antenna resonance frequency is shifted from 910 MHz to 901 MHz. At the resonance, the measured radiation efficiency is 16%, while the simulated radiation efficiency is 15.2%. The deviation is 0.8%. However, the deviation becomes as large as 4 % at 910 MHz, and this is due to the worse impedance matching at that frequency.

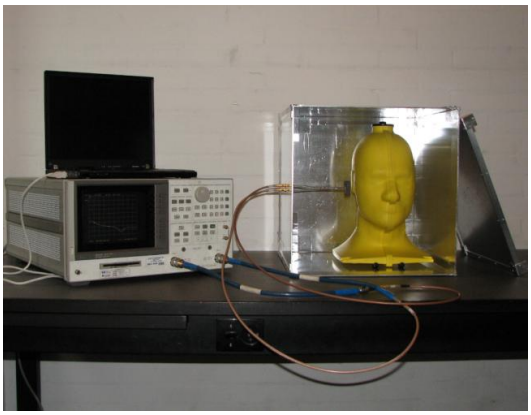

Figure 7 – The setup used in the measurements.

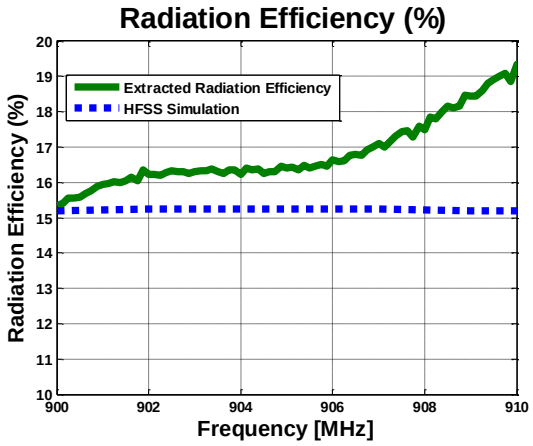

Figure 8 –The simulated and measured radiation efficiency for the small loop antenna, in presence of the head phantom.

In summary, the steps for this measurement can be given as follows.

- The calibration of the VNA is performed at the SMA connectors of the test fixture using the standard calibration kits.
- The de-embedding calculation of the test fixture must be performed. The parameters of the coaxial cable are extracted from a short circuit measurement.
- The calibration of the cavity losses and head phantom losses is performed by using a calibrated reference antenna with the known radiation efficiency.
- The full two port S-parameters of the balanced small antenna, together with the head phantom, are measured in free space.
- The full two port S-parameters of the balanced small antenna, together with the head phantom, are measured inside the Wheeler cap.
- The circle fitting technique is used to re-construct the antenna reflection coefficient inside the Wheeler cap.
- The antenna impedance and radiation efficiency are extracted together with the compensation of the losses in the test fixture, cavity, and head phantom.

6. Conclusions

The main results are summarized as follows. A technique is proposed for the radiation efficiency measurement of balanced small antennas by using the modified Wheeler cap method. It is shown that the limitation on the dimensions of the cavity size can be overcome with this method and the influence of cavity resonances can be removed by a proper circle fitting technique. Hence, it is possible to perform the radiation efficiency measurement inside a large cavity. The proposed method can also be applied for broadband antennas. Finally, the measurement technique for small antennas in complex environments inside the Wheeler cap is proposed. A calibration technique for the losses in the cavity and phantom is introduced. The device, in which the antenna is integrated, can be involved in the measurement, as well as the human body or human head phantom. Hence, the antenna on-body measurements become possible by using the proposed modified Wheeler cap method, which is inexpensive, fast, and able to provide accurate results.

One of the planned improvements to be tested is a new test fixture with thin cables and ultra small connectors, which is expected to reduce the influence of test fixture. Future development is the investigation on the antenna-on-body measurement in a cavity, which is larger than the one presented now. Different circle re-constructing techniques can be compared, aiming at improvement of the accuracy. Another future development is the ultra wideband antenna measurements in complex environment.

8. REFERENCES

[1] H. A. Wheeler, “The radian sphere around a small antenna,” Proceedings of the IRE, pp. 1325-1331, August 1959.

[2] R. H. Johnston and J. G. McRory, “An improved small antenna radiation efficiency measurement method,” IEEE Antennas Propagat. Mag., vol. 40, pp. 40-48, October 1998.

[3] M. Geissler, O. Litschke, D. Heberling, P. Waldowand I. Wolff, "An improved method for measuring theradiation efficiency of mobile devices", Proceedings of the IEEE Antennas and Propagation Society International Symposium, 2003, Vol. 4 , pp. 743 -746, 2003.

[4] J. Zhang, S. Pivnenko, and O. Breinbjerg. “A modified Wheeler cap method for radiation efficiency measurement of balanced electrically small antennas,” Eucap 2010, Barcelona, Spain.

[5] K. D. Palmer and M. W. V. Rooyen, “Simple broadband measurements of balanced loads using a network analyzer,” IEEE Trans. Microw. Theory Tech., vol. 55, no. 2, pp. 266-272, February 2006.

[6] X. Qing, C. K. Goh, and Z. N. Chen, “Impedance characterization of RFID tag antennas and application in tag co-design,” IEEE Trans. Instrum. Meas., vol. 57, no. 5, pp. 1268-1274, May 2009.

[7] http://www.ansoft.com/

Paper VIII

Electromagnetic Model of a Near-Field Cable-Free Impedance and Gain Measurement Technique for Electrically Small Antennas

Jiaying Zhang, Pivnenko Sergey and Olav Breinbjerg

Submitted to Proceedings of the Fifth European Conference on Antennas and Propagation (EuCAP 2011)

Rome, Italy, April 2011.

Electromagnetic Model of a Near-Field Cable-Free Impedance and Gain Measurement Technique for Electrically Small Antennas

Jiaying Zhang*[1], S. Pivnenko* and Olav Breinbjerg*
*Department of Electrical Engineering, Technical University of Denmark
Ørsteds Plads, Building 348, DK-2800 Kgs. Lyngby, Denmark
[1]jz@elektro.dtu.dk

***Abstract*—In this paper, a novel near-field cable-free impedance and gain measurement technique for electrically small antennas is proposed. In this technique, with the electrically small antenna placed in the near-field region of the probe, the properties of this antenna are extracted by measuring the signal scattered by it when it is loaded in turn with three known loads. The determination of the antenna impedance and gain is formulated by using the spherical wave expansion technique. The advantages of this measurement technique are summarized as follows. First, the limited dynamic range problem is avoided by the measurement close to the probe. As a result of this, the effect of noise is reduced and the measurement accuracy is improved significantly. Second, only a compact anechoic environment is required, which is easy to build. The expense of this technique is the increased complexity of the model.**

I. Introduction

In recent years, due to the rapid development of antenna miniaturization techniques, there is a strong demand for accurate characterization techniques for electrically small antennas (ESAs). Although several measurement techniques are being used for ESAs, some problems remain unsolved. When a small antenna is connected to a feeding cable, the electrical size of which is comparable to that of the ESA, the leaking current along the outer surface of the coaxial cable and the scattering from the cable may cause unwanted radiation. Although ferrite cores or quarter-wavelength baluns can be added to avoid the leaking current, the scattering effect can not be removed. Moreover, the size of balun is comparable to that of ESAs, which causes additional scattering, and the balun needs to be adjusted carefully. Thus, the measurement techniques for ESAs without using the coaxial cable are highly desirable. There exist such measurement techniques, the radar cross section method and the far-field cable-free measurement technique, which can provide antenna characteristics without using the cable. These techniques have been applied to small antennas [1-8]. However, the limited dynamic range and the effect of noise may cause problems since the radiation efficiency of small antennas can be low. For instance, the cross-polarization gain may not be extracted accurately from the measurement due to the limited dynamic range.

The purpose of this work is to derive a solution for a near-field measurement problem for ESAs without using the coaxial cable, by using which the limited dynamic range issue can be avoided and thus the measurement accuracy is improved. In this paper, an electromagnetic model of the near-field cable-free impedance and gain measurement technique for ESAs is proposed. It is noted that this technique is applicable for such electrically small antennas that can be modeled by a single Hertzian electric or magnetic dipole. It is also noted that there are many antennas which do not resemble a single dipole, and for those antennas the proposed technique may not be directly applicable. The approximation by a single dipole do not significantly limit the application range of this technique, since many practically designed ESAs resemble either small dipoles or small loops. For these antennas, the resonance frequency and the maximum gain are two parameters of particular interest. However, the traditional measurement techniques can not provide accurate measurement results for these parameters because of the feed line. Here we assume that most of the antenna characteristics are known from the design phase and from simulations, but the manufactured antennas may have different characteristics due to losses in dielectrics, finite manufacturing precision, etc. The proposed technique is then applied directly to validate the characteristics of manufactured antennas.

In this measurement setup, an electrically small antenna under test (AUT) is placed in the near-field region of the transmitting and receiving probe, and the measurement is performed at the input terminal of the probe by using a vector network analyzer. The AUT parameters are extracted by measuring the signal scattered by the AUT, when it is loaded in turn with three different loads. We assume here that the probe is an arbitrary electrically antenna. The advantages of using an electrically large probe can be explained as follows. First, the influence of the feed line on the electrically large probe is negligible. Second, it is easy to find a commercial available electrically large antenna with high gain and radiation efficiency. Also, with a directive probe the scattering effects from the room are suppressed.

In the proposed technique, the electromagnetic model of the measurement setup is represented in terms of the spherical wave expansion (SWE), which is used to model the probe, the propagation in-between and the AUT, respectively. The electrically small AUT is represented by a single spherical mode corresponding to the Hertzian dipole mode for simplic-

ity, while the probe is modeled by an arbitrary antenna with all necessary spherical modes taken into account. The propagation in-between is accounted for by a transmission formula. Then the measurement setup is modeled by the cascade of the above three coupled multiple-port network. The distance between the probe and AUT in this technique requires a special description. The application of SWE requires that the minimum spheres of the probe and AUT do not intersect, and moreover, there are additional couple of wavelengths between the radii of the minimum sphere. The further apart the probe and AUT are placed, the smaller is the effect of multiple reflections, but also the smaller is the signal received by the probe. Thus, a certain compromise is required when choosing the distance. Moreover, in order to reduce the multiple reflections, a probe with a minimum structural scattering can be chosen.

II. Electromagnetic Model of the Measurement System

In this section, the electromagnetic model of the measurement system is outlined. In this model, the mono-static configuration is described where the probe is both transmitting and receiving, while the AUT is located at a near-field distance from the probe. The models for the probe, the AUT, the propagation in-between and the overall measurement system are formulated. The time convention e^{-iwt} is adopted in the following derivations. The electric field $\vec{E}(\vec{r})$ around an antenna, enclosed by the minimum sphere of radius r_0, can be expressed by using SWE for $r > r_0$ [10], that is

$$\vec{E}(\vec{r}) = \frac{k}{\sqrt{\eta}} \sum_{s=1}^{2} \sum_{n=1}^{N} \sum_{m=-n}^{n} \{a_{smn} \vec{F}^{(4)}_{smn}(\vec{r}) + b_{smn} \vec{F}^{(3)}_{smn}(\vec{r})\} \tag{1}$$

where the superscript $c = 3, 4$ denotes outward and inward propagating waves, respectively. a_{smn} and b_{smn} are the expansion coefficients. $\vec{F}^{(c)}_{smn}$ are the power-normalized spherical vector wave functions. k is the wave number, η is the intrinsic admittance of the medium and $\vec{r}$ is the position vector for a point with (r, θ, ϕ) spherical coordinate system. For practical measurements only a finite number of spherical modes are needed to represent the fields, and the truncation number N is used for the n summation to ensure the convergence.

An antenna can be modeled as a multi-port network with one excitation port that is connected to the generator/load and the radiation ports. Each radiation port represents one spherical mode outside the antenna minimum sphere r_0. The equivalent network can be illustrated as shown in Fig. 1 (a) and (b). The total scattering matrix for the antenna can be written as [10]

$$\begin{bmatrix} w \\ \bar{\mathbf{b}}_{smn} \end{bmatrix} = \underbrace{\begin{bmatrix} \Gamma & \bar{\mathbf{R}}_{s'm'n'} \\ \bar{\mathbf{T}}_{smn} & \bar{\bar{\mathbf{S}}}^{smn}_{s'm'n'} \end{bmatrix}}_{[\bar{\bar{\mathbf{S}}}]} \cdot \begin{bmatrix} v \\ \bar{\mathbf{a}}_{s'm'n'} \end{bmatrix} \tag{2}$$

where v and w are the complex amplitudes of the incoming and outgoing waves on the excitation port of the antenna. $\bar{\mathbf{a}}_{s'm'n'}$ and $\bar{\mathbf{b}}_{smn}$ are column vectors that represent the complex amplitudes of the incoming and outgoing spherical modes, respectively. $\bar{\mathbf{R}}_{s'm'n'}$ is a row vector containing the antenna receiving coefficients. $\bar{\mathbf{T}}_{smn}$ is a column vector containing the antenna transmitting coefficients. $\bar{\bar{\mathbf{S}}}^{smn}_{s'm'n'}$ is a square matrix that contains the antenna structural scattering coefficients. $[\bar{\bar{\mathbf{S}}}]$ is the total scattering matrix. If there is no incoming wave, $\bar{\mathbf{a}}_{s'm'n'} = 0$, eq. (2) leads to

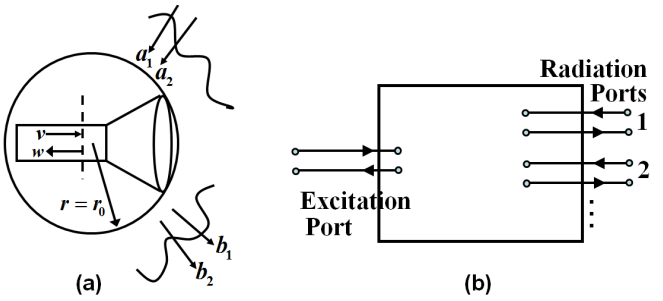

Fig. 1. The network representation for an antenna. (a) presents an antenna with spherical wave modes in its minimum sphere. (b) presents the network representation of the antenna modes. Reproduced from [10].

$$w = \Gamma v. \tag{3}$$

$$\bar{\mathbf{b}}_{smn} = v \bar{\mathbf{T}}_{smn}, \tag{4}$$

Both the probe and AUT can be modeled by a scattering matrix $[\bar{\bar{\mathbf{S}}}]$ in the form (2), which are denoted as $[\bar{\bar{\mathbf{S}}}^{Probe}]$ and $[\bar{\bar{\mathbf{S}}}^{AUT}]$, respectively.

In this derivation, we define the un-primed coordinates (x, y, z) with respect to the probe, and the primed coordinates (x', y', z') with respect to the AUT, as illustrated in Fig. 2. The primed coordinate system of the AUT is related to the unprimed coordinate system of the probe by 3 rotations - through the so-called Euler angles ϕ, θ, χ and one translation of the distance A, see [10]. The transmission formula describes the complex signal received by the AUT in terms of the transmission coefficients of the probe, the receiving coefficients of the AUT, the 3 rotation angles and the translation distance A [10]. The transmission formula for an arbitrary distance in-between (but larger that the sum of the AUT and probe radii of minimum spheres) is

$$\begin{aligned} w(A, \chi, \theta, \phi) &= \frac{v}{2} \sum_{\substack{smn \\ \sigma'\mu'\nu'}} T^{Probe}_{smn} e^{im\phi} e^{i\mu'\chi} d^n_{\mu' m}(\theta) \\ &\quad \cdot C^{sn(3)}_{\sigma'\mu'\nu'}(kA) R^{AUT}_{\sigma'\mu'\nu'}, \end{aligned} \tag{5}$$

where

$$\begin{aligned} s = 1, 2; m = -n, -n+1, ..., n; n = 1, 2... \\ \sigma' = 1, 2; \mu' = -\nu', -\nu'+1, ..., \nu'; \nu' = 1, 2... \end{aligned} \tag{6}$$

where smn and $\sigma'\mu'\nu'$ are the indices of the SWEs of the probe and AUT, respectively. T^{Probe}_{smn} are transmitting coefficients of the probe antenna and $R^{AUT}_{\sigma'\mu'\nu'}$ are the receiving coefficients of the AUT. $e^{im\phi}$, $e^{i\mu'\chi}$ and $d^n_{\mu' m}(\theta)$ are the rotation coefficients and $C^{sn(3)}_{\sigma'\mu'\nu'}(kA)$ are the translation coefficients. This analysis is started from a situation that the AUT is oriented along the $\hat{x}'$-axis. The electrically small AUT

is modeled by the single spherical mode that is corresponding to the electric Hertzian dipole mode. Hence, this leads to the following spherical modes for the AUT, $\sigma, \mu, \nu = 2, \pm 1, 1$. Then the transmission formula becomes

$$w(A,\chi,\theta,\phi) = \frac{v}{2} R_{211}^{AUT} \sum_{smn} T_{smn}^{Probe} e^{im\phi} [d_{1m}^{n}(\theta) e^{i\chi} \cdot C_{211}^{sn(3)}(kA) - d_{-1m}^{n}(\theta) e^{-i\chi} C_{2-11}^{sn(3)}(kA)], \quad (7)$$

where the relation of AUT receiving coefficients $R_{2-11}^{AUT} = -R_{211}^{AUT}$ is used. For $\mu' = \pm 1$, the translation coefficients $C_{211}^{sn(3)}(kA)$ and $C_{2-11}^{sn(3)}(kA)$ becomes

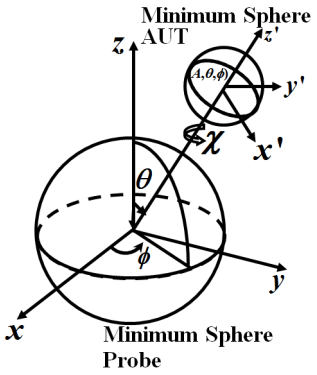

Fig. 2. Coordinates of the transmitting and receiving probe and AUT. Redrawn from [10].

$$C_{211}^{sn(3)}(kA) = \frac{\sqrt{3}}{2}\sqrt{2n+1}[\delta_{s,2} R_{2n}^{(3)}(kA) + \delta_{3-s,2} \cdot R_{1n}^{(3)}(kA)] \quad (8)$$

$$C_{2-11}^{sn(3)}(kA) = \frac{\sqrt{3}}{2}\sqrt{2n+1}[\delta_{s,2} R_{2n}^{(3)}(kA) - \delta_{3-s,2} \cdot R_{1n}^{(3)}(kA)] \quad (9)$$

where $R_{sn}^{(3)}(kA)$ is the radial dependence of the spherical wave function defined in [10; eq. (A1.6)]. Inserting (8) and (9) to (7) gives

$$\begin{aligned} w(A,\chi,\theta,\phi) = {} & \frac{v}{2} R_{211}^{AUT} \sum_{smn} T_{smn}^{Probe} e^{im\phi} \frac{\sqrt{3}}{2}\sqrt{2n+1} \\ & \{\delta_{3-s,2}[-(d_{1,m}^{n} + d_{-1,m}^{n})\cos\chi - i \cdot \\ & (d_{1,m}^{n} - d_{-1,m}^{n})\sin\chi] i R_{1n}^{(3)} + \\ & \delta_{s,2}[-(d_{1,m}^{n} - d_{-1,m}^{n})\cos\chi - i \cdot \\ & (d_{1,m}^{n} + d_{-1,m}^{n})\sin\chi] i R_{2n}^{(3)}\} \end{aligned} \quad (10)$$

By application of equations (A2.18) and (A2.19) in [10], the terms $(d_{1,m}^{n} + d_{-1,m}^{n})$ and $(d_{1,m}^{n} - d_{-1,m}^{n})$ in (10) are

$$d_{1,m}^{n} + d_{-1,m}^{n} = -\frac{2}{\sqrt{n(n+1)}} \frac{m d_{0m}^{n}(\theta)}{\sin\theta}, \quad (11)$$

$$d_{1,m}^{n} - d_{-1,m}^{n} = -\frac{2}{\sqrt{n(n+1)}} \frac{d}{d\theta}\{d_{0m}^{n}(\theta)\}, \quad (12)$$

with $d_{0m}^{n}(\theta)$ being

$$d_{0m}^{n}(\theta) = \left(\frac{-m}{|m|}\right)^{-1} \sqrt{\frac{2}{2n+1}} \bar{P}_{n}^{|m|}(\cos\theta). \quad (13)$$

Inserting the relations given in (11), (12) and (13) to (10), the transmission formula (10) becomes

$$w(A,\chi,\theta,\phi) = \frac{v}{2} R_{211}^{AUT} \sum_{smn} T_{smn}^{Probe} 2\sqrt{3\pi} \cdot \{[\bar{F}_{smn}^{(3)}]_{\theta}\cos\chi + [\bar{F}_{smn}^{(3)}]_{\phi}\sin\chi\}. \quad (14)$$

In the direction $\chi = \theta = 0^{o}$, (14) becomes

$$w(A,0,0,\phi) = v\sqrt{3\pi} R_{211}^{AUT} \sum_{s,m,n} T_{smn}^{Probe} [\bar{F}_{smn}^{(3)}]_{\theta}. \quad (15)$$

where the term $\sum_{s,m,n} T_{smn}^{Probe} [\bar{F}_{smn}^{(3)}]_{\theta}$ is proportional to the θ-component of probe electric field at the position of AUT. In the case the AUT is arbitrary oriented, the received signal will be expressed in terms of the probe field component along the direction of AUT orientation. It can be shown that the gain of AUT can be written as follows

$$G_{x}^{AUT} = \frac{3|R_{211}^{AUT}|^{2}}{1 - |\Gamma^{AUT}|^{2}}. \quad (16)$$

Combining (15) with (16), and taking into account the reflection coefficients of the probe and AUT, it can be derived

$$\frac{\frac{1}{2}|w|^{2}}{\frac{1}{2}|v|^{2}} = (1 - |\Gamma^{AUT}|^{2})(1 - |\Gamma^{Probe}|^{2})\pi G_{x}^{AUT} \cdot \left| \sum_{s,m,n} T_{smn}^{Probe} [\bar{F}_{smn}^{(3)}]_{\theta} \right|^{2}. \quad (17)$$

For the total measurement setup, a two-port scattering matrix can be established for reference planes at the input terminal of the probe and AUT. The total scattering matrix can be writhen as

$$[\bar{\bar{\mathbf{S}}}^{T}] = \begin{bmatrix} S_{11}^{T} & S_{12}^{T} \\ S_{21}^{T} & S_{22}^{T} \end{bmatrix}. \quad (18)$$

Equation (17) is related to S_{12}^{T} in the form

$$|S_{12}^{T}|^{2} = \frac{\frac{1}{2}|w|^{2}}{\frac{1}{2}|v|^{2}}, \quad (19)$$

and thus the gain of AUT is determined from

$$G_{x}^{AUT} = \frac{1}{(1 - |\Gamma^{AUT}|^{2})(1 - |\Gamma^{Probe}|^{2})} \cdot \frac{|S_{12}^{T}|_{x}^{2}}{\pi \left| \sum_{s,m,n} T_{smn}^{Probe} [\bar{F}_{smn}^{(3)}]_{\theta} \right|^{2}}. \quad (20)$$

where the probe parameters are obtained from a separate calibration and $|S_{12}^{T}|^{2}$ is extracted from the measurement results, as will be explained in Section III. The equation (20) is one of key equations in this measurement technique. It is noted that only the partial gain is determined from (20), and one more gain measurement may be required in the

orthogonal orientation of the AUT. The cross-polarization gain is determined from

$$G_y^{AUT} = \frac{1}{(1-|\Gamma^{AUT}|^2)(1-|\Gamma^{Probe}|^2)} \cdot \frac{|S_{12}^T|_y^2}{\pi \left|\sum_{s,m,n} T_{smn}^{Probe}[\bar{F}_{smn}^{(3)}]_\phi\right|^2}. \quad (21)$$

Then the total gain of AUT is determined from

$$G^{AUT} = G_x^{AUT} + G_y^{AUT}. \quad (22)$$

Similarly, for an $\hat{x}'$-oriented electrically small AUT that represents a single magnetic dipole, the gain of AUT can be determined from

$$G_m^{x,AUT} = \frac{1}{(1-|\Gamma^{AUT}|^2)(1-|\Gamma^{Probe}|^2)} \cdot \frac{|S_{12}^T|_x^2}{\pi \left|\sum_{s,m,n} T_{smn}^{Probe}[\bar{F}_{3-s,m,n}^{(3)}]_\theta\right|^2}. \quad (23)$$

Again, only the partial gain is determined from (23), and one more gain measurement may be required in the orthogonal orientation of the AUT. The cross-polarization gain is

$$G_m^{y,AUT} = \frac{1}{(1-|\Gamma^{AUT}|^2)(1-|\Gamma^{Probe}|^2)} \cdot \frac{|S_{12}^T|_y^2}{\pi \left|\sum_{s,m,n} T_{smn}^{Probe}[\bar{F}_{3-s,m,n}^{(3)}]_\phi\right|^2}. \quad (24)$$

Then the total gain of AUT is determined from

$$G_m^{AUT} = G_m^{x,AUT} + G_m^{y,AUT}. \quad (25)$$

III. Determination of the Total Scattering Matrix

The measurement setup is illustrated in Fig. 3. When the AUT is loaded, the measured scattering parameter at the input terminal of the probe antenna is denoted by $S_{11}^{T'}$, which is related to the two-port scattering parameter $[\bar{\bar{S}}^T]$ as

$$S_{11}^{T'} = S_{11}^T + \frac{S_{12}^T S_{21}^T \Gamma_L}{1 - S_{22}^T \Gamma_L} \quad (26)$$

where Γ_L is the known reflection coefficient of the load of the AUT.

In the measurement setup which is illustrated in Fig. 3, the AUT is loaded in turn by a short-circuit, an open circuit and a known load, and the input reflection coefficient of the transmitting probe is measured. Then the scattering parameters S_{11}^T, S_{22}^T and $S_{12}^T S_{21}^T$ of the total scattering matrix can be extracted. S_{11}^T and S_{22}^T are determined from

$$\begin{bmatrix} S_{11}^T \\ S_{22}^T \end{bmatrix} = \begin{bmatrix} (\frac{1}{\Gamma_L^{(1)}} - \frac{1}{\Gamma_L^{(2)}}) & (S_{11}^{T',(1)} - S_{11}^{T',(2)}) \\ (\frac{1}{\Gamma_L^{(1)}} - \frac{1}{\Gamma_L^{(3)}}) & (S_{11}^{T',(1)} - S_{11}^{T',(3)}) \end{bmatrix}^{-1} \cdot \begin{bmatrix} \frac{S_{11}^{T',(1)}}{\Gamma_L^{(1)}} - \frac{S_{11}^{T',(2)}}{\Gamma_L^{(2)}} \\ \frac{S_{11}^{T',(1)}}{\Gamma_L^{(1)}} - \frac{S_{11}^{T',(3)}}{\Gamma_L^{(3)}} \end{bmatrix} \quad (27)$$

where $\Gamma_L^{(1),(2),(3)}$ are the measured reflection coefficient

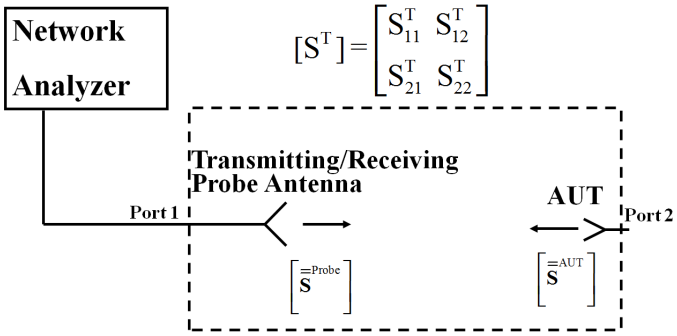

Fig. 3. Setup of the monostatic measurement for the reflection coefficient and gain of electrically small antennas.

of each load, and $S_{11}^{T',(1),(2),(3)}$ are the measured reflection coefficient of the transmitting probe antenna when the AUT is loaded in three cases. $S_{12}^T S_{21}^T$ can be extracted after S_{11}^T and S_{22}^T are determined, that is

$$S_{12}^T S_{21}^T = (S_{11}^{T',(i)} - S_{11}^T)(1 - S_{22}^T \Gamma_L^{(i)})/\Gamma_L^{(i)}, \quad (28)$$

where i=1,2,3. It is noted that there are three sets of data available for this equation, which are obtained from three measurements, and they should lead to the same results of $S_{12}^T S_{21}^T$. Taking an average of the results from different sets will result in an improvement of the accuracy.

IV. Impedance and Gain Determination

The relations between the total scattering matrix $\bar{\bar{\mathbf{S}}}^T$ and the scattering matrix of the probe and AUT that are $\bar{\bar{\mathbf{S}}}^{Probe}$ and $\bar{\bar{\mathbf{S}}}^{AUT}$ are presented in [8]- [9], and these will not be repeated here. The reflection coefficient of the AUT is related to S_{22}^T in the form

$$S_{22}^T = \Gamma^{AUT} + \bar{\mathbf{R}}^{AUT}[\bar{\bar{\mathbf{I}}}^{AUT} - \bar{\bar{\mathbf{G}}}^+(\bar{\bar{\mathbf{S}}}^{Probe} - \bar{\bar{\mathbf{I}}}^{Probe}) \cdot \bar{\bar{\mathbf{G}}}^-(\mathbf{S}^{AUT} - \mathbf{I}^{AUT})]^{-1}\bar{\bar{\mathbf{G}}}^+(\bar{\bar{\mathbf{S}}}^{Probe} - \bar{\bar{\mathbf{I}}}^{Probe}) \cdot \bar{\bar{\mathbf{G}}}^- \bar{\mathbf{T}}^{AUT}. \quad (29)$$

The second term on the right side of (29) represents the influence of the structural scattering from the probe on the S_{22}^T of the AUT. This term can be assumed negligibly small compared to the first term for two reasons. First, if a minimum scattering probe is employed, and, second, due to the spatial attenuation in $\bar{\bar{\mathbf{G}}}^+$ and $\bar{\bar{\mathbf{G}}}^-$ that represent the propagation between the probe and AUT, for details see expressions in [8]-[9]. We assume that a minimum scattering probe is chosen for this measurement. Thus (29) is approximated by

$$S_{22}^T \simeq \Gamma^{AUT}. \quad (30)$$

In some cases, multiple reflections may have noticeable effect. Then the whole theory of the measurement can be repeated as changing distances between antennas by a quarter wavelength. Averaging the results from two distances suppress the multiple reflections.

Then the impedance of the AUT, Z^{AUT}, can be determined from S_{22}^T by using the formula

$$Z^{AUT} = \frac{1+\Gamma^{AUT}}{1-\Gamma^{AUT}} Z_0, \tag{31}$$

where Z_0 is the reference impedance.

In summary, the steps of this near-field cable-free impedance and gain measurement are given as follows.

- First, three measurement sets of the reflection coefficient of the probe are performed, when the AUT is loaded in turn by a short, open, and a known impedance.
- Second, the reflection coefficient of these three loads, the short, open, and known impedance, are measured.
- Third, the parameters S_{22}^T and $S_{12}^T S_{21}^T$ are extracted by solving the equations (27) and (28).
- The AUT impedance is determined using (31). For an electrically small AUT that resembles a single electric dipole, the AUT partial gain, along $\hat{x}'$-axis, is determined using (27), (28) and (20). It is noted that the probe parameters are obtained from a separate calibration. Moreover, since only the partial gain is determined from (20), one more gain measurement , for instance with AUT being loaded with a short, is required in the orthogonal orientation of the AUT. The cross-polarization gain and total gain are determined from (21) and (22), respectively. For an electrically small AUT that is resembled by a single magnetic dipole, the AUT gain is determined from (23), (24) and (25).

V. Conclusions

In summary, a cable-free near-field impedance and gain measurement technique for ESAs is proposed in this paper. The electromagnetic model and the formulation of impedance and gain measurements are presented. The idea of this measurement is that with the electrically small AUT placed in the near-field region of the probe, the properties of AUT are extracted by measuring the signal scattered by it without using the feed line, when it is loaded in turn with three known loads. This technique is a further development of cable-free measurement technique [8]- [9], with the distance between the probe and AUT being reduced.

This technique has the following advantages. First, the limited dynamic range problem is avoided by performing the measurement in the near-field region of the probe. As a result, the effect of noise is reduced and thus the measurement accuracy is improved significantly.Second, only a compact anechoic environment is required, which is easy to build. The expense of this technique is increasing complexity of the model. The future work will be focused on the analysis and discussions on the simulation and measurement results.

References

[1] R. J. Garbacz, "Determination of antenna parameters by scattering cross section measurements," *Proc. Inst. Elect. Eng.*, vol. 111, no. 10, pp. 1679-1686, Oct. 1964.

[2] J. Appel-Hansen, "Accurate determination of gain and radiation patterns by radar crosssection measurements," *IEEE Trans. Antennas Propagat.*, vol. AP-27, pp. 640-645, Sept. 1979.

[3] W. Wiesbeck and E. Heidrich, "Wide-band multiport antenna characteriztion by polarimetric RCS measurement," *IEEE Trans. AnreMos Propogat.*, vol. AP-46. pp. 341-350, March 1998.

[4] Hsin-Chia Lu and Tah-Hsiung Chu, "Antenna Gain and Scattering Measurement Using Reflective Three-Antenna Method," *Antennas and Propagation Society International Symposium*, 1999.

[5] B. Monsalve, S. Blanch, J.Romeu, and L. Jofre, "A contact-less small antenna characterization through impedance modulation," *3rd European Conference on Antennas and Propagation, EuCAP 2009*, pp. 696-698, 2009.

[6] M. H. Capstick, J. O. Jekkonen, A. C. Marvin, I. D. Flintoft, L. Dawson, "A Novel Indirect Method to Determine the Radiation Impedance of a Handheld Antenna Structure" *IEEE Trans. Instrum. Meas.*, vol. 58, iss. 3, pp. 578-585, March 2009.

[7] J. Zhang, S. Pivnenko, A.Khatun, T.Laitinen, and J.Carlsson, "Characterization of Small Antennas for Hearing Aids by Several Measurement Technique," *4th European Conference on Antennas and Propagation, EuCAP*, 2010.

[8] Jiaying Zhang, Sergey Pivnenko and Olav Breinbjerg, "A Cable-Free Impedance and Gain Measurement Technique for Electrically Small Antennas," *Proceedings of the 32nd Annual Symposium of Antenna Measurement Techniques Association , AMTA2010*, Atlanta, US, Oct. 2010.

[9] Jiaying Zhang, Sergey Pivnenko and Olav Breinbjerg, "Theory and Practice of a Cable-Free Impedance and Gain Measurement Technique for Electrically Small Antennas," *In Submitting*, 2011.

[10] J. E. Hansen, "Spherical Near-Field Antenna Measurements", *Peter Peregrinus Ltd. London*, 1988.

[11] P. Koivisto, "Analytical solution for characteristic modal power distribution and truncation limit for spherical wave expansion of antenna radiation pattern" *Journal of electromagnetic waves and applications* , vol. 16, iss. 9, pp. 1307-1328, 2002.

Curriculum Vitae

Jiaying Zhang was born in Harbin, China, on September 17, 1980. She graduated with her Bachelor of Engineering (B.Eng.) degree from Harbin Institute of Technology (HIT), China, in July 2003. She graduated with M.Sc degree in Electrical Engineering from Technical University of Denmark (DTU), Denmark, in September 2007. Her master thesis focused on the antenna systems for the Pico-Satellite (DTUsat). In January 2008, she started her research work as a Ph.D. candidate at the Electromagnetic System group (EMS) , Electrical Engineering Department, Technical University of Denmark (DTU), Denmark. Her research work in DTU, which is presented in this dissertation, focused on the antenna miniaturization for ultra small wireless devices, especially for the hearing-aids application, as well as the small antenna measurement techniques.

She was awarded the Travel Grant of 950 Euros from the summer school "Compact Antennas", within the European School of Antennas, at Technical University of Catalonia (UPC), Barcelona, July 2009. She was awarded the Travel Grant of 25,000 DKK from Mogens Balslevs Fund in October 2010, for the short scientific visit at University of Arizona, US. She received the Honorable Mention Award in the AMTA student paper contest, 32nd Annual Symposium of Antenna Measurement Techniques Association (AMTA 2010), Atlanta, October 2010.

Bibliography

[1] R. C. Hansen. *Electrically Small, Superdirective, and Superconducting Antennas*. Wiley-Interscience, 2006.

[2] Douglas B. Miron. *Small Antenna Design*. Newnes, 2006.

[3] John Volakis. *Antenna Engineering Handbook (Fourth Edition)*. McGraw-Hill Professional, 2007.

[4] K. Fujimoto, A. Henderson, A. Hirasawa, and J. R. James. *Small Antennas (Electronic and Electrical Engineering Research Studies/Antennas Series, No 7)*. John Wiley & Sons, January 1987.

[5] B.D. Popović, M.B. Dragović, and A.R. Djordjević. *Analysis and synthesis of wire antennas*. Research Studies Press in Chichester, 1982.

[6] John Volakis, Chi-Chih Chen, and Kyohei Fujimoto. *Small Antennas:Miniaturization Techniques & Applications*. McGraw-Hill Professional, June, 2010.

[7] H.A. Wheeler. Fundamental limitations of small antennas. *Proceedings of the IRE*, 35(12):1479 – 1484, 1947.

[8] Ronold W. P. King and Charles Harrison. *Antennas and Waves: A Modern Approach*. The MIT Press, 1970.

[9] R.C. Hansen. Fundamental limitations in antennas. *Proceedings of the IEEE*, 69(2):170 – 182, 1981.

[10] Peter Meincke. *Wireless Communications*. Lecture notes 31405 (Technical University of Denmark), Spring, 2006.

[11] L. J. Chu. Physical limitations of omni-directional antennas. *Journal of Applied Physics*, 19(12):1163 –1175, December 1948.

[12] R. Collin and S. Rothschild. Evaluation of antenna q. *Antennas and Propagation, IEEE Transactions on*, 12(1):23 – 27, January 1964.

[13] J. S. McLean. A re-examination of the fundamental limits on the radiation q of electrically small antennas. *Antennas and Propagation, IEEE Transactions on*, 44(5):672, May 1996.

[14] H.D. Foltz and J.S. McLean. Limits on the radiation q of electrically small antennas restricted to oblong bounding regions. In *Antennas and Propagation Society International Symposium, 1999. IEEE*, volume 4, pages 2702 –2705 vol.4, August 1999.

[15] G.A. Thiele, P.L. Detweiler, and R.P. Penno. On the lower bound of the radiation q for electrically small antennas. *Antennas and Propagation, IEEE Transactions on*, 51(6):1263 – 1269, 2003.

[16] W. Geyi. Physical limitations of antenna. *Antennas and Propagation, IEEE Transactions on*, 51(8):2116 – 2123, 2003.

[17] R. Fante. Quality factor of general ideal antennas. *Antennas and Propagation, IEEE Transactions on*, 17(2):151 – 155, March 1969.

[18] A.D. Yaghjian and S.R. Best. Impedance, bandwidth, and q of antennas. *Antennas and Propagation, IEEE Transactions on*, 53(4):1298 – 1324, 2005.

[19] S.R. Best. The performance properties of electrically small resonant multiple-arm folded wire antennas. *Antennas and Propagation Magazine, IEEE*, 47(4):13 – 27, 2005.

[20] S.R. Best. Bandwidth and the lower bound on q for small wideband antennas. In *Antennas and Propagation Society International Symposium 2006, IEEE*, pages 647 –650, 2006.

[21] S.R. Best. The radiation properties of electrically small folded spherical helix antennas. *Antennas and Propagation, IEEE Transactions on*, 52(4):953 – 960, 2004.

[22] S.R. Best. Low q electrically small linear and elliptical polarized spherical dipole antennas. *Antennas and Propagation, IEEE Transactions on*, 53(3):1047 – 1053, 2005.

[23] S.R. Best and J.D. Morrow. On the significance of current vector alignment in establishing the resonant frequency of small space-filling wire antennas. *Antennas and Wireless Propagation Letters, IEEE*, 2003.

[24] H.L. Thal. New radiation limits for spherical wire antennas. *Antennas and Propagation, IEEE Transactions on*, 54(10):2757 –2763, 2006.

[25] H.L. Thal. Gain and q bounds for coupled tm-te modes. *Antennas and Propagation, IEEE Transactions on*, 57(7):1879 –1885, 2009.

[26] Mats Gustafsson, Christian Sohl, and Gerhard Kristensson. Physical limitations on antennas of arbitrary shape. *Proceedings of the Royal Society A: Mathematical, Physical and Engineering Science*, 463(2086):2589–2607, 2007.

[27] Christian Sohl, Mats Gustafsson, and Gerhard Kristensson. Physical limitations on broadband scattering by heterogeneous obstacles. *Journal of Physics A: Mathematical and Theoretical*, 40(36):11165, 2007.

[28] Christian Sohl, Mats Gustafsson, and Gerhard Kristensson. The integrated extinction for broadband scattering of acoustic waves. *The Journal of the Acoustical Society of America*, 122(6):3206–3210, 2007.

[29] Christian Sohl, Mats Gustafsson, and Gerhard Kristensson. Physical limitations on metamaterials: restrictions on scattering and absorption over a frequency interval. *Journal of Physics D: Applied Physics*, 40(22):7146, 2007.

[30] A. Derneryd, M. Gustafsson, G. Kristensson, and C. Sohl. Application of gain-bandwidth bounds on loaded dipoles. *Microwaves, Antennas Propagation, IET*, 3(6):959 –966, 2009.

[31] Peter Meincke. *31430 Antennas Exercise Notes*. Lecture notes 31430 (Technical University of Denmark), Fall, 2006.

[32] Warren L. Stutzman and Gary A. Thi. *Antenna Theory and Design (2nd Edition)* . Wiley, December 15, 1997.

[33] David M. Pozar. *Microwave Engineering (3rd Edition edition)*. John Wiley & Sons, Jan, 2004.

[34] Jr. Thomas R. Cuthbert. *Broadband Direct-Coupled and Matching RF Networks*. TRCPEP, 1999.

[35] Jiaying Zhang. *Antenna Systems for the Pico Satelite DTUsat*. Master Thesis, 2007.

[36] R.L. Li, G. DeJean, E. Tsai, E. Tentzeris, and J. Laskar. Novel small folded shorted-patch antennas. In *Antennas and Propagation Society International Symposium, 2002. IEEE*, volume 4, pages 26 – 29 vol.4, 2002.

[37] P. M. Mendes, A. Polyakov, M. Bartek, J. N. Burghartz, and J. H. Correia. Design of a folded-patch chip-size antenna for short-range communications. In *Microwave Conference, 2003. 33rd European*, pages 723 –726, oct. 2003.

[38] RongLin Li, G. DeJean, M.M. Tentzeris, and J. Laskar. Development and analysis of a folded shorted-patch antenna with reduced size. *Antennas and Propagation, IEEE Transactions on*, 52(2):555 – 562, feb. 2004.

[39] Jiaying Zhang and O. Breinbjerg. Miniaturization of multiple-layer folded patch antennas. In *Antennas and Propagation, 2009. EuCAP 2009. 3rd European Conference on*, pages 3502 –3506, 2009.

[40] A. Erentok and R.W. Ziolkowski. Metamaterial-inspired efficient electrically small antennas. *Antennas and Propagation, IEEE Transactions on*, 56(3):691 –707, 2008.

[41] A. Alu, N. Engheta, A. Erentok, and R.W. Ziolkowski. Single-negative, double-negative, and low-index metamaterials and their electromagnetic applications. *Antennas and Propagation Magazine, IEEE*, 49(1):23 –36, 2007.

[42] A. Erentok and R.W. Ziolkowski. A hybrid optimization method to analyze metamaterial-based electrically small antennas. *Antennas and Propagation, IEEE Transactions on*, 55(3):731 –741, 2007.

[43] R.W. Ziolkowski and A. Erentok. Metamaterial-based efficient electrically small antennas. *Antennas and Propagation, IEEE Transactions on*, 54(7):2113 – 2130, 2006.

[44] R.W. Ziolkowski and A. Erentok. At and below the chu limit: passive and active broad bandwidth metamaterial-based electrically small antennas. *Microwaves, Antennas Propagation, IET*, 1(1):116 –128, 2007.

[45] R.W. Ziolkowski, Peng Jin, and Chia-Ching Jin. Electrically small metamaterial-inspired antennas: Designs and measurements, efficiency and bandwidth performance. In *Antenna Technology, 2009. iWAT 2009. IEEE International Workshop on*, pages 1 –4, 2009.

[46] Peng Jin and R.W. Ziolkowski. Metamaterial-inspired, electrically small huygens sources. *Antennas and Wireless Propagation Letters, IEEE*, 2010.

[47] Peng Jin and R.W. Ziolkowski. Low-q, electrically small, efficient near-field resonant parasitic antennas. *Antennas and Propagation, IEEE Transactions on*, 57(9):2548 –2563, 2009.

[48] R.W. Ziolkowski, Chia-Ching Lin, J.A. Nielsen, M.H. Tanielian, and C.L. Holloway. Design and experimental verification of a 3d magnetic ez antenna at 300 mhz. *Antennas and Wireless Propagation Letters, IEEE*, 2009.

[49] Chia-Ching Lin, Richard W. Ziolkowski, Jean A. Nielsen, Minas H. Tanielian, and Christopher L. Holloway. An efficient, low profile, electrically small, three-dimensional, very high frequency magnetic ez antenna. *Applied Physics Letters*, 96(10):104102 –104102–3, March 2010.

[50] David E. Goldberg. *Genetic Algorithms in Search, Optimization, and Machine Learning*. Addison-Wesley Professional, 1 edition, January 1989.

[51] A. E. Eiben and J. E. Smith. *Introduction to Evolutionary Computing (Natural Computing Series)*. Springer, October 2008.

[52] Yahya Rahmat-Samii and Eric Michielssen. *Electromagnetic Optimization by Genetic Algorithms (1st edition) (Wiley Series in Microwave and Optical Engineering)*. Wiley-Interscience, July 23, 1999.

[53] http://www.ansoft.com.

[54] Jeff Solum. Hearing aids: Cutting edge technology. *https://mentor.ieee.org/802.15/folder?p=3021500003&n=4*, May 2008.

[55] H. Choo and H. Ling. Design of electrically small planar antennas using inductively coupled feed. *Electronics Letters*, 39(22):1563 – 1565, oct. 2003.

[56] Hosting Choo and Hao Ling. Design of planar, electrically small antennas with inductively coupled feed using a genetic algorithm. In *Antennas and Propagation Society International Symposium, 2003. IEEE*, volume 1, pages 300 – 303 vol.1, june 2003.

[57] Kamil Boratay Alici and Ekmel Ozbay. Electrically small split ring resonator antennas. *Journal of Applied Physics*, 101(8):083104 –083104–4, apr 2007.

[58] Kin-Lu Wong and Tzung-Wern Chiou. Single-patch broadband circularly polarized microstrip antennas. In *Antennas and Propagation Society International Symposium, 2000. IEEE*, volume 2, pages 984 –987 vol.2, 2000.

[59] Kamil Boratay Alici and Ekmel Ozbay. Electrically small split ring resonator antennas. *Journal of Applied Physics*, 101(8):083104 –083104–4, apr 2007.

[60] Constantine A. Balanis. *Antenna Theory: Analysis and Design, 2ed Edition, Chapter 9*. John Wiley & Sons, Inc., 1997.

[61] C. Icheln, M. Popov, P. Vainikainen, and S. He. Optimal reduction of the influence of rf feed cables in small antenna measurements. *Microw Opt. Technol. Lett.*, 2000.

[62] H.A. Wheeler. The radiansphere around a small antenna. *Proceedings of the IRE*, 47(8):1325 –1331, 1959.

[63] R.H. Johnston and J.G. McRory. An improved small antenna radiation-efficiency measurement method. *Antennas and Propagation Magazine, IEEE*, 40(5):40 –48, October 1998.

[64] M. Geissler, O. Litschke, D. Heberling, P. Waldow, and I. Wolff. An improved method for measuring the radiation efficiency of mobile devices. In *Antennas and Propagation Society International Symposium, 2003. IEEE*, volume 4, pages 743 – 746 vol.4, 2003.

[65] C. Mendes and C. Peixeiro. Theoretical and experimental validation of a generalized wheeler cap method. In *Antennas and Propagation, 2007. EuCAP 2007. The Second European Conference on*, pages 1 –6, 2007.

[66] R. Meys and F. Janssens. Measuring the impedance of balanced antennas by an s-parameter method. *Antennas and Propagation Magazine, IEEE*, 40(6):62 –65, December 1998.

[67] K.D. Palmer and M.W. van Rooyen. Simple broadband measurements of balanced loads using a network analyzer. *Instrumentation and Measurement, IEEE Transactions on*, 55(1):266 – 272, 2006.

[68] Xianming Qing, Chean Khan Goh, and Zhi Ning Chen. Impedance characterization of rfid tag antennas and application in tag co-design. *Microwave Theory and Techniques, IEEE Transactions on*, 57(5):1268 –1274, May 2009.

[69] Jiaying Zhang, S. Pivnenko, and Olav Breinbjerg. A modified wheeler cap method for radiation efficiency measurement of balanced electrically small antennas. In *Antennas and Propagation (EuCAP), 2010 Proceedings of the Fourth European Conference on*, pages 1 –5, 2010.

[70] R.J. Garbacz. Determination of antenna parameters by scattering cross-section measurements. *Electrical Engineers, Proceedings of the Institution of*, 111(10):1679 –1686, 1964.

[71] Hsin-Chia Lu and Tah-Hsiung Chu. Antenna gain and scattering measurement using reflective three-antenna method. In *Antennas and Propagation Society International Symposium, 1999. IEEE*, volume 1, pages 374 –377 vol.1, August 1999.

[72] Hansen J. E. *Spherical Near-Field Antenna Measurements*. Peter Peregrinus Ltd. London, 1988.

[73] Peter S. Hall and Yang Hao. *Antennas And Propagation for Body-Centric Wireless Communications*. Artech House Publishers, 2006.

[74] Theodore S. Rappaport. *Wireless Communications: Principles and Practice (2nd Edition)* . Prentice Hall, 2002.

[75] C Gabriel, S Gabriel, and E Corthout. The dielectric properties of biological tissues: I. literature survey. *Physics in Medicine and Biology*, 41(11):2231, 1996.

[76] S Gabriel, R W Lau, and C Gabriel. The dielectric properties of biological tissues: Ii. measurements in the frequency range 10 hz to 20 ghz. *Physics in Medicine and Biology*, 41(11):2251, 1996.

[77] S Gabriel, R W Lau, and C Gabriel. The dielectric properties of biological tissues: Iii. parametric models for the dielectric spectrum of tissues. *Physics in Medicine and Biology*, 41(11):2271, 1996.

[78] Camelia Gabriel. Dielectric properties of biological tissue: Variation with age. *Bioelectromagnetics*, 26(S7):S12–S18, 2005.

[79] Camelia Gabriel. Compilation of the dielectric properties of body tissues at rf and microwave frequencies. *U.S. Air Force Report AFOSRTR-96*, 1996.

[80] Y. Rahmat-Samii and K.W. Kim. Antennas and human in personal communications: applications of modern em computational techniques. In *Microwaves and Radar, 1998. MIKON '98., 12th International Conference on*, volume 4, pages 36 –55 vol.4, may 1998.

[81] Claude M. Weil. Absorption characteristics of multilayered sphere models exposed to uhf/microwave radiation. *Biomedical Engineering, IEEE Transactions on*, BME-22(6):468 –476, nov. 1975.

[82] Y. Kamimura, E. Murata, and Y. Yamada. Frequency dependence of energy deposition in the multilayered spherical model of a human head near a half wavelength dipole. In *Electromagnetic Compatibility, 1999 International Symposium on*, pages 329 –332, 1999.

[83] http://www.speag.com/products/over-the-air-performance/head-phantoms/sam v45bs/.

[84] http://www.speag.com/assets/downloads/products/ota/OTAUser Manual.pdf.